

**A NUMERICAL STUDY OF
CAVITATION INCEPTION IN COMPLEX FLOW FIELDS**

by

Georges L. Chahine, Chao-Tsung Hsiao, and Jin-Keun Choi

December 2007

DYNAFLOW, INC.
10621-J Iron Bridge Road
Jessup, MD 20794

Phone: (301)604 3688
e-mail: info@dynafow-inc.com
<http://www.dynafow-inc.com/>

Report Documentation Page			Form Approved OMB No. 0704-0188	
<p>Public reporting burden for the collection of information is estimated to average 1 hour per response, including the time for reviewing instructions, searching existing data sources, gathering and maintaining the data needed, and completing and reviewing the collection of information. Send comments regarding this burden estimate or any other aspect of this collection of information, including suggestions for reducing this burden, to Washington Headquarters Services, Directorate for Information Operations and Reports, 1215 Jefferson Davis Highway, Suite 1204, Arlington VA 22202-4302. Respondents should be aware that notwithstanding any other provision of law, no person shall be subject to a penalty for failing to comply with a collection of information if it does not display a currently valid OMB control number.</p>				
1. REPORT DATE 01 DEC 2007	2. REPORT TYPE N/A	3. DATES COVERED -		
4. TITLE AND SUBTITLE A Numerical Study Of Cavitation Inception In Complex Flow Fields			5a. CONTRACT NUMBER	
			5b. GRANT NUMBER	
			5c. PROGRAM ELEMENT NUMBER	
6. AUTHOR(S)			5d. PROJECT NUMBER	
			5e. TASK NUMBER	
			5f. WORK UNIT NUMBER	
7. PERFORMING ORGANIZATION NAME(S) AND ADDRESS(ES) DYNAFLOW, INC. 10621-J Iron Bridge Road Jessup, MD 20794			8. PERFORMING ORGANIZATION REPORT NUMBER	
9. SPONSORING/MONITORING AGENCY NAME(S) AND ADDRESS(ES)			10. SPONSOR/MONITOR'S ACRONYM(S)	
			11. SPONSOR/MONITOR'S REPORT NUMBER(S)	
12. DISTRIBUTION/AVAILABILITY STATEMENT Approved for public release, distribution unlimited				
13. SUPPLEMENTARY NOTES The original document contains color images.				
14. ABSTRACT				
15. SUBJECT TERMS				
16. SECURITY CLASSIFICATION OF: a. REPORT b. ABSTRACT c. THIS PAGE unclassified unclassified unclassified			17. LIMITATION OF ABSTRACT UU	18. NUMBER OF PAGES 167
				19a. NAME OF RESPONSIBLE PERSON

TABLE OF CONTENTS

LIST OF TABLES.....	3
LIST OF FIGURES.....	4
FOREWORD AND ACKNOWLEDGMENTS	5
1. BACKGROUND.....	6
2. SUMMARY OF THE WORK.....	8
2.1 SCALING EFFECTS ON CAVITATION INCEPTION OF FINITE-SPAN HYDROFOIL [4]	8
2.2 EFFECT OF VORTEX/VORTEX INTERACTION ON CAVITATION INCEPTION FOR DUCTED PROPULSOR [12] ...	11
2.3 EFFECT OF PRESSURE FLUCTUATIONS ON CAVITATION INCEPTION FOR A DUCTED PROPULSOR [13]	13
2.4 EFFECT OF VORTEX/WAKE INTERACTION ON CAVITATION INCEPTION IN AN OPEN PROPELLER	15
2.5 NON-SPHERICAL BUBBLE EFFECTS ON CAVITATION INCEPTION [14,15]	18
2.6 STUDY OF CAVITATION INCEPTION NOISE [16,17,18].....	21
3. ATTACHED Publications.....	25
4. REFERENCES	26

LIST OF TABLES

TABLE 1. SUMMARY OF THE POWER CONSTANT IN THE SCALING LAW FOR THE NACA HYDROFOILS IN THE CASE OF A RELATIVELY LARGE VOID FRACTION.....	10
TABLE 2. SUMMARY OF THE POWER CONSTANT IN THE SCALING LAW FOR THE NACA HYDROFOILS IN THE CASE OF A RELATIVELY LOW VOID FRACTION.....	10

LIST OF FIGURES

FIGURE 1. LOCATION AND SIZE OF RANDOMLY DISTRIBUTED NUCLEI.....	8
FIGURE 2. EXAMPLE OF CAVITATION INCEPTION SIMULATION USING DF_UNCLE TM AND DF_MULTI_SAP [®]	9
FIGURE 3. SCALING OF CAVITATION INCEPTION FOR A SET OF NACA HYDROFOILS.	9
FIGURE 4. COMPUTATIONAL DOMAIN FOR THE DNSS SIMULATIONS WITH BUBBLE DYNAMICS AND RANS INPUT SOLUTION	11
FIGURE 5. COMPARISON OF THE PRESSURE COEFFICIENT VERSUS DOWNSTREAM DISTANCE FROM THE PROPELLER BLADE TIP BETWEEN RANS SOLUTION AND OUR DNSS SIMULATIONS.	12
FIGURE 6. ISO-PRESSURE SURFACES EQUIVALENT TO CAVITATION EXTENT AT VARIOUS CAVITATION NUMBERS AS OBTAINED BY THE RANS SOLUTION AND THE CURRENT DNSS SOLUTION.....	12
FIGURE 7. COMPARISON OF CAVITATION EXTENT BETWEEN THE NUMERICAL SIMULATIONS AND THE EXPERIMENTAL OBSERVATIONS OF CHESNAKAS AND JESSUP, 2003.	12
FIGURE 8. BUBBLE TRAJECTORIES AND SIZE VARIATIONS DURING CAVITATION EVENTS FOR THREE CASES.	13
FIGURE 9. TIME VARIATIONS OF $C_{P_{MIN}}$ AND ITS LOCATION FOR SEVERAL CONDITIONS OF IMPOSED FLUCTUATIONS ABOUT THE RANS INPUT BOUNDARY CONDITIONS IN THE DIRECT NAVIER STOKES NUMERICAL SOLUTIONS.....	14
FIGURE 10. PRESSURE COEFFICIENTS BEHIND THE DUCTED PROPULSOR BLADE COMPUTED BY RANS AND BY DIRECT NAVIER STOKES NUMERICAL SOLUTION WITH AND WITHOUT FLUCTUATIONS IMPOSED ON THE UPSTREAM INLET TO THE COMPUTATIONAL DOMAIN.....	14
FIGURE 11. CAVITATING BUBBLES LOCATIONS FROM THE NAVIER STOKES NUMERICAL SOLUTION AND DF_MULTI_SAP BUBBLE SIMULATIONS. COMPARISON BETWEEN USING THE RANS SOLUTION AT THE COMPUTATIONAL DOMAIN UPSTREAM INLET AND IMPOSING UNSTEADY FLUCTUATIONS TO THE RANS SOLUTION. $\sigma=10.75$	15
FIGURE 12. A VIEW OF THE FINER GRID REDUCED COMPUTATIONAL DOMAIN USED IN THE DNSS COMPUTATIONS.....	15
FIGURE 13. COMPARISON OF VORTICITY CONTOURS FOR THE SOLUTIONS OBTAINED BY RANS AND DNSS.	16
FIGURE 14. COMPARISON OF THE PRESSURE COEFFICIENT FOR THE SOLUTIONS OBTAINED BY RANS AND DNSS.	16
FIGURE 15. COMPARISON OF THE VOID FRACTION VARIATIONS ALONG X FOR THE RANS AND DNSS SOLUTIONS.	17
FIGURE 16. COMPARISON OF THE BUBBLE SIZE DISTRIBUTION AT $X = 0.2$ M FOR THE RANS AND DNSS SOLUTIONS... <td>17</td>	17
FIGURE 17. COMPARISON OF THE DOWNSTREAM VOID FRACTIONS FOR THE RANS AND DNSS SOLUTIONS.	18
FIGURE 18. EXAMPLE OF A BUBBLE BEHAVIOR WITH TWO JETS AT $\Sigma=2.50$ AS PREDICTED BY 2DYNAFS [®] IN A TIME SEQUENCE FROM LEFT TO RIGHT.....	18
FIGURE 19. AMPLITUDE SPECTRA OF THE ACOUSTIC PRESSURE SIGNAL FROM 100 NUCLEI OF SIZE 20 MM WITH SPLITTING COMPARED TO THAT WITHOUT SPLITTING. $\Sigma = 2.10$. ALSO SHOWN IN THE SPECTRA IS THE INFLUENCE OF THE INCLUSION OF THE REENTRANT JET NOISE ON THE RESULTS.....	19
FIGURE 20. BUBBLE BEHAVIOR IN A VORTEX FLOW FIELD: CORE RADIUS = 4.51 MM, CIRCULATION = $0.2123 \text{ m}^2/\text{s}$; $\sigma =$ 1.72 ; $U_\infty = 10 \text{ m/s}$; INITIAL RADIUS OF THE BUBBLE = $750\mu\text{m}$. THREE-DIMENSIONAL VIEW OF THE BUBBLE JUST BEFORE SPLITTING PREDICTED BY 2DYNAFS [®]	19
FIGURE 21. SUPERIMPOSED SUCCESSIVE IMAGES OF LASER-INDUCED BUBBLES BEHAVIOR AT THE CENTER OF A VORTEX; $\sigma = 1.72$; $U_\infty = 10 \text{ m/s}$. IMAGE DIMENSIONS (H 26.0 MM X V 8.3 MM. (FROM[15]).....	20
FIGURE 22. THE BUBBLE SIZE AND SHAPE VARIATIONS AND THE CORRESPONDING EMITTED ACOUSTIC SIGNAL FOR A SINGLE CAVITATION EVENT CAPTURED STUDYING THE VORTEX CHAMBER WITH VENTURI.....	20
FIGURE 23. BUBBLE SIZE AND SHAPE AT SUPERPOSED SUCCESSIVE TIME STEPS WITH THE BACKGROUND FLOW FIELD ILLUSTRATED BY PRESSURE CONTOURS.....	21
FIGURE 24. RESULTS OF SAP SIMULATION OF CAVITATION WITH GAS DIFFUSION ON PROP5168 PROPELLER. THE BUBBLES IN SECTION A ARE TO SCALE. THE BUBBLES UPSTREAM AND DOWNSTREAM WERE MAGNIFIED BY FIVE TO MAKE THEM MORE VISIBLE.....	22
FIGURE 25. CLOSE UP OF THE VELOCITY AND PRESSURE FIELD OF THE BUBBLES DURING SPLITTING; $T/T^* = 6$, RE_Γ $= 4 \times 10^5$, $\Sigma_C = 0.3$, $L_B/D_B = 2$ (FROM [17])	23
FIGURE 26. ACOUSTIC PRESSURE SIGNALS PREDICTED BY THE AXISYMMETRIC BOUNDARY ELEMENT METHOD, 2DYNAFS [®] , WHICH ALLOWS BUBBLE ELONGATION AND SPLITTING. DATA FOR TWO REYNOLDS NUMBERS, FOUR INITIAL NUCLEI SIZES, AND THREE VORTEX CORE SIZES FALL ON VERY CLOSELY NEAR THE CURVE FIT.....	24
FIGURE 27. BUBBLE RADIUS AND ACOUSTIC PRESSURE SIGNAL AMPLITUDE AS FUNCTIONS OF TIME PREDICTED FOR 20 MM NUCLEI AT $\Sigma=2.26$ (CAVITATION INCEPTION).....	24
FIGURE 28. MAXIMUM OF THE ACOUSTIC PRESSURE SIGNAL VS. CAVITATION NUMBERS PREDICTED WITH 20 MM NUCLEI.....	25

FOREWORD AND ACKNOWLEDGMENTS

This report describes DYNALFOW's efforts over the past three years to develop and apply innovative methods to study and model the cavitation inception in complex flow fields. Our approach is rooted in recognizing the fundamental dependence of cavitation inception on the presence of nuclei in the liquid. The study addresses fundamental interactions between the bubble nuclei distribution and the host liquid. It also addresses the importance of proper modeling of the flow in the host liquid, especially in vortical regions where the pressures depend critically on the proper description of the time dependence of the vorticity. This work was conducted under the contract N00014-04-C-0110. This study has benefited from the support of many DYNALFOW colleagues who have helped in various aspects. We would like to thank them. The support and interest of Dr. Ki-Han Kim at the Office of Naval Research are also greatly appreciated.

1. BACKGROUND

Prediction of cavitation inception on Navy propulsors is a very challenging task that has preoccupied propulsor designers for many years. This is in fact true for predictions using scaled experimental tests as well as for predictions based on analytical/numerical modeling. Over the past few years very significant progress has been accomplished by the community in terms of both experimental measurements and numerical techniques development and their application to the problem. Novel sophisticated velocity flow field measurement techniques and their efficient practical application to propulsor studies both at Navy research centers and at other Navy funded laboratories has enabled impressive measurements of the complex flow field in details never observed before. These observations quantified mainly the space variations of the flow field using some time and space averaging. Some effort, but so far less impressive, has also illustrated the time unsteady nature of the challenging phenomena. However, additional efforts are necessary but require tremendous capabilities in data storage and analysis to provide us with time fluctuations of pressures. In parallel impressive progress in computational techniques and in computer power has enabled more and more complex and large simulations. These have included Reynolds Averaged Navier Stokes (RANS) simulation, Large Eddy Simulations (LES) and Direct Numerical Simulations (DNS) applied to larger and larger problems.

This sophistication in the investigative tools has brought out that original assumptions concerning vortex cavitation inception in a propulsor were too simple, understandably due to the lack of knowledge, measurement, and prediction of the detailed flow phenomena. While '*developed*' cavitation follows the rules already established by the community, cavitation inception prediction and detection appears to be a moving target function of the progress in the technology. Indeed, recent observations seem to indicate that unsteadiness of the flow field and phenomena initially thought to be secondary may be predominant factors for '*early*' inception. Here, we are using '*early*' (and '*developed*') to denote that the definition of cavitation inception itself is an evolving concept with detection occurring '*earlier*' and earlier with advances in acoustic means of detection and reduction in background noise.

Our contribution to propeller cavitation study was to address the problem of bubble nuclei in the liquid flow field and their dynamics. We have successfully undertaken efforts to consider the interaction between the nuclei dynamic and the 'basic' liquid flow field, and considered the influence of the inclusion of bubble dynamics effects on cavitation inception predictions. As contradictory as it may appear, most predictions ignore the presence of bubble nuclei ignoring numerous studies that have indicated significant differences in the experimental cavitation inception results between tests even on the simplest geometries (head forms, disks, NACA 2D and 3D foils). This has been observed systematically when tests were conducted on the same body in two different facilities as well as when tests were conducted in the same facility at different times using different start-up conditions (different nuclei content). This was again restated at the 2003 ASME meeting and the Cavitation Inception symposium in Hawaii [1-3].

Basing their procedures on the *engineering* definition that a liquid will cavitate when the pressure in the liquid, p , drops below the vapor pressure, p_v , most (if not all) designer predictions

are based on a single-phase (liquid) flow studies and totally disregard bubble presence and behavior. This was in fact quite acceptable and accurate when the considered liquids, at laboratory and full scales, were assumed to be fully saturated, and when cavitation inception was not ‘called’ under the present much stricter conditions. Our studies have established that when the bubble nuclei sizes and their numbers are small (deep submergence, or well degassed laboratory conditions) deviations from the $p=p_v$ inception criterion can be very significant. This results in under-prediction of cavitation inception which occurs as intermittent bursts of single bubble noise.

Our approach has resulted in the development of the following tools:

1. DF_MULTI_SAP[©] : A Lagrangian bubble nuclei tracking method, which works in a complex flow field provided by either a numerical flow field solver, or from detailed experimental observations of the flow field.
2. 2D/3DYNAFS[©] A: 2D/3D numerical method to compute cavitation bubble and cavity dynamics including cavitation on solid surfaces which allow discretized panels to switch from solid to free surfaces when the cavitation criterion is reached (sheet cavitation).
3. DF_UNCLE: A numerical method which enables full 3D cavity dynamics and two-way interaction in complex flow fields described by a RANS or a direct Navier Stokes Solution (DNS) method.
4. A combined RANS and DNS method to enhance flow field simulation.

Using the vortex flow fields generated either by a finite-span hydrofoil, an open propeller, or a ducted propulsor, we have applied the above tools to study the influence on maximum bubble size (visual cavitation inception detection) and on emitted acoustic noise of the following parameters:

- Nuclei size distribution,
- Initial bubble nuclei size,
- Cavitation number,
- Vortex flow field properties,
- Bubble deformation, splitting, reentrant jets,
- Scale effect.

This enabled us to elucidate the importance of the inception criterion selection on the results, and allowed provision of preliminary scaling rules for inception, as well as for maximum bubble size, amplitude and frequency of the emitted sound

The work conducted under this project is detailed in the attached publications. A summary of some aspects of the work and results, as well as additional information not covered in these publications are given in the following section.

2. SUMMARY OF THE WORK

2.1 SCALING EFFECTS ON CAVITATION INCEPTION OF FINITE-SPAN HYDROFOIL [4]

DYNAFLOW's approach to investigate the cavitation inception problem is to follow the individual bubble nuclei present in the flow field in a Lagrangian way using DF_MULTI_SAP[®] and observe whether the bubbles experience explosive growth to make them visible or generate large acoustic pressure signals, which make them detectable. The nuclei, when subjected to variations in the local liquid pressures, respond dynamically by changing volume, oscillating, and eventually growing to become visible due to explosive growth. This is followed by a succession of collapse and growth phases and cumulative gas transfer into the bubbles. DF_MULTI_SAP[®] solves the bubble motion equations and bubble dynamics accounting for flow non-uniformity through incorporation of bubble surface averaged quantities: pressures and velocities and a bubble slip velocity pressure term [4-7]. This numerical model allows consideration of the spatio-temporal variations of the location and size of the bubble nuclei.

Using the above approach, we have studied cavitation inception under different conditions. The first is that in the tip vortex of a hydrofoil. We consider a practical nuclei distribution model obtained by randomly distributing the nuclei in space and time according to observed nuclei size distributions. This model is applied to emit randomly in time and space nuclei for a tip vortex flow over an elliptic hydrofoil at different scales (Figure 1). In this study the flow field was obtained by a steady-state Navier-Stokes computation which provided the velocities and pressures flow field for the bubble dynamics computations. The SAP spherical model is then used to track the nuclei emitted in a pre-selected nuclei release area and to record the acoustic signals generated by their volume oscillations. Figure 2 shows an example of a time sequence of a visible cavitating bubble and the corresponding pressure signals emitted when cavitation events occur.

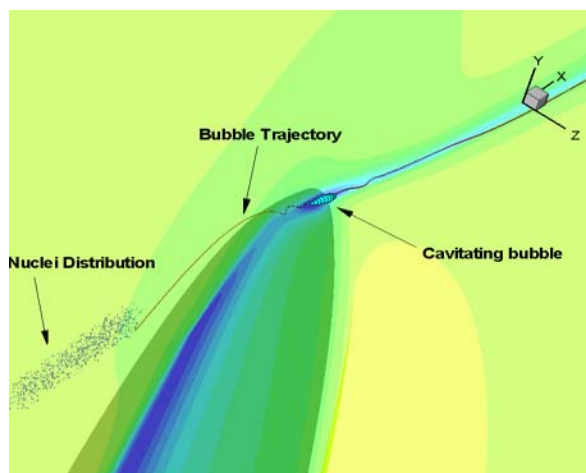


Figure 1. Location and size of randomly distributed nuclei.

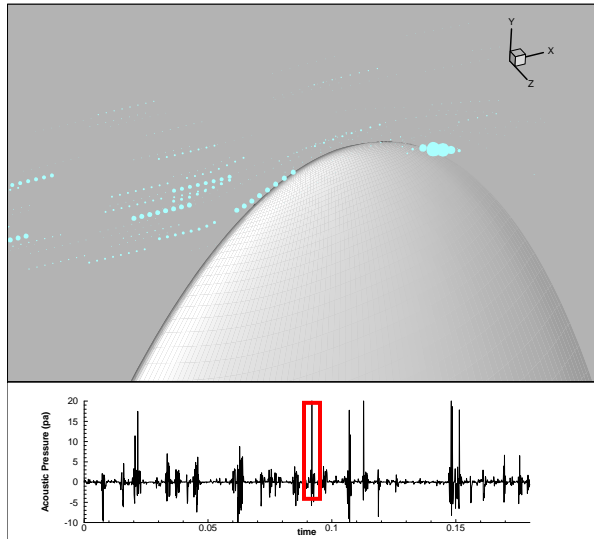


Figure 2. Example of cavitation inception simulation using DF_UNCLETM and DF_MULTI_SAP[®].

An “acoustic” criterion, which defines the cavitation inception by counting the number of acoustical signal peaks that exceed a certain level per unit time, was then applied to deduce the cavitation inception number for three different scales (small, medium and large) which correspond to three different Reynolds numbers, 1.44×10^6 , 2.88×10^6 and 5.76×10^6 . Figure 3 shows such curves when two limit acoustic pressure levels, 10 and 40 Pa, are used to call cavitation at the two scales. With a criterion to call cavitation based on the number of detected peaks and acoustic pressure level, one can determine the cavitation inception number from Figure 3. Here, the deduced cavitation inception numbers for the three scales for the criteria: 10 peaks/second which exceed 10 Pa and 50 peaks/second which exceed 40 Pa, are shown in Table 1 for weak water and in Table 2 for strong water. The deduced cavitation numbers and $-Cp_{min}$ can then be fitted to the classical power formula $\sigma_i \propto R_e^\gamma$, and the fitted values of γ are also shown in the two tables.

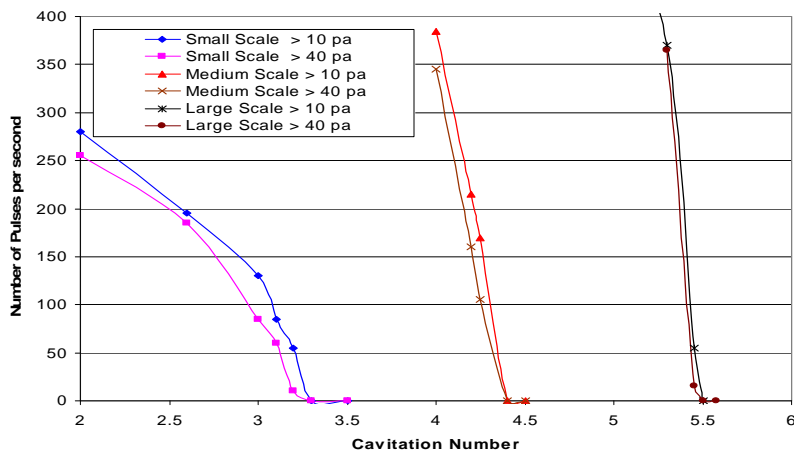


Figure 3. Scaling of cavitation inception for a set of NACA hydrofoils.

$\sigma_i \sim Re^\gamma$	Cavitation Inception Number σ_i			Re $^\gamma$ curve fit
	Small Scale	Medium Scale	Large Scale	γ
- Cp_{min}	3.34	4.34	5.48	0.357
10 peaks/sec over 10 Pa	3.28	4.33	5.47	0.369
50 peaks/sec over 40 Pa	3.12	4.28	5.44	0.401

Table 1. Summary of the power constant in the scaling law for the NACA hydrofoils in the case of a relatively large void fraction.

$\sigma_i \sim Re^\gamma$	Cavitation Inception Number σ_i			Re $^\gamma$ curve fit
	Small Scale	Medium Scale	Large Scale	γ
- Cp_{min}	3.34	-	5.48	0.357
10 peaks/sec over 10 Pa	3.20	-	5.40	0.377
50 peaks/sec over 40 Pa	2.00	-	5.18	0.687

Table 2. Summary of the power constant in the scaling law for the NACA hydrofoils in the case of a relatively low void fraction.

From this study we have learned that scaling effects and deviations from the classical $\sigma_i \propto Re^{0.4}$ increase as the inception criteria become more stringent (i.e. as the threshold pressures for cavitation is lower –less background noise– and as the number of peaks is lowered). More cavitation inception events are detected per unit time for the larger scales than those obtained by using the classical scaling. This is due to the fact that a relatively larger number of nuclei is excited by the tip vortex at the larger scale due to both increase of the nuclei capture area and of the size of the vortex core.

The average nuclei size in the nuclei distribution was also found to have an important impact on the cavitation inception number. Scaling effects (i.e. deviation from classical expressions) become more important as the average nuclei size decreases. This study was however conducted before we learned about the importance of the interaction between the tip vortex and the wake, as described later below, and it should be repeated using more accurate flow field description of the tip vortices.

2.2 EFFECT OF VORTEX/VORTEX INTERACTION ON CAVITATION INCEPTION FOR DUCTED PROPULSOR [12]

Experimental observations [8] of cavitation inception on ducted propulsors have indicated that the interaction between tip-leakage vortex and trailing-edge vortex may cause early cavitation in the strong interaction region of the two vortices. RANS simulations [9-11], have failed to predict both the value of the cavitation inception number and the location of cavitation inception on a tested ducted propulsor. Analysis procedures based on the Reynolds averaging concepts and/or using averaged experimentally measured quantities were also not successful in correlating the observed inception location and index with the deduced Cp_{min} value and location. Our investigations [12] proved that the hypothesis that vortex/vortex/nuclei interaction involve highly transient phenomena that need time accurate solutions or measurements (not time averaged) to reproduce the correct predictions. Using a direct Navier Stokes solution (DNS) simulation of the region of interest (Figure 4) combined with bubble dynamics using realistic nuclei size distribution and our DF_Multi_SAP[®] approach, we were able to recover very well the experimental results.

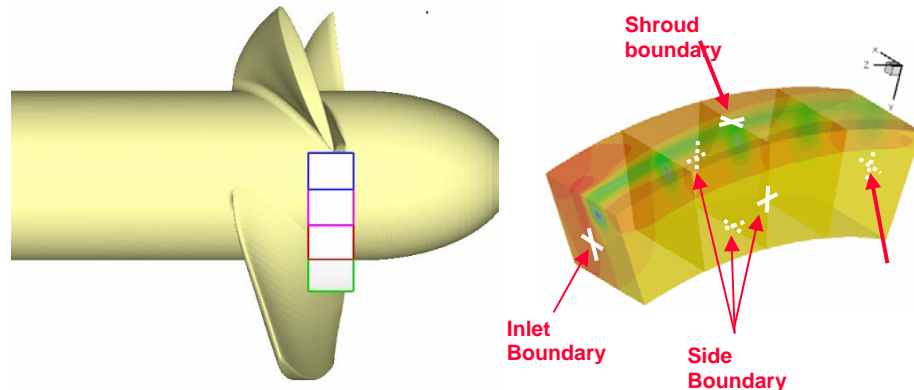


Figure 4. Computational domain for the DNS simulations with bubble dynamics and RANS input solution

We used the RANS solution to impose boundary conditions on the inner computational domain where DNS simulations were conducted (Figure 4). The Cp_{min} vs. downstream distance curve obtained with the new approach and time-accurate solution showed a much lower value of the Cp_{min} and a much further downstream location from the blade of this minimum (Figure 5).

Figure 6 shows the comparison of iso-pressure surfaces between the DNS results and the previous RANS computations. The resulting solutions illustrated with iso-pressure surfaces agree much better than the RANS computations with experimental observations for fully developed cavitation in the vortex core as well as for the value of the cavitation inception number and the cavitation inception location (Figure 7, Figure 8).

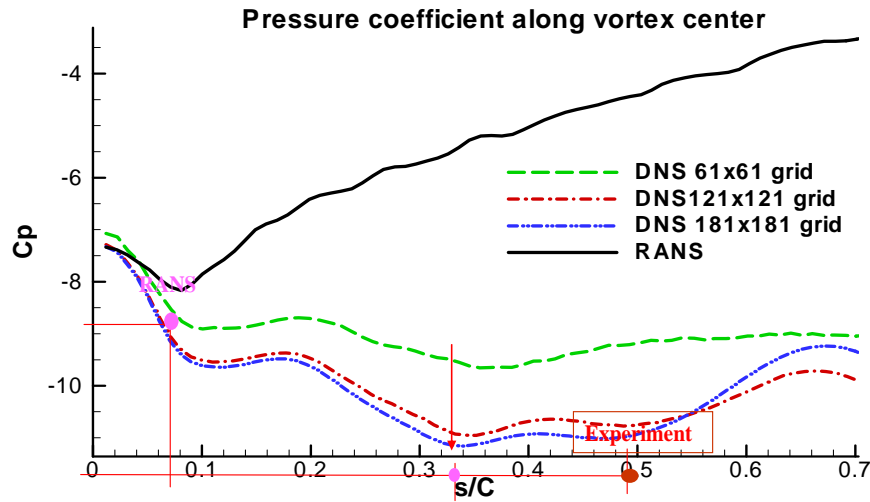


Figure 5. Comparison of the pressure coefficient versus downstream distance from the propeller blade tip between RANS solution and our DNS simulations.

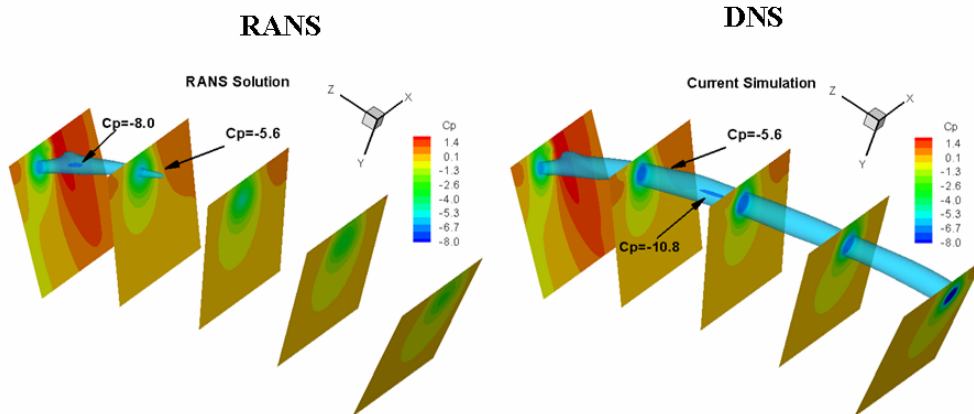


Figure 6. Iso-pressure surfaces equivalent to cavitation extent at various cavitation numbers as obtained by the RANS solution and the current DNS solution.

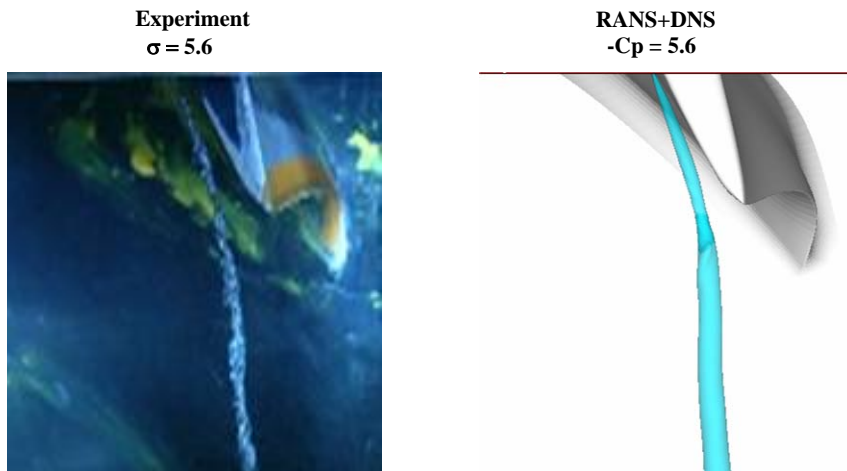


Figure 7. Comparison of cavitation extent between the numerical simulations and the experimental observations of Chesnakes and Jessup, 2003.

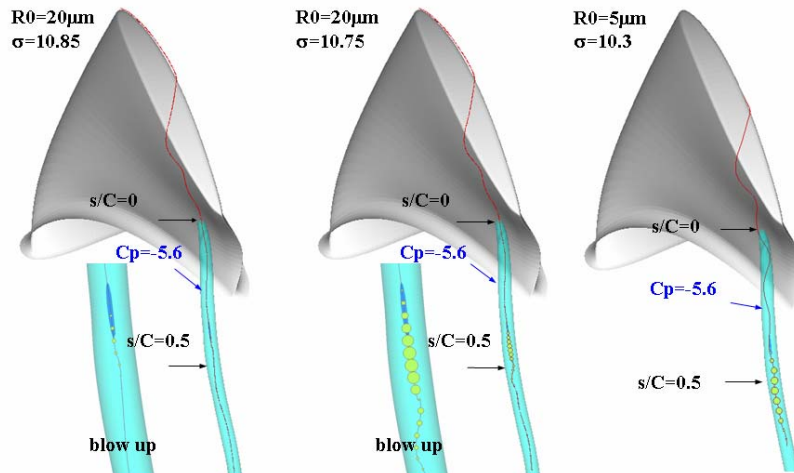


Figure 8. Bubble trajectories and size variations during cavitation events for three cases.

2.3 EFFECT OF PRESSURE FLUCTUATIONS ON CAVITATION INCEPTION FOR A DUCTED PROPELLOR [13]

Although the improvements were significant using the combined RANS and DNS simulations as described in the previous section, the predicted location of cavitation inception was still a little farther upstream than the locations observed in the experiments. In addition, it did not vary much over time as in the observations, which showed intermittent cavitation inception events in a relatively large area.

We have improved on the work described in the previous section by including the presence of unsteady turbulence fluctuations from the upstream flow field [13], implicitly neglected when using the RANS solution to define the boundary conditions. While any unsteadiness of the flow field due to the vortex/vortex interaction can be resolved by the direct numerical simulation, the turbulence fluctuations entering the computational domain are inherently filtered out when the RANS solution is applied at the inlet boundary. To investigate the importance of unsteady velocity and pressure fluctuations as well as vortex wandering on the results, the magnitude of the velocity components and the location of the two vortices were made to vary in time at the entrance of the computational domain in manners similar to experimental observations. To do so, random fluctuations were imposed with realistic characteristic amplitudes and frequencies. Based on existing PIV and anemometry experimental observations, the locations of the gap and trailing-edge vortices were oscillated around the average position with various amplitudes and frequencies within the measured values. The same was imposed on the transverse and longitudinal velocities.

Computations with different fluctuation levels were conducted and their effects on the vortex/vortex interaction and the resulting time-varying minimum pressure and location were compared. As illustrated in Figure 9 the value of the minimum pressure coefficient, $C_{p_{min}}$, fluctuated moderately remaining in the -12 to -13 range, while the location of inception varied in the presence of fluctuations much more significantly, i.e. between 0.3 and 0.7 chord length. This is explained by the $C_{p_{min}}$ curve shown in Figure 10, which in fact possesses two minima. Depending on the location of capture of the incoming nucleus, bubble explosive growth would

occurs in either of the two regions. This analysis further confirmed our earlier results, and resulted in even better correlations with the experimental observations for cavitation inception location and index value.

Realistic bubble nuclei distribution were also propagated through the computed unsteady flow field and cavitation events was monitored using DF_MULTI_SAP[®] to study cavitation inception and noise generation [7]. The results of bubble nuclei simulations obtained in presence or absence of unsteady inlet flow fluctuations are illustrated in Figure 11, which shows a superposition of all visible cavitation bubbles in the domain. This figure illustrates the fact that the fluctuations result in the bubbles growing explosively at different locations at different time, between the two C_p minima. This explains why experimental observations reported inception at different locations larger than 0.3 chord length.

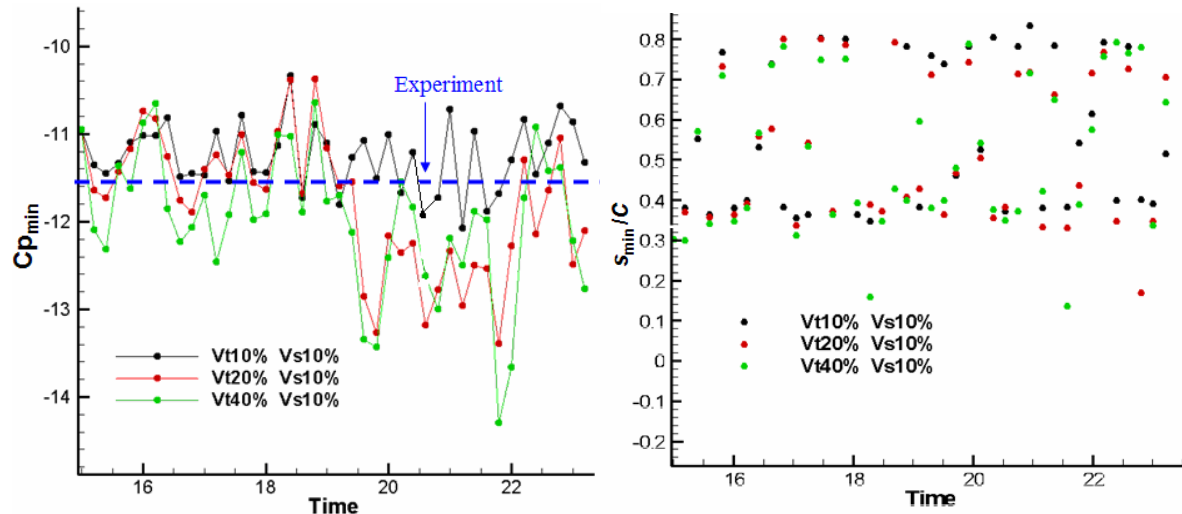


Figure 9. Time variations of $C_{p\min}$ and its location for several conditions of imposed fluctuations about the RANS input boundary conditions in the direct Navier Stokes numerical solutions.

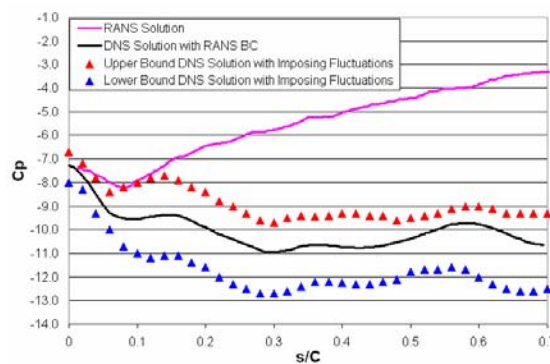


Figure 10. Pressure coefficients behind the ducted propulsor blade computed by RANS and by direct Navier Stokes numerical solution with and without fluctuations imposed on the upstream inlet to the computational domain.

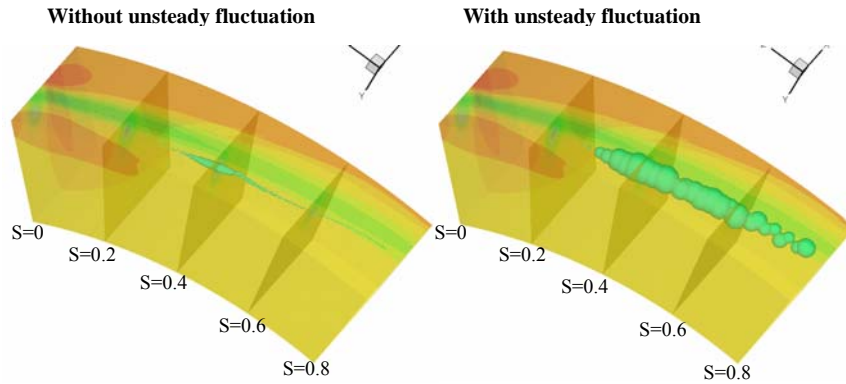


Figure 11. Cavitating bubbles locations from the Navier Stokes numerical solution and DF_MULTI_SAP bubble simulations. Comparison between using the RANS solution at the computational domain upstream inlet and imposing unsteady fluctuations to the RANS solution. $\sigma=10.75$

2.4 EFFECT OF VORTEX/WAKE INTERACTION ON CAVITATION INCEPTION IN AN OPEN PROPELLER

We have applied the same combined RANS and DNSS simulations to improve the solution of the flow field in a tip vortex flow of an open propeller to better describe the interaction between the blade wake and the tip vortex (i.e. the roll-up process). Figure 12 illustrates the location of the selected reduced computational domain relative to the propeller and the much finer grid used in the reduced domain.

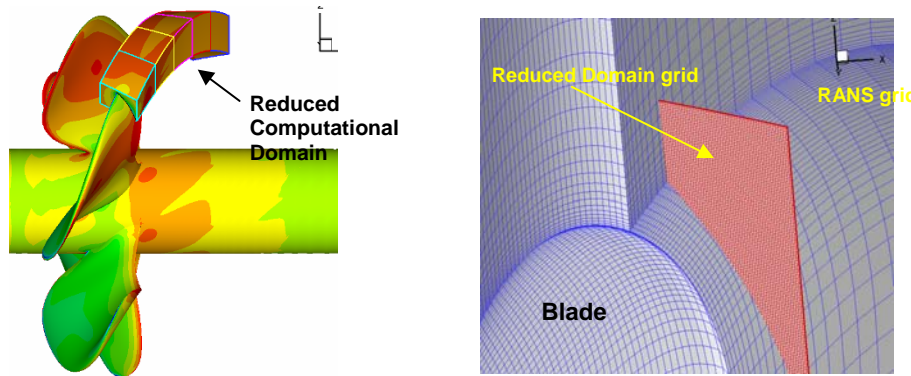


Figure 12. A view of the finer grid reduced computational domain used in the DNSS computations.

Figure 13 shows the streamwise vorticity contours on grid planes perpendicular to the vortex trajectory for both the RANS and DNSS solutions. We can see that the interaction between the tip vortex and the wake (vortex sheet) is much weaker for the RANS solution due to excessive vortex diffusion and dissipation in the RANS computation. On the other hand, in the more accurate DNSS solution, the tip vortex is seen to preserve its strength as the vortex sheet continuously rolls up into the tip vortex. The resulting pressure coefficient along the vortex center is shown in Figure 14. The figure shows that continuous rollup of the vortex sheet

enhances significantly the strength of the tip vortex and results in a much low pressure region further downstream.

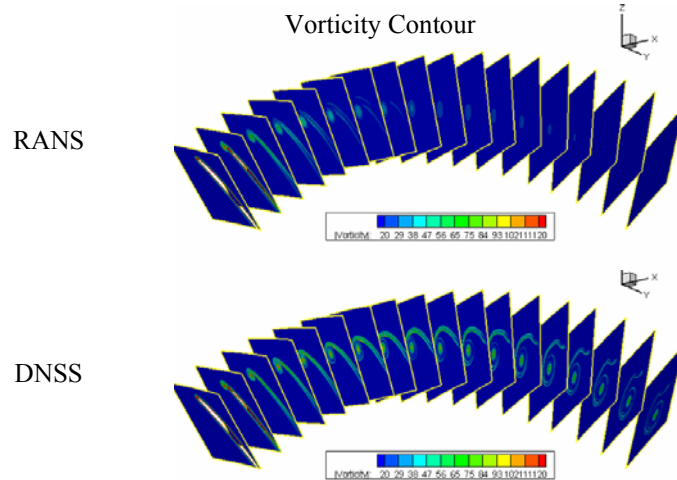


Figure 13. Comparison of vorticity contours for the solutions obtained by RANS and DNS.

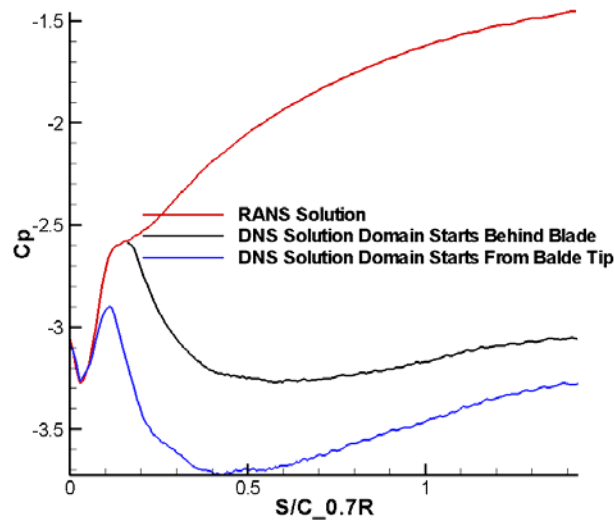


Figure 14. Comparison of the pressure coefficient for the solutions obtained by RANS and DNS.

Figure 15 and Figure 16 show a comparison of the time-averaged void fraction and downstream nuclei size distribution obtained with the RANS and DNS solutions at $\sigma = 1.75$. We can see that the void fraction is significantly increased downstream of the propeller for the more correct DNS solution. Larger bubbles with larger oscillation periods are observed when the tip vortex and wake interactions are well captured. Figure 17 shows a comparison of the void fraction contours at several downstream locations for both RANS and DNS solutions. We can see that high void fractions are locally concentrated near the tip vortex region in both cases. However, the high concentration area is much more extended for the DNS solution.

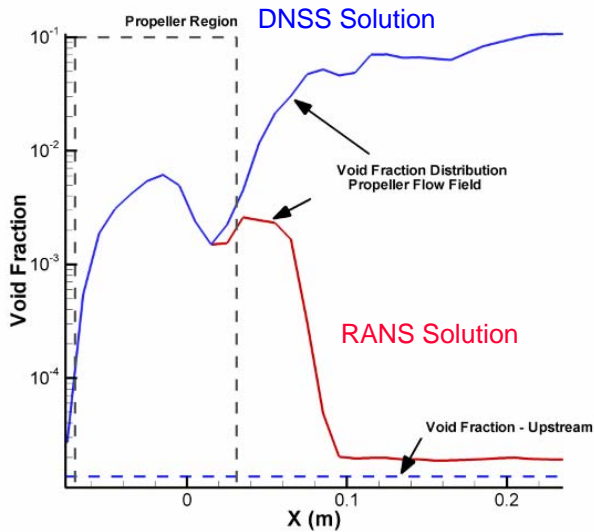


Figure 15. Comparison of the void fraction variations along x for the RANS and DNS solutions.

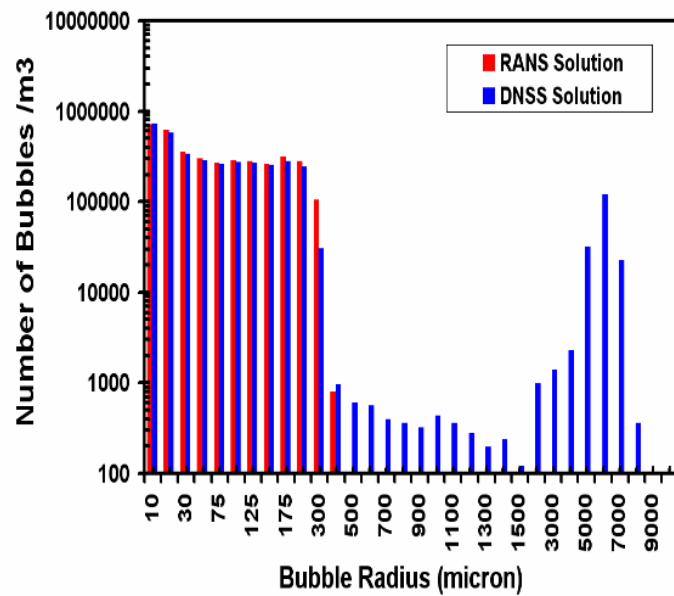


Figure 16. Comparison of the bubble size distribution at $x = 0.2$ m for the RANS and DNS solutions.

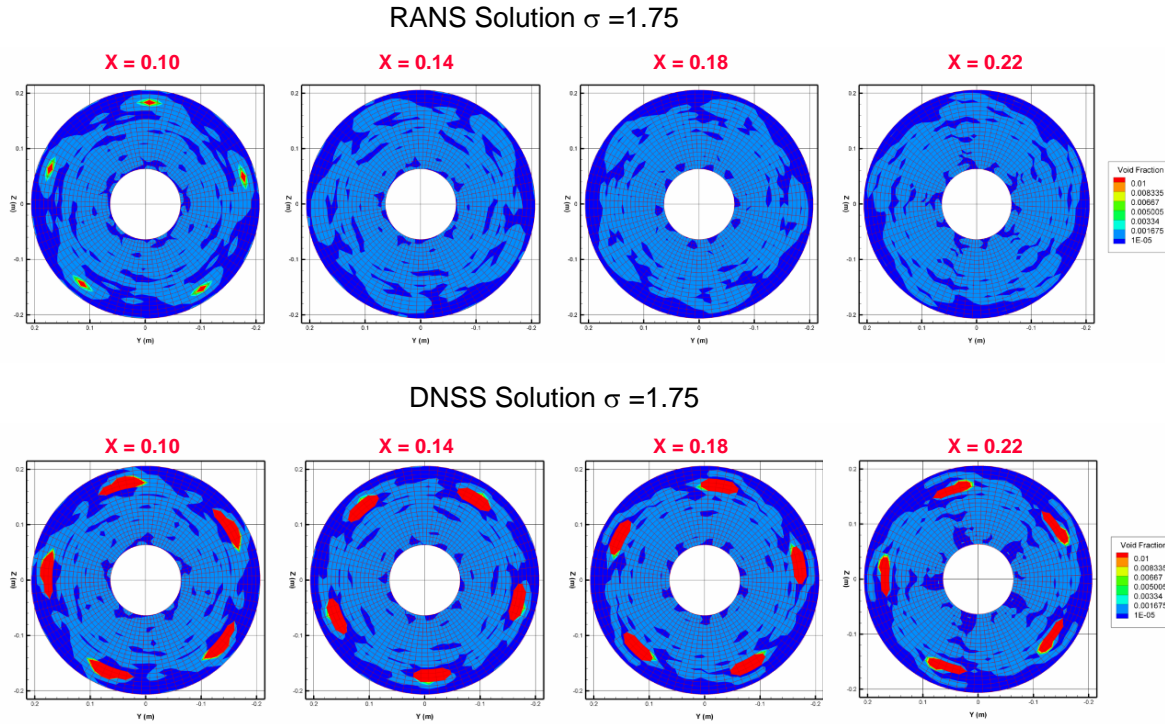


Figure 17. Comparison of the downstream void fractions for the RANS and DNS solutions.

2.5 NON-SPHERICAL BUBBLE EFFECTS ON CAVITATION INCEPTION [14,15]

Experimental observation and 3D bubble simulations (DF_UNCLETM and 3DYNAFS[©]) indicate that bubbles in vortex fields deform into non-spherical shapes and may split into smaller sub-bubbles. We have extensively studied during this project bubble splitting and the phenomena of breakup and re-entering jet formation and piercing of the other side of the bubble [14]. Our axisymmetric inviscid bubble dynamics code (2DYNAFS[©]) was applied to a wider range of nuclei sizes and cavitation numbers in the tip vortex flow fields at different Reynolds numbers. An example of such bubble behavior is shown in Figure 18. We have found that for cavitation numbers below inception, non-spherical bubble deformations (such as bubble break-up or splitting) are a significant source of noise which is an order of magnitude higher than the noise of spherical bubble collapse/rebound. Through a systematic numerical study, we could model the bubble splitting behavior in the tip vortex, and included this model in our DF_MULTI_SAP[©] simulation.

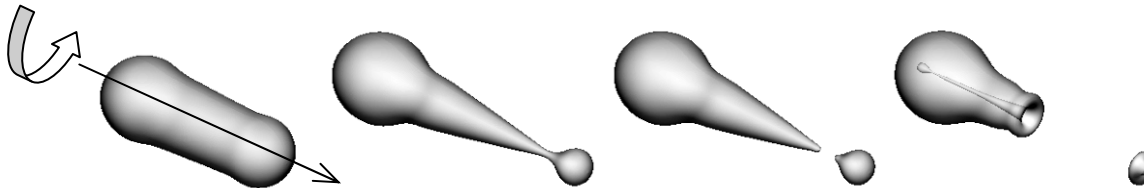


Figure 18. Example of a bubble behavior with two jets at $\sigma=2.50$ as predicted by 2DYNAFS[©] in a time sequence from left to right.

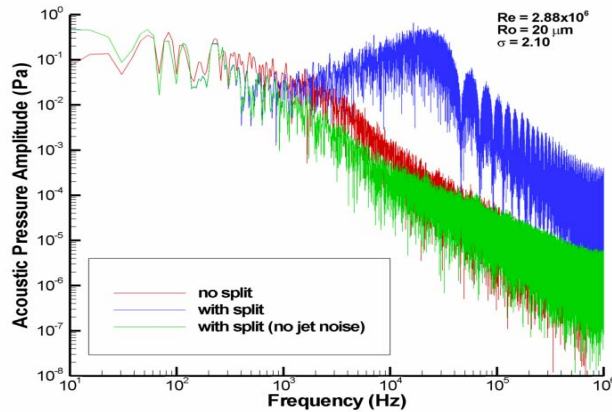


Figure 19. Amplitude spectra of the acoustic pressure signal from 100 nuclei of size 20 μm with splitting compared to that without splitting. $\sigma = 2.10$. Also shown in the spectra is the influence of the inclusion of the reentrant jet noise on the results.

The bubble splitting criteria as well as the characterization of the noise and offspring sub-bubble obtained in the non-spherical study were implemented in DF_MULTI_SAP[©], and numerical results with multiple nuclei of a realistic field were then studied. Through these studies, the inclusion of bubble splitting in the cavitation inception prediction studies was found to have little effect on the visual detection of the cavitation but have significant effect on the acoustic noise of cavitation. The acoustic pressure in the presence of splitting includes strong noise resulting from reentrant jet formation after splitting. This jet noise appears as a peculiar peak in the corresponding noise spectrum. Noise spectra with successive splitting have more high frequency content and less low frequency content than the spectrum obtained without splitting. An example of a pressure spectrum obtained from a simulation with 100 bubble nuclei is shown in Figure 19.

Experimental validation of the bubble splitting predicted by 2DYNAPS[©] was performed at DYNAFLOW and at the University of Michigan. Predicted bubble behaviors and corresponding experimental photographs were compared in [15]. Examples of this comparative study are shown in Figure 20 and Figure 21. In general, the predictions of the bubble elongation along the axis and the splitting at the end of the elongation were very similar to those observed during the experiments. However, some discrepancy was also found in the maximum extent of the elongation and the timing of the splitting. This is related to the two-way interaction between the bubble and the flow field, which was not included in 2DYNAPS[©] but is included in DF_UNCLE[©].



Figure 20. Bubble behavior in a vortex flow field: core radius = 4.51 mm, circulation = 0.2123 m^2/s ; $\sigma = 1.72$; $U_\infty = 10 \text{ m/s}$; initial radius of the bubble = 750 μm . Three-dimensional view of the bubble just before splitting predicted by 2DYNAPS[©].

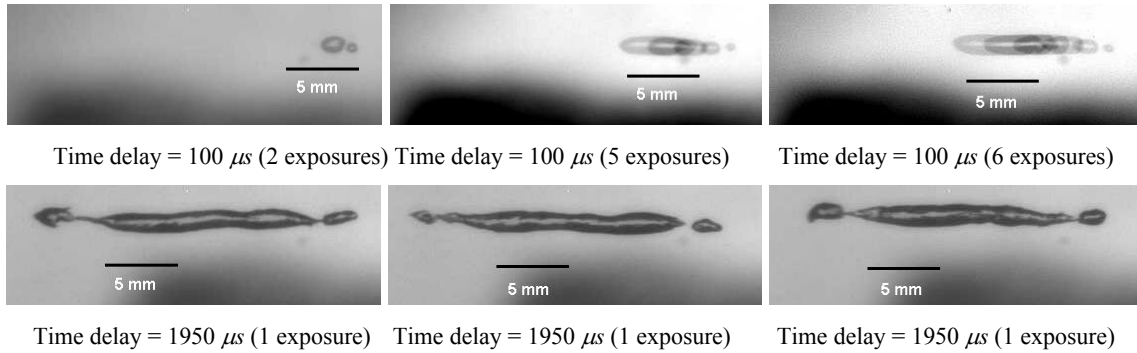


Figure 21. Superimposed successive images of laser-induced bubbles behavior at the center of a vortex; $\sigma = 1.72$; $U_\infty = 10$ m/s. Image dimensions (H 26.0 mm x V 8.3 mm. (From [15])

We have also conducted at DYNAFLOW experimental observations and numerical simulations on bubble dynamics and cavitation noise in a swirl chamber. A venturi was added to a swirl chamber to create a pressure drop followed by a pressure increase along the line vortex. High speed videos and pressure measurements were used to capture the bubble growth and collapse during cavitation events and to measure the resulting noise. Small nuclei were introduced upstream in the swirl chamber using electrolysis. In the experimental measurements we were able to capture single cavitation events and successfully correlate the bubble shape variations with the emitted acoustic signals.

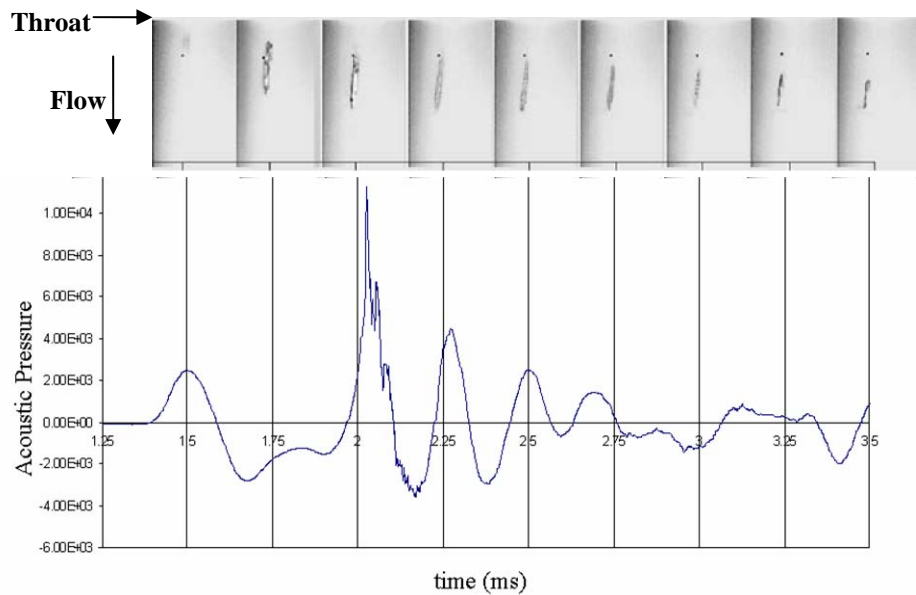


Figure 22. The bubble size and shape variations and the corresponding emitted acoustic signal for a single cavitation event captured studying the vortex chamber with venturi.

Figure 22 shows the bubble size and shape variations and the corresponding acoustic signal emitted for a single cavitation event. We can see that once the bubble passes the throat of the venturi where the minimum pressure is located an explosive bubble growth occurs. The

bubble elongates as it grows. The emitted acoustic signal can be related to the bubble volume variations and bubble splitting. The flow field of the swirl chamber with a venturi was also computed using RANS. Figure 23 shows the bubble sizes and shapes at different time steps with the background flow field illustrated by the pressure contour. Both the bubble size and shape correspond well to the experimental observations.

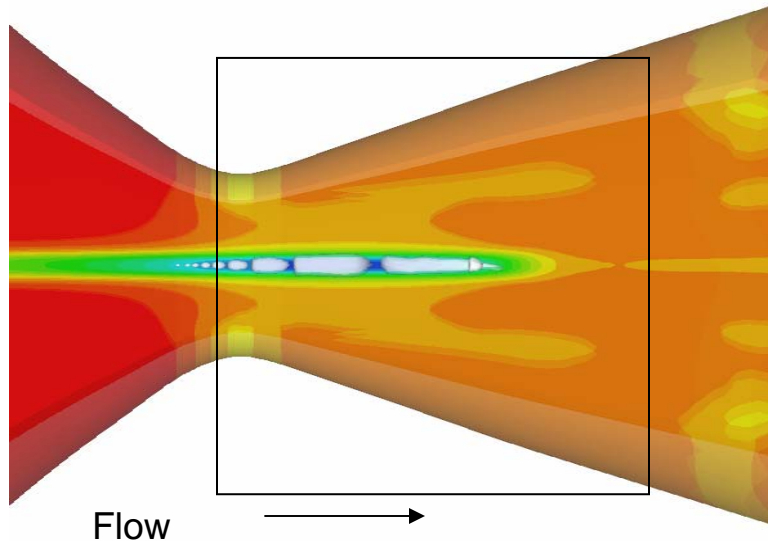


Figure 23. Bubble size and shape at superposed successive time steps with the background flow field illustrated by pressure contours.

2.6 STUDY OF CAVITATION INCEPTION NOISE [16,17,18]

Cavitation inception is a problem of interaction between nuclei and local pressure field variations including turbulent oscillations and large scale pressure variations. Various types of behaviors fundamentally depend on the relative sizes of the nuclei and the length scale of the pressure field, as well as the relative importance of the bubble natural period of oscillation and the characteristic time of the pressure field variations. Ignoring this statement and basing cavitation inception predictions only on the value of the pressure coefficients of the pure liquid flow, without account for bubble dynamics, could result in significant errors in the predictions.

A summary of the state of art of the cavitation inception prediction and a practical simulation method using a multi-bubble Surface Averaged Pressure scheme (DF_MULTI_SAP[®]) were presented in [16]. In this key note presentation, cavitation inception was defined based on the nucleus bubble behavior and dynamics. The bubble dynamics theory behind the Surface Averaged Pressure model, its validation and applications, and issues with non-spherical deformation and such modeling were described. This practical method enables us to actually conduct bubble dynamics numerical experiments as in the real liquid. This allows actual nuclei fields to interact with the computed flow field. This method, which we have successfully used with RANS solvers and a DNS solver, could be used with experimentally measured flow fields and become a design tool for cavitation avoidance.

In fact, the method has also been used more recently to simulate an advanced cavitation state such as shown in Figure 24 and could prove with further development to be a powerful design and scaling tool. One of its major strengths is that it allows the engineer to reproduce and mimic the actual experimental procedures. For instance, both acoustical and optical criteria of cavitation inception could be ‘measured’. Concerning the acoustical criteria, the technique provides in addition to amplitude of measured signals, the number of events per second, and the spectra of the sound generated, which both could be used to simulate detection. The engineer could therefore utilize the same criteria and tools as used in the real life experiments to make predictions.

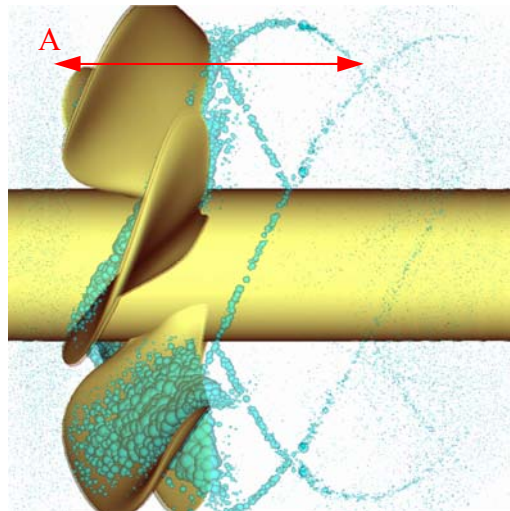


Figure 24. Results of SAP simulation of cavitation with gas diffusion on Prop5168 propeller. The bubbles in Section A are to scale. The bubbles upstream and downstream were magnified by five to make them more visible.

In Choi et al. [17], the dynamics and noise emission of cavitation bubbles forming within the core of a single line vortex were examined experimentally and numerically. For the experiments, a steady vortex line was formed downstream of a hydrofoil mounted in the test section of a re-circulating water tunnel, allowing for the detailed examination of the growth, splitting and collapse of individual cavitation bubbles as they experience a reduction and recovery of the local static pressure. The growth and collapse of bubbles with maximum aspect ratios of 60 were examined. The acoustic emissions from the bubbles were detected during growth, splitting and collapse. Experiments showed that the bubble splitting was on average associated with the start of bubble collapse, and that the bubble diameter scales the daughter bubble diameters which form at its ends.

The behavior of highly elongated (i.e. two-dimensional) cylindrical vortex cavitation bubbles for both equilibrium conditions and during bubble growth was calculated. DF_UNCLE was used to compute the growth, splitting, and collapse of spherical nuclei in the vortex.

Changes in the Reynolds number resulted in noticeable differences in bubble growth for low values of core tension. Figure 25 shows a close-up of the velocity field along with the local static pressure, leading to splitting at both ends of the bubble. There are high pressure regions at the bubble neck which lead to the bubble splitting and high pressure at the axial extents of the bubble, which produce a reentrant jet. Bubbles undergo fission upon collapse and produce

daughter bubbles at the extreme ends of the original elongated bubble. And, since the radius of the elongated bubble is much smaller than its length, the bubble could collapse in the radial direction much sooner, leading to splitting. The axial growth rates of the bubbles agreed well with those observed experimentally.

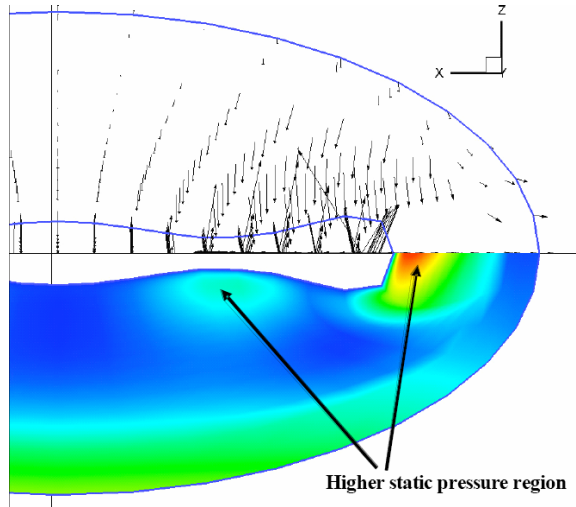


Figure 25. Close up of the velocity and pressure field of the bubbles during splitting; $t/t^* = 6$, $Re_f = 4 \times 10^5$, $\sigma_c = 0.3$, $L_b/D_b = 2$ (from [17])

Observation of bubble nuclei in tip vortex flows indicate bubble elongation followed by a splitting [18]. Non-spherical simulations capture this dynamics and show reentrant jet formation and emission of very high noise. However, applying the non-spherical method to a field of nuclei is prohibitively expensive. We overcame this difficulty by performing simulations with an improved spherical model accounting for the pressure gradient through a Surface Averaged Pressure (SAP) method which also accounts for bubble splitting [18]. Non-spherical numerical simulations were used to develop splitting criteria and to characterize the offspring split sub-bubbles and the resulting noise (Figure 26). The method accounts for a cascade of splits of the sub-bubbles and includes noise from reentrant jets. During the development of the model, we have found that the bubble can lead to splitting even further downstream of the minimum pressure region, allowing successive multiple splitting of the sub-bubbles. Our numerical simulations show that at least the second splitting of sub-bubbles has characteristics very similar to those of the first splitting. This enhanced SAP model is applied to single and multiple nuclei simulations in a typical tip vortex flow field.

Application of the model to various conditions and bubble sizes show that visual detection of the cavitation is not affected by the inclusion of the successive nuclei splitting because the sub-bubbles never grow larger than the first maximum size (an example case is shown in Figure 27). However, bubble splitting has the following effects on the acoustic detection of cavitation:

(a) The noise from the reentrant jets after bubble splitting dominates the pressure signal and exceeds the pressures from the rebounds of the original nucleus and its daughter bubbles (Figure 28). The jet noise contributes to a distinct peak in the spectrum (Figure 19).

(b) The acoustic pressure resulting from the rebounds of the sub-bubbles is smaller than the pressure from the rebounds of the original nucleus without splitting (Figure 28). However, compared to the spectrum without splitting, the sub-bubble noise has an amplitude spectrum with more high frequency content and less low frequency content. This trend of shifting of frequency contents in the spectrum is a direct result of the bubble population redistribution from the large size original nucleus to many small size sub-bubbles.

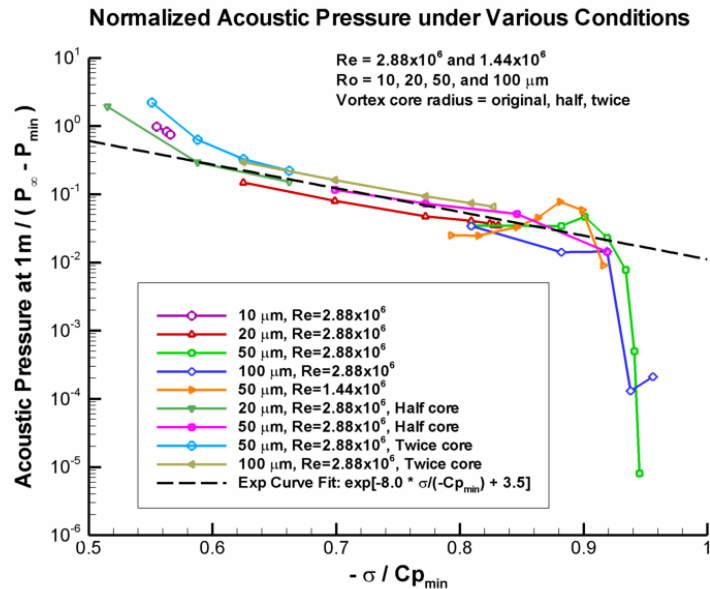


Figure 26. Acoustic pressure signals predicted by the axisymmetric boundary element method, 2DYNAFS®, which allows bubble elongation and splitting. Data for two Reynolds numbers, four initial nuclei sizes, and three vortex core sizes fall on very closely near the curve fit.

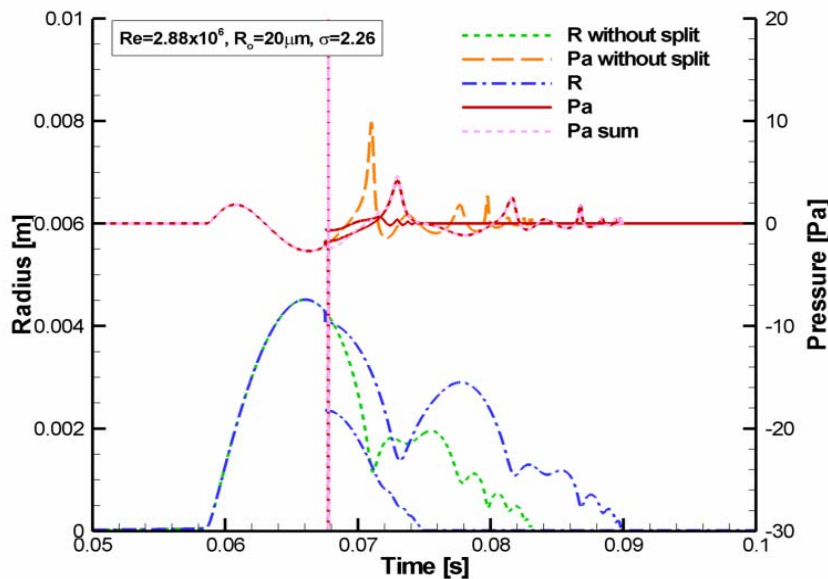


Figure 27. Bubble radius and acoustic pressure signal amplitude as functions of time predicted for 20 μm nuclei at $\sigma=2.26$ (cavitation inception).

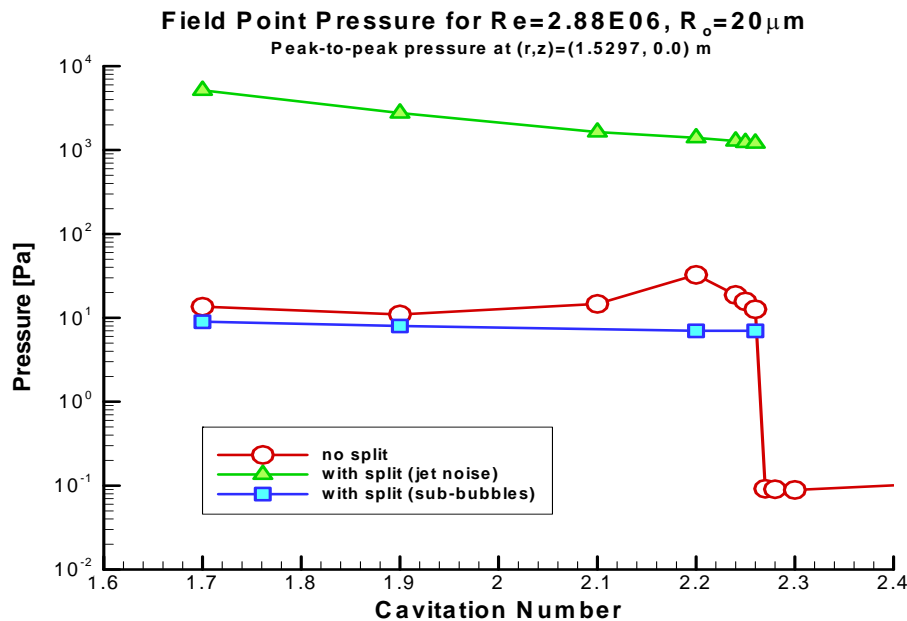


Figure 28. Maximum of the acoustic pressure signal vs. cavitation numbers predicted with $20 \mu\text{m}$ nuclei.

3. ATTACHED PUBLICATIONS

The work conducted under this project is detailed in the publications listed below, copies of which are attached.

1. “Nuclei Effects on Cavitation Inception and Noise,” G.L. Chahine, 25th Symposium on Naval Hydrodynamics, St. John’s, NL, Canada, August 8-13, 2004.
2. “Numerical Study of Cavitation Inception Due to Vortex/Vortex Interaction in a Ducted Propulsor,” C.-T. Hsiao and G.L. Chahine, 25th Symposium on Naval Hydrodynamics, St. John’s, NL, Canada, August 8-13, 2004.
3. “Tip Vortex Cavitation Inception Study Using the Surface Averaged Pressure (SAP) Model Combined with a Bubble Splitting Model,” J.-K. Choi, C.-T. Hsiao and G.L. Chahine, 25th Symposium on Naval Hydrodynamics, St. John’s, NL, Canada, August 8-13, 2004.
4. “Experimental Validation of BEM CODE Analysis of Bubble Splitting in a Tip Vortex Flow,” M. Rebow, J. Choi, J.-K. Choi, G.L. Chahine, S.L. Ceccio, 11th International Symposium on Flow Visualization, University of Notre Dame, Indiana, August 9-12, 2004.

5. "Scaling of Tip Vortex Cavitation Inception Noise with a Bubble Dynamics Model Accounting for Nuclei Size Distribution," Hsiao, C.-T., Chahine, G.L., ASME Journal of Fluid Engineering, Vol. 127, pp. 55-65, January 2005.
6. "Dynamics and Noise Emission of Vortex Cavitation Bubbles," J. Choi, C.-T. Hsiao and G.L. Chahine, S. Ceccio, 26th Symposium on Naval Hydrodynamics, Rome, Italy, September 17-22, 2006.
7. "Effect of Unsteady Turbulent Fluctuations on Vortex/Vortex/Nuclei Interaction," C.-T. Hsiao and G.L. Chahine, 26th Symposium on Naval Hydrodynamics, Rome, Italy, September 17-22, 2006.
8. "Modeling of Bubble Generated Noise in Tip Vortex Cavitation Inception," J-K. Choi, G.L. Chahine, Acta Acustica United with Acustica, Vol. 93, pp. 555-565, 2007.
9. "Numerical Study of Cavitation Inception Due to Vortex/Vortex Interaction in a Ducted Propulsor," C.-T. Hsiao and G.L. Chahine, to appear in Journal of Ship Research 2008.

4. REFERENCES

1. Arndt, R., Keller, A., "A Case Study of International Cooperation: 30 Years of Collaboration in Cavitation Research", *Proc. ASME Symposium on Cavitation Inception*, FEDSM2003-45307, Honolulu, Hawaii, July, 2003.
2. Billet, M., "Cavitation Inception Research for the International Towing Tank Conference", *Proc. ASME Symposium on Cavitation Inception*, Honolulu, Hawaii, July, 2003.
3. Keller, A., Pan, S., Yang, Z., "Comparison Tests for Checking Relations for Cavitation Scale Effects", *Proc. ASME Symposium on Cavitation Inception*, FEDSM2003-45308, Honolulu, Hawaii, July, 2003.
4. Hsiao, C.-T., Chahine, G.L., "Scaling Effect on Prediction of Cavitation Inception in a Line Vortex Flow", *J. of Fluids Engineering*, vol. 125, pp53-60, 2005.
5. Hsiao, C.-T., Chahine, G.L., "Scaling of Tip Vortex Cavitation Inception Noise with a Bubble Dynamics Model Accounting for Nuclei Size Distribution", *Proc. ASME Symposium on Cavitation Inception*, FEDSM2003-45315, Honolulu, Hawaii, July, 2003.
6. Choi, J.-K., Chahine, G.L., "Noise due to Extreme Bubble Deformation near Inception of Tip Vortex Cavitation", *Proc. ASME Symposium on Cavitation Inception*, FEDSM2003-45313, Honolulu, Hawaii, July, 2003.
7. Hsiao, C.-T., Chahine, G.L., "Prediction of Vortex Cavitation Inception Using Coupled Spherical and Non-Spherical Models and Navier-Stokes Computations", *Journal of Marine Science and Technology*, 8(3), pp. 99-108, 2004.
8. Chesnakas, C.J., Jessup, S.D., 2003, "Tip-Vortex Induced Cavitation on a Ducted Propulsor," *Proceeding of the ASME Symposium on Cavitation Inception*, FEDSM2003-45320, Honolulu, Hawaii, July 6-10.
9. Brewer, W.H., Marcum, D.L., Jessup, S.D., Chesnakas, C., Hyams, D.G., Sreenivas, K., 2003, "An Unstructured RANS Study of Tip-Leakage Vortex Cavitation Inception,"

Proceeding of the ASME Symposium on Cavitation Inception, FEDSM2003-45311, Honolulu, Hawaii, July 6-10.

10. Chen, A.L., Jacob, J.D., Savas, O., "Dynamics of Co-rotating Vortex Pairs in the Wakes of Flapped Airfoils," *J. Fluid Mech.*, vol. 382, 1999, pp. 155-193.
11. Kim, J., "Sub-Visual Cavitation and Acoustic Modeling for Ducted Marine Propulsor," Ph.D. Thesis, 2002, Department of Mechanical Engineering, The University of Iowa, Adviser F. Stern.
12. Hsiao, C.-T. and Chahine, G.L., "Numerical Study of Cavitation Inception Due to Vortex/Vortex Interaction in a Ducted Propulsor," *25th Symposium on Naval Hydrodynamics*, St. John's, NL, Canada, August 8-13, 2004.
13. Hsiao, C.-T. and Chahine, G.L., "Effect of Unsteady Turbulent Fluctuations on Vortex/Vortex/Nuclei Interaction," *26th Symposium on Naval Hydrodynamics*, Rome, Italy, September 17-22, 2006.
14. Choi, J.-K and Chahine, G. L., Hsiao C.-T. Hsiao, "Characteristics of Bubble Splitting in a Tip Vortex Flow Fifth International Symposium on Cavitation", *CAV2003*, Osaka, Japan, Nov. 2003.
15. Rebow, M., Choi, J., Choi, J.-K., Chahine, G.L. and Ceccio, S.L., "Experimental Validation of BEM Code Analysis of Bubble Splitting in a Tip Vortex Flow", *Proc. 11th International Symposium on Flow Visualization*, Univ. of Notre Dame, Notre Dame, Indiana, 2004.
16. Chahine, G.L., "Nuclei Effects on Cavitation Inception and Noise" *25th Symposium on Naval Hydrodynamics*, St. John's, NL, Canada, August 8-13, 2004.
17. Choi, J., Hsiao, C.-T., Chahine, G.L., and Ceccio, S., "Dynamics and Noise Emission of Vortex Cavitation Bubbles," *26th Symposium on Naval Hydrodynamics*, Rome, Italy, September 17-22, 2006.
18. Choi, J-K., Chahine, G.L. "Modeling of Bubble Generated Noise in Tip Vortex Cavitation Inception," *Acta Acustica United with Acustica*, Vol. 93, pp. 555-565, 2007.

Nuclei Effects on Cavitation Inception and Noise

Georges L. Chahine
(DYNAFLOW, INC., U.S.A.)

ABSTRACT

Cavitation is a problem of interaction between nuclei and local pressure field variations including turbulent oscillations and large scale pressure variations. Various types of behaviors fundamentally depend on the relative sizes of the nuclei and the length scales of the pressure variations as well as the relative importance of the bubble natural period of oscillation and the characteristic time of the field pressure variations. Ignoring this observation and basing cavitation inception predictions on pressure coefficients of the flow of the pure liquid, without account for bubble dynamics could result in significant errors in predictions. We present here a practical method using a multi-bubble Surface Averaged Pressure (DF-Multi-SAP) to simulate cavitation inception and scaling, and connect this with more precise 3D simulations.

INTRODUCTION

Cavitation and bubble dynamics have been the subject of extensive research since the early works of Besant in 1859 [1] and Lord Rayleigh in 1917 [2]. Thousands of papers and articles and several books [e.g., 3-10] have been devoted to the subject. Various aspects of the bubble dynamics have been considered at length under various assumptions and each contribution included one or several physical phenomena such as inertia, interface dynamics, gas diffusion, heat transfer, bubble deformation, bubble-bubble interaction, electrical charge effects, magnetic field effects, ...etc. Unfortunately, very little of the resulting knowledge has succeeded in crossing from the fundamental 'research world' to the 'applications world', and it is uncommon to see bubble dynamics analysis made or bubble dynamics computations conducted for cavitation avoidance by the hydrodynamics marine designer community, such as propeller designers. This is due in part to the failure of the scientific community to frame the advances made in a format usable by the design

community, but much more importantly to the perceived impracticality of using the methods developed with the existing design resources. This has made the use of bubble dynamics seem inconceivable but by experts.

Recently, however, there have been tremendous advances in available computing resources placed at the reach of non-experts. Personal computers with phenomenal speed, memory, and storage size, when compared to what existed a decade ago, are now in the hands of most engineers at a small fraction of the cost of an entry computer a decade ago. This computer 'revolution' has definitely affected the operating procedures of the designers. For instance, while a few years ago, use of CFD viscous solvers by designers was out of reach and only very simplified codes were used to design and model rotating machinery, it is now common to use repeatedly in-house or commercial Navier Stokes solver CFD codes to seek better solutions [11-13]. The challenge is thus presently for the cavitation community to bring its techniques to par with the single phase CFD progress. It is this challenge that is been undertaken here and to which we wish to significantly contribute.

In this paper, we discuss first the various definitions of cavitation because of their significant implications on modelling and then describe the analytical and numerical tools that have become available. We will try to convey the need to include the presence of nuclei and nuclei dynamics in the predictive tools for advanced designs. Some of these tools are at the reach of all users and should be adopted by the design community in conjunction with the CFD tools presently used for advanced design.

Definition(s) of Cavitation

Liquid phase only: Engineering definition

In the phase diagram of a substance the curve which separates the liquid phase from the

vapour phase defines the liquid vapour pressure values at different temperatures. Any process that raises the temperature or reduces the pressure will result in a phase change from liquid to vapour. Conventionally, boiling is defined as the phase change resulting from raising the temperature at ambient pressure, while cavitation is the process inducing phase change at ambient temperature through a pressure drop. This has provided the following traditional cavitation engineering definition: "a liquid flow experiences cavitation if the local pressure drops below the liquid vapour pressure, P_v ."

One root of the technology transfer problem discussed above stems from this accepted engineering definition of cavitation. Even though this definition has allowed significant progress in practical cavitation studies and design work, it is responsible for a lack of further advance of the technology, since it has been used at many decision points to ignore bubble dynamics effects. Indeed this definition assumes that the process occurs in the regime where heat transfer is negligible and where a large free surface is present. This over-simplification serves the purpose in most engineering cases but could lead to erroneous conclusions if used to explain or model new complex problem areas. The dangerous implication of this definition is that understanding of the liquid one-phase flow only is sufficient to predict and therefore avoid cavitation.

We discuss in the following more advanced definitions, which can help us to better understand the scaling of the cavitating results between laboratory and full scale. They should also help cavitation test results comparison between different testing facilities, and enable making more accurate cavitation predictions.

Presence of cavitation nuclei

The above definition of cavitation inception is only true in static conditions when the liquid is in contact with its vapour through the presence of a large free surface. For the more common condition of a liquid in a flow, or in a rotating machine, liquid vaporization can only occur through the presence of "micro free surfaces" or microbubbles, also called "cavitation nuclei". Indeed, a pure liquid free of nuclei can sustain very large tensions, measured in the hundreds of atmospheres, before a cavity can be generated

through separation of the liquid molecules [3]. In fact researchers agree that cavitation initiates at weak spots of the liquid or *nuclei*. These are very small microscopic bubbles or particles with gas trapped in crevices in suspension in the liquid. Several techniques have been used to measure these nuclei distributions both in the ocean and in laboratory cavitation channels. These include Coulter counter, holography, light scattering methods, cavitation susceptibility meters, and acoustic methods [15-21]. Figure 1 shows typical nuclei size distribution curves in cavitation water tunnels and in the ocean [14, 22, 23]. The figure shows the number density distribution, n , in m^{-4} , as a function of the bubble size, R . $n(R_n)$ is the number of nuclei bubbles in the range R_n to R_n+dR . Distributions of the shape $n(R) \approx R_n^{-4}$ are usually reported.

Therefore, any fundamental analysis of cavitation inception has to start from the observation that, *any real liquid contains nuclei which when subjected to variations in the local ambient pressure will respond dynamically by oscillating and eventually growing explosively (i.e. cavitating)*.

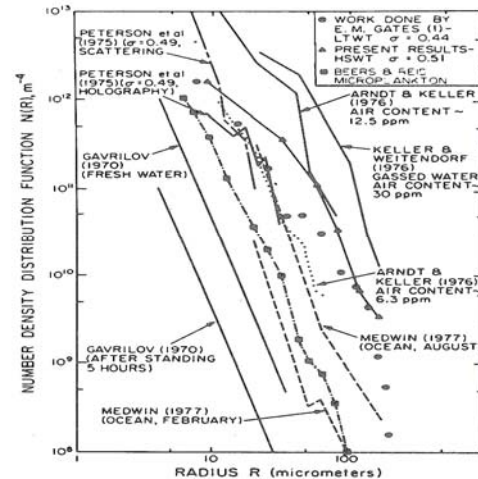


Figure 1. Nuclei Size distribution as measured in the ocean and in the laboratory (from [22]).

Cavitation inception in fact appears under several forms, such as:

- Explosive growth of individual travelling bubbles,
- Sudden appearance of transient cavities or "flashes" on boundaries,
- Sudden appearance of attached partial cavities, or sheet cavities,

- d. Appearance, growth, and collapse of bubble clouds, behind attached cavities or a vibrating surface.
- e. Sudden appearance of cavitating rotating filaments, or vortex cavitation.

Upon further analysis, all these forms can be related initially to the explosive growth of pre-existing cavities or nuclei in the liquid when subjected to pressure drops generated by various forms of local pressure disturbances¹. These are either imposed pressure variations, uniform pressure drops due to local liquid accelerations, or strongly non-uniform pressure fields due to streamwise or transverse large vortical structures. The presence of nuclei or weak spots in the liquid is therefore essential for cavitation inception to occur when the local pressure in the liquid drops below some critical value, P_c , which we address next.

Bubble Static Equilibrium

A first correction to the common engineering definition of cavitation inception is based on consideration of the static equilibrium of a bubble nucleus. The nucleus is assumed to be spherical and to contain non condensable gas of partial pressure, P_g , and vapor of the liquid of partial pressure, P_v . Therefore, at the bubble surface, the balance between the internal pressure, the liquid pressure, and surface tension can be written:

$$P_L = P_v + P_g - \frac{2\gamma}{R}, \quad (1)$$

where P_L is the pressure in the liquid, γ is the surface tension parameter, and R is the radius of the bubble.

If the liquid ambient pressure changes very slowly, the bubble radius will change accordingly to adapt to the new balance. This is accompanied with a modification of the pressure inside the bubble. The vaporization of the liquid at the bubble-liquid interface occurs very fast relative to the time scale of the bubble dynamics, so that the liquid and the vapor can be considered in equilibrium at every instant, and the partial pressure of the vapor in the bubble remains constant. On the other hand, gas diffusion occurs at a much longer time scale, so that the amount of gas inside the bubble remains constant². This results in

a gas partial pressure which varies with the bubble volume. For quasi-steady equilibrium, P_g as considered in this section, the gas follows an isothermal compression law, and is related to the initial or reference values, P_{go} , R_o , and to the new bubble radius R through:

$$P_g = P_{go} \left(\frac{R_o}{R} \right)^3. \quad (2)$$

The balance of pressures at the bubble wall becomes:

$$P_L(R) = P_v + P_{go} \left(\frac{R_o}{R} \right)^3 - \frac{2\gamma}{R}, \quad (3)$$

where the notation $P_L(R)$ is meant to associate the liquid pressure, P_L to the bubble radius, R . An understanding of the bubble static equilibrium can be obtained by considering the curve; $P_L(R)$. As illustrated in Figure 2, this curve has a minimum below which there is no equilibrium bubble radius. Only the left side branch of the curve corresponds to a stable equilibrium.

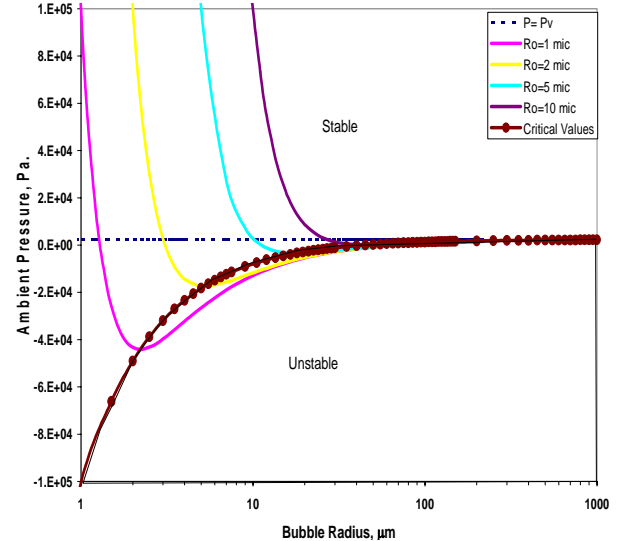


Figure 2. Static equilibrium curves of spherical bubbles and definition of critical curves. Example given for bubbles of 1, 2, 5, and 10 μm initially at equilibrium at a pressure of 1 atmosphere.

Solving for the minimum of $P_L(R)$ using Equation (3) provides the values of the "critical pressure", P_c , and corresponding critical radius, r_c :

$$P_c = P_v - \frac{4\gamma}{3r_c}, \quad (4)$$

$$r_c = \left[\frac{3R_o^3}{2\gamma} \left(P_{L_o} - P_v + \frac{2\gamma}{R_o} \right) \right]^{1/2}.$$

¹ This could be followed by extreme bubble deformation and merger to result in the various cavitation forms.

² More generally, both gas diffusion and vaporization can be modeled and taken into account

If the pressure in the flow field drops below the “*critical pressure*” an explosive bubble growth, i.e. cavitation, is provoked. This provides an improved definition for cavitation inception: “*a liquid flow experiences cavitation if the local pressure drops below the critical pressure, P_c .*”. The reason such a definition has not been adopted is that the critical pressure is not a liquid only definition and a different value is obtained for each nucleus size. To use it, one requires knowledge of the nuclei size distribution in the liquid (which is ultimately needed for any serious scale up study of cavitation.) Expression (4) illustrates the fact that the critical pressures are always lower than the vapor pressure. P_c is close to P_v only for very large initial nuclei sizes. This probably explains why such a criterion has been ignored by the practitioners, the reasoning being that using P_v is on the safe side. This reasoning, however, results in large margins of safety. In addition, this cannot be used to scale up experimental small scale tests, since cavitation would occur when bubbles actually grow explosively in the laboratory experiments and not when $p \approx P_v$, but the scaling would assume $p = P_v$.

Cavitation inception cannot be defined accurately independent of the liquid bubble population (sometimes characterized by liquid “strength” [24]) and independent of the means of cavitation detection. The cavitation inception is in fact a complex dynamic interaction between the nuclei and their surrounding pressure and velocity fields; interaction that can be different between small and large scales. In addition, the experimental means to detect and decide cavitation inception (practical threshold used by the experimentalists) will affect the results and could be different between a laboratory experiment and full scale.

Dynamical Effects

When the pressure variations to which the bubble is subjected are not slow compared to the bubble response time, the nuclei cannot instantaneously adapt to the new pressure, inertia effects become important, and thus one needs to consider the bubble dynamics equation. This is the case for nuclei travelling through a rotating machinery. The nuclei /bubbles then act as resonators excited by the flow field temporal and spatial variations. In the case of a vortical flow field the strong spatial pressure gradients (in

addition to the temporal) strongly couple with the actual bubble motion (i.e. position vs time) to result in a driving force that depends on the resonator reaction. This makes such a case much more complex than what occurs for a travelling bubble about a foil where, relatively speaking, the position of the bubble is less coupled to its dynamics.

The flow field pressure fluctuations have various time scales: e.g. relatively long for travelling cavitation bubbles over a blade or captured in a vortical region flow, or very short for cavitation in turbulent strongly sheared flow regions. The amplitudes of these fluctuations and the relationship between the various characteristic times determine the potential for cavitation inception.

Spherical Bubble Dynamics

The first improvement to the static equilibrium analysis of a bubble nucleus is to consider the nucleus dynamics when it is assumed to conserve a spherical shape during its motion. This has been extensively studied following the original works of Rayleigh [1] and Plesset [25]. For instance, if we limit the phenomena to be modelled to inertia, small compressibility of the liquid, compressibility of the bubble content, we obtain the Gilmore [26] differential equation for the bubble radius $R(t)$. We modified this equation to account for a slip velocity between the bubble and the host liquid, and for the non-uniform pressure field along the bubble surface [27]. The resulting Surface-Averaged Pressure (SAP) equation applied to Gilmore’s equation[27-28] becomes:

$$(1 - \frac{\dot{R}}{c})R\ddot{R} + \frac{3}{2}(1 - \frac{\dot{R}}{3c})\dot{R} = \frac{1}{\rho}(1 + \frac{\dot{R}}{c} + \frac{R}{c}\frac{d}{dt}) \left[p_v + p_g - p_{encounter} - \frac{2\sigma}{R} - 4\mu\frac{\dot{R}}{R} \right] + \frac{(\mathbf{u} - \mathbf{u}_b)^2}{4}, \quad (5)$$

where c is the sound speed, μ is the liquid viscosity, \mathbf{u} is the liquid convection velocity and \mathbf{u}_b is the bubble travel velocity.

Equation (5) degenerates to the classical Rayleigh-Plesset [10] equation for negligible compressibility effects. If in addition, gas diffusion effects are neglected and a polytropic law of gas compression is assumed, the resulting modified SAP equation becomes:

$$R\ddot{R} + \frac{3}{2}\dot{R}^2 = \frac{1}{\rho} \left(p_v + p_{g0} \left(\frac{R_0}{R} \right)^{3k} - P_{encounter} \right) + \frac{1}{\rho} \left(\frac{2\gamma}{R} + \frac{4\mu\dot{R}}{R} \right) + \frac{(\mathbf{u} - \mathbf{u}_b)^2}{4}, \quad (6)$$

where k is the polytropic compression law constant.

In the Surface-Averaged Pressure (SAP) bubble dynamics equation, we have accounted for a slip velocity between the bubble and the host liquid, and for a non-uniform pressure field along the bubble surface. In this SAP method the definition of $P_{encounter}$ as the average of the liquid pressures over the bubble surface results in a major improvement over the classical spherical bubble model which uses the pressure at the bubble center in its absence [27-29]. For instance, a bubble does not always continuously grow once it is captured by a vortex. Instead, it is subjected to an increase in the average pressure once it grows and this leads to a more realistic bubble dynamics. In general, the gas pressure, p_g , is obtained from the solution of the gas diffusion problem and the assumption that the gas is an ideal gas [30].

The bubble trajectory is obtained using the following motion equation [32]

$$\begin{aligned} \frac{d\mathbf{u}_b}{dt} &= \frac{3}{\rho} \nabla P + \frac{3}{4} C_D (\mathbf{u} - \mathbf{u}_b) | \mathbf{u} - \mathbf{u}_b | \\ &+ C_L (\mathbf{u} - \mathbf{u}_b) \times | \mathbf{u} - \mathbf{u}_b | + \frac{3}{R} (\mathbf{u} - \mathbf{u}_b) \dot{R}, \end{aligned} \quad (7)$$

where the drag coefficient C_D is given by an empirical equation such as that of Haberman and Morton [31]:

$$\begin{aligned} C_D &= \frac{24}{R_{eb}} (1 + 0.197 R_{eb}^{0.63} + 2.6 \times 10^{-4} R_{eb}^{1.38}); \\ R_{eb} &= \frac{2\rho R |\mathbf{u} - \mathbf{u}_b|}{\mu}. \end{aligned} \quad (8)$$

Non-spherical Bubble Dynamics: Axisymmetry

Spherical bubble models, as briefly described above, can be efficient tools for studying cavitation inception, scaling, bubble entrainment, and cavitation noise. They can become more powerful if they are provided with further "intelligence" based on more precise non-spherical models which account for bubble behavior near boundaries, in pressure gradients, and in high shear regions, resulting in bubble

deformation, elongation, splitting, coalescence, and non-spherical sound generation.

One such refinement, important for propulsor studies, consists of considering the case of bubbles captured on a vortex axis. The bubble then elongates along the axis and may split into two or more sub-bubbles, and/or form jets on the axis. In order to investigate this behavior the commercial boundary element method axisymmetric bubble dynamics code 2DYNAPS® [33-38] was exercised and was able to simulate bubble dynamics through reentrant jet formation, jet break through, and bubble splitting. The code can handle as input vortex flow fields obtained from CFD viscous computations or from experimental measurements.

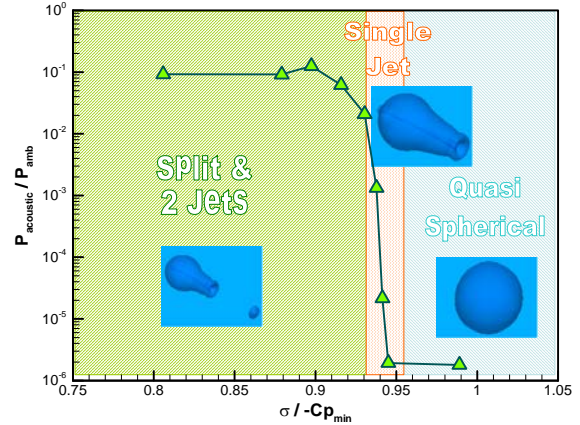


Figure 3: Illustration of the acoustic pressure emitted by a bubble in a vortex field as a function of the cavitation number. Note that the bubble behaviour near and above the cavitation inception is quasi-spherical [35].

By simulating the dynamics behavior of a bubble captured on a vortex axis under a significant number of conditions using the 2DYNAPS®, the followings conclusions illustrated in Figure 3 were found [35,41]:

- If the bubble is captured by the vortex far upstream from the minimum pressure, it remains spherical while oscillating at its natural frequency.
- When the bubble reaches the axis just upstream of the minimum pressure, it develops an axial jet on its downstream side which shoots through the bubble moving in the upstream direction. Even at this stage, the spherical model provides a very good approximation because the bubble is more or less spherical until a thin jet develops on the axis.

- The bubble behavior becomes highly non-spherical once it passes the minimum pressure location. It elongates significantly and can reach a length to radius ratio that can exceed 10. The bubble then splits into two or more daughter bubbles emitting a strong pressure spike followed later by other strong pressure signals when daughter bubbles collapse. Two axial jets originating from the split and a strong pressure signal during the formation of the jets are observed.

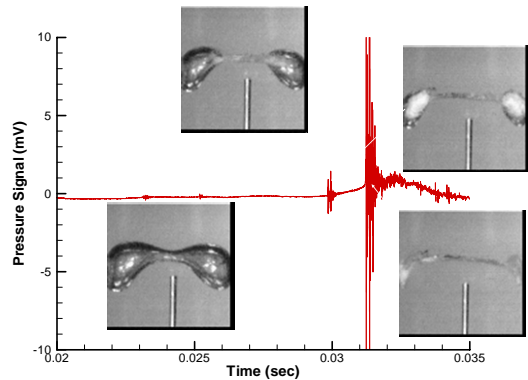


Figure 4. High speed photos of spark-generated bubble collapsing between two solid walls, and resulting acoustic signal indicating peak signal at splitting and subsequent sub-bubbles collapse [35]

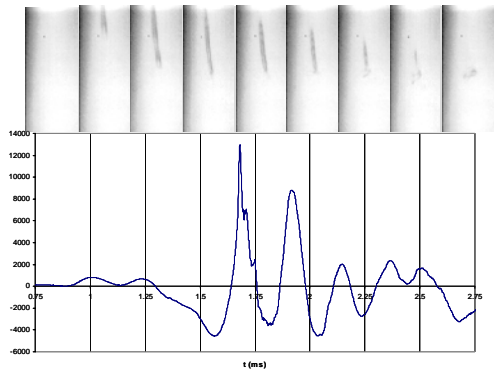


Figure 5. High speed photos of an electrolysis bubble captured in a line vortex, and resulting acoustic signal indicating peak signals at splitting and collapse [40].

Experimental Verification

This behavior supports the hypothesis that the noise at the inception of the vortex cavitation may originate from bubble splitting and/or the

jets formed after the splitting. This is an important conclusion that has been preliminarily confirmed experimentally [35,38].

Three types of tests were conducted and are still on-going: spark generated bubbles, laser generated bubbles, and electrolysis bubbles injected in vortex lines. Figure 4 shows high speed photography and acoustic signals of bubble splitting between two rigid walls. A small but distinct pressure spikes is formed at splitting followed but a more significant spike during the collapse of the sub-bubbles. The second set of experiments was conducted in a vortex tube, where bubbles generated by electrolysis were injected and observed once captured by the vortex line. Figure 5 shows the elongated bubble dynamics and the corresponding signals measured by a hydrophone [38]. The third set of experiments was conducted at the University of Michigan [39] using laser induced bubbles (in the vortex and far upstream) and the flow field of a tip vortex behind a foil. Comparisons between the observations and the 2DYNAPS® simulations showed very good correspondence as shown in Figure 6.

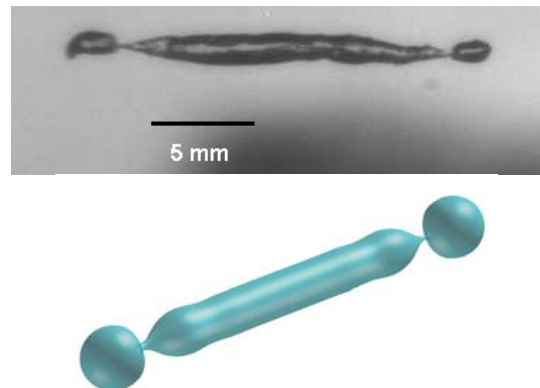


Figure 6. Bubble behaviour in a vortex flow field: $R_c = 4.51\text{mm}$, $\Gamma = 0.2123 \text{ m}^2/\text{s}$, $\sigma = 1.72$; $U_\infty = 10 \text{ m/s}$; $R_0 = 750 \mu\text{m}$. Three-dimensional view of the bubble just before splitting predicted by 2DYNAPS® and observed at University of Michigan using laser-induced bubbles at the center of the vortex [39].

Bubble splitting criteria

A large series of computer simulations of axisymmetric bubbles captured in a vortex indicated some definite trends, which can be used in a predictive model [34-38]:

- An explosively growing bubble splits into two sub-bubbles after it reaches its maximum volume, (equivalent radius, R_{max}) and then drops to $0.95 R_{max}$.
 - The two resulting sub-bubbles have the following equivalent radii: $0.90 R_{max}$ and $0.52 R_{max}$.
 - The locations of the two sub-bubbles after the splitting are at $-0.95 R_{max}$ and $4.18 R_{max}$.
 - The pressure generated by the subsequent formation of reentrant jets in the sub-bubbles can be approximated by a function of σ [41]:

Since the noise associated with the jet formation appears to be much higher than the pressure signal from the collapse of a spherical bubble, it is desirable to include the splitting and the associated jet noise in simulations with multiple bubble nuclei.

Fully Non-spherical Bubble Dynamics

In order to study the full 3D interaction between a bubble and a complex flow field, two methods were developed. The first, using the commercial boundary element code, 3DYNAFS[®] [42], enables study of full bubble deformations during capture but neglects the effects that the bubble may have on the underlying flow field. The second method accounts for the full two-way bubble/flow field interaction, and considers viscous interaction. This model is embedded in an Unsteady Reynolds-Averaged Navier-Stokes code, DF-UNCLE³, with appropriate free surface boundary conditions and a moving Chimera grid scheme [28,42]. This full two-way interaction non-spherical bubble dynamics model has been successfully validated in simple cases by comparing the results with reference results obtained from the Rayleigh-Plesset equation and 3DYNAFS for bubble dynamics in an infinite medium both with and without gravity [43].

As an illustration Figure 7 shows results of a bubble interacting with the tip vortex of an elliptical foil. The bubble elongates once it is captured, and depending on the cavitation number, either forms a reentrant jet directed upstream or splits into two sub-bubbles. When two-way interaction is taken into account further smoothing of the bubble surface is exerted by viscosity resulting in a more distorted but overall more rounded bubble. Figure 8 illustrates the

various stages of the interaction between a bubble and a tip vortex flow.

Validation of the SAP model

In order to evaluate the various models, we combined the SAP spherical model and the two-way interaction non-spherical bubble dynamics model to predict tip vortex cavitation inception for a tip vortex flow generated by a finite-span elliptic hydrofoil [28].

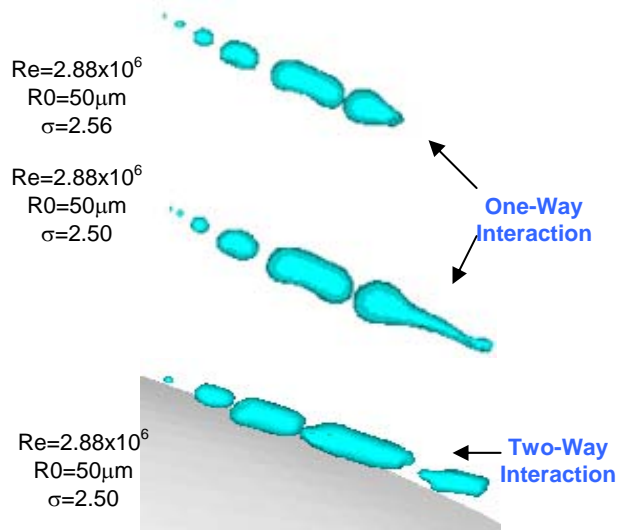


Figure 7. Bubble behavior in a vortex flow field [28].

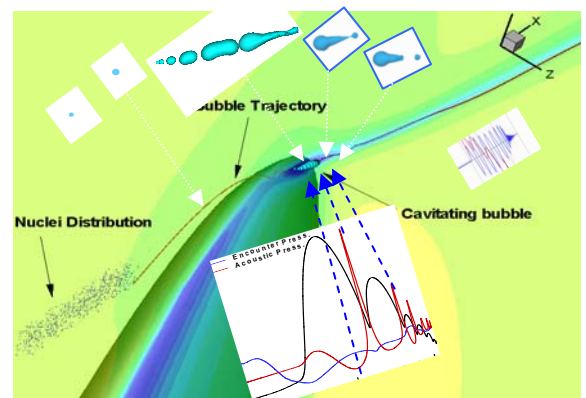


Figure 8. Sketch of the successive phases of a bubble behavior in a vortex flow field.

The flow field was obtained by a RANS computation and provided the velocity and pressure fields for all compared models: the classical spherical model; the SAP model, the one-way interaction model where the bubble deformed and evolved in the vortex field but did not modify it, and finally the fully coupled 3D

³ DF-UNCLE is a DYNAFLOW modified version of UNCLE developed by Mississippi State University

model in which unsteady viscous computations included modification of the flow field by the presence of the bubbles.

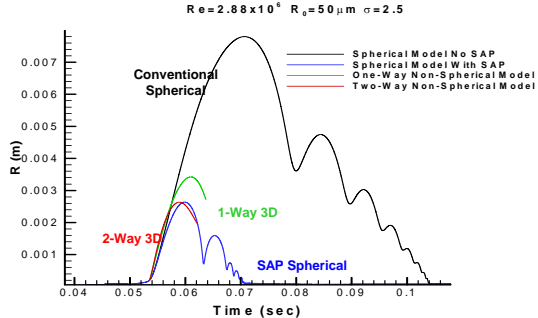


Figure 9. Comparison of the bubble radius versus time for the spherical models (the conventional and the SAP model) and the 3D 1-way and 2-way UnRANS computations [28].

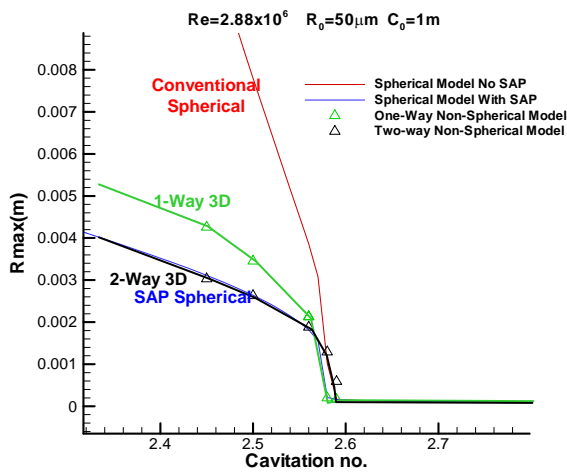


Figure 10. Comparison of the maximum bubble radius vs. cavitation number between the spherical models (the conventional and the SAP model) and the 3D 1-way and 2-way UnRANS computations [28].

Comparisons between the various models of the resulting bubble dynamics history, and of the cavitation inception values obtained from many tested conditions, reveal the following conclusions, illustrated in Figures 9 and 10:

- The bubble volume variations obtained from the full two-way interaction model deviate significantly from the classical spherical

model due to the interaction between the bubble and the vortex flow field.

- Differences between the one-way and two interaction models exist but are not major.
- Using the Surface Averaged Pressure (SAP) scheme significantly improves the prediction of bubble volume variations and cavitation inception. SAP appears to offer a very good approximation of the full two-way interaction model.

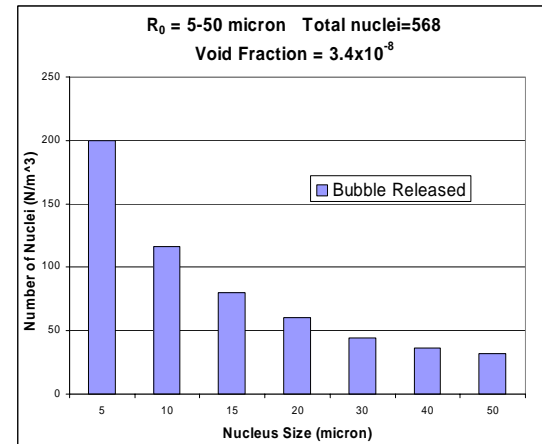
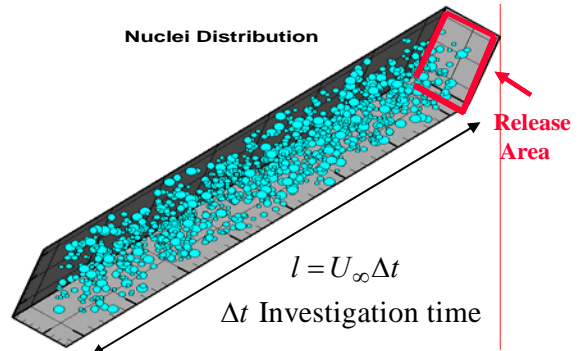


Figure 11. Illustration of the fictitious volume feeding the inlet to the nuclei tracking computational domain (or release area) and example of resulting nuclei size distribution satisfying a given nuclei density distribution function.

Modelling of a Real Nuclei field

In order to simulate the water conditions with a known distribution of nuclei of various sizes, as illustrated in Figure 11, the nuclei are considered to be distributed randomly in a fictitious supply volume feeding the inlet surface or release area of the computational domain. The fictitious volume size is determined by the sought physical

duration of the simulation and the characteristic velocity in the release area as illustrated in Figure 11. The liquid considered has a known nuclei size density distribution function, $n(R)$, which can be obtained from experimental measurements [16–21] and can be expressed as a discrete distribution of M selected nuclei sizes. Thus, the total void fraction, α , in the liquid can be obtained by

$$\alpha = \sum_{i=1}^M N_i \frac{4\pi R_i^3}{3}, \quad (10)$$

where N_i is the discrete number of nuclei of radius R_i used in the computations. The position and thus timing of nuclei released in the flow field are obtained using random distribution functions, always ensuring that the local and overall void fraction satisfy the nuclei size distribution function.

Vortex/Vortex Interaction and Inception

Recent experiments on ducted propellers [44] have shown a cavitation inception value and a cavitation inception location which were very different than those predicted by several state of the art CFD RANS codes. The most disturbing conclusion made from this comparison was that cavitation inception does not occur in the minimum pressure region, which would contradict our understanding of cavitation inception as the explosive growth of nuclei in low pressure regions.

One hypothesis for explaining this doubtful conclusion was that in both the experiments and the simulations unsteady effects were not accounted for, with the RANS solutions smearing out the computed fluctuations and the experimental measurement techniques filtering them through time averaging. The reason this effect was enhanced in the concerned experiment is that the flow field was inherently unsteady and thus significantly affected bubble dynamics in a complex fashion. Indeed, in the considered ducted propeller there is strong interaction between a tip-leakage vortex and a trailing-edge vortex as illustrated in Figure 12 at a low cavitation number, showing cavitation development and interaction between the two structures. This evolving vorticity may cause early cavitation wherever the two vortices strongly interact. We therefore set out to analyze whether unsteady vortex/vortex interactions

affect bubble dynamics in a way as to explain the above observations.

To address this issue we exercised the methods described above to study the effect of vortex/vortex interaction on bubble dynamics and cavitation noise [45,46]. The liquid phase flow was solved by direct numerical simulation of the Navier-Stokes equations and was coupled with the SAP spherical bubble dynamics model to track the evolution of the bubbles at each time step.

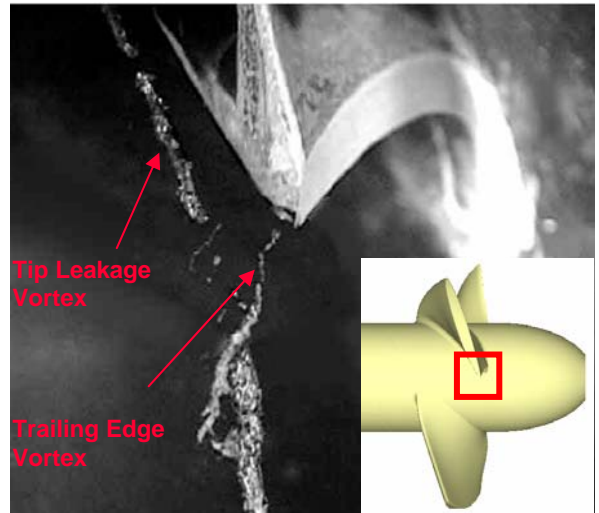


Figure 12. Advanced cavitation on Propeller 5206 visualizing both the tip leakage vortex and the trailing edge vortex (taken from [44])

Canonical problem

A canonical problem was considered first. Bubble dynamics in the flow field of two-unequal co-rotating vortices with different configurations was considered and resulted in the following conclusions [45].

- A stronger interaction between the two vortices was observed when the strengths of the two vortices were closer.
- The minimum pressure value and location is strongly affected by the two-vortices interaction. It could occur at, before, or after the two vortices have completely merged depending on the relative strength of the two vortices (see Figure 13).
- The pressure reaches its minimum when the vorticity of the weaker vortex is spread and sucked into the stronger vortex. This also results in an acceleration of the flow and leads to a *maximum streamwise velocity* at the vortex center.

- The shape, size and location of study of the “window of opportunity”, i.e. area in the inlet to the computational domain from which emitted nuclei are captured in the vortices, are highly dependent on the relative strength of the two vortices and on the nuclei sizes. A large size of “window of opportunity” was found for the stronger interaction case and for larger nuclei.

- The unsteady flow resulting from the interaction of the two vortices may result in some nuclei initially starting to be entrapped by one vortex to be ejected by the other during the merging process (see Figure 13).

Propulsor study

The same approach as discussed above was applied to the David Taylor Propeller 5206 [44] shown in Figure 12. Three RANS codes have been used by three groups to simulate numerically cavitation inception on this propulsor [46-49]. All three codes followed the simple engineering criterion for cavitation inception, $\sigma_i = -c_{p_{\min}}$, and gave close inception values: $6.5 < \sigma < 8$, at a location 0.1 chord length downstream of the trailing edge of the blade. The experiments however, showed a much higher inception value, $\sigma \approx 11$, and, more disturbing, at a location much further downstream, 0.5 chord length!, much far away for the $c_{p_{\min}}$ location.

To improve the numerical solution from these RANS computations, we considered a reduced computational domain behind the trailing edge of the propulsor blade that encompassed only the region of interaction of the two vortices. The RANS solution of Yang [49] provided the initial conditions for the grid points of the reduced domain, and the boundary conditions everywhere but at the downstream end of the domain, where an extrapolation scheme was used [46]. As in the previous section, a direct numerical simulation (DNS) of the Navier Stokes equations was performed, for a set of increasingly finer grids.

Figure 15 shows a comparison of the resulting pressure coefficient, C_p , along the vortex center line between the RANS computation [49] and the DNS computations for three different grids. As the gridding is refined, $C_{p_{\min}}$ converge to about -11 at a location 0.34 chord length downstream from the tip trailing edge. Another

minimum of the pressure is also seen at 0.5 chord length and has a value of -10.8.

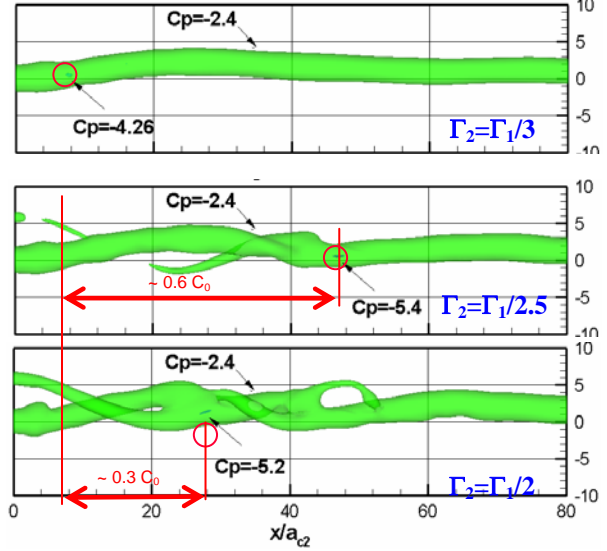


Figure 13. Effect of the strength of two vortices on the location and intensity of the minimum pressure [45].

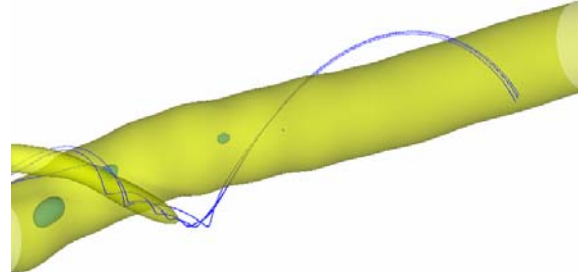


Figure 14. Interaction between two vortices resulting in ejection of initially trapped nuclei out of the main vortex [45].

The two co-rotating vortices periodically approach each other during the vortex merger. As they move closer, the flow in the axial direction is accelerated and results in a decreased pressure in the vortex center. Figure 16 indicates that this pressure drop is directly connected to the enhancement of the axial velocity to a maximum value by the merger.

A bubble population was allowed to propagate through the propeller flow field and the resulting dynamic cavitation inception was studied using both 3D bubble dynamics and SAP [46]. Figure 17 illustrates where the cavitation event occurs in the flow field, the bubble trajectory and size variations are plotted with the

propulsor blade and iso-pressure surface. It is seen that the cavitation event occurs at a location very close to the experimental observation, since the bubble grow to their maximum size near a location 0.5 chord length downstream of the tip trailing edge.

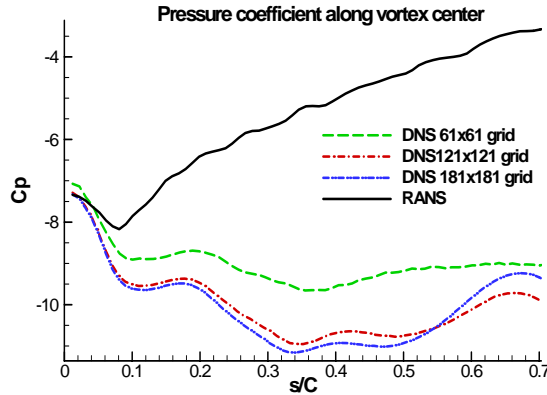


Figure 15. Pressure coefficient at various distances from the propeller blade as computed by RANS and by the direct Navier Stokes solution with an increasing number of grids [46].

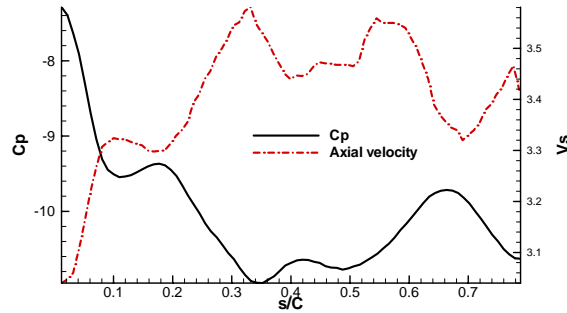


Figure 16. Pressure coefficient and axial velocity at various downstream distances from the propeller blade [46].

Conclusions

Difficulties in considering real fluid effects have led the user community to select a liquid only simple engineering definition of cavitation inception as the basis for cavitation predictions and scaling. While this has served the community very well for decades, advances in silencing and detection has made such a definition unsuitable for advanced designs.

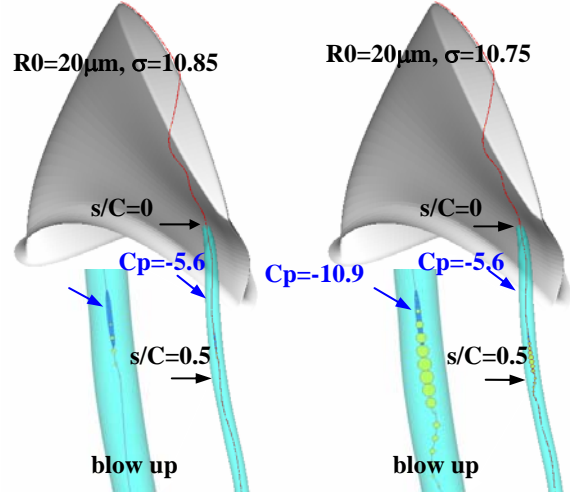


Figure 17. Bubble trajectories and size variations during bubble capture by the two-vortex system [46].

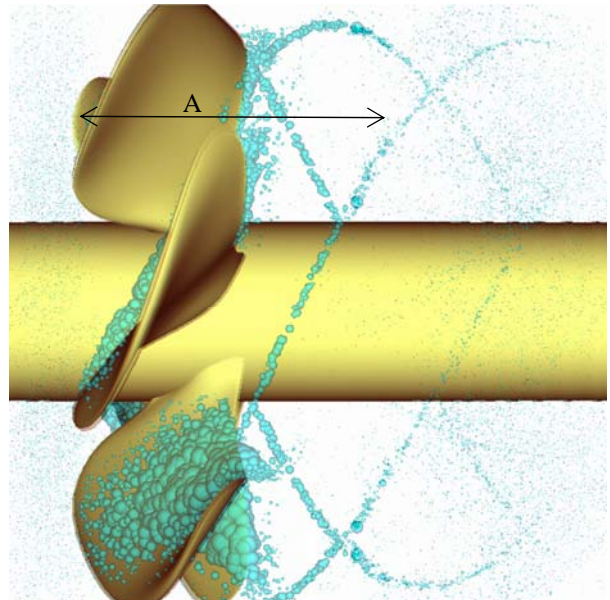


Figure 18. Results of SAP simulation of cavitation with gas diffusion on the Prop5168 propeller. The bubbles in Section A are to scale. The bubbles upstream and downstream were magnified by 5 to become visible.

One has then to resort to the more basic definition of cavitation as that of the explosive growth of initially microscopic nuclei in a liquid, resulting in visible bubbles (optical criterion) or in detectable emitted sound signals (sub-visual cavitation and acoustical criterion). The required simulations of the nuclei behavior in complex flow fields and turbulent structures were previously out of reach of the community and

thus were out the question. However, with the advent of desktop high speed computers and with the development of advanced computational techniques, this is now within the reach of designers who are increasingly using CFD (such as RANS) to select their designs. In this communication, we have proposed a practical method to actually conduct bubble dynamics numerical experiments as in the real flow field. This allows actual nuclei fields to interact with the computed flow field. This method, which we have successfully used with RANS solvers, a DNS solver, could be used with experimentally measured flow fields and become a design tool for cavitation avoidance.

We have shown some simulations in the body of the communication for cavitation inception. In fact, the method has also been used more recently to simulate advanced cavitation such as shown in Figure 18 and could prove with further development to be a powerful design and scaling tool. One of its major strengths is that it allows the engineer to reproduce and mimic the actual experimental procedures. For instance, both acoustical and optical criteria of cavitation inception could be ‘measured’. Concerning the acoustical criteria, the technique provides in addition to amplitude of measured signals, the number of events per second, and the spectra of the sound generated, which both could be used to simulate detection. The engineer could therefore utilize the same criteria and tools as used in the real life experiments to conduct the predictions.

Acknowledgment

This work could not have been done without the sustained support of ONR, Dr. Ki-Han Kim monitor, and the significant contribution of many DF colleagues, most particularly Dr. Chao-Tsung Hsiao and Dr. Jin-Keun Choi who developed and conducted most of the numerical simulations presented here.

References

1. Besant, W.H. Hydrostatics and hydrodynamics, Cambridge University Press, London, Art. 158, 1859.
2. Lord Rayleigh, On the pressure developed in a liquid during collapse of a spherical cavity, Phil. Mag; 34:94-98, 1917.
3. Knapp R.T., Daily, J.W., and Hammitt F.G., Cavitation, McGraw Hill Book Co., NY, 1970.
4. Hammitt F.G., Cavitation and Multiphase Flow Phenomena, McGraw-Hill International Book Co., NY, 1980.
5. Young, F.R. Cavitation. McGraw Hill Book Co., NY, 1989.
6. Franc, J. P., Avellan, F., Belhadji, B., Billard, J.Y., Briançon-Marjollet, Fréchou, D., Fruman, D.H., Karimi, A., Kueny, J.L., Michel, J.M., La Cavitation. Mécanismes Physiques et Aspects Industrielles, Collection Grenoble Sciences, Presses Universitaires de Grenoble, 1995.
7. Brennen, C.E., Cavitation and Bubble Dynamics, Oxford Engineering Sciences Series 44, Oxford University Press, 1995.
8. Isay, W. H. Kavitation, Schiffahrts-Verlag “Hansa” C. Shroedter & co. Hamburg, 1981
9. Leighton, T.G. The Acoustic Bubble, Academic Press, 1994.
10. Plesset, M. S., “Bubble Dynamics” in Cavitation in Real Liquids, Editor Robert Davies, Elsevier Publishing Company, pp. 1-17, 1964
11. Hsiao, C.-T. and Pauley, L.L., “Numerical Computation of the Tip Vortex Flow Generated by a Marine Propeller,” ASME *Journal of Fluids Engineering*, Vol. 121, No. 3, pp. 638-645, 1999.
12. Chen, B., and Stern, F., “Computational Fluid Dynamics of Four-Quadrant Marine-Propulsor Flow,” ASME Symposium on Advances in Numerical Modeling of Aerodynamics and Hydrodynamics in Turbomachinery, Washington, D.C., 1998.
13. Gorski, J.J., “Present State of Numerical Ship Hydrodynamics and Validation Experiments,” Journal of Offshore Mechanics and Arctic Engineering -- May 2002 -- Volume 124, Issue 2, pp. 74-80.
14. Wu J., “Whitecaps, Bubbles and Spray”, in Oceanic Whitecaps, Editors Monahan, E.C. and Niocaill, G. M., D. Reidel Publishing Company, pp. 113-123, 1986.
15. F. MacIntyre, “On reconciling optical and acoustical bubble spectra in the mixed layer,” in Oceanic Whitecaps, edited by E.C. Monahan and G. Macniocaill, Reidell, New York, 75-94, 1986.
16. D.M. Oldenziel, “A new instrument in cavitation research: the cavitation susceptibility meter,” Journal of Fluids Engineering., 104, 136-142, 1982.

17. M. L. Billet, "Cavitation nuclei measurements - a review," ASME Cavitation and Multiphase Flow Forum," FED-vol 23, June 1985.
18. N. Breitz and H. Medwin, "Instrumentation for in situ acoustical measurements of bubble spectra under breaking waves," J. Acoust. Soc. Am., 86, 739-743, 1989.
19. R. Duraiswami, S. Prabhukumar and G.L. Chahine, "Bubble Counting Using an Inverse Acoustic Scattering Method", Journal of the Acoustical Society of America, Vol. 105, No. 5, November 1998.
20. Chahine, G.L., Kalumuck, K.M., Cheng, L.-Y., and G. Frederick, 2001, "Validation of Bubble Distribution Measurements of the ABS Acoustic Bubble Spectrometer with High Speed Video Photography," 4th International Symposium on Cavitation, California Institute of Technology, Pasadena, CA.
21. Chahine, G.L. and Kalumuck, K.M., "Development of a Near Real-Time Instrument for Nuclear Measurement: The ABS Acoustic Bubble Spectrometer," 4th ASME-JSME Joint Fluids Engineering Conference, Honolulu, HI, July 6-10/2003
22. Franklin, R.E., 1992, "A note on the Radius Distribution Function for Microbubbles of Gas in Water," ASME Cavitation and Mutliphase Flow Forum, FED-Vol. 135, pp.77-85.
23. Katz, J. and Acosta, A. "Observations of nuclei in cavitating flows,' in Mechanics and Physics of Bubbles in Liquids, L. van Wijngaarden, editor, Martinus Nijhoff Publishers, pp. 123-133, 1982.
24. Arndt, R.E., Keller, A.P., "Water Quality Effects on Cavitation Inception in a Trailing Vortex, "ASME Journal of Fluid Engineering, Vol. 114, pp. 430-438, 1992.
25. Plesset, M. S., "Dynamics of Cavitation Bubbles," Journal of Applied Mechanics, Vol. 16, 1948, pp. 228-231, 1948.
26. Gilmore, F. R., "The growth and collapse of a spherical bubble in a viscous compressible liquid," California Institute of Technology, Hydro. Lab. Rep, 26-4, 1952.
27. Hsiao, C.-T., Chahine, G. L., Liu, H.-L., "Scaling Effects on Prediction of Cavitation Inception in a Line Vortex Flow," Journal of Fluid Engineering, Vol. 125, pp.53-60, 2003.
28. Hsiao, C.-T., Chahine, G. L., "Prediction of Vortex Cavitation Inception Using Coupled Spherical and Non-Spherical Models and Navier-Stokes Computations," Journal of Marine Science and Technology, Vol. 8, No. 3, pp. 99-108, 2004.
29. Hsiao, C.-T., Chahine, G. L., "Scaling of Tip Vortex Cavitation Inception Noise with a Statistic Bubble Dynamics Model Accounting for Nuclei Size Distribution," to appear ASME Journal of Fluid Engineering 2005.
30. G.L. Chahine and K.M. Kalumuck, "The Influence of Gas Diffusion on the Growth of a Bubble Cloud", ASME Cavitation and Multiphase Flow Forum, Cincinnati, Ohio, Vol. 50, pp. 17-21, June 1987.
31. Haberman, W.L., Morton, R.K., "An Experimental Investigation of the Drag and Shape of Air Bubbles Rising in Various Liquids," Report 802, DTMB, 1953.
32. Johnson V.E., Hsieh, T., "The Influence of the Trajectories of Gas Nuclei on Cavitation Inception," Sixth Symposium on Naval Hydrodynamics, pp. 163-179, 1966.
33. Chahine, G.L., Choi. J.-K., "2DYNAFSTM- Axisymmetric Boundary Element Method for Bubble and Free Surface Dynamics," DYNAFLOW, INC. User Manual 7-026, February 2004.
34. Choi, J.-K and Chahine, G. L., "Non-Spherical Bubble Behavior in Vortex Flow Fields," Computational Mechanics, Vol. 32, No. 4-6, pp.281-290, December 2003 (also in IABEM 2002 Conference, Univ. of Texas at Austin, TX, May 2002).
35. Choi, J.-K and Chahine, G. L., Noise due to Extreme Bubble Deformation near Inception of Tip Vortex Cavitation", FEDSM'03, International Symposium on Cavitation Inception, 4th ASME/JSME Joint Fluids Eng. Conference, Honolulu, Hawaii, July 2003.
36. Choi, J.-K and Chahine, G. L., "A Numerical Study on the Bubble Noise and the Tip Vortex Cavitation Inception, "Eighth International Conference on Numerical Ship Hydrodynamics, Busan, Korea, September 2003.
37. Choi, J.-K, Chahine, G. L., and Hsiao C.-T., "Characteristics of Bubble Splitting in a Tip Vortex Flow Fifth International Symposium

on Cavitation," CAV2003, Osaka, Japan, November 2003.

38. Choi, J.-K., Chahine, G.L., "Noise due to Extreme Bubble Deformation near Inception of Tip Vortex Cavitation", Physics of Fluids, Vol.16, No.7, July 2004.
39. Rebow, M., Choi, J., Choi, J.-K., Chahine, G.L., and Ceccio, S.L., "Experimental Validation of BEM Code Analysis of Bubble Splitting in a Tip Vortex Flow", 11th International Symposium on Flow Visualization, Notre Dame, Indiana, Aug. 9-12, 2004.
40. Chahine, G.L., Hsiao, C.-T., and Delfino, C. "Cavitation Inception and Noise Scaling Using Measured Bubble Size Distribution," Dynaflow Technical Report. 2M2014-1-DTRC, July, 2004.
41. Choi, J.-K., Hsiao, C.-T., and Chahine, G.L., "Tip Vortex Cavitation Inception Study Using the Surface Averaged Pressure (SAP) Model Combined with a Bubble Splitting Model", 25th Symposium on Naval Hydrodynamics, St. John's, Newfoundland and Labrador, Canada, Aug. 8-13, 2004.
42. Chahine, G.L., Hsiao, C.-T., "3DYNAFSTM - A Three dimensional Free Surface and Bubble Dynamic Code", DYNAFLOW, INC. User Manual 7-038, October 2004
43. Hsiao, C.-T., Chahine, G.L., "Numerical Simulation of Bubble Dynamics in a Vortex Flow Using Navier-Stokes Computations and Moving Chimera Grid Scheme," 4th International Symposium on Cavitation CAV2001, Pasadena, CA, June 20-23, 2001.
44. Chesnakas, C. J., Jessup, S. D., "Tip-Vortex Induced Cavitation on a Ducted Propulsor," Fifth International Symposium on Cavitation CAV2003, Osaka, Japan, November 1-4, 2003.
45. Hsiao, C.-T. and Chahine, G. L., "Effect of Vortex/Vortex Interaction on Bubble Dynamics and Cavitation Noise", Fifth International Symposium on Cavitation CAV2003, Osaka, Japan, November 1-4, 2003.
46. Hsiao, C.-T., Chahine, G. L., "Numerical Study of Cavitation Inception due to Vortex/Vortex Interaction in a Ducted Propulsor", 25th Symposium on Naval Hydrodynamics, St. John, Newfoundland and Labrador, Canada, August 8-13, 2004.
47. Brewer, W.H., Marcum, D.L., Jessup, S.D., Chesnakas, C., Hyams, D.G., Sreenivas, K., "An Unstructured RANS Study of Tip-Leakage Vortex Cavitation Inception," Proceedings of the ASME Symposium on Cavitation Inception, FEDSM2003-45311, Honolulu, Hawaii, July 6-10, 2003.
48. Kim, J., "Sub-Visual Cavitation and Acoustic Modeling for Ducted Marine Propulsor," Ph.D. Thesis, 2002, Department of Mechanical Engineering, The University of Iowa, Adviser F. Stern.
49. Yang, C.I., Jiang, M., Chesnakas, C.J., and Jessup, S.D., 2003, "Numerical Simulation of Tip Vortices of Ducted-Rotor", NSWCCD-50-TR-2003/46

Numerical Study of Cavitation Inception due to Vortex/Vortex Interaction in a Ducted Propulsor

C.-T. Hsiao and G. L. Chahine (DYNAFLOW, INC., USA)

ABSTRACT

Cavitation inception in a ducted propulsor was numerically studied using Navier-Stokes computations and bubble dynamics models. Previous experimental observations and RANS computations indicated the presence of two interacting vortices in the region where cavitation inception occurred. A direct numerical simulation with initial and boundary conditions provided from the RANS solution of a full ducted propulsor flow was conducted in a reduced computational domain in the wake region in order to improve the numerical solution of the liquid flow. Bubbles were then released in this flow field, and bubble dynamics models including spherical and non-spherical models were applied to study cavitation inception. The numerical results were compared to experimental measurements and observations. Good agreement, far superior to that obtained by RANS alone, was found in terms of cavitation inception number and inception location as well as the characteristics of acoustic signals and bubble shapes during a cavitation event.

1. Introduction

Prediction of vortex cavitation inception on marine propulsors is of great interest to the Navy and has been the subject of many studies in recent years in order to derive scaling laws for the prediction of cavitation inception. However, these scaling laws, are typically formulated based on data from open propellers and may not be applicable to a ducted propulsor. Unlike most open propellers, which generally have an elliptical shape and form a single trailing vortex, a ducted propulsor typically forms two well-defined vortices in the tip region. In addition to a trailing vortex formed near the tip trailing edge, a much stronger tip-leakage vortex is generated in the gap region between the shroud wall and the blade tip. These two unequal co-rotating vortices introduce small-scale unsteady motions during vortex merging

that are in addition to upstream turbulent fluctuations and vortex wandering (Chen *et al.* 1999, Devenport *et al.* 1999).

Recent experimental observations of cavitation inception on a ducted propulsor (Chesnakas and Jessup 2003) have indicated that the interaction between the tip-leakage vortex and the trailing-edge vortex may cause cavitation inception to occur in the region where the two vortices merge. However, predictions of cavitation inception using the pressure field either inferred from experimental measurements (Oweis *et al.* 2003) or obtained by Reynolds-Averaged Navier-Stokes (RANS) computations (Brewer *et al.* 2003, Yang 2003) are in poor agreement with the experimental observations in terms of cavitation inception number and inception location.

A preliminary controversial conclusion made by Chesnakas and Jessup was that cavitation inception does not occur near the minimum pressure region. This conclusion, however, was drawn based on the inferred pressure field obtained from the measured average tangential velocity field using a Rankine vortex assumption. This method not only neglected the axial velocity effect on the pressure field, but also relied on a time-averaged tangential velocity which could be significantly smear out due to the vortex wandering, especially at downstream locations. Furthermore, the inferred pressure in the vortex core cannot explain the shape and extent of the fully developed cavitation vortex in the vortex core observed at lower cavitation numbers (see Figure 6).

RANS computations with inadequate turbulence models and grid resolution are also known to cause over diffusion and dissipation in the vortex flow (Dacles-Mariani *et al.* 1995, Hsiao and Pauley 1998). This usually leads to a significant underprediction of the velocities in the vortex core at downstream locations. In a combined numerical and experimental study of a tip vortex flow, Dacles-Mariani *et al.* (1995) used the measured flow field to specify the inflow and outflow boundary conditions

and investigated the vortex preservation in the wake region. With the turbulence model turned off and significant grid refinement they were able to match the numerical solution to the experimental measurements.

Besides the flow field which is not well resolved, the effect of bubble dynamics on the cavitation inception has also not been fully addressed. Previous studies (Hsiao and Chahine 2003b, 2003c, 2004) have shown that inclusion of bubble dynamics significantly affects the prediction of cavitation inception for a steady-state tip vortex flow as well as for an unsteady vortex/vortex interaction flow field.

In the current study we aim to improve the numerical prediction of cavitation inception for a ducted propulsor in two ways. First, a reduced computational domain is considered which excludes propulsor solid surfaces to reduce geometric complexity and only encompasses the region of interaction of the two vortices. A direct numerical simulation is conducted for this reduced computational domain but with initial and boundary conditions provided by the RANS computation of the full ducted propulsor flow field. Second, a one-way coupled spherical bubble dynamics model developed by Hsiao and Chahine (2003b,c) and a two-way coupled non-spherical bubble dynamics model developed by Hsiao and Chahine (2004) are applied to study bubble dynamics and to predict cavitation inception.

2. Numerical Approach

2.1 Flow Configuration

We consider the David Taylor Propeller 5206, a rotating ducted propulsor, which is a three-bladed propeller with a constant chord of 0.3812m from hub to tip and a tip diameter of 0.8503m and operates in a duct of diameter 0.8636m. The detailed propulsor geometry can be found in Chesnaks and Jessup (2003). There have been three numerical studies (Kim 2002, Brewer et al. 2003 and Yang 2003) applying RANS codes to obtain a time-averaged flow field for this ducted propulsor. They all give reasonable agreement with the experimental measurements.

To improve the numerical solution from the RANS computations, We construct a reduced computational domain behind the trailing edge of the propulsor blade that encompasses only the region of interaction of the two vortices. This computational domain has a square cross area of $0.094\text{m} \times 0.094\text{m}$ and extends from the tip trailing edge to the downstream location 0.34m from the tip trailing edge. Figure 1 illustrates the location of the reduced computational domain relative to the ducted propulsor.

We consider a 4-block grid system with 101 grid points in the streamwise direction and three different numbers of grid points in the cross flow plane, 61×61 , 121×121 and 181×181 . All grid points are evenly distributed without stretching. This results in a uniform grid size of 3mm in the streamwise direction and 0.5mm in both cross directions for the finest grid. At least 34 grid points are within the vortex core in each direction for the finest grid since the vortex core size is about 17mm in diameter at the trailing edge.

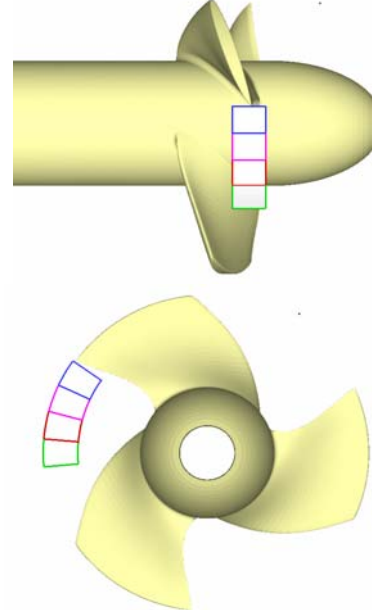


Figure 1. A view of the reduced computational domain used for the current computations.

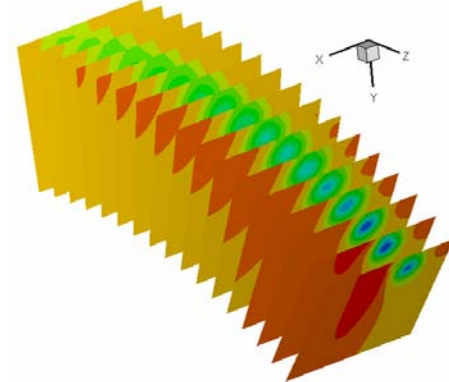


Figure 2. The interpolated pressure field of the reduced computational domain.

To conduct our numerical computations in this reduced domain, the solution of a RANS computation obtained by Yang (2003) is interpolated to provide the initial conditions at the grid points of the reduced domain. We consider the case of an advance coefficient, $J=0.98$, with an inflow velocity, $U_\infty = 6.96\text{ m/s}$. This results in a Reynolds number

based on the blade tip radius and the inflow velocity of $Re = 3 \times 10^6$. Figure 2 shows the interpolated pressure contours at different streamwise locations to indicate the position of the main vortex in the reduced domain. Figure 3 shows the pressure contour and velocity vectors at the inlet boundary on the $x-r$ plane. The two co-rotating vortices (the tip-leakage vortex and the trailing edge vortex) can be readily seen. The strength of the tip-leakage vortex is much larger than that of the trailing-edge vortex.

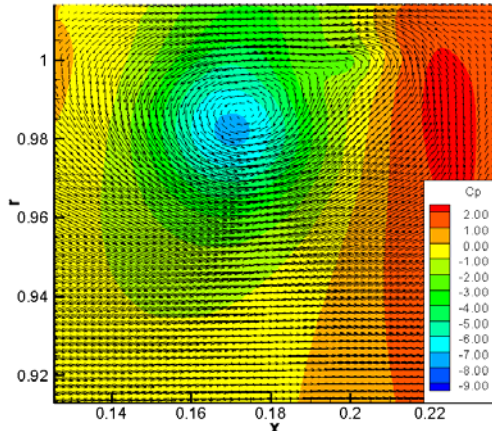


Figure 3. The pressure contours and velocity vectors at the inlet boundary on the $x-r$ plane.

2.2 Navier-Stokes Computations

For the vortex interaction study in the reduced domain, the flow is obtained via direct numerical simulation of the Navier-Stokes Equations without turbulence modeling. Since the present computation is conducted on a rotating frame attached to the rotating propeller blade, the steady-rotating reference frame source terms, *i.e.* the centrifugal force and the Coriolis force terms, are added to the momentum equation. The resulting unsteady incompressible continuity and Navier-Stokes equations written in non-dimensional vector form and Cartesian notations are given as

$$\nabla \cdot \mathbf{u} = 0, \quad (1)$$

$$\frac{D\mathbf{u}}{Dt} = -\nabla p + \frac{1}{R_e} \nabla^2 \mathbf{u} + \Omega^2 \mathbf{r} - 2\Omega \times \mathbf{u}, \quad (2)$$

where $\mathbf{u} = (u, v, w)$ is the velocity, p is the pressure, \mathbf{r} is the radial position vector, Ω is the angular velocity, $R_e = \rho u^* L^* / \mu$ is the Reynolds number, u^* and L^* are the characteristic velocity and length, ρ is the liquid density, and μ is its dynamic viscosity.

To solve Equations (1) and (2) numerically, a three-dimensional incompressible Navier-Stokes solver, DF_Uncle, developed at Mississippi State University and modified by DYNAFLOW, INC. is

applied. DF_Uncle is based on the artificial-compressibility method (Chorin 1967) in which a time derivative of pressure is added to the continuity equation as

$$\frac{1}{\beta} \frac{\partial p}{\partial t} + \nabla \cdot \mathbf{u} = 0, \quad (4)$$

where β is the artificial compressibility factor. As a consequence, a hyperbolic system of equations is formed that can be solved using a time marching scheme. This method can be marched in pseudo-time to reach a steady-state solution. To obtain a time-dependent solution, a Newton iterative procedure needs to be performed at each physical time step in order to satisfy the continuity equation. In the present study the time-accurate solution was obtained when the maximum normalized velocity divergence was less than 1.0×10^{-3} . Detailed descriptions of the numerical scheme can be found in Vanden and Whitfield (1993).

The boundary conditions for this reduced domain are also deduced from the RANS solution. The initial values of the pressure and velocities interpolated from the RANS solution are imposed at all boundaries except the inlet and outlet boundaries. At the inlet boundary the method of characteristics is applied with all three components of velocities specified from the RANS solution. For the outlet boundary all the variables are extrapolated from the inner grid points but with the initial value of the pressure fixed at one grid point.

2.3 Bubble Dynamics Models

Two bubble dynamics models, a spherical model and a non-spherical model, are applied in this study. In the spherical bubble dynamics model each bubble is tracked by a Lagrangian scheme in the flow field which combines the RANS solution and the current DNS solution by oversetting the grid of the reduced domain with the overall propulsor grid. As a bubble is released upstream of the reduced domain the flow field from the RANS solution is used. Once the bubble enters the reduced domain, the flow field obtained from the current simulation is applied. Bubble transport is modeled via the motion equation described by Johnson and Hsieh (1966) while the bubble dynamics is simulated by solving a surface Averaged Pressure (SAP) Rayleigh-Plesset equation developed by Hsiao and Chahine (2003a,b).

The non-spherical bubble dynamics model is embedded in the unsteady Navier-Stokes solver, DF-UNCLE, with appropriate free surface boundary

conditions and a moving Chimera grid scheme. Since unsteady Navier-Stokes computations are time-consuming, this non-spherical model is combined with the spherical model mentioned above. The spherical model is used to track the bubble during its capture by the vortex and the non-spherical model is turned on only when the bubble size exceeds a preset limit value. When the non-spherical model is turned on, the flow field due to the spherical bubble motion and volume change is superimposed on the liquid phase flow field solution to provide an initial condition for the unsteady viscous computation. This model allows the bubble to deform non-spherically and a full two-way interaction between the bubble and the flow field can be obtained. Detailed description of this model and numerical implementations can be found in Hsiao and Chahine (2001,2004).

3. Results and Discussion

3.1 Liquid Flow

The simulation of vortex interaction in the reduced computational domain is conducted with the turbulence model turned off. The mean flow solution is specified at the inlet boundary. Additional unsteady turbulent fluctuations from upstream will be simulated in future efforts. The two-vortex interaction is then simulated for different discretizations.

Three levels of grid resolution as described in Section 2.1 were tested. Although unsteady computations were conducted for this study, all three cases converged to a practically steady-state solution. The instability due to strong vortex/vortex interaction as shown in Hsiao and Chahine (2003c) is not observed in the current simulation. This is probably due to a relatively weak trailing-edge vortex. Hsiao and Chahine have shown that the interaction between the two co-rotating vortices becomes weaker as the relative strength of the main vortex is increased. To further resolve the instability due to a weak interaction, further grid refinement may be required.

Figure 4 shows a comparison of the resulting pressure coefficient, C_p , along the vortex center line for these three cases. It is seen that as the grid is refined, $C_{p\min}$ approaches about -11 at a location 0.35 chord length downstream from the tip trailing edge. The solutions of the 121×121 and 181×181 grids are quite close. Since the 121×121 grid only yields a small difference in the minimum pressure as compared to the finest grid, this grid solution was used for subsequent bubble dynamics computations for the sake of CPU time reduction.

The pressure coefficient along the vortex center obtained with the 121×121 grid is also compared with the RANS solution and shown in Figure 4. Major fundamental differences are seen

between these two results. The RANS computation predicts $C_{p\min} = -8.2$ at $s/C = 0.1$ while the current simulation shows $C_{p\min} = -11$ at $s/C = 0.35$. This is probably due to excessive vortex diffusion and dissipation in the RANS computation. The comparison is also made by showing various iso-pressure surfaces in Figure 5. This is similar to visualizing a cavitating vortex at different cavitation numbers. The current results seem to agree with the experimental observation much better because the experimental videos show a long-extended fully cavitating vortex core at $\sigma = 5.6$ (see Figure 6), and also indicate cavitation inception at $\sigma \sim 10.8$ at about 0.35 chord length downstream of the trailing edge.

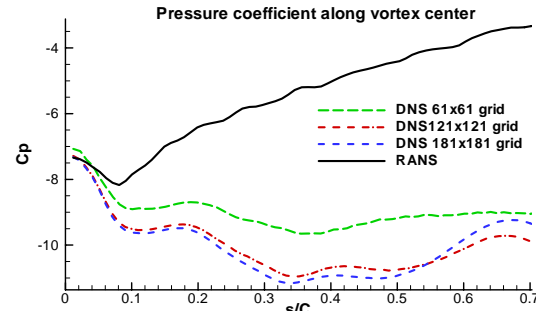


Figure 4. Comparison of the pressure coefficient variation along the vortex center for three different DNS grids and for the RANS solution.

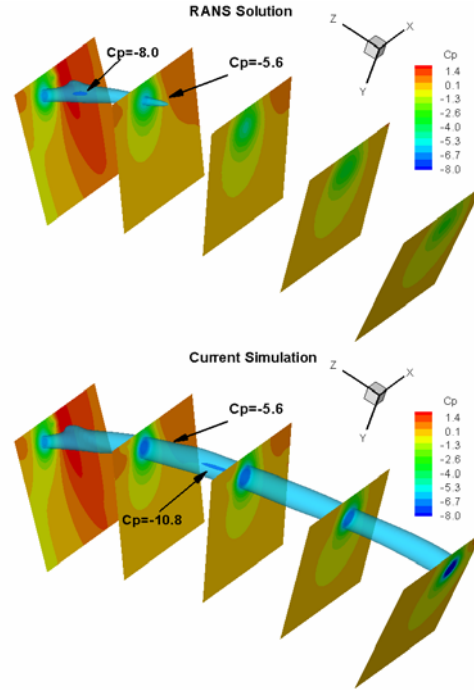


Figure 5. Iso-pressure surfaces equivalent to cavitation extent at various cavitation numbers as obtained by the RANS solution and the current DNS solution with the 121×121 grid.



Figure 6. Fully developed cavitation in the vortex core at $\sigma = 5.6$ (Chesnaks and Jessup 2003).

It is important to examine the flow field near the location where the pressure reaches the minimum value. In our previous study (Hsiao and Chahine 2003c), we showed that the two co-rotating vortices periodically approach each other during the vortex merger. As they move closer, the flow in the axial direction is accelerated and results in a decreased pressure in the vortex center. It is found that as the axial velocity reaches a maximum value, the pressure in the vortex center will drop to its minimum. This is also observed in the current simulation. The computed C_p and axial velocity along the vortex center line are shown in Figure 7.

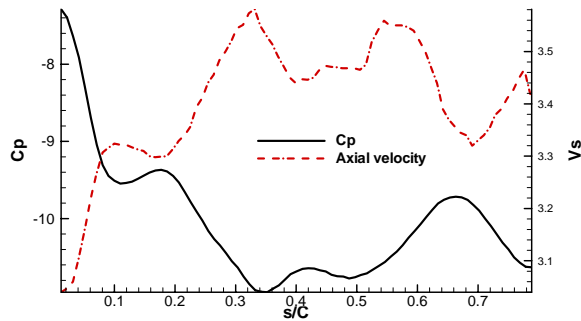


Figure 7. Pressure coefficient and axial velocity as a function of the distance from the tip trailing edge.

3.2 Area of Bubble Capture: “Window of Opportunity”

The “window of opportunity” through which a nucleus needs to enter to be captured by the vortex and generate strong acoustic signals has been studied for a finite-span tip vortex flow by Hsiao and Chahine (2003b). It is also important to determine this “window of opportunity” for the current flow field because with the knowledge of the location and size

of this small window, we are able to distribute and follow nuclei more efficiently. Near inception the size of the “window of opportunity” is strongly related to the probability of the cavitation events.

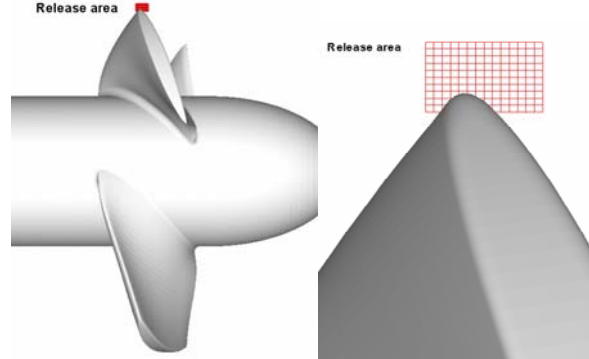


Figure 8. The location of the release area for establishing the “window of opportunity”.

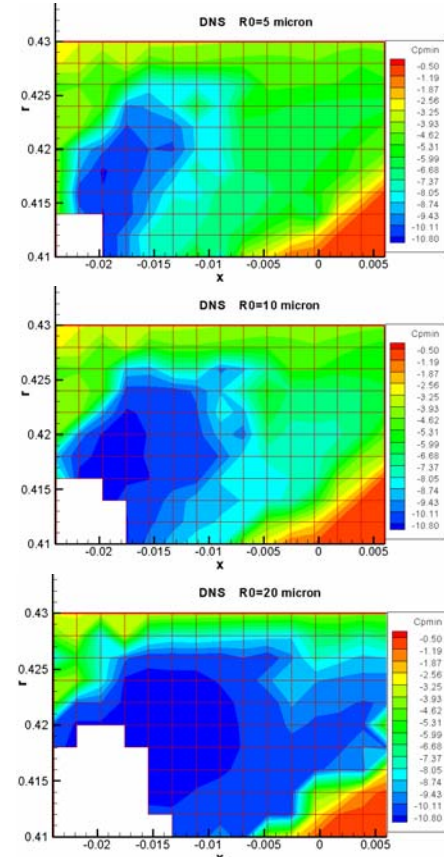


Figure 9. Contours of encountered $C_{p\min}$ for nuclei with $R_0=5, 10$, and 20 microns.

To establish the “window of opportunity” a rectangular release area was specified ahead of the tip leading edge of the propulsor on the $x-r$ plane with 165 nuclei of a given size released from a 15×11 grid

point array. Figure 8 illustrates the location of the release area related to the propulsor blade. The cavitation number was specified high enough ($\sigma=12$) such that the maximum growth size of a nucleus was less than 10 %. Each nucleus was tracked and the minimum pressure it encountered during its travel was recorded and assigned to the release grid point. This enables us to plot a contour of the minimum encountered pressure coefficient for the release grid points and to obtain the “window of opportunity” for each case.

Figure 9 shows contours of minimum encountered pressure coefficient for three different nuclei sizes, $R_0 = 5, 10, 20$ microns. The contours are blanked out for the release points where the nucleus collides with the propeller surface. It is seen that the size of the “window of opportunity” becomes smaller and its location shifts closer to the propeller pressure side surface when the nuclei size decreases.

3.3 Single Bubble Dynamics for Prediction of Cavitation Inception

Experiments conducted by Chesnaks and Jessup (2003) with a high speed video camera and a sensitive hydrophone captured the bubble and its emitted acoustic signal during sub-visual cavitation events. According to the duration of the acoustic signal, the cavitation events were categorized into “popping” and “chirping” events. They stated that the “popping” event has a very short duration of noticeable acoustic signal less than 0.3ms and that the bubble virtually remained spherical when its size was less than 0.1mm in diameter. The “chirping” event has a much longer duration ranging from 0.3 to 10ms, and the bubble has an elongated shape. They found that all the cavitation inception events occurred near or behind a location 0.5 chord length downstream of the tip trailing edge.

To simulate the cavitation events, we investigated the bubble behavior and the emitted acoustic signal for different initial nuclei sizes at different cavitation numbers. We found that “popping” cavitation events can be observed at a cavitation number just slightly smaller than the negative minimum pressure coefficient, $-Cp_{min}=11$. Figure 11 shows the bubble size variation and the emitted acoustic signals for an initial nucleus size, $R_0=20\mu\text{m}$ at $\sigma=10.85$. It is seen that the maximum bubble size is about 0.1mm in diameter and the noticeable acoustic signal only lasts about 0.3ms. As the cavitation number is reduced the bubble grows to a much larger size and the duration of the acoustic signal is much longer as shown in Figure 12 for $R_0=20\mu\text{m}$ at $\sigma=10.75$.

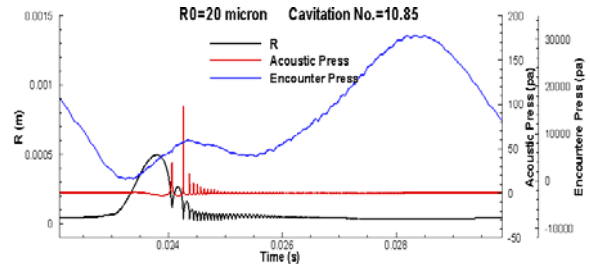


Figure 11. The bubble radius, emitted acoustic pressure signal and encountered pressure during a cavitation event for $R_0=20\mu\text{m}$ at $\sigma=10.85$.

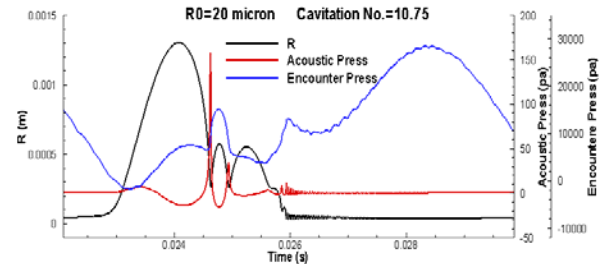


Figure 12. Bubble radius, emitted acoustic pressure and encountered pressure during a cavitation event for $R_0=20\mu\text{m}$ at $\sigma=10.75$

Figures 11 and 12 also show the pressure encountered by the bubble during its journey. There is a small delay in time for the bubble to grow to its maximum size after encountering the minimum pressure. This delay significantly increases when a cavitation event is produced by a small size nucleus. An example of such a cavitation event is shown in Figure 13 for $R_0=5\mu\text{m}$ at $\sigma=10.3$. To illustrate where the cavitation event occurs in the flow field, the bubble trajectory and size variations are plotted with the propulsor blade and iso-pressure surface as shown in Figure 14. It is seen that for the larger R_0 the cavitation event occurs at a location slightly earlier than the experimental observation while the smaller R_0 grows to its maximum size near a location 0.5 chord length downstream of the tip trailing edge.

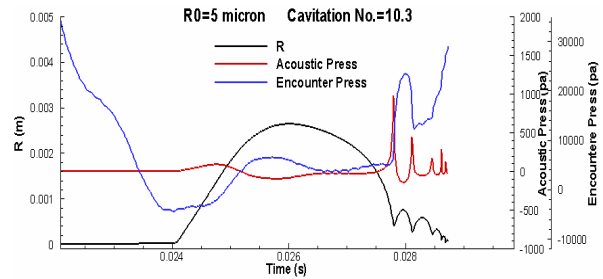


Figure 13. Bubble radius, emitted acoustic pressure and encountered pressure during a cavitation event for $R_0=5\mu\text{m}$ at $\sigma=10.3$.

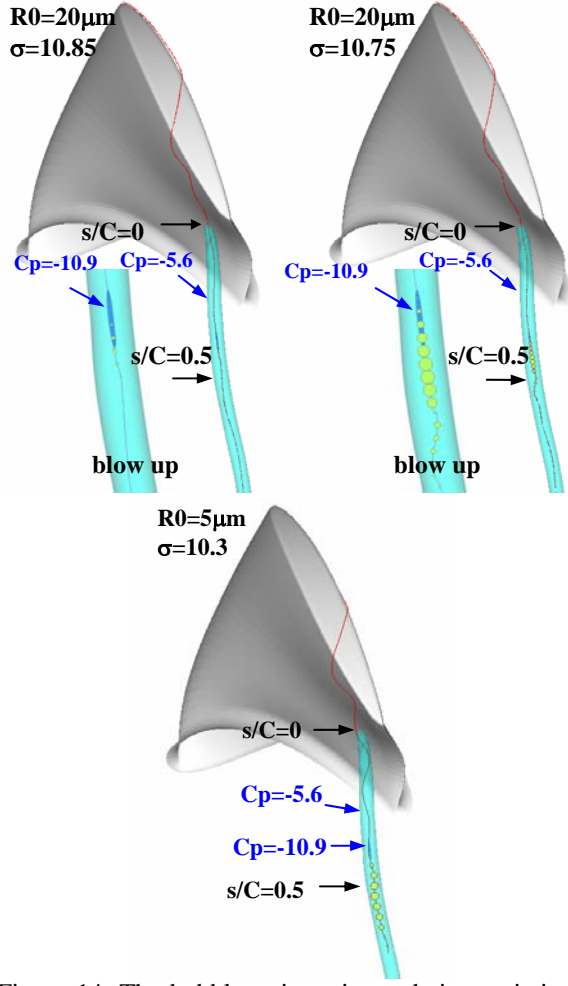


Figure 14. The bubble trajectories and size variations during the cavitation event for three cases.

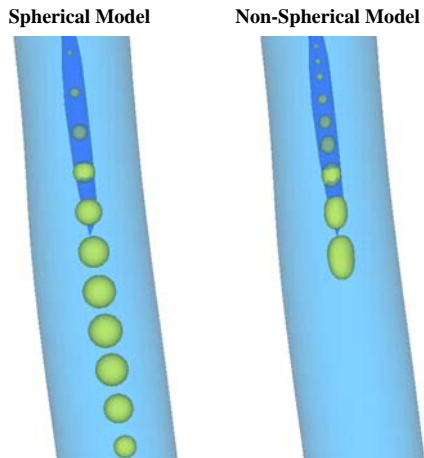


Figure 15. Computed bubble sizes and shapes of both spherical and non-spherical modes plotted with two levels of iso-Cp for $R_0 = 20 \mu\text{m}$ at $\sigma = 10.75$.

The bubble dynamics is also studied with the non-spherical model. Figure 15 compares the bubble shapes obtained with the spherical and the non-spherical model for $R_0 = 20 \mu\text{m}$ at $\sigma = 10.75$. It is seen that both models predict almost the same maximum growth size. The non-spherical model also shows that the bubble elongates in the axial direction and becomes a cylindrical shape as it grows. However, for $R_0 = 20 \mu\text{m}$ at $\sigma = 10.85$ the bubble remains almost spherical at its maximum size as shown in Figure 16. For both cases the bubble starts to collapse after reaching its maximum size. The non-spherical computations, however, fail to continue once strong deformations develop over the bubble surface during the collapse.

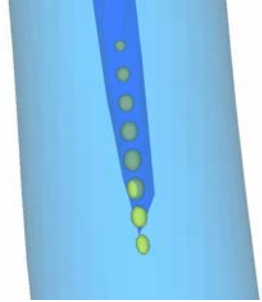


Figure 16. Computed bubble sizes and shapes of non-spherical modes for $R_0 = 20 \mu\text{m}$ at $\sigma = 10.85$

3.4 Multiple Bubble Dynamics for Prediction of Cavitation Inception

In order to simulate a real nuclei flow field as exists in nature or in the waters of a cavitation tunnel, Hsiao and Chahine (2004b) used a statistical nuclei distribution model and showed that the nuclei size distribution has a strong influence on the prediction of cavitation inception. Since the nuclei size distribution is not available for the experiments conducted on the ducted propulsor flow, we have selected two very different nuclei size distributions and compared their effect on the prediction of cavitation inception. The first nuclei size distribution contains larger nuclei sizes ranging from 2.5 to $25 \mu\text{m}$ while the other one contains smaller nuclei sizes ranging from 2.5 to $10 \mu\text{m}$ (see Figure 17). In both cases we randomly released the nuclei from a $0.02\text{m} \times 0.03\text{m}$ window. A total of 600 nuclei were released within 0.4 second. The nuclei size distribution for both cases is shown in Figure 17.

As the nuclei travel in the computational domain, the resulting acoustic signals are monitored. The acoustic pressure is monitored on the shroud wall at a location 0.5 chord length downstream of the tip trailing edge. A series of computations were conducted at different cavitation numbers for both nuclei distributions to obtain acoustic signals for conditions above and below cavitation inception. Figure 18

illustrates the acoustic signals for the larger nuclei size distribution at three different cavitation numbers.

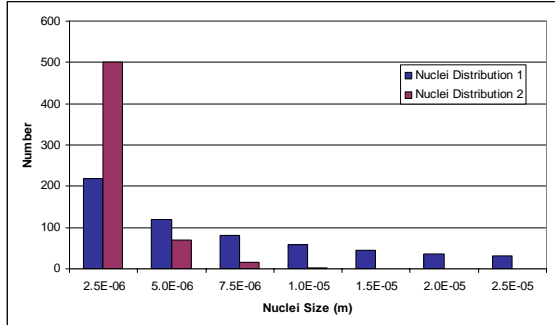


Figure 17. The number of nuclei released versus nuclei size for two different nuclei size distributions considered in this study.

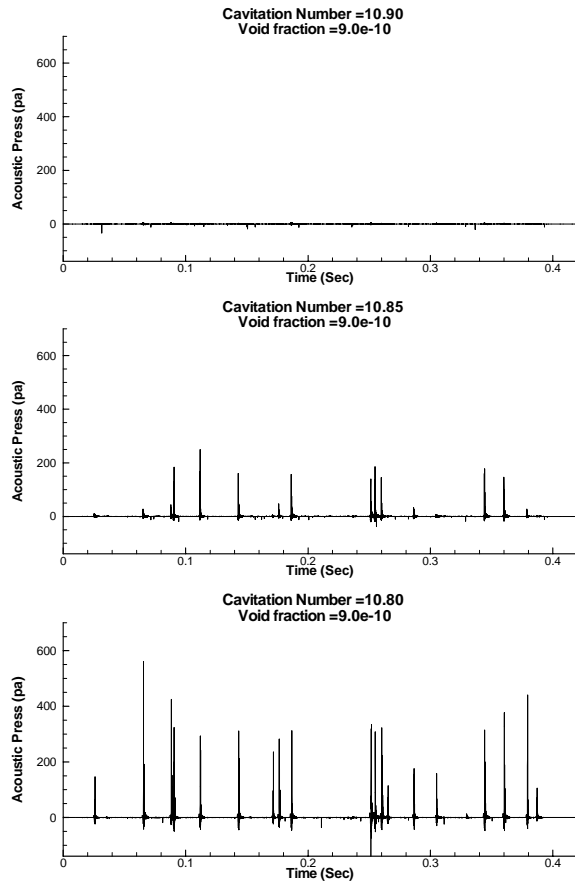


Figure 18. The acoustic signals for the large size nuclei distribution case at three different cavitation numbers.

From the results shown in Figures 18, we can define a cavitation inception number based on the number of cavitation events per unit time exceeding a certain value. Here a cavitation event is defined arbitrarily when a cavitating bubble emits an acoustic

signal higher than 100pa. The curve of the number of cavitation events per second versus cavitation number is shown in Figure 19. It can be seen that there is a critical cavitation number above which no cavitation events occur. For nuclei size distribution No. 1 (larger bubbles) an abrupt rise in the number of cavitation events is seen when the cavitation number is below the critical cavitation number. Based on these curves one can determine the cavitation inception number for both cases by defining a criterion. For example, if 10 events per second is defined for cavitation inception, then a cavitation inception number $\sigma_i=10.89$ for the larger nuclei size distribution and $\sigma_i=10.6$ for the smaller nuclei size distribution can be deduced from Figure 19. Chesnaks and Jessup (2003) defined the cavitation inception criterion as one event per second and obtained a cavitation inception number about 11. This inception number is very close to the critical cavitation number (~ 10.9) for the larger nuclei size distribution, but these results are subject to the two criteria selected: amplitude of the peak and number of peaks per unit time.

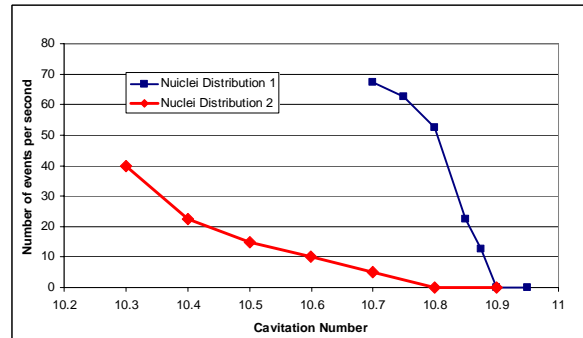


Figure 19. Number of events per second versus cavitation number for the nuclei size distributions shown in Figure 17.

4. Conclusions

A direct numerical simulation of the two interacting vortices in a ducted propulsor flow field was conducted in a reduced computational domain to address the grid resolution issue in RANS computation. It was found that vortex diffusion and dissipation were significantly reduced with grid refinement. The resulting solutions illustrated with iso-pressure surfaces agree much better than RANS computations with experimental observations for fully developed cavitation in the vortex core and for cavitation inception number and location. No instability was seen due to a weak vortex/vortex interaction between the tip-leakage vortex and the trailing-edge vortex in the simulations. Further grid refinement may be required to resolve any such instability.

The location and size of the “window of opportunity” through which a nucleus needs to enter to be captured by the vortex was identified for different nuclei sizes.

From the study of single bubble dynamics we showed that the characteristics of the acoustic signals and bubble shapes as well as the location of cavitation inception resemble those observed experimentally. A multiple bubble dynamics model was also applied to study the effect of nuclei size distribution and to predict cavitation inception in real flow field conditions. Different nuclei size distributions and definitions of the cavitation inception event were found to influence the cavitation inception number. However, the range of cavitation inception number ($\sigma_i \sim 11$) was found to agree much better than previous studies ($\sigma_i \sim 5$) with the experimental measurements.

ACKNOWLEDGMNETS

This work was conducted at DYNAFLOW, INC. (www.dynaflow-inc.com) and was supported by the Office of Naval Research under contract No. N00014-04-C-0110 monitored by Dr. Ki-Han Kim. The RANS solution of the full propulsor flow was provided by C. I. Yang from NSWCD and the experimental data was provided by Christopher J. Chesnakas from NSWCD. Their cooperation on this study is greatly appreciated.

REFERENCES

- [1] Brewer, W.H., Marcum, D.L., Jessup, S.D., Chesnakas, C., Hyams, D.G., Sreenivas, K., “An Unstructured RANS Study of Tip-Leakage Vortex Cavitation Inception,” Proceedings of the ASME Symposium on Cavitation Inception, FEDSM2003-45311, Honolulu, Hawaii, July 6-10, 2003.
- [2] Chen, A.L., Jacob, J.D., Savas, O., “Dynamics of Co-rotating Vortex Pairs in the Wakes of Flapped Airfoils,” J. Fluid Mech., vol. 382, 1999, pp. 155-193.
- [3] Chesnakas, C.J., Jessup, S.D., “Tip-Vortex Induced Cavitation on a Ducted Propulsor,” Proceedings of the ASME Symposium on Cavitation Inception, FEDSM2003-45320, Honolulu, Hawaii, July 6-10, 2003.
- [4] Chorin, A. J., “A Numerical Method for Solving Incompressible Viscous Flow Problems,” Journal of Computational Physics, Vol. 2, 1967, pp. 12-26.
- [5] Dacles-Mariani, J., Zilliac, G.G., Chow, J.S., Bradshaw, P., “Numerical/Experimental Study of a Wingtip Vortex in the Near Field,” AIAA Journal, Vol. 33, No. 9, 1995, pp.1561-1568.
- [6] Devenport, W.J., Vogel, C.M., Zsoldos, “Flow Structure Produced by the Interaction and Merger of a Pair of Co-Rotating Wing-Rip Vortices,” J. Fluid Mech., vol. 394, 1999, pp. 357-377.
- [7] Hsiao, C.-T., Pauley, L.L., “Numerical Study of the Steady-State Tip Vortex Flow over a Finite-Span Hydrofoil,” ASME Journal of Fluid Engineering, Vol. 120, 1998, pp. 345-349.
- [8] Hsiao, C.-T., Chahine, G.L., Liu, H.L., “Scaling Effects on Prediction of Cavitation Inception in a Line Vortex Flow,” ASME Journal of Fluids Engineering, Vol. 125, 2003a, pp. 53-60.
- [9] Hsiao, C.-T., Chahine, G.L., “Scaling of Tip Vortex Cavitation Inception Noise with a Statistic Bubble Dynamics Model Accounting for Nuclei Size Distribution,” Proceedings of the ASME Symposium on Cavitation Inception, FEDSM2003-45315, Honolulu, Hawaii, 6-10 July, 2003b.
- [10] Hsiao, C.-T., Chahine, G.L., “Effect of Vortex/Vortex Interaction on Bubble Dynamics and Cavitation Noise”, Fifth International Symposium on Cavitation CAV2003, Osaka, Japan, November 1-4, 2003c.
- [11] Hsiao, C.-T., Chahine, G.L., “Prediction of Vortex Cavitation Inception Using Coupled Spherical and Non-Spherical Models and Navier-Stokes Computations,” Journal of Marine Science and Technology, Vol. 8, No. 3, 2004, pp. 99-108.
- [12] Johnson, V.E., Hsieh, T., “The Influence of the Trajectories of Gas Nuclei on Cavitation Inception,” Sixth Symposium on Naval Hydrodynamics, 1966, pp. 163-179.
- [13] Kim, J., “Sub-Visual Cavitation and Acoustic Modeling for Ducted Marine Propulsor,” Ph.D. Thesis, 2002, Department of Mechanical Engineering, The University of Iowa, Adviser F. Stern.
- [14] Oweis, G., Ceccio, S., Chesnakas, C. Fry, D., Jessup, S., “Tip Leakage Vortex (TLV) Variability from a Ducted Propeller under Steady Operation and its Implications on Cavitation Inception,” 5th International Symposium on Cavitation, Osaka, Japan, November 1-4, 2003.
- [15] Vanden, K., Whitfield, D. L., “Direct and Iterative Algorithms for the Three-Dimensional Euler Equations,” AIAA-93-3378, 1993.
- [16] Yang, C.I., Jiang, M., Chesnakas, C.J., and Jessup, S.D., 2003, "Numerical Simulation of Tip Vortices of Ducted-Rotor", NSWCCD-50-TR-2003/46

Tip Vortex Cavitation Inception Study Using the Surface Averaged Pressure (SAP) Model Combined with a Bubble Splitting Model

Jin-Keun Choi, Chao-Tsung Hsiao, and Georges L. Chahine
(DYNAFLOW, INC., U.S.A.)

ABSTRACT

Non-spherical simulations of bubble nuclei in a tip vortex flow indicate bubble elongation followed by splitting and reentrant jet formation. The associated noise is much higher than the pressure signal from the collapse of a spherical bubble. A major difficulty in applying such a non-spherical method to a field of nuclei is the prohibitively expensive cost of corresponding computations. In this paper, we attempt to overcome this difficulty by performing simulations with an improved Surface Averaged Pressure (SAP) spherical model that accounts for bubble splitting. Non-spherical numerical studies are used to develop splitting criteria and characterize the resulting noise and offspring sub-bubbles. These criteria are implemented in the SAP spherical model, and numerical results with single bubble and with a realistic field are then presented. The effect of the inclusion of bubble splitting on the cavitation inception prediction is then investigated.

INTRODUCTION

Conducting numerical cavitation inception experiments using a distribution of nuclei as in a real liquid has been very successful in providing a numerical tool to study tip vortex cavitation inception and its scaling. We have developed a Surface Averaged Pressure (SAP) spherical bubble dynamics model (Hsiao, Chahine, and Liu, 2003, Hsiao and Chahine, 2003a, 2003b) that has provided bubble dynamics results very similar to those obtained using a 3-D two-way interaction model (Figure 1). The SAP model is especially appropriate for simulations with a large number ($\sim 10^3$ used so far) of bubble nuclei because of its reasonable memory and computational time requirements. The success of this model in the study of cavitation inception is partly due to the fact that the spherical approximation is valid at cavitation numbers

near and above the cavitation inception number (Figure 2).

On the other hand, our recent studies with a more precise non-spherical axisymmetric method (Choi and Chahine, 2003a, 2003b, 2004, Choi, Chahine, and Hsiao, 2003a, 2003b) revealed that the bubble nucleus behavior at cavitation numbers just below the cavitation inception number is associated with extreme bubble elongation and splitting. Furthermore, these studies showed that the bubble splitting is followed by strong reentrant jets in the resulting offspring bubbles (Figure 3) and by the emission of very high pressure signals. A pressure signal is generated at the bubble splitting; however, much stronger pressures may be subsequently generated during the impact of the reentrant jets and the collapse of the offspring bubbles. The fact that the pressure signal from the subsequent behavior of the offspring bubbles is much higher than that from the collapse (splitting) of the original bubble suggests the need to include the bubble splitting in the SAP model in on-going and future studies. In addition, bubble splitting obviously results in the modification of the original nuclei size distribution, and this effect is included in the present upgraded SAP model.

In order to avoid the higher computational cost of non-spherical methods and, at the same time, to include bubble splitting effects in the multiple bubble simulations, we need to identify the conditions for occurrence and to model the bubble splitting. Through an extensive series of non-spherical simulations under various conditions, we have developed rules for the conditions under which a bubble splits, the timing of the splitting, and the characteristics of the resulting offspring bubbles. These rules are then implemented in the upgraded SAP spherical model resulting in dynamic modification of the bubble nuclei sizes and distribution during a SAP simulation.

In this paper, we illustrate the method for the study of cavitation inception in the flow field of a tip vortex. First, the non-spherical numerical studies on bubble

splitting leading to the development of splitting criteria and characterization of the resulting offspring bubbles are introduced and the implementation of the model within the context of the SAP spherical model is described. Numerical results with single and multiple bubble nuclei are then presented, and the effect of inclusion of bubble splitting on the cavitation inception prediction is discussed.

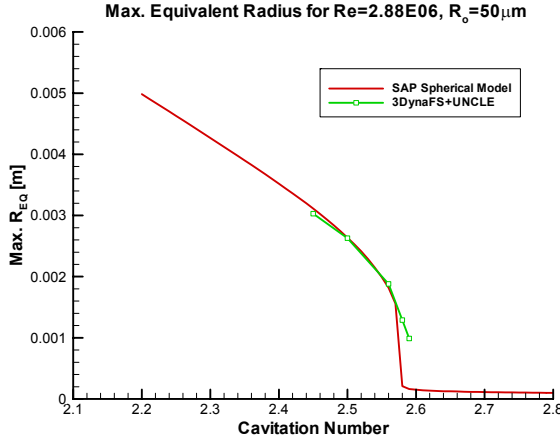


Figure 1: Comparison of maximum bubble sizes from SAP spherical model and those from a non-spherical bubble model. Note the excellent agreement between the SAP spherical model and the 3-D two-way interaction model (3DynaFS+DF_UNCLE) from Hsiao and Chahine (2003b).

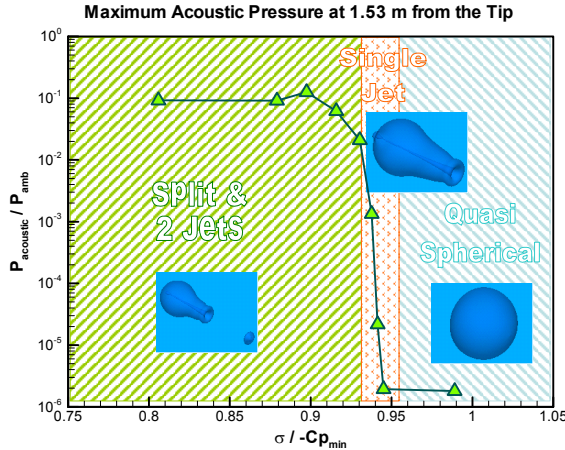


Figure 2: The maximum acoustic pressure as a function of cavitation number. Note that the bubble behavior near and above the cavitation inception (approx. 2.58 in this case) is quasi-spherical. (from Choi and Chahine (2004))

BUBBLE SPLITTING MODEL

In our previous work (Choi and Chahine, 2003a, Choi, Chahine, and Hsiao, 2003), we have developed a

bubble splitting model based on axisymmetric simulations of bubble nucleus under various conditions in a typical tip vortex flow field of a hydrofoil. In this section, we briefly summarize our observations of the bubble splitting and the characterization of the phenomena.

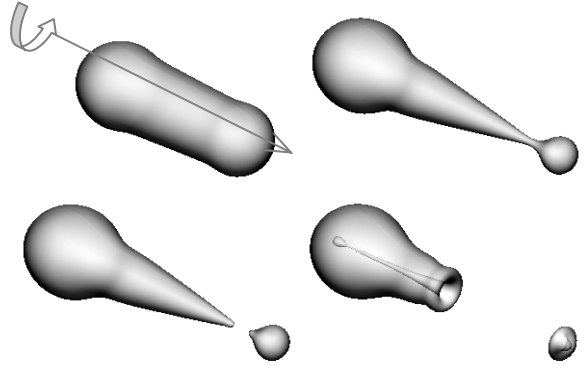


Figure 3: Bubble splitting and jet development of a nucleus captured by a tip vortex (in time sequence from top left to bottom right). (from Choi and Chahine (2004))

The tip vortex flow field used in the development of the splitting model is that of an elliptic hydrofoil of 1 m chord and 1.5 m half span subject to 2.88 m/s inflow. The splitting model is derived from observations of the equivalent radius¹ at which a bubble splits and the equivalent radii of the sub-bubbles. As shown in Figure 4, these radii form a common set of curves regardless of the initial nucleus size within the range of 10 to 100 μm . We have also found that if the curves are normalized by the equivalent radius of the bubble just before the splitting, the ratios are constant over a wide range of cavitation numbers as shown in Figure 5. The ratio of the maximum equivalent radius, R_{\max} , to the equivalent radius just before the splitting is very close to 1.06, and the radii of the two sub-bubbles just after the split are 0.95 R_{\max} and 0.55 R_{\max} regardless of the initial bubble size. These observations are the basis for the bubble splitting criterion and the initial size of the resulting sub-bubbles that are used below.

The axial location of the sub-bubble centers obtained from numerous computations with various initial bubble nuclei size is shown in Figure 6. The sub-bubble centers normalized by the equivalent radius at splitting, R_{split} , fall on the same curves throughout the range of cavitation numbers we have studied. The center position of the downstream sub-bubble is

¹ The equivalent radius is defined as the radius of a sphere of the same volume.

observed to be near $4.4 R_{split}$, and the axial location of the upstream sub-bubble varies from approximately $-1.0 R_{split}$ for the low cavitation numbers to 0.0 at the cavitation number where splitting starts to occur.

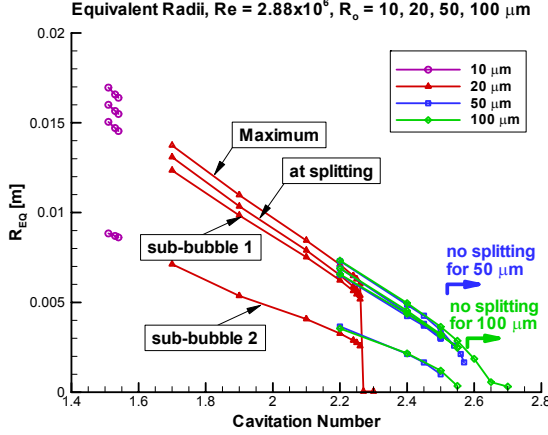


Figure 4: The equivalent radii predicted by the axisymmetric boundary element method (2DYNAPS) which allows bubble elongation and splitting. Four initial nuclei sizes, 10, 20, 50, and 100 μm , are considered, and the maximum radii, radii at splitting, and two radii of the sub-bubbles are shown.

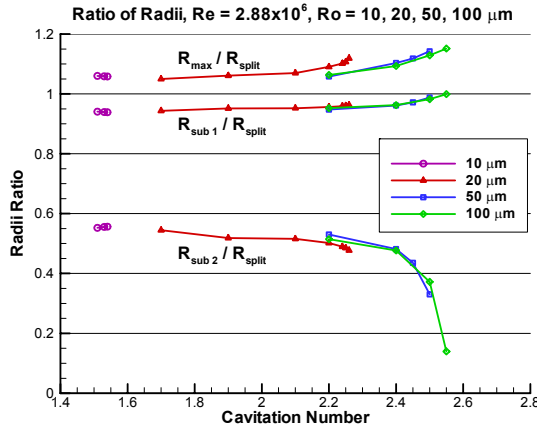


Figure 5: The ratios of the maximum equivalent radius, R_{max} , and the equivalent radii of the two sub-bubbles, R_{sub1} , R_{sub2} , relative to the equivalent radius just before the splitting, R_{split} , for the four initial nuclei sizes, 10, 20, 50, and 100 μm .

The radial velocity of the sub-bubbles just after the split was found to be close to zero for both sub-bubbles. It was also found that the initial locations of the sub-bubbles depend weakly on the Reynolds numbers but more strongly on the cavitation numbers. For cavitation numbers in the mid-low range ($1.7 \leq \sigma \leq 2.2$), the locations of the sub-bubbles relative to the bubble center just before the splitting are fairly

constant and are $-1.0 R_{split}$ and $4.4 R_{split}$, respectively for the upstream and the downstream sub-bubbles.

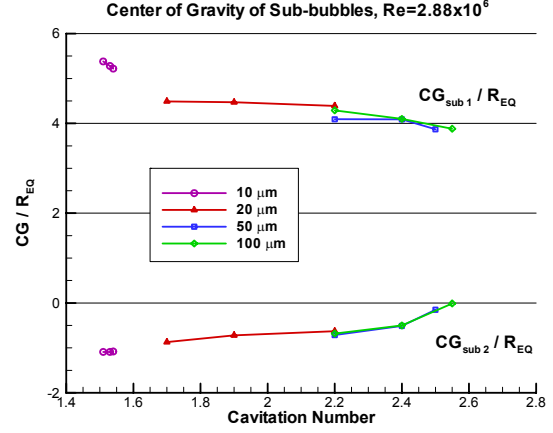


Figure 6: The axial locations of the sub-bubbles just after the splitting normalized by the equivalent radius just before the splitting, R_{split} . Four initial nuclei sizes, 10, 20, 50, and 100 μm are considered.

Based on the observations of the bubble splitting described above, the following bubble splitting model for low cavitation numbers (or smaller nuclei) was developed. The model consists of a splitting criterion and initial conditions for the sub-bubbles.

Bubble splitting criterion: After a bubble has grown explosively ($\sigma < \sigma_{inception}$), it will split at the beginning of the collapse once its radius reaches 95% of the maximum radius.

Initial condition of sub-bubbles: The radii of the larger and smaller sub-bubbles are respectively, 0.95 and 0.55 of the radius at splitting, R_{split} . The initial gas pressure in each sub-bubble is that of the original bubble pressure at splitting, and the initial radial velocities are zero. The initial location of the larger sub-bubbles is $1.0 R_{split}$ upstream of the original bubble center, and that of the smaller one is $4.4 R_{split}$ radii downstream of the original bubble center.

REENTRANT JET NOISE MODEL

The peak-to-peak values of the acoustic pressure signal are shown in Figure 7. The acoustic pressure data predicted with 10, 20, 50, and 100 μm nuclei also fall on a common curve regardless of the initial bubble sizes. The maximum pressure peaks predicted by 2DYNAPS[©] are always observed at the development of the jets in the sub-bubbles following the bubble splitting. We can use this observation to develop a model for the reentrant jet noise.

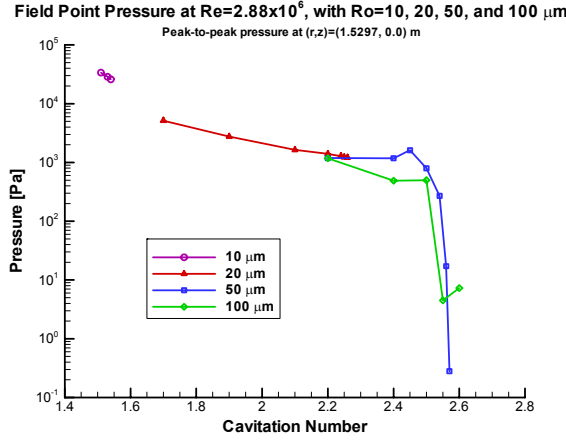


Figure 7: Acoustic pressure signals predicted by the axisymmetric boundary element method (2DYNAPS) which allows bubble elongation and splitting. Data for the four initial nuclei sizes, 10, 20, 50, and 100 μm form a common curve.

The modeling of the jet noise is based on the observations of a typical acoustic pressure from the reentrant jet as shown in Figure 8. To model the timing of the jet noise, the time delay between the splitting and the zero crossing of the jet noise is defined as t_1 , and the time interval between the minimum and the maximum of the jet noise is defined as t_2 . These two time intervals and the peak-to-peak values of the acoustic pressure signal are plotted for a range of cavitation numbers in Figure 9. These data are fit into exponential curves resulting in the following expressions:

$$\begin{aligned} p(\sigma) &= \exp(-2.5217\sigma + 12.7754), \\ t_1(\sigma) &= \exp(-2.7698\sigma - 2.0205), \\ t_2(\sigma) &= \exp(-2.3703\sigma - 5.7600). \end{aligned} \quad (2)$$

Then, the acoustic pressure signal due to the jet is modeled with the following sine signal.

$$p_{jet}(t) = \frac{p(\sigma)}{2} \cdot \sin\left(\frac{t-t_1(\sigma)}{t_2(\sigma)}\pi\right), \quad t_1 - t_2 \leq t \leq t_1 + t_2 \quad (3)$$

The jet noise from this model is compared with the original pressure signal for $\sigma=2.10$ in Figure 10. The duration of the signal from the model is shorter than the original signal at this cavitation number because the curve fit for t_2 underestimates the duration of the signal as shown in Figure 9. We will improve this approximation in our next studies.

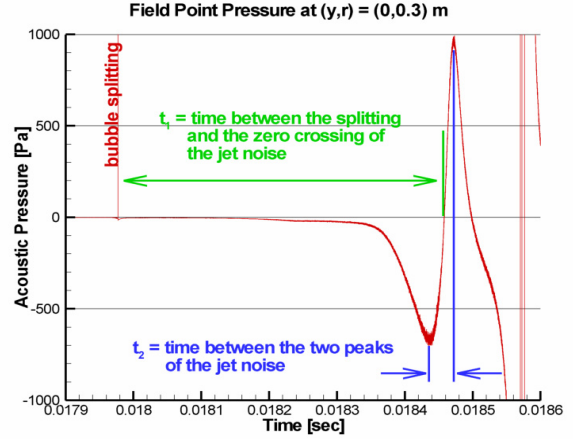


Figure 8: Typical pressure signal from the reentrant jet after a bubble splitting.

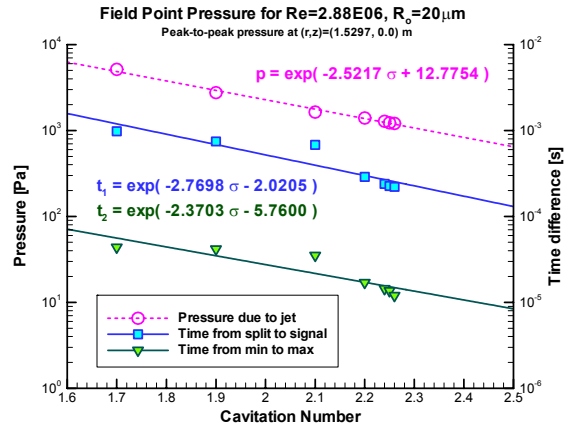


Figure 9: Exponential curve fit of the acoustic pressure from the jet and the two time intervals of the jet noise.

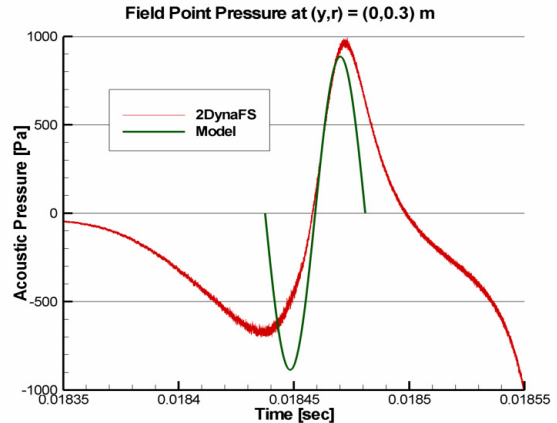


Figure 10: Comparison of the pressure signal from the reentrant jet between the 2DYNAPS prediction and the model equation (3) at $\sigma=2.10$.

SINGLE SPLITTING OF A NUCLEUS

The improved SAP spherical model is first applied to a $20 \mu\text{m}$ nucleus at $\sigma=1.70$. The tip vortex flow field used here is the same flow field in which the splitting model was developed (Choi and Chahine, 2003a, Choi, Chahine, and Hsiao, 2003). The resulting time history of the bubble radius is shown in Figure 11 and the associated acoustic pressure signal is shown in Figure 12. When the nucleus grows to its maximum size and reaches 95% of the maximum radius, it splits into two sub-bubbles as expected from the model explained earlier. The larger sub-bubble shrinks monotonically after the split, while the smaller sub-bubble begins with a small growth followed by violent collapses and rebounds. The acoustic pressure has an initial peak corresponding to the initial growth of the nucleus, followed by a sharp jet noise after the split. Then, there are two contributions to the acoustic pressure, one for each sub-bubble. The resulting signal from the sub-bubbles has a smaller maximum peak than that without splitting.

Another simulation of $20 \mu\text{m}$ nucleus at a higher cavitation number, $\sigma=2.10$, is shown in Figure 13. In this case, both of the sub-bubbles experience collapse and rebound cycles. However, the combined pressure signal still has smaller peaks than that from the simulation without the splitting if the strong jet noise of about 800 Pa appearing at 0.066 s is excluded. In Figure 14, the bubble behavior at the cavitation inception number is shown. In this case, the larger sub-bubble is more active, yet producing weaker signal than the simulation without splitting.

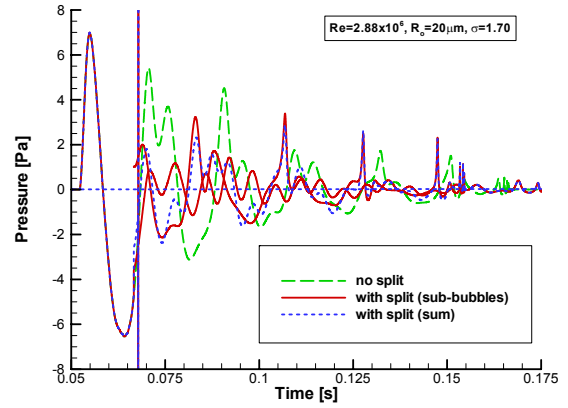


Figure 12: Acoustic pressure signals predicted with $20 \mu\text{m}$ nucleus at $\sigma=1.70$.

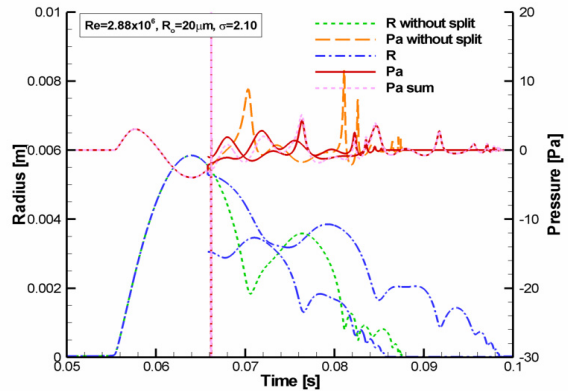


Figure 13: Bubble radius and the acoustic pressure signal as functions of time predicted with $20 \mu\text{m}$ nucleus at $\sigma=2.10$.

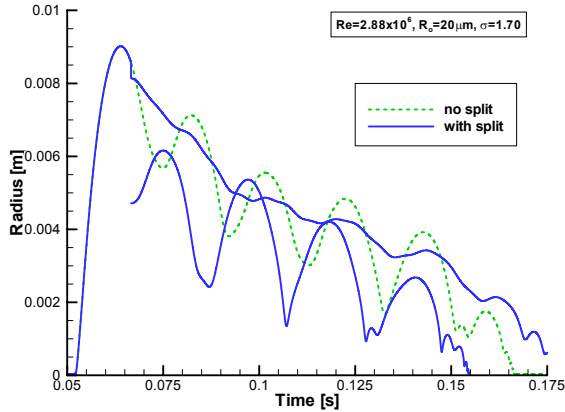


Figure 11: Bubble radius history predicted with $20 \mu\text{m}$ nucleus at $\sigma=1.70$.

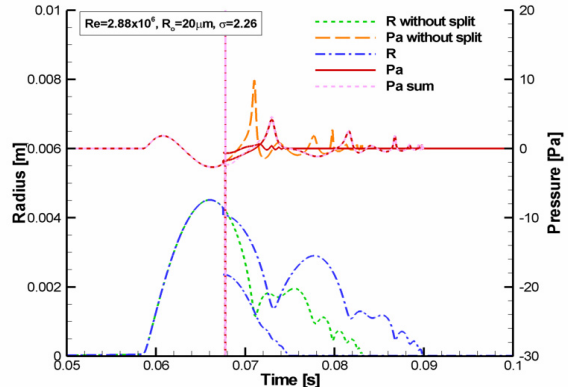


Figure 14: Bubble radius and the acoustic pressure signal as functions of time predicted with $20 \mu\text{m}$ nucleus at $\sigma=2.26$ (cavitation inception).

Based on the results of the three cavitation numbers, we can arrive at the following conclusions for a single split of a nucleus. Visual detection of cavitation, which is based on detecting the maximum bubble size, is not affected by the splitting because the sub-bubble sizes are always smaller than the maximum size observed before the inclusion of splitting in the model and never grow larger than this. The acoustic pressure signal with splitting has a strong jet noise, but the resulting signals of the collapsing sub-bubbles are smaller than such a signal of one big bubble without splitting. This is more obviously seen in Figure 15, where the maximum of the resultant acoustic pressure signal from sub-bubble collapses for each cavitation number is always slightly smaller than the maximum peak observed from original SAP simulations without splitting.

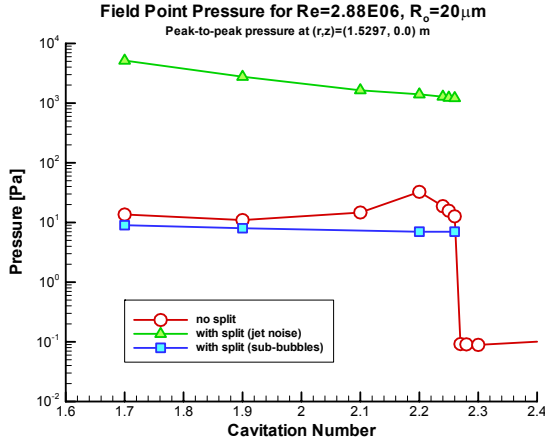


Figure 15: Maximum of the acoustic pressure signal vs. cavitation numbers predicted with $20 \mu\text{m}$ nucleus.

MULTIPLE NUCLEI WITH SINGLE SPLITTING

Simulations with multiple nuclei can provide an insight for the cavitation noise in a real flow field. The improved SAP spherical model is applied to the same tip vortex flow field at $\sigma=2.10$ with a set of 100 nuclei of the same size $20 \mu\text{m}$. The nuclei are distributed randomly in space within a rectangular box of $0.1 \text{ m} \times 0.01 \text{ m} \times 0.006 \text{ m}$ just in front of the blade tip and the computation stops when all these bubbles have gone through the $0.01 \text{ m} \times 0.006 \text{ m}$ window.² This distribution corresponds to a void fraction of 5.59×10^{-7} .

² Note that the same nuclei population is assumed everywhere in the flow domain, but only the nuclei coming through this window has the opportunity to grow explosively.

The acoustic pressure signal from this simulation is shown in Figure 16. Compared to the acoustic signal without splitting, the signal with splitting is much noisier due to the jet noise, but the contribution from the sub-bubble collapses is weaker than the signal without splitting.

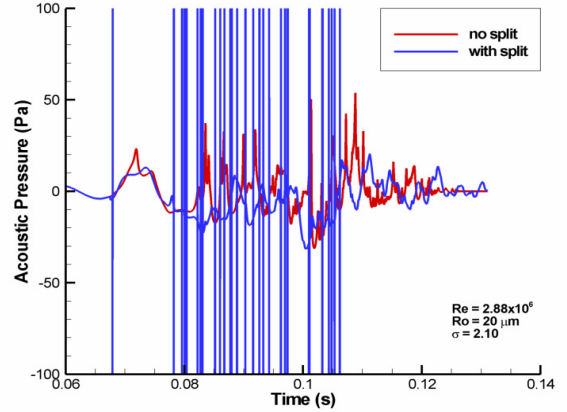


Figure 16: Acoustic pressure signal from 100 nuclei of size $20 \mu\text{m}$ with splitting compared to that without splitting.

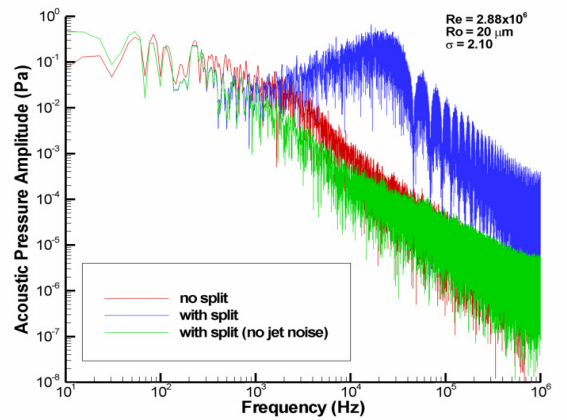


Figure 17: Amplitude spectrum of the acoustic pressure signal from 100 nuclei of size $20 \mu\text{m}$ with splitting compared to that without splitting. Also shown is the influence of the reentrant jet noise on the results.

The amplitude spectrum can be obtained from the pressure signal, $p(t)$, through the finite Fourier transformation.

$$P(f, T) = \int_0^T p(t) e^{-i2\pi f t} dt \quad (4)$$

where T is the time duration for the finite Fourier transformation and f is the frequency. The amplitude

spectrum of the acoustic signal is shown in Figure 17. When the spectrum with splitting but without the jet noise is compared with the spectrum with splitting, the noise contents of frequency lower than $50\text{--}100\text{ kHz}$ have decreased and those at higher frequency have increased. This redistribution of the frequency contents is due to the smaller sub-bubbles created by the bubble splitting. If the jet noise is considered, the spectrum has a peak at 25 kHz . This frequency corresponds to the duration of the jet noise, $\approx 40\text{ }\mu\text{s}$, at this cavitation number.

MULTIPLE SPLITTING

The bubble splitting model used above is based on the non-spherical axisymmetric bubble simulations starting from the first cycle of the bubble growth. In such simulations, the numerical computations usually cannot be continued through the collapse and rebound of the sub-bubbles because of the touchdown of the developed reentrant jets and the instabilities of the collapsing bubbles. Therefore, the non-spherical simulations cannot tell if the newly born sub-bubbles would split again or not. The first cycle usually has the strongest growth because it occurs just after the nucleus passes the minimum pressure region of the tip vortex. The bubble growth in the second and later cycles is weaker than the first because the pressure becomes higher and higher as the bubble moves downstream. Would the sub-bubble placed a little downstream of the minimum pressure region of the tip vortex split again? This question can be answered by performing a non-spherical simulation from the second cycle of the SAP spherical simulation because the local pressure encountered by the bubble nucleus a bubble cycle downstream would be very similar to that of the sub-bubble after the splitting.

In Figure 18, two 2DYNAs[®] simulations are shown, one starting from the beginning of the first cycle and the other from the beginning of the second cycle of the SAP prediction. Even though the local pressure encountered by the bubble in the second cycle is higher than that of the first, the bubble elongates and splits in the same way. The only major difference between the two cases is the amount of the growth, i.e. about 400 times in the first cycle vs. about twice in the second cycle. The characteristics of the splitting in the second cycle are very similar to those in the first cycle as summarized in Table 1.

Because the sub-bubbles also split under very similar criteria as the first splitting, we can apply the same bubble splitting model to successive splitting of the sub-bubbles. Results from such a simulation are shown in Figure 19 for a $20\text{ }\mu\text{m}$ nucleus. The bubble

radii obtained for a cavitation number of 1.70 show several radii curves due to successive splits. None of the sub-bubbles grow larger than the first maximum radius reached by the initial nucleus. The corresponding acoustic pressure signal shown in Figure 20 becomes very complex with many new small signals appearing as the sub-bubbles become smaller and smaller. The amplitude spectrum of the combined signal is shown in Figure 21. Compared to the spectrum without splitting, the spectrum with multiple splitting has richer contents over all frequencies above a couple of hundreds kHz .

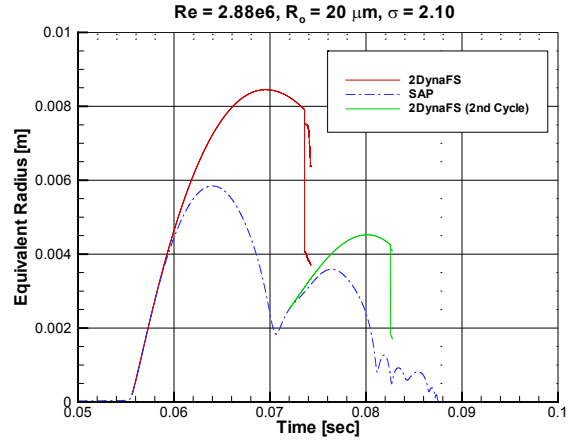


Figure 18: Two 2DYNAs[®] simulations, one starting from the beginning of the first cycle and the other from the second cycle of the bubble growth predicted by SAP with $20\text{ }\mu\text{m}$ nucleus at $\sigma=2.10$.

Table 1: Characteristics of the bubble splitting in the first and the second cycles.

	1 st cycle	2 nd cycle
$R_{\text{eq},\text{split}} / R_{\text{eq},\text{max}}$	0.95	0.94
$R_{\text{eq},1} / R_{\text{eq},\text{split}}$	0.95	0.97
$R_{\text{eq}2} / R_{\text{eq},\text{split}}$	0.55	0.43

The successive splits of sub-bubbles can also be applied to simulations in the field of nuclei. Following the nuclei distribution used by Hsiao and Chahine (2003a), 142 nuclei of size distributions between 5 and $50\text{ }\mu\text{m}$, as shown in Figure 22, are randomly distributed in the box-like volume of $0.1\text{ m} \times 0.01\text{ m} \times 0.006\text{ m}$ just in front of the blade tip. The void fraction based on the bubble distribution and the box-like volume is 1.46×10^{-6} .

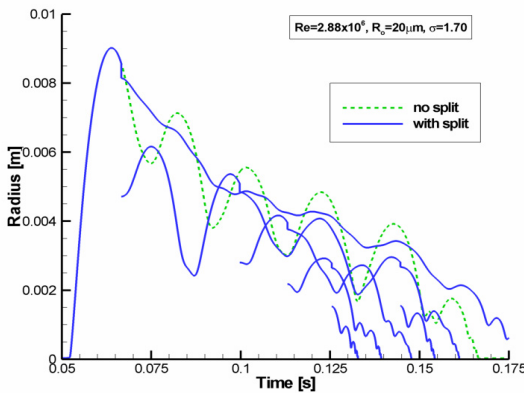


Figure 19: Bubble radii of the sub-bubbles from a $20 \mu\text{m}$ nucleus with multiple splitting at $\sigma=1.70$.

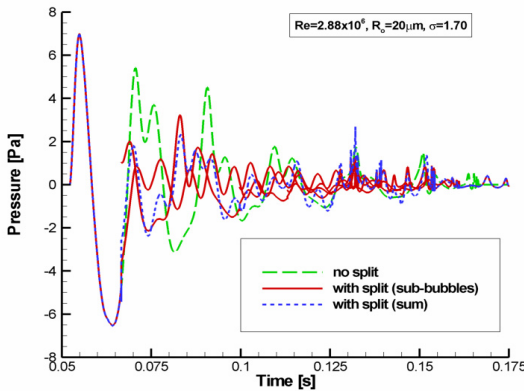


Figure 20: Acoustic pressure signals of the sub-bubbles and their sum from a $20 \mu\text{m}$ nucleus with multiple splitting at $\sigma=1.70$.

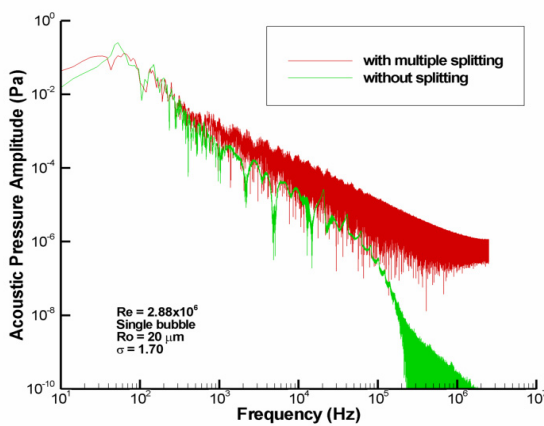


Figure 21: Amplitude spectrum of the acoustic pressure signal from $20 \mu\text{m}$ nucleus with multiple splitting at $\sigma=1.70$.

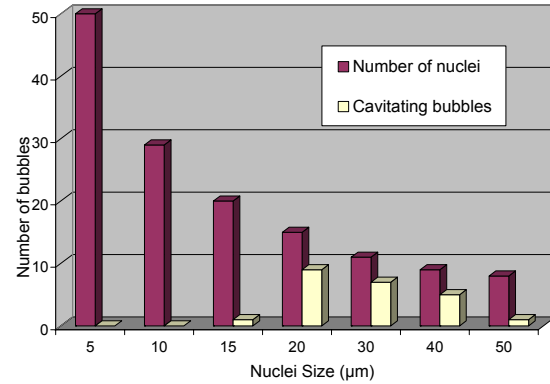


Figure 22: Distribution of 142 nuclei of sizes from 5 to $50 \mu\text{m}$ and the resulting number of nuclei that cavitate in the simulation.

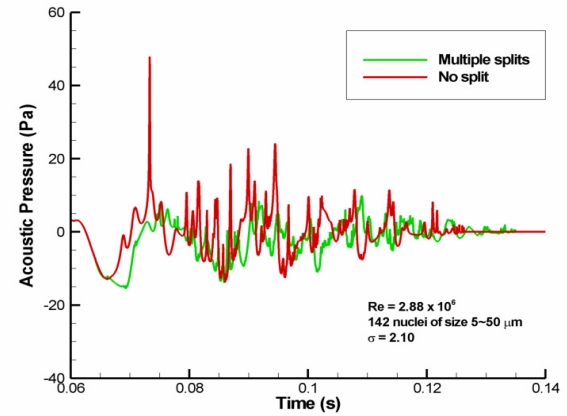


Figure 23: Acoustic pressure signal from 142 nuclei of size distribution from 5 to $50 \mu\text{m}$ with multiple splitting at $\sigma=2.10$ compared to that without splitting.

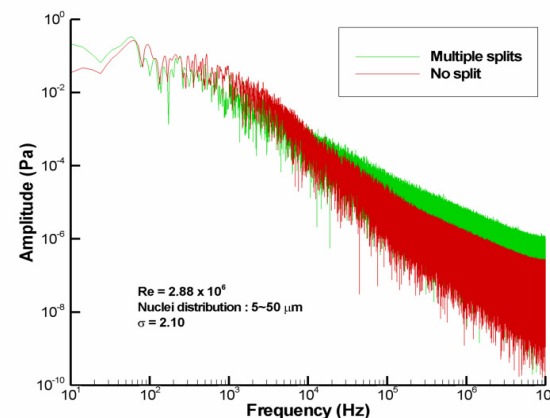


Figure 24: Amplitude spectrum of the acoustic pressure signal from 142 nuclei of size distribution from 5 to $50 \mu\text{m}$ with multiple splitting at $\sigma=2.10$ compared to that without splitting.

The acoustic pressure signal obtained from the simulation is shown in Figure 23, and its amplitude spectrum is shown in Figure 24. The pressure signal obtained from the distribution of nuclei sizes with multiple splits has smaller peaks, and has increased higher frequency contents (approximately higher than 10 kHz) and less low frequency contents (approximately lower than 10 kHz) than that without splits.

CONCLUSIONS

In order to further develop a tool to study scaling of cavitation inception and noise, we have improved the Surface Averaged Pressure (SAP) spherical model by combining it with a bubble splitting model derived from non-spherical bubble simulations. The method accounts for a cascade of splits of the sub-bubbles and includes the reentrant jet noise. During the development of the model, we have found that the bubble can lead to splitting even further downstream of the minimum pressure region, allowing successive multiple splitting of sub-bubbles. Our numerical simulations show that at least the second splitting of sub-bubbles has characteristics very similar to those of the first splitting. This enhanced SAP model is applied to single and multiple nuclei simulations in a typical tip vortex flow field.

Through the applications of the enhanced SAP model to various cases, we have concluded that the visual detection of the cavitation is not affected by the successive nuclei splitting because the sub-bubbles never grow larger than the first maximum size within the range of our study. However, the bubble splitting has the following effects on the acoustic detection of cavitation: (a) The noise from reentrant jets after the split dominates the pressure signal from the rebounds of the original nucleus and sub-bubbles created from it through splitting. The jet noise contributes to a distinct peak in the spectrum. (b) The resulting acoustic pressure from the rebounds of the sub-bubbles is smaller than the pressure from the rebounds of the original nucleus without splitting. However, compared to the spectrum without splitting, the sub-bubble noise has an amplitude spectrum with more high frequency content and less low frequency content. This trend of shifting of frequency contents in the spectrum is a direct result of the bubble population redistribution from the large size original nucleus to many small size sub-bubbles. We are currently working on the expansion of the model and applications to a wider range of cavitation numbers, initial nuclei distributions, and Reynolds numbers.

ACKNOWLEDGEMENT

This work was conducted at DYNAFLOW, INC. (www.dynaflow-inc.com). The research has been supported by the Office of Naval Research under the contract number N00014-04-C-0110 monitored by Dr. Ki-Han Kim. The authors greatly appreciate this support.

REFERENCES

- Choi, J.-K. and Chahine, G.L., "A Numerical Study on the Bubble Noise and the Tip Vortex Cavitation Inception", *Journal of Ship and Ocean Technology*, Vol.7, No.3, Sep. 2003a, pp.13-33.
- Choi, J.-K. and Chahine, G.L., "Non-spherical Bubble Behavior in Vortex Flow Fields", *Computational Mechanics*, Vol. 32, No. 4-6, Dec. 2003b, pp. 281-290.
- Choi, J.-K. and Chahine, G.L., "Noise due to Extreme Bubble Deformation near Inception of Tip Vortex Cavitation", *Physics of Fluids*, Vol.16, No.7, Jul. 2004.
- Choi, J.-K., Chahine, G.L., and Hsiao, C.-T., "Characteristics of Bubble Splitting in a Tip Vortex Cavitation", *Proceedings of the 5th International Symposium on Cavitation, CAV2003*, Nov. 2003, Osaka, Japan.
- Hsiao, C.-T. and Chahine, G.L., "Effect of Vortex / Vortex Interaction on Bubble Dynamics and Cavitation Noise", *Proceedings of the 5th International Symposium on Cavitation, CAV2003*, Nov. 2003a, Osaka, Japan.
- Hsiao, C.-T. and Chahine, G.L., "Prediction of Vortex Cavitation Inception Using Coupled Spherical and Non-Spherical Models and Navier-Stokes Computations," *Journal of Marine Science and Technology*, 2003b (in print).
- Hsiao, C.-T., Chahine, G.L., and Liu, H., "Scaling Effects on Prediction of Cavitation Inception in a Line Vortex Flow," *Journal of Fluid Engineering*, Vol. 125, 2003, pp. 53-60.



EXPERIMENTAL VALIDATION OF BEM CODE ANALYSIS OF BUBBLE SPLITTING IN A TIP VORTEX FLOW

M. Rebow^{1,2}, J. Choi¹, J.-K. Choi³, G.L. Chahine³, S.L. Ceccio¹

¹University of Michigan, W.E. Lay Laboratory, Ann Arbor, MI 48109, USA

²Warsaw University of Technology, Nowowiejska 21/25, 00-665 Warsaw, POLAND

³DYNAFLOW, INC., 10621-J Iron Bridge Road, Jessup, MD 20794, USA

Keywords: *Non-spherical bubble dynamics, Tip vortex cavitation, Code validation, Stereo PIV*

ABSTRACT

The growth and collapse of a cavitation bubble within the core of a line vortex is examined experimentally and numerically. This paper presents some preliminary results. A steady line vortex is formed downstream of a hydrofoil mounted in the test section of the UM 9-Inch Water Tunnel. A laser is used to initiate a nucleus in the core of the vortex. This nucleus grows and collapses as it experiences a reduction and recovery of the local static pressure. This pressure change is produced when the vortical flow in the test section passes through a reduction in area. Particle image velocimetry is used to measure the axial velocity and average tangential velocity of the tip vortex. Images of the bubble's growth, deformation and splitting are captured with a pulse-synchronize camera. The results are then compared with those obtained with the boundary element method (BEM) code 2DYNAFS[®], which describes large free surface deformations in an axisymmetric potential flow to validate the extreme deformations and splitting model of the bubble. The experimentally observed and numerically predicted bubble dynamics are compared.

1 INTRODUCTION

The dynamics of spherical cavitation bubbles has been examined by many researchers and is relatively well understood. The growth, collapse, and noise emission of non-spherical bubbles has also been examined [1, 2, 16, 17]. In many cases, spherical bubble dynamics can scale these processes, even when the bubbles are significantly deformed but maintain aspect ratios close to unity [3]. However, cavitation bubbles that form in the low-pressure cores of concentrated coherent vortices can have aspect ratios that are significantly larger than unity. Such bubbles can break into several smaller bubbles before the first collapse. This can lead to multiple acoustic emissions from the collapse of a single bubble, and the frequency spectra and intensity of the noise produced by the collapse may not be easily scaled.

Vortical cavitation can occur in the wakes of lifting surfaces or as coherent vortical motions in the turbulent shear flows. Vortex cavitation is often the first cavitation observed, since the formation and stretching of coherent vorticity in the flow can lead to significant local reductions in the static pressure. Experimental and numerical treatments of vortex cavitation have been reported [4-6], and Arndt [7] has provided a review. Oweis *et al.* [3] measured the noise pulse and spectra associated with single cavitation bubble events as they occur within the core of a vortex. The rapid growth and collapse of individual cavitation bubbles was observed, and the noise produced by the collapsing

bubbles was successfully scaled with spherical bubble dynamics. The aspect ratio of the collapsing bubbles was near unity (*i.e.* these bubbles were not highly deformed). However, numerical simulations of highly elongated bubbles in the cores of concentrated vortices suggest that the bubbles may fission during their collapse [8-12]. This could significantly alter the character of the noise produced by such an event.

In the present work, we experimentally produce an elongated bubble in the core of a concentrated vortex and examine its growth and collapse. The experimental flow conditions are characterized and used as boundary conditions for a numerical simulation of the bubble dynamics. A steady line vortex is formed downstream of a hydrofoil mounted in the test section of the UM 9-Inch Water Tunnel. A laser is used to initiate a nucleus in the core of the vortex. This nucleus grows and collapses as it experiences a reduction and recovery of the local pressure. This pressure change is produced when the vortical flow in the test section passes through a reduction in area. Stereo Particle Image Velocimetry is used to measure the axial velocity and average tangential velocity of the tip vortex. Images of the bubble's growth, deformation and splitting are captured with a pulse-synchronize camera. These experimental results are compared with those obtained with the Boundary Element Method (BEM) code 2DYNAPS[®] [18], which describes large free surface deformations in an axisymmetric potential flow to validate the extreme deformations and splitting model of the bubble.

2 EXPERIMENTAL APPARATUS, TECHNIQUES AND PROCEDURE

A finite aspect ratio hydrofoil was used to create steady line vortex in the test section of the University of Michigan 9-Inch Water Tunnel. The tunnel has a circular contraction downstream of a series of flow management screens with area contraction ratio 6.4:1. The test section has a 22.9 cm (9 inch) diameter round inlet that is then faired into a rectangular test section with widely rounded corners. A specially designed acrylic hump, 300 mm in length and 18 mm in maximum height (Figure 1), was mounted at a station 21 cm downstream of the trailing edge in order to slightly change static pressure field in the tunnel. The area ratio of the test section with and without the hump was 0.0354 and 0.0378 m², respectively. Four acrylic windows (93.9 cm by 10.0 cm viewing area) permit optical access to the test section flow. A de-aeration system can be used to vary the dissolved gas content of the flow measured with an Orion Model 810 dissolved oxygen meter.

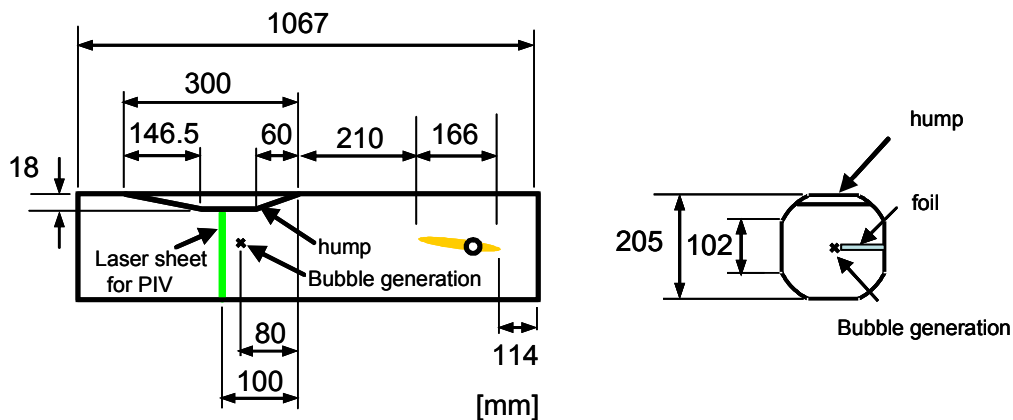


Fig. 1. Dimension and position of the hump in the water cavitation tunnel along with locations of the laser sheet for PIV and the generation of the laser-induced bubble.

EXPERIMENTAL VALIDATION OF BEM CODE ANALYSIS OF BUBBLE SPLITTING IN A TIP VORTEX FLOW

A vortical flow was created using a cambered hydrofoil mounted to one window of the test section. The hydrofoil has a rectangular platform of 9.5 cm span and 16.6 cm chord. The tip of the hydrofoil was rounded. The incident flow angle was fixed to 3.5°. A series of tip and trailing edge vortices are shed near the tip, and these vortices merge to form a single vortex within one-half chord length downstream of the trailing edge. Measurements of bubble behavior in the vortex core were taken for free-stream velocities U_∞ in the range of 9.7 to 10.3 m/s and a variety of static pressures, P_∞ . The Reynolds number of the flow based on the U_∞ and chord length C_0 ($\text{Re} = U_\infty C_0 / \nu$) ranged from $1.76 \cdot 10^6$ to $1.87 \cdot 10^6$, where ν is the liquid kinematic viscosity. The free-stream cavitation number is defined as $\sigma_\infty = (P_\infty - P_v) / 0.5 \rho U_\infty^2$, where the free-stream velocity and pressure are measured at the inlet of the test section upstream of the hydrofoil, and P_v is the liquid vapor pressure.

Stereo Particle Imaging Velocimetry (SPIV) was used to measure the vortical flow field at a station 31 cm downstream of the trailing edge with and without the hump. A double-pulsed light sheet 5 mm thick was created perpendicular to the mean flow direction using two pulsed Nd:YAG lasers (Spectra Physics model Pro-250 Series). 15.3 micron average diameter silver coated glass spheres (from Potters Industries) were used to seed the flow. Acrylic prisms were optically mounted to opposite windows of the test-section for viewing of the light sheet with reduced optical distortion. Double-pulsed images of the light sheet were acquired with two digital cameras with 1280×1024 pixels from LaVision Inc. The 50 mm Nikon lenses were used with Scheimpflug mounts. Optical distortion of the planar light sheet image was corrected through a calibration procedure that employed the imaging of a regular grid in the location of the light sheet plane. Velocity vectors were produced from the double-pulsed images using the LaVision image analysis software Davis 6.0.4. Multi-pass processing with a final window size of 32×32 pixels was used with 50% window overlap in the final pass to produce 82×53 in plane velocity vectors at 1 mm spacing. Since the camera-imaging plane was not parallel to the light sheet and it had an angular shift of 40° with the horizontal direction.

Single cavitation bubbles were controllably initiated in the core of the line vortex through the optical initiation of a small nucleus. Laser-induced bubbles were generated by optical breakdown near the axis of the vortex and approximately in the middle of the hump (80 mm from its upstream edge). The beam of a Q-switched Nd:YAG laser (Spectra Physics PRO 250) producing 10 ns pulses with a maximum energy of 280 mJ at 1064 nm is focused to a point about 20 μm in diameter at the vortex centerline. The laser energy was reduced to the threshold level necessary to just creating a single nucleus. By varying the free-stream pressure and laser energy, the initial size of the laser-induced bubble could be controlled [13]. Such a bubble consists of vapor and contains additionally an amount of non-condensable gas. Such gas likely results from diffusion, plasma recombination, and chemical reactions. Akhatov *et al.* [14] show that the presence of even a small amount of non-condensable gas strongly influences the bubble dynamics. The schematic diagram of the experimental system for the generation of single cavitation bubbles in a vortical flow is shown in Figure 2. The free-stream dissolved gas content was kept below 20%, significantly decreasing the number of free-stream nuclei. Consequently, only laser induced cavitation bubbles consistently occurred in the core of the vortex.

Images of the bubbles were observed with a “FlashCam” digital camera (Cooke Corporation). This camera has an effective resolution of 752 by 240 pixels, and is capable of recording up to 10 consecutive exposures on the same image frame, with varying integration times and delays between each exposure. A pulse delay generator (Stanford Research Systems model DG535) was used to

trigger the camera at varying delays from the laser Q-switch pulse. These images were then recorded digitally and saved onto a PC hard drive for post-processing. Images of the bubble's growth and splitting were captured with the pulse-synchronized digital camera after an appropriate delay, as described above. More details of the experimental arrangements and procedure are given in [3].

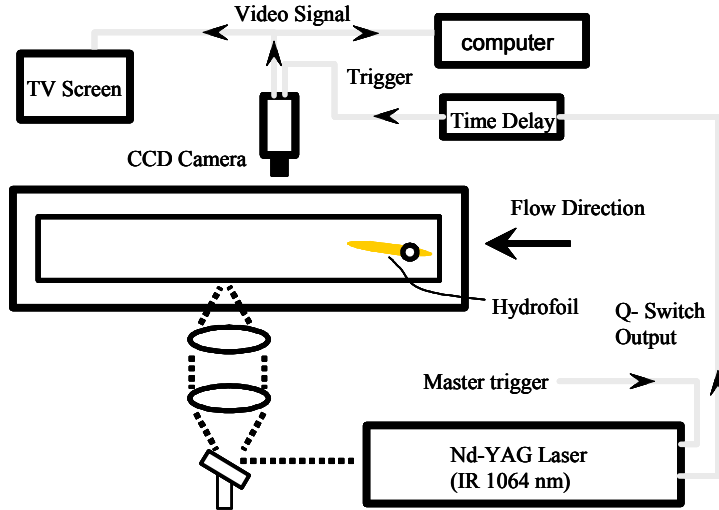


Fig. 2. The schematic diagram of the experimental system for the generation of single cavitation bubbles in a vortical flow

3 EXPERIMENTAL RESULTS

Figure 3a shows a vector map of the average planar vortical flow field measured perpendicular to the vortex axis produced after averaging 50 instantaneous flow field without the hump for $U_\infty = 10$ m/s. Note that the axial velocity of the vortex is about 8% higher than that of the free-stream. Figure 4 plots the average tangential velocity $u_\theta(r)$, as a function of the distance from the vortex center r derived from the measured flow fields. The radial velocity distribution of the vortex is nearly that of a Gaussian vortex:

$$u_\theta(r) = \frac{\Gamma_0}{2\pi r} (1 - e^{-\alpha(r/r_c)^2}) \quad (1)$$

Here, $\alpha \approx 1.255$ which make r_c the “core radius” defined as the radius where the tangential velocity is maximum. For the measured vortex, the fitted core radius r_c was 4.8 mm and the circulation Γ_0 was $0.22 \text{ m}^2/\text{s}$. These parameters are averaged for the vortex upstream and over the hump. Details of the identification process of the Gaussian vortex properties can be found in [3].

As the vortical flow passes over the contraction, the vortex is stretched, and stream-wise flow accelerates on the axis of the vortex. Figure 3b presents the averaged flow field for the vortex passing over the hump. Note that the axial velocity of the vortex is greater up to 12 m/s than the surrounding flow. The pressure in the core of the vortex as it passes over the hump is given by

EXPERIMENTAL VALIDATION OF BEM CODE ANALYSIS OF BUBBLE SPLITTING IN A TIP VORTEX FLOW

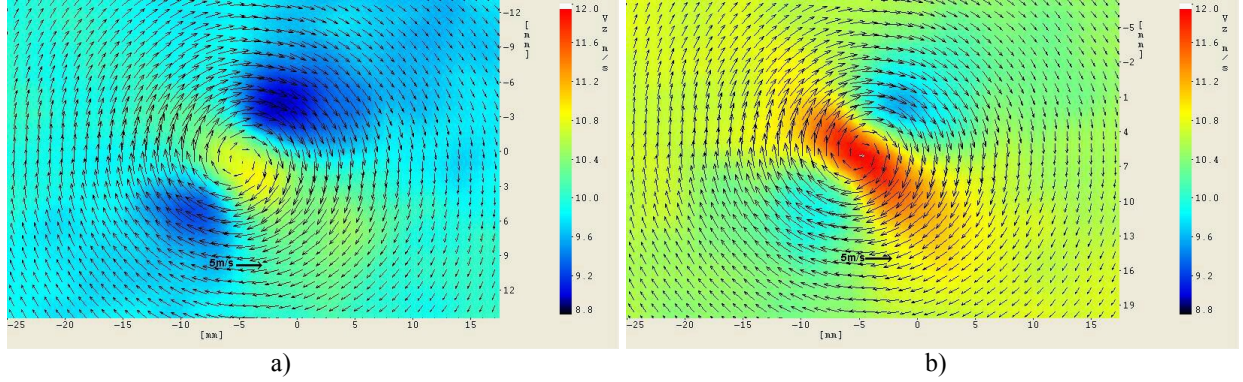


Fig. 3. Axial velocity contours with in-plane velocity vectors for the flow without (a) and with the hump (b).

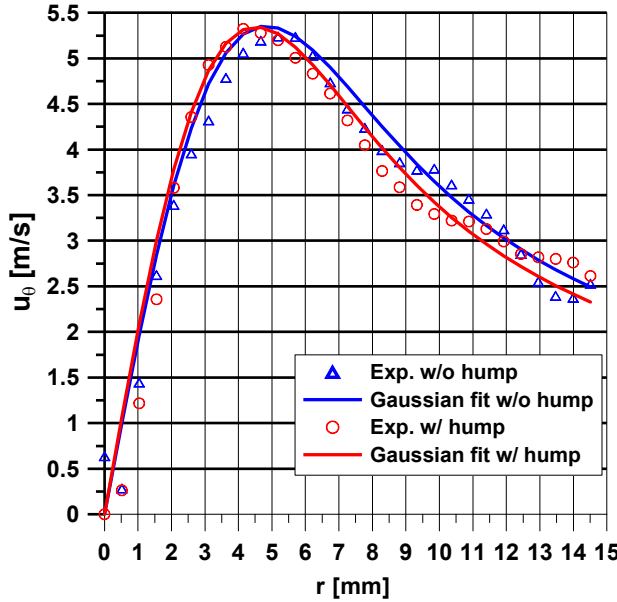


Fig. 4. The measured tangential velocity $u_\theta(r)$, along with the velocity distribution for the Gaussian vortex with $r_c = 4.9$ mm and $\Gamma_0 = 0.213 \text{ m}^2/\text{s}$ (with the hump) and $r_c = 5$ mm and $\Gamma_0 = 0.236 \text{ m}^2/\text{s}$ (without the hump)

$$\frac{P_{CH} - P_\infty}{\rho} = -\eta \left(\frac{\Gamma_0}{2\pi r_c} \right)^2 - \frac{U_\infty^2}{2} \left[1 - \frac{U_{CH}^2}{U_\infty^2} \right] \quad (2)$$

where U_∞ is the local free-stream velocity and pressure far from the vortex, U_{CH} is the axial velocity at the center of the vortex as it passes over the hump, and $\eta = 0.870$, following the approximate analysis of Batchelor [15]. Cavitation can occur in the vortex when $P_{CH} < P_V$, the vapor pressure. $\sigma_{\infty,i}$ is the free-stream cavitation inception number for the vortex as it passes over the hump. We expect that nuclei will grow when

$$\sigma_{\infty,i} \leq \frac{\eta}{2} \left(\frac{\Gamma_0}{\pi r_c U_\infty} \right)^2 - \left[1 - \frac{U_{CH}^2}{U_\infty^2} \right] \quad (3)$$

For the vortex here, $\sigma_{\infty,i} = 1.13$.

With the pulse of the nuclei producing laser, a small bubble is created at the center of the vortex upstream of the hump. Figure 5 shows a series of images illustrating how the bubble grows and collapses ($\sigma_{\infty} = 1.72$ and $U_{\infty} = 10$ m/s). The time delay is the time between the laser firing and the first image, and the time between exposures is 100 μ s. The bubble grows due to the high pressure produced by gases generated within the breakdown volume of the laser beam , even though the core pressure is above vapor pressure. The bubble grows along the axis of the vortex. The maximum radius R_{max} of the bubble is equal to 0.75 mm, and the maximum length is 20 mm, making the maximum aspect ratio (length to diameter) of ~13. As the bubble begins to collapse, small satellite bubbles are detached from either end of the primary bubble. The splitting moment from the both sides of the bubble occurs after 1.9 ms when the bubble's elongation reaches about 20 mm.

Figure 6 presents some examples of the images of the bubbles created with different free-stream cavitation numbers σ_{∞} and $U_{\infty} = 10$ m/s. With higher $\sigma_{\infty} = 1.88$, the bubble's elongation is similar but the radius is significant smaller, about 0.5 mm. Figure 7 shows images of the bubbles just before splitting with the same $\sigma_{\infty} = 1.78$ and $U_{\infty} = 10$ m/s.

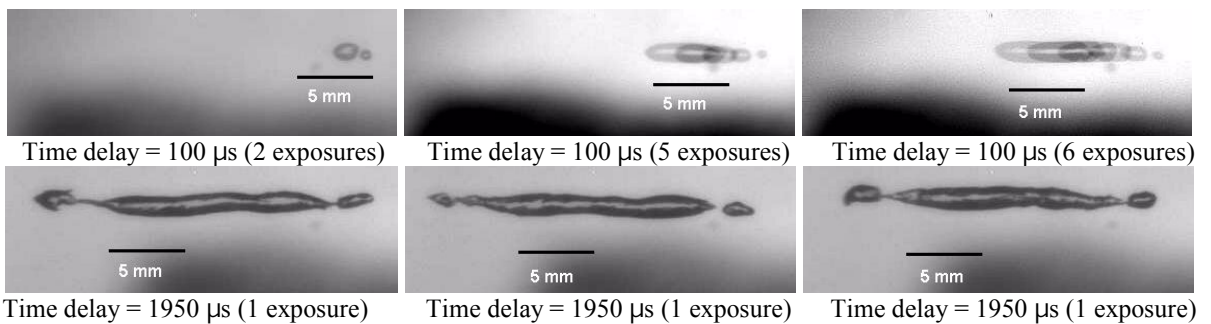


Fig. 5. Superimposed images for the laser-induced bubbles in the center of the vortex; $\sigma_{\infty} = 1.72$; $U_{\infty} = 10$ m/s.
Image dimensions (H 26.0 x V 8.3 mm)

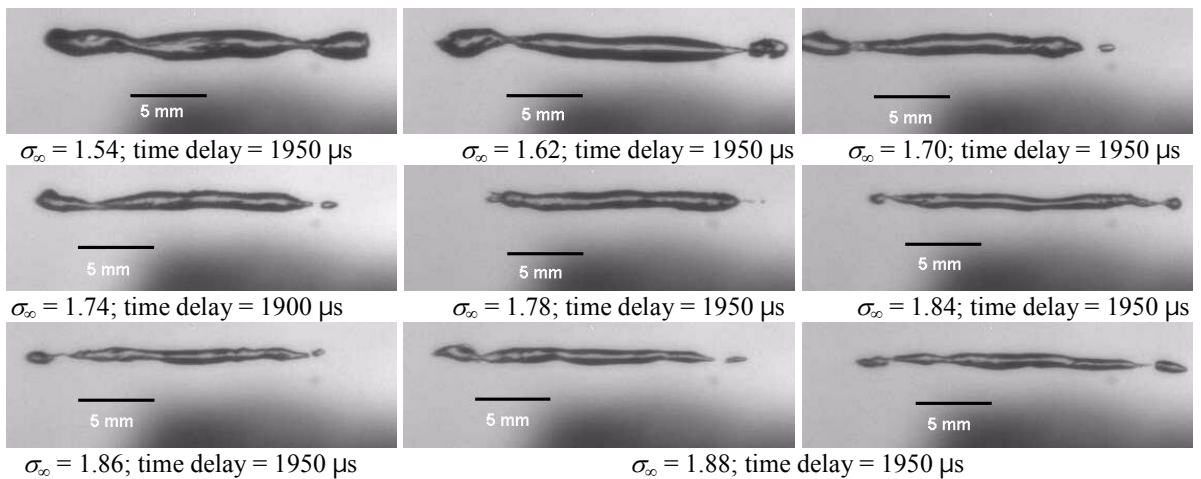


Fig. 6. Images for the bubbles induced in the center of the vortex with different σ_{∞} : 1.54÷1.88;
Image dimensions (H 26.0 x V 8.3 mm)

EXPERIMENTAL VALIDATION OF BEM CODE ANALYSIS OF BUBBLE SPLITTING IN A TIP VORTEX FLOW

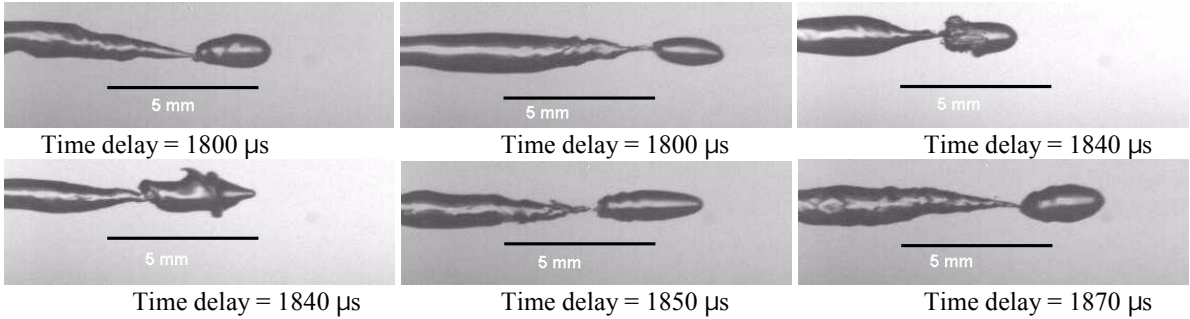


Fig. 7. Images for the bubbles induced in the center of the vortex; $\sigma_\infty = 1.78$.

Image dimensions (H 13.0 x V 4.15 mm)

4 NUMERCIAL SIMULATIONS

The growth and collapse of elongated bubbles in a line vortex was simulated using an axisymmetric simulation code employing the Boundary Element Method (BEM) called 2DYNAPS[®] from Dynaflo Inc. [8-10, 18]

The bubble surface is discretized by straight line segments on a meridian plane. The potential is assumed to vary linearly over each segment, while the normal gradient of the potential is assumed constant over each segment. The integral equation is then collocated at the center of each segment, and the resulting matrix equation is solved by using a standard LU decomposition technique. The normal velocity is known from the solution of the integral equation while the tangential velocity is obtained by numerical differentiation of the potential along the bubble surface. The new bubble geometry is obtained by advancing each node according to the sum of this local velocity and the velocity of the ambient vortex field. The time step size is controlled by an adaptive scheme that ensures that smaller time steps are chosen when the potential changes rapidly. Once the solution is obtained at any time step, the pressure signals at given field points can be calculated by using the Green identity and the unsteady Bernoulli equation. First, the Green identity is used to calculate the potential at given field points, and then the velocity is obtained from numerical differentiation. Finally, the pressure can be calculated by the Bernoulli equation.

A bubble placed on the vortex axis usually elongates along this axis. When bubble splitting occurs, a special treatment is necessary to continue the simulation. When a node approaches the axis within a specified small distance, three nodes including two neighboring nodes are tested to find the two nodes that are closest to the axis. The segment connecting these two nodes is detected as the segment to split. This detection procedure can be complex if multiple nodes approach the axis simultaneously or the bubble splits into more than three sub-bubbles at the same time step. Once a segment to split is found, the segment is removed by placing the two end nodes of the segment exactly on the axis [12, 19].

The pressure inside each bubble is assumed homogeneous, and the gas inside each bubble is assumed to be composed of both vapor of the liquid and an amount of non-condensable gas, here neglected (vapor bubble model) [14]. If this condition is satisfied, the liquid motion can be treated in the same manner as for an empty cavity, where the saturated vapor pressure P_V inside the bubble is opposed to the pressure in the vortex as acting on the outside of the bubble wall. It is simply assumed that the vapor pressure inside the bubble does not remain equal to the equilibrium liquid vapor pressure at the ambient temperature and the cooling of the bubble contents takes place in stepwise manner. Experimental data is used as input data (initial radius of the bubble equal to R_{max} , core

radius r_c , circulation Γ_0 , and static pressure depression under the hump) for the simulations of the bubble growth. The details of this formulation are provided in [9, 12].

The simulated bubble behavior for $\sigma_\infty = 1.72$ and $U_\infty = 10$ m/s is shown in Figure 8. The bubble elongates extremely from the initial radius equal to 0.75 mm without any cyclic fluctuations up to 22 mm as it travels downstream along the axis. At the maximum elongation, the length to radius ratio reaches about 20. The bubble growth in the radial direction is rather large compared to the local core radius of the vortex in absence of the bubble, $r_c = 4.51$ mm. The elongated bubble forms two necks which break resulting in three sub-bubbles. This behavior is very similar to that one observed during the experiments (see Figures 5 and 6), but the bubble is more elongated and time of the splitting is much longer, about 5 ms. These discrepancies can be caused by the vapor model of the bubble and non-uniform axial velocity of the vortex.

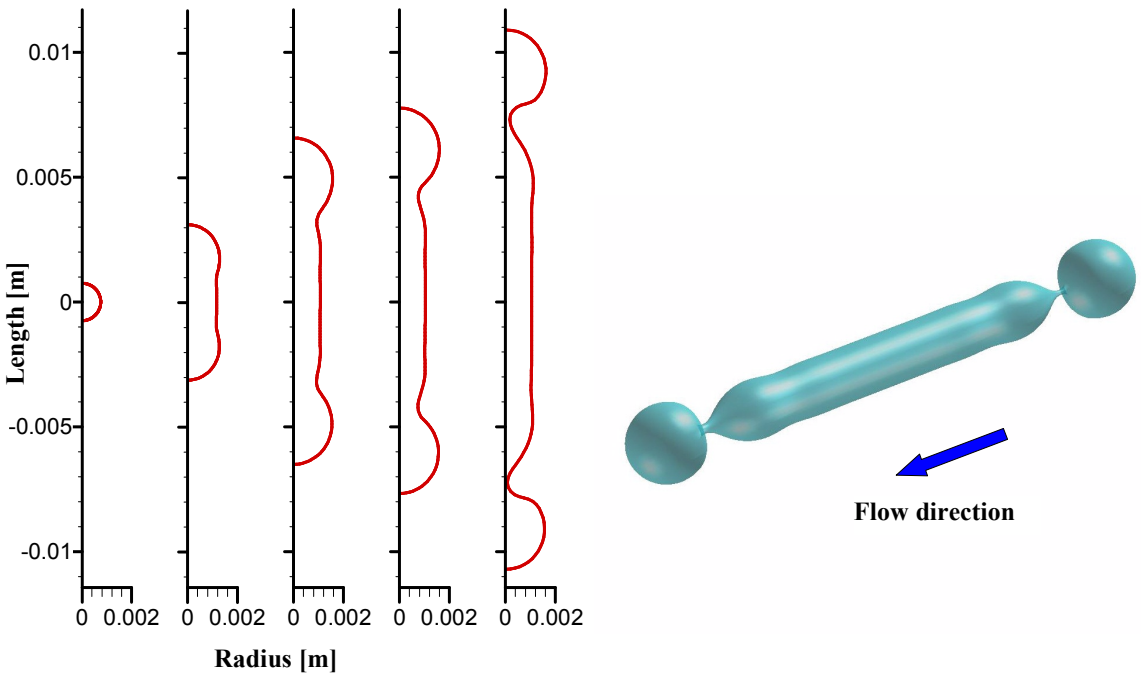


Fig. 8. The bubble behavior in a vortex flow field: $r_c = 4.51$ mm; $\Gamma_0 = 0.2123 \text{ m}^2/\text{s}$; $\sigma_\infty = 1.72$; $U_\infty = 10$ m/s; initial radius of the bubble $R_o = 750 \mu\text{m}$. 3 Dimensional view of the bubble just before splitting.

4 CONCLUDING REMARKS

Bubble splitting phenomena was investigated both experimentally and numerically in a tip vortex flow. Due to a slight modification of the flow conditions in the water cavitation tunnel laser-induced cavitation bubbles created at the vortex centreline grow, elongate and split. The results from this observation are then compared with those obtained with a boundary element method (BEM) code 2DYNALFS[®], which describes large free surface deformations in an axisymmetric potential flow. Comparisons of the calculations and experimental findings show good agreement and thus positively validate the BEM code. Therefore, one can conclude that this code provide reliable computational tool for the extreme deformations and splitting model of the bubble in the vortex flow.

However, additional detailed comparisons are needed to improve numerical models which are used in this code e.g. the splitting prediction model. During experiments, after the first splitting

EXPERIMENTAL VALIDATION OF BEM CODE ANALYSIS OF BUBBLE SPLITTING IN A TIP VORTEX FLOW

elongated bubble forms subsequent necks which probably brake resulting in another three sub-bubbles as is shown in Figure 9. These phenomena should be investigated in more details during additional experiments. Further work is in progress to obtain more precise input data for the simulations of the bubble growth.

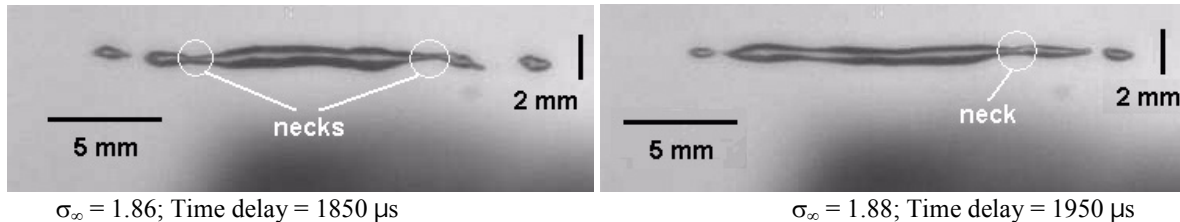


Fig. 9. The bubble splitting in a vortex flow field. Three sub-bubbles and visible necks in the larger sub-bubble

ACKNOWLEDGMENTS

The authors would like to thank Dr. Ghanem Oweis for his valuable suggestions during experiments.

REFERENCES

1. Ceccio S.L., Brennen C.E.: Observations of the dynamics and acoustics of traveling bubble cavitation. *J. of Fluids Mech.*, Vol. 233, pp. 633-660, 1991.
2. Kuhn de Chizelle Y., Ceccio S.L., Brennen C.E.: Observations and scaling of traveling bubble cavitation. *J. of Fluids Mech.*, Vol. 293, pp. 99-126, 1995.
3. Oweis G.F., Choi J., Ceccio S.L. Dynamics and noise emission of laser induced cavitation bubbles in a vortical flow field. *J. Acoust. Soc. Am.*, Vol. 115, No. 3, pp 1049-1058, 2004.
4. Sridhar G. and Katz J. Drag and lift forces on microscopic bubbles entrained by a vortex. *Physics of Fluids*, Vol. 7, No. 2, pp. 389-399, 1995.
5. Ceccio, S. L., Iyer C., Sasanelli G. Numerical studies of bubbles captured by a Gaussian vortex. *Proc. CAV2001*, Pasadena, CA, 2001.
6. Chahine G. L. *Fluid Vortices*, S. Green (ed.), Kluwer Academic, Chapter 18, 1995.
7. Arndt R. Cavitation in vortical flow. *Annu. Rev. Fluid Mech.*, Vol. 34, pp 143-175, 2002.
8. Choi J.-K and Chahine G.L. A numerical study on the bubble noise and the tip vortex cavitation inception. *The 8th International Conference on Numerical Ship Hydrodynamics*, Busan, Korea, 2003.
9. Choi J.-K. and Chahine G. L. Non-spherical bubble behavior in vortex flow fields. *Computational Mechanics*, Vol. 32, pp 281-290, 2003.
10. Choi J.-K. and Chahine G. L. Characteristics of bubble splitting in a tip vortex flow. *Fifth International Symposium on Cavitation (CAV2003)*.
11. Hsiao C-T and Chahine G.L. Prediction of tip vortex cavitation inception using coupled spherical and nonspherical bubble models and Navier-Stokes computations, *Journal of Marine Science and Technology*, Vol 8, p. 99-108, 2004.
12. Choi, J.-K., Chahine, G. L. Non-spherical bubble behavior in vortex flow fields. *IABEM 2002*, Int. Assoc. for Boundary Element Methods, Austin, TX, 2002.
13. Tomita Y., Tsubota M. and Annaka N. Energy evaluation of cavitation bubble generation and shock wave emission by laser focusing in liquid nitrogen. *Journal of Applied Physics*, Vol. 93, No. 5, pp 3039-3048, 2003.
14. Akhatov I., Lindau O., Topolnikov A., Mettin R., Vakhitova N. and Lauterborn W. Collapse and rebound of a laser-induced cavitation bubble. *Physics of Fluids*, Vol. 13, No. 10, pp 205-2819, 2001.
15. Batchelor G.K. Axial flow in trailing line vortices. *J. of Fluids Mech.*, part 20, pp. 645-658, 1964.
16. Chahine G.L. and Bovis A.G. Pressure Field Generated by Nonspherical Bubble Collapse. *Journal of Fluids Engineering*, Vol. 105, No. 3, pp. 356-364, 1983.

M. REBOW, J. CHOI, J.K. CHOI, G.L. CHAHINE, S.L. CECCIO

17. Chahine G.L. Dynamics of the Interaction of Non-Spherical Cavities. *Mathematical Approaches in Hydrodynamics*, ed. T. Miloh, SIAM Publications, 1991.
18. Chahine G.L. and Choi J.-K. 2DynaFS- Axisymmetric Boundary Element Method for Bubble and Free Surface Dynamics-Version 3.02: User Manual, *DYNAFLOW, INC. Manual Report 7.026*, February 2004.
19. Choi J.-K. and Chahine G. L. Noise due to extreme bubble deformation near inception of tip vortex cavitation, *Physics of Fluids*, Vol. 16, No. 7, pp.2411-2418, 2004.

Scaling of Tip Vortex Cavitation Inception Noise With a Bubble Dynamics Model Accounting for Nuclei Size Distribution

Chao-Tsung Hsiao

e-mail: ctsung@dynaflo-w-inc.com

Georges L. Chahine

e-mail: glchahine@dynaflo-w-inc.com

Dynaflow, Inc.

10621-J Iron Bridge Road, Jessup, MD 20794

The acoustic pressure generated by cavitation inception in a tip vortex flow was simulated in water containing a realistic bubble nuclei size distribution using a surface-averaged pressure (SAP) spherical bubble dynamics model. The flow field was obtained by the Reynolds-averaged Navier-Stokes computations for three geometrically similar scales of a finite-span elliptic hydrofoil. An “acoustic” criterion, which defines cavitation inception as the flow condition at which the number of acoustical “peaks” above a pre-selected pressure level exceeds a reference number per unit time, was applied to the three scales. It was found that the scaling of cavitation inception depended on the reference values (pressure amplitude and number of peaks) selected. Scaling effects (i.e., deviation from the classical $\sigma_i \propto R_e^{0.4}$) increase as the reference inception criteria become more stringent (lower threshold pressures and less number of peaks). Larger scales tend to detect more cavitation inception events per unit time than obtained by classical scaling because a relatively larger number of nuclei are excited by the tip vortex at the larger scale due to simultaneous increase of the nuclei capture area and of the size of the vortex core. The average nuclei size in the nuclei distribution was also found to have an important impact on cavitation inception number. Scaling effects (i.e., deviation from classical expressions) become more important as the average nuclei size decreases. [DOI: 10.1115/1.1852476]

1 Introduction

Scaling of the results of a propeller tip vortex cavitation inception studies from laboratory to large scales has not always been very successful. Aside from the problems associated with properly scaling the flow field, existing scaling laws as derived or used by previous studies, e.g., [1–6], lack the ingredients necessary to explain sometimes major discrepancies between model and full scale. One of the major aspects which has not been appropriately incorporated in the scaling law is nuclei presence and nuclei size distribution effects. Another issue which may cause scaling problems is the means of detection of cavitation inception. Practically, the flow condition is considered to be at cavitation inception when either an “acoustic” criterion or an “optical” criterion is met [7,8]. These two detection methods are known to provide different answers in the most practical applications. Furthermore, for practical reasons inception may be detected by one method at model scale and by another at full scale. To address this issue in a more consistent manner for different scales, the present study considers an “acoustic” criterion which determines the cavitation inception event by counting the number of acoustical signal peaks that exceed a certain level in unit time.

To theoretically address the above issues in a practical way spherical bubble dynamics models were adopted in many studies in order to simulate the bubble dynamics and to predict tip vortex cavitation inception [8–10]. In our previous studies [8,11], an improved surface-averaged pressure (SAP) spherical bubble dynamics model was developed and applied to predict single bubble trajectory, size variation and resulting acoustic signals. This model was later shown to be much superior than the classical spherical model through its comparison to a two-way fully three-dimensional (3D) numerical model which includes bubble shape

deformation and the full interaction between the bubble and the viscous flow field [11]. In the present study we incorporate the SAP spherical bubble dynamics model with a statistical nuclei distribution in order to enable prediction of cavitation inception in a practical liquid flow field with known nuclei size distribution. This is realized by randomly distributing the nuclei in space and time according to the given nuclei size distribution. According to previous studies [12,13] the number of nuclei to use in the computation can be reduced by considering only the nuclei that pass through a so-called “window of opportunity” and are captured by the tip vortex.

In order to study scale effects in a simple vortex flow field we consider the tip vortex flows generated by a set of three geometrically similar elliptic hydrofoils. The flow fields are obtained by steady-state Navier-Stokes computations which provide the velocity and pressure fields for the bubble dynamics computations. The SAP spherical model is then used to track all nuclei released randomly in time and space from the nuclei release area and to record the acoustic signals generated by their dynamics and volume oscillations.

2 Numerical Models

2.1 Navier-Stokes Computations. To best describe the tip vortex flow field around a finite-span hydrofoil, the Reynolds-averaged Navier-Stokes (RANS) equations with a turbulence model are solved. These have been shown to be successful in addressing tip vortex flows [14] and general propulsor flows [15,16]. The three-dimensional unsteady Reynolds-averaged incompressible continuity and Navier-Stokes equations in nondimensional form and Cartesian tensor notations are written as

$$\frac{\partial u_i}{\partial x_i} = 0 \quad (1)$$

Contributed by the Fluids Engineering Division for publication on the JOURNAL OF FLUIDS ENGINEERING. Manuscript received by the Fluids Engineering Division September 13, 2003; revised manuscript received August 13, 2004. Review conducted by: S. Ceccio.

$$\frac{\partial u_i}{\partial t} + u_j \frac{\partial u_i}{\partial x_j} = - \frac{\partial p}{\partial x_i} + \frac{\partial \tau_{ij}}{\partial x_j} \quad (2)$$

where $u_i = (u, v, w)$ are the Cartesian components of the velocity, $x_i = (x, y, z)$ are the Cartesian coordinates, p is the pressure, $R_e = \rho u^* L^*/\mu$ is the Reynolds number, u^* and L^* are the characteristic velocity and length selected to be, respectively, the free stream velocity, V_∞ and root chord length, C_0 . ρ is the liquid density, and μ is its dynamic viscosity. The effective stress tensor τ_{ij} is given by

$$\tau_{ij} = \frac{1}{R_e} \left[\left(\frac{\partial u_i}{\partial x_j} + \frac{\partial u_j}{\partial x_i} \right) - \frac{2}{3} \delta_{ij} \frac{\partial u_k}{\partial x_k} \right] - \overline{u_i' u_j'} \quad (3)$$

where δ_{ij} is the Kronecker delta and $\overline{u_i' u_j'}$ is the Reynolds stress tensor resulting from the Reynolds averaging scheme.

To numerically simulate the tip vortex flow around a finite-span hydrofoil, a body-fitted curvilinear grid is generated and Eqs. (1) and (2) are transformed into a general curvilinear coordinate system. The transformation provides a computational domain that is better suited for applying the spatial differencing scheme and the boundary conditions. To solve the transformed equations, we use the three-dimensional incompressible Navier–Stokes flow solver, DF_UNCLE, derived from the code UNCLE developed at Mississippi State University. The DF_UNCLE code is based on the artificial-compressibility method [17] which a time derivative of the pressure multiplied by an artificial-compressibility factor is added to the continuity equation. As a consequence, a hyperbolic system of equations is formed and is solved using a time marching scheme in pseudo-time to reach a steady-state solution.

The numerical scheme in DF_UNCLE uses a finite volume formulation. First-order Euler implicit differencing is applied to the time derivatives. The spatial differencing of the convective terms uses the flux-difference splitting scheme based on Roe's method [18] and van Leer's MUSCL method [19] for obtaining the first-order and the third-order fluxes, respectively. A second-order central differencing is used for the viscous terms which are simplified using the thin-layer approximation. The flux Jacobians required in the implicit scheme are obtained numerically. The resulting system of algebraic equations is solved using the Discretized Newton Relaxation method [20] in which symmetric block Gauss–Seidel sub-iterations are performed before the solution is updated at each Newton interaction. A $k - \epsilon$ turbulence model is used to model the Reynolds stresses in Eq. (3).

All boundary conditions in DF_UNCLE are imposed implicitly. Here, a free stream constant velocity and pressure condition is specified at all far-field side boundaries. The method of characteristic is applied at the inflow boundary with all three components of velocities specified while a first-order extrapolation for all variables is used at the outflow boundary. On the solid hydrofoil surface, a no-slip condition and a zero normal pressure gradient condition are used. At the hydrofoil root boundary, a plane symmetry condition is specified.

2.2 Statistical Nuclei Distribution Model. In order to address a realistic liquid condition in which a liquid flow field contains a distribution of nuclei with different sizes, a statistical nuclei distribution is used. We consider a liquid with a known nuclei size density distribution function, $n(R)$. $n(R)$ is defined as the number of nuclei per cubic meter having radii in the range $[R, R + \delta R]$. This function has a unit m^{-4} and is given by

$$n(R) = \frac{dN(R)}{dR} \quad (4)$$

where $N(R)$ is the number of nuclei of radius R in a unit volume. This function can be obtained from experimental measurements such as light scattering, cavitation susceptibility meter and ABS Acoustic Bubble Spectrometer® measurements [21] and can be expressed as a discrete distribution of M selected nuclei sizes. Thus, the total void fraction, α , in the liquid can be obtained by

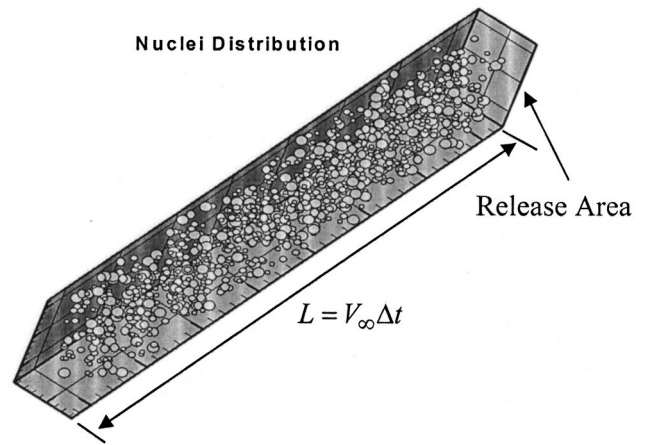
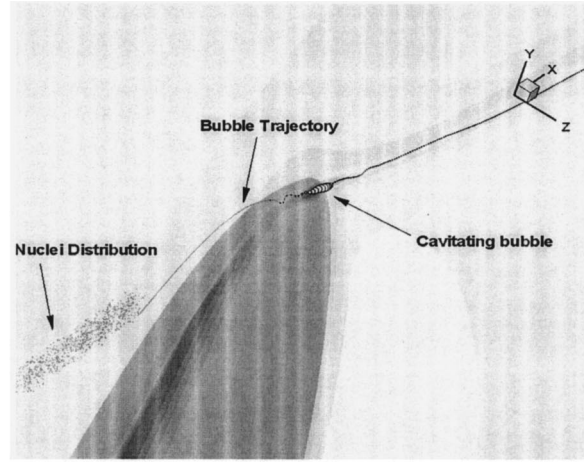


Fig. 1 The location and size of a fictitious volume for randomly distributing the nuclei

$$\alpha = \sum_{i=1}^M N_i \frac{4 \pi R_i^3}{3} \quad (5)$$

where N_i is the discrete number of nuclei of radius R_i used in the computations. The position and timing of nuclei released in the flow field are obtained using random distribution functions, always ensuring that the local and overall void fraction satisfy the nuclei size distribution function.

From previous studies [12,13], we know that only nuclei that “enter” a given region or “window of opportunity” are actually captured by the vortex and generate strong acoustic signals. Therefore, it is economical to consider only nuclei emitted from this “window of opportunity.” This is similar to considering a fictitious volume of cross area equal to the window area and of length equal to $V_\infty \Delta t$, where V_∞ is the free stream velocity and Δt is the total time of signal acquisition (see Fig. 1).

2.3 Bubble Dynamics. The nuclei convected in the flow field are treated using a spherical bubble dynamics model. To do so, we use the Rayleigh–Plesset equation modified to account for a slip velocity between the bubble and the host liquid, and for the nonuniform pressure field along the bubble surface [10]. The resulting modified surface-averaged pressure (SAP) Rayleigh–Plesset equation can be written as:

$$R\ddot{R} + \frac{3}{2}\dot{R}^2 = \frac{1}{\rho} \left(p_v + p_{g0} \left(\frac{R_0}{R} \right)^{3k} - P_{\text{encounter}} - \frac{2\gamma}{R} - \frac{4\mu\dot{R}}{R} \right) + \frac{(\mathbf{u} - \mathbf{u}_b)^2}{4} \quad (6)$$

where R is the time varying bubble radius, R_0 is the initial or reference bubble radius, γ is the surface tension parameter, p_v is the vapor pressure. p_{g0} is the initial or reference gas pressure inside the bubble, and k is the polytropic compression law constant. \mathbf{u} is the liquid convection velocity and \mathbf{u}_b is the bubble travel velocity. $P_{\text{encounter}}$ is the ambient pressure “seen” by the bubble during its travel. In the SAP method $P_{\text{encounter}}$ is defined as the average of the liquid pressures over the bubble surface [11].

The bubble trajectory is obtained using the following motion equation [22]

$$\frac{d\mathbf{u}_b}{dt} = \frac{3}{\rho} \nabla P + \frac{3}{4} C_D (\mathbf{u} - \mathbf{u}_b) |\mathbf{u} - \mathbf{u}_b| + \frac{3}{R} (\mathbf{u} - \mathbf{u}_b) \dot{R} \quad (7)$$

where the drag coefficient C_D is given by an empirical equation such as that of Haberman and Morton [23]

$$C_D = \frac{24}{R_{eb}} (1 + 0.197 R_{eb}^{0.63} + 2.6 \times 10^{-4} R_{eb}^{1.38}); \quad R_{eb} = \frac{2\rho R |\mathbf{u} - \mathbf{u}_b|}{\mu} \quad (8)$$

The pressure at a distance l from the bubble center generated by the bubble dynamics is given by the expression

$$p_a = \frac{\rho}{l} [R^2 \ddot{R} + 2R \dot{R}^2] - \rho \left[\frac{R^4 \dot{R}^2}{2l^4} \right] \quad (9)$$

When $l \gg R$, Eq. (9) becomes the expression for the acoustic pressure p_a of Fitzpatrick and Strasberg [24] after introduction of the delayed time t' due to a finite sound speed, c

$$p_a(t') = \frac{R\rho}{l} [R\ddot{R}(t') + 2\dot{R}^2(t')], \quad t' = t - \frac{r-R}{c}. \quad (10)$$

To determine the bubble motion and its volume variation, a Runge–Kutta fourth-order scheme is used to integrate Eqs. (6) and (7) through time. The liquid velocity and pressures are obtained directly from the RANS computations. The numerical solution of the RANS equations, however, offers the solution directly only at the grid points. To obtain the values for any specified location (x, y, z) on the bubble we need to interpolate from the background grid. To do so, an interpolation stencil and interpolation coefficients at any specified location are determined at each time step. We use a three-dimensional point-locating scheme based on the fact that the coordinates (x, y, z) of the bubble location are uniquely represented relative to the eight corner points of the background grid stencil by

$$x = \sum_{i=1}^8 N_i \bar{x}_i, \quad y = \sum_{i=1}^8 N_i \bar{y}_i, \quad z = \sum_{i=1}^8 N_i \bar{z}_i, \quad (11)$$

where

$$\begin{aligned} N_1 &= (1-\phi)(1-\psi)(1-\varphi), & N_2 &= \phi(1-\psi)(1-\varphi), \\ N_3 &= (1-\phi)\psi(1-\varphi), & N_4 &= \phi\psi(1-\varphi), \\ N_5 &= (1-\phi)(1-\psi)\varphi, & N_6 &= \phi(1-\psi)\varphi, \\ N_7 &= (1-\phi)\psi\varphi, & N_8 &= \phi\psi\varphi. \end{aligned} \quad (12)$$

ϕ, ψ, φ are the interpolation coefficients, and $(\bar{x}_i, \bar{y}_i, \bar{z}_i)$ are the coordinates of the eight corner points of a grid stencil in the background grid. Equation (11) is solved using a Newton–Raphson method. For a bubble point to be inside the grid stencil requires that the corresponding ϕ, ψ, φ satisfy $0 \leq \phi \leq 1, 0 \leq \psi \leq 1, 0 \leq \varphi \leq 1$.

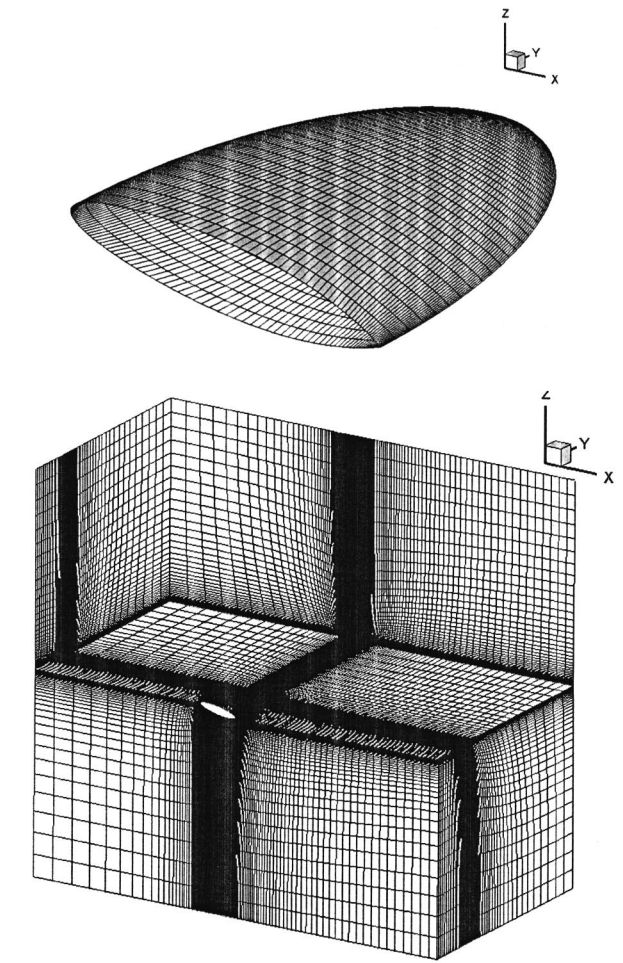


Fig. 2 Computational domain and grid for the current study

Once the interpolation stencil and interpolation coefficients are determined, the pressure and velocities can be obtained by using a similar equation to Eq. (11).

2.4 Computational Domain and Grid Generation. To compute the flow around the finite-span elliptic hydrofoil we generated an H–H type grid with a total of 2.7 million grid points in which $191 \times 101 \times 101$ grid points were created in the streamwise, spanwise and normal direction, respectively, and 81×61 grid points were used to discretize the hydrofoil surface. The grid is subdivided into 12 blocks for a computational domain which has all far-field boundaries located six (6) chord lengths away from the hydrofoil surface (see Fig. 2). Grid resolution was determined according to previous numerical studies [14,25] in which extensive investigations of the grid resolution for the tip vortex flow showed that the minimum number of grid points needed for good resolution is at least 15 grid points across the vortex core. Here, the grid resolution for the tip vortex was optimized through repeated computations and regridding to align grid clustering around the tip vortex centerline. The final refined grid selected for the results shown below had at least 16 grid points in the spanwise direction and 19 grid points in the crosswise direction within the vortex core. The first grid above the hydrofoil surface was located such that $y^+ \approx 1$ in order to properly apply the turbulence model.

3 Results

3.1 3D Steady-State Tip Vortex Flow. The selected finite-span elliptic foil has a NACA16020 cross section with an aspect ratio of 3 (based on semispan). The flow field at an angle of attack

Table 1 Characteristics of the three NACA16020 foil used

	Small scale	Medium scale	Large scale
C_0	0.144 m	0.288 m	0.576 m
V_∞	10 m/s	10 m/s	10 m/s
R_e	1.44×10^6	2.88×10^6	5.76×10^6
$-C_{p_{\min}}$	3.34	4.34	5.48

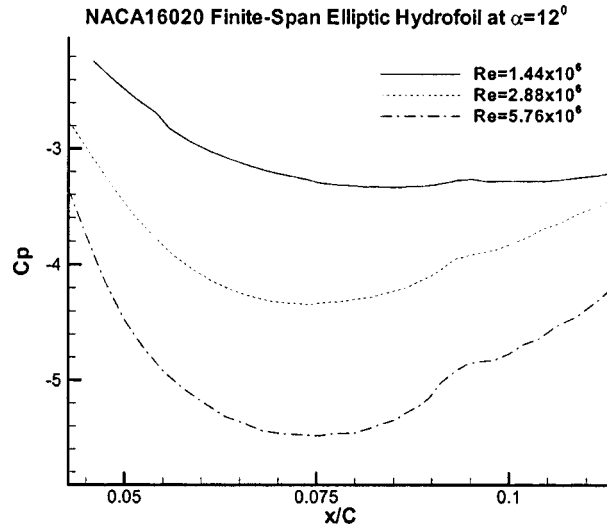


Fig. 3 Pressure coefficient variations along the NACA16020 elliptic foil for three values of the Reynolds number

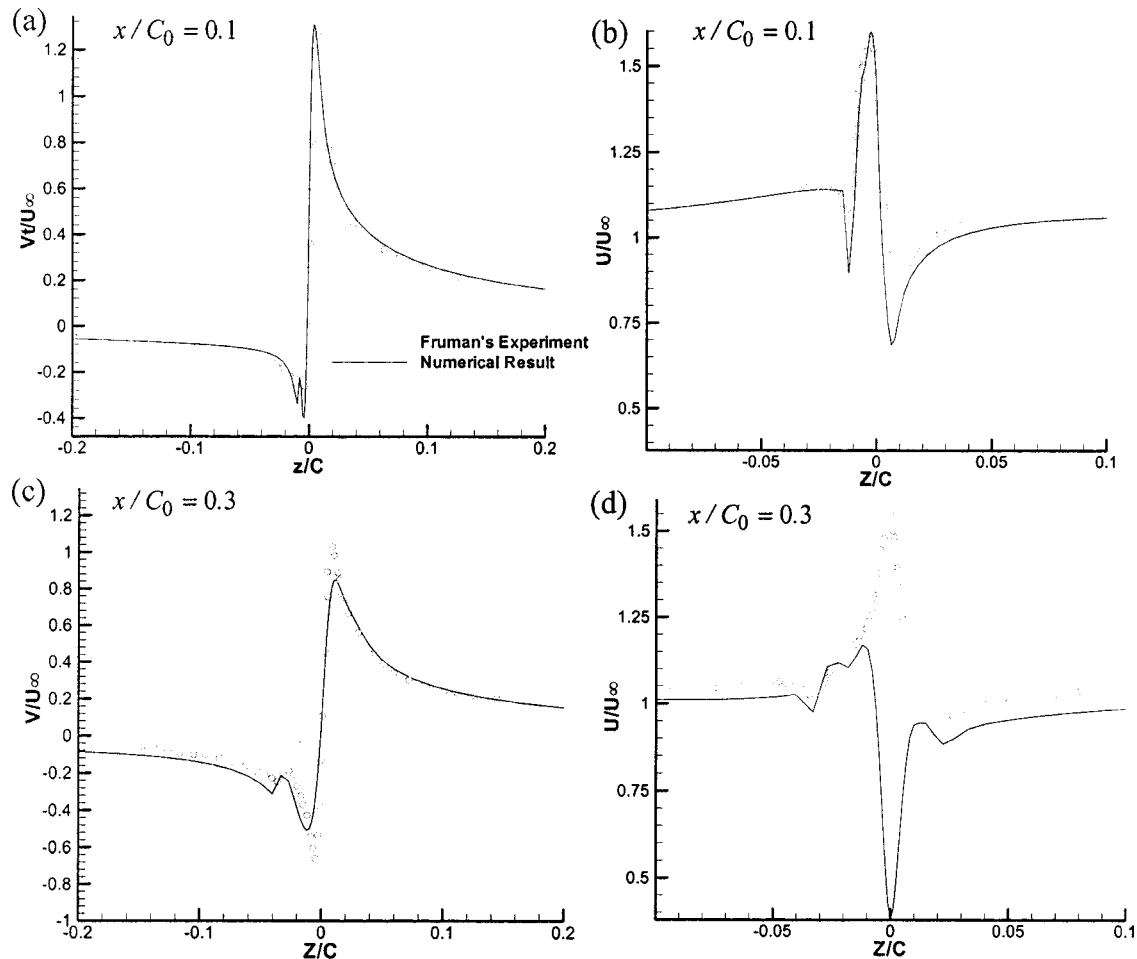


Fig. 4 Comparison of tangential and axial velocity components across the tip vortex core at $x/C_0 = 0.1$ and 0.3 between present numerical result and experimental measurements (Fruman et al. 1992)

of 12 deg was computed for three foil sizes or three different Reynolds numbers in order to study cavitation scaling effects. These correspond to the three scales shown in Table 1. In all three cases a steady-state solution was considered achieved when $\nabla \cdot \bar{V} \leq 1 \times 10^{-4}$. The resulting pressure coefficients along the tip vortex centerline are shown in Fig. 3. It is seen that the locations of the minimum pressure for all three cases are very close to the hydrofoil tip and are located at $x/C_0 = 0.085$, 0.075, and 0.075. The corresponding minimum pressure coefficients are shown in Table 1. If the cavitation inception number is assumed to be $-C_{p_{\min}}$, then these values correlate with the power formulation: $\sigma_i \propto R_e^{0.36}$.

To validate the steady state computations an additional case was computed at an angle of attack equal to 10° and $R_e = 4.75 \times 10^6$. The results were compared to the available experimental measurements of [2] by considering the tangential and axial velocity components across the tip vortex core at two streamwise locations. As seen in Fig. 4, the comparison indicates that the tip vortex flow is well predicted in the near-field region in which the pressure coefficient along the vortex center reaches its minimum. However, over-diffusion in vortex core size and over-dissipation in velocities are seen for the numerical solution further downstream especially for the axial velocity component whose velocity profile changes from excess to deficit. Notice, however, that this occurs beyond the region of interest here for bubble dynamics studies. Indeed, the bubble dynamics simulations show that the bubble growth and collapse durations are relatively very short (see Fig. 5) and occur before $x/C_0 = 0.1$. In this region, our numerical solution

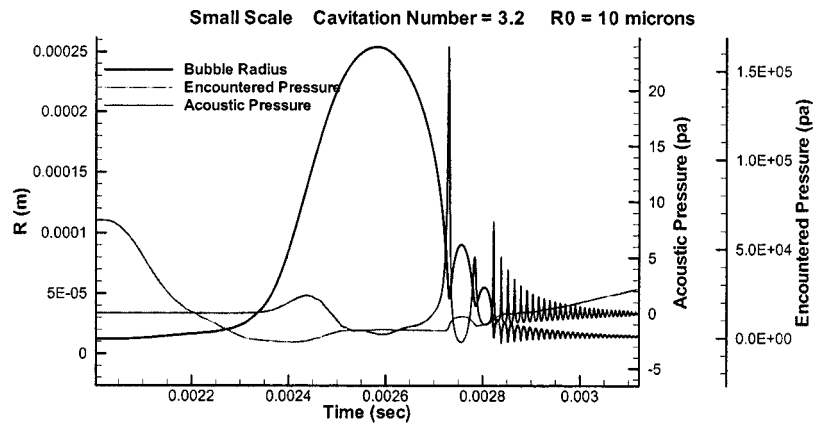


Fig. 5 Example computation of bubble dynamics for bubble radius, encountered pressure, and emitted acoustic pressure versus time during bubble capture in the tip vortex

agrees quite well with the experimental measurements. Therefore, the present Navier–Stokes computations are reliable for studying the bubble behavior in the $C_{p\min}$ region of interest.

3.2 Window of Opportunity. The “window of opportunity” can be determined by releasing nuclei upstream of the foils and tracking their trajectories to see if they enter into the low pressure areas in the tip vortex flow. A release plane located at $x/C_0 = -0.1$ ahead of the hydrofoil tip ($x/C_0 = 0$) was used. Nuclei were released from this plane at various locations, tracked, and the minimum pressure they encountered is recorded at the corresponding release point.

Initially, 300 nuclei of a given size were released from the release plane. All properties are defined at 20°C. The cavitation number was specified high enough such that the maximum growth size of nucleus was less than 10%. Figure 6 shows a contour plot of the minimum pressure coefficient encountered for each release location for different nuclei sizes in the small scale. The contours are blanked out for the release points where the nuclei collide with the hydrofoil surface. It is seen that the size of the “window of opportunity” becomes smaller and its location shifts closer to the hydrofoil surface of pressure side when the nuclei sizes decrease. The contours of minimum encounter pressure coefficient for dif-

ferent scales with the same initial nuclei size are shown in Fig. 7. It is seen that the size of the “window of opportunity” increases as the scale increases. This implies that larger scales capture more nuclei into the vortex for the same nuclei sizes and duration of observation time when compared to smaller scales.

3.3 Statistical Nuclei Size Distribution. Nuclei size distribution studies in water tunnels, lakes and oceans [26,27] show a power-law distribution for the number density distribution function, with $n(R) \approx 1/R^\beta$, where the exponent β lies between 2.5 and 4. In the present study we consider a nuclei size distribution ranging from 10 to 100 μm with a void fraction $\alpha \approx 1 \times 10^{-6}$ as shown in Fig. 8. In order to consider a same bubble population for all scales, we have accounted for the fact that a bubble will change its radius in a static equilibrium fashion when the ambient pressure is changed. Therefore, for the same scaled cavitation number, initial nuclei sizes are reduced for the larger scales where the ambient pressure would be larger. This is not a major change in the values since gas pressure inside the bubble varies like the cube of the radius, while surface tension which is predominant varies like the inverse of the radius. This results in nuclei sizes

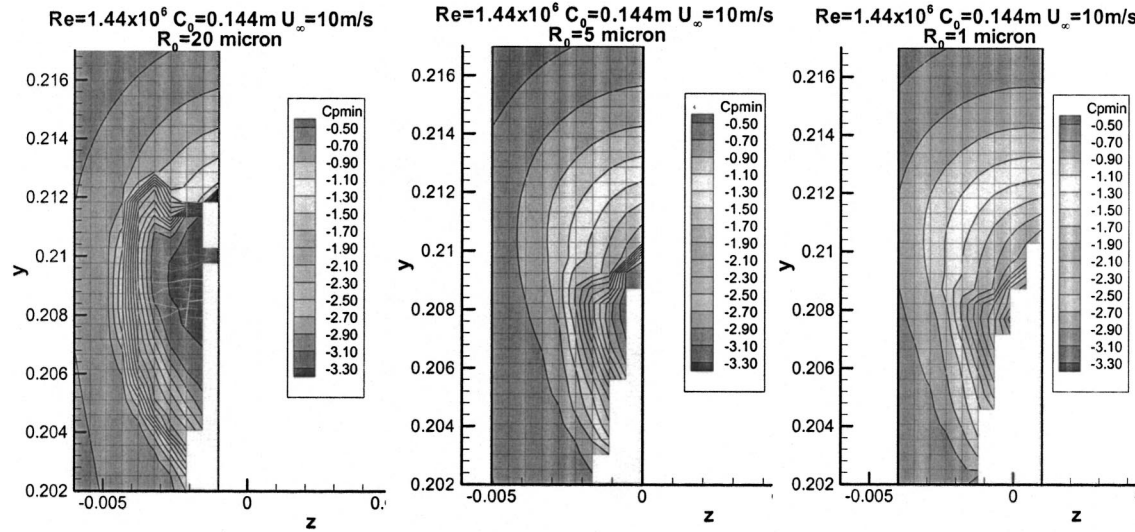


Fig. 6 Contours of the minimum pressure coefficient encountered at high cavitation number for different nuclei size in the small foil scale

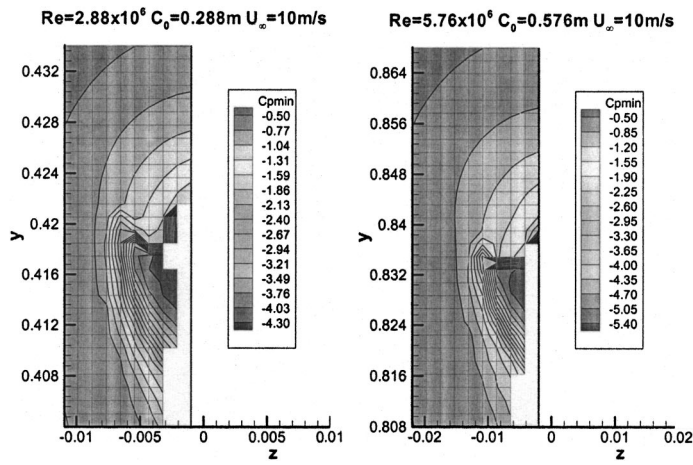


Fig. 7 Contours of the minimum pressure coefficient encountered at high cavitation number for $R_0=20\ \mu\text{m}$ and for the medium and large foil scale

ranging from 10 to 100 μm for the small scale, 9.2–92 μm for the medium scale, and from 8.5 to 85 μm for the large scale. These curves are used to generate the nuclei field.

With the void fraction and size distribution provided, the total number of nuclei released for each scale is then determined based on the length of signal acquisition time and the size of the release area. To determine an appropriate statistically meaningful observation time we tested two different signal acquisition times $\Delta t=0.2$ and 1 s. Both cases were conducted for the small scale at cavitation number $\sigma=3.0$. The number of nuclei released and the number of nuclei reaching critical (cavitating) condition versus nuclei size for these two cases are shown in Fig. 9. In this figure a nucleus is considered to be a cavitation bubble when $P_{\text{encounter}} < P_{\text{cr}}$, where the critical pressure is defined as

$$P_{\text{cr}} = p_v - (3k-1) \left(\frac{2\gamma}{3k} \right)^{3k/3k-1} (p_g R_0^{3k})^{-1/3k-1} \quad (13)$$

with $k=1.4$. Comparison between these two cases shows that the smaller acquisition time only results in a slightly smaller probability for cavitation. Therefore, $\Delta t=0.2$ second is statistically sufficient and was used for the other tests. For the release window, we consider an area to be large enough to cover the “windows of opportunity” for all nuclei sizes released. Here, the size of the release area is specified as 7 mm \times 5 mm, 14 mm \times 10 mm, and 28

mm \times 20 mm for the small, medium, and large scale, respectively. As a result, the number of nuclei in each population is 142, 568, and 2272 for the three scales, respectively.

3.4 Scaling of Cavitation Inception Noise. As nuclei travel in the computational domain, the resulting acoustic pressure is monitored. The acoustic pressure was computed at a location 0.3 m away from the hydrofoil tip for all cases. A series of computa-

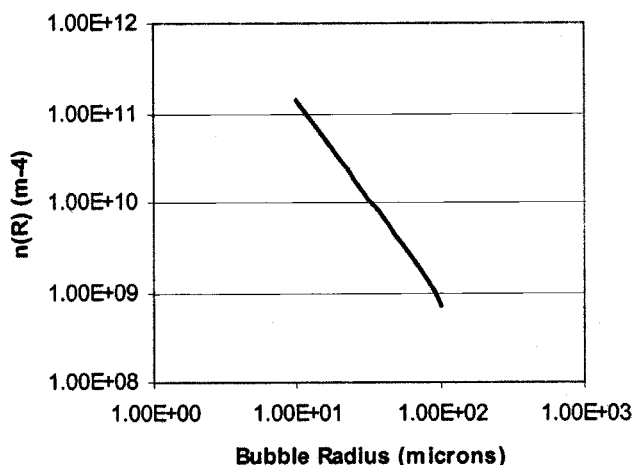
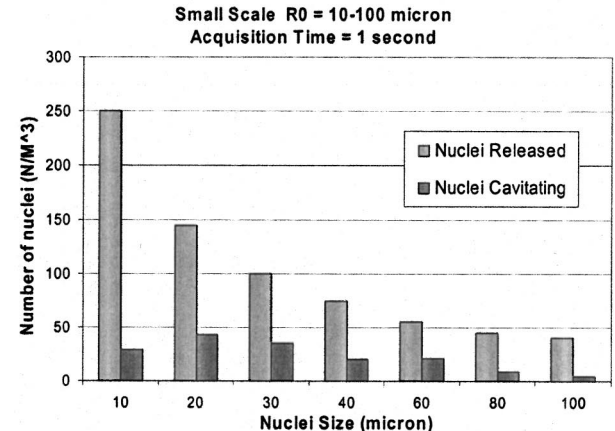
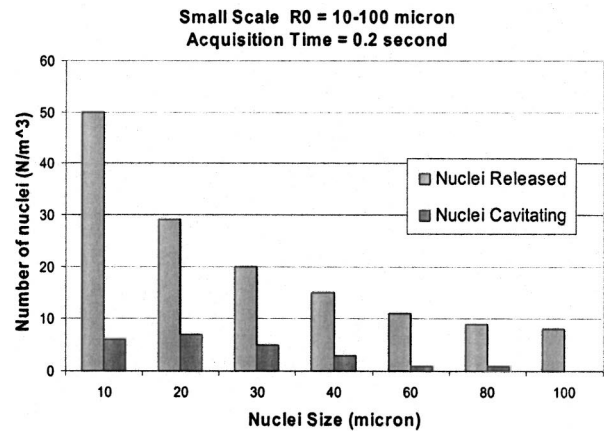


Fig. 8 Nuclei size number density distributions applied at the three scales

Fig. 9 The number of nuclei released and the number of nuclei reaching critical pressure (cavitating) versus nuclei size obtained at $\sigma=3.0$ for two different acquisition times

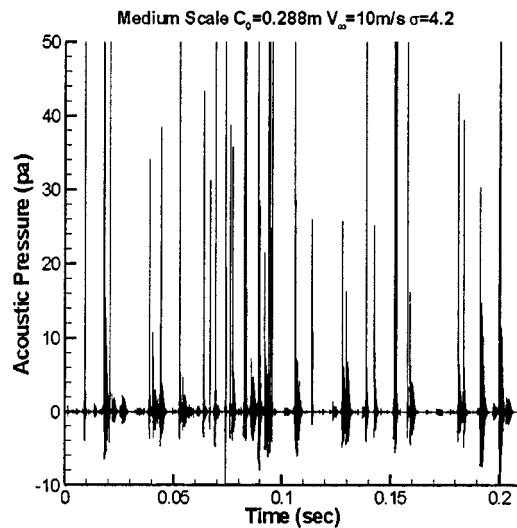
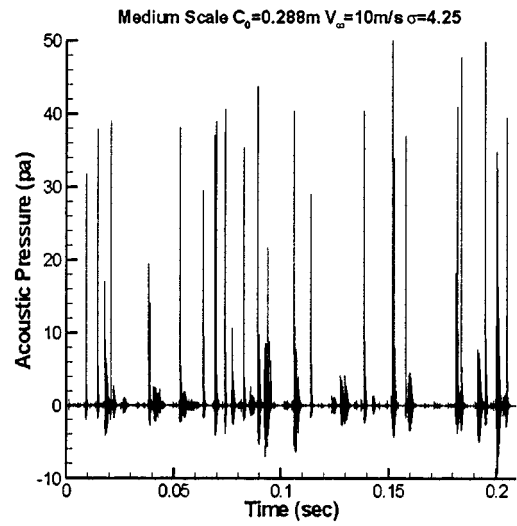
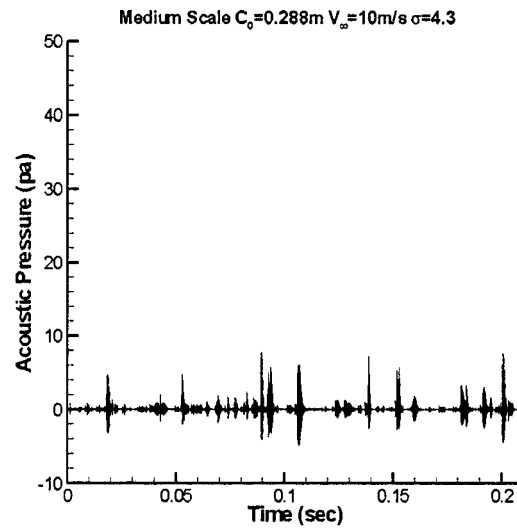
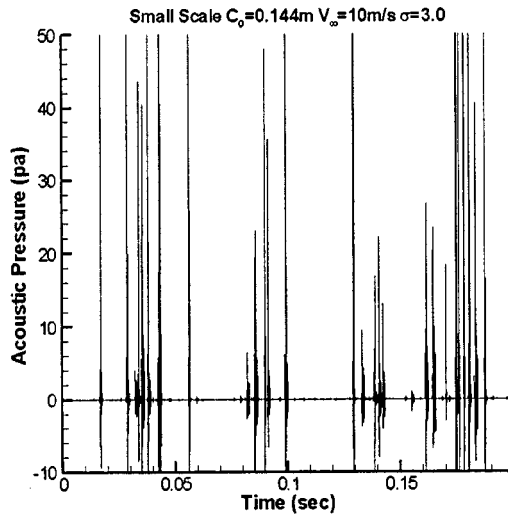
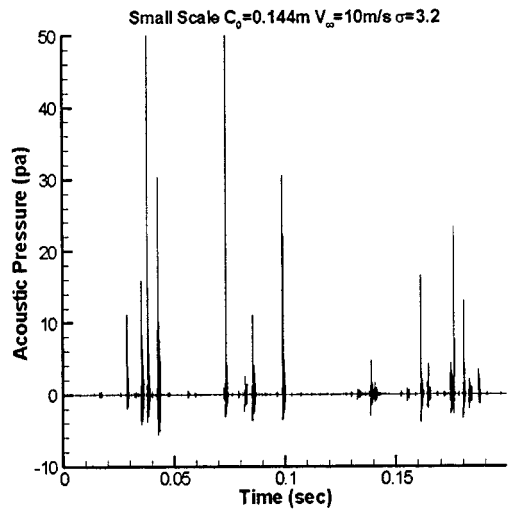
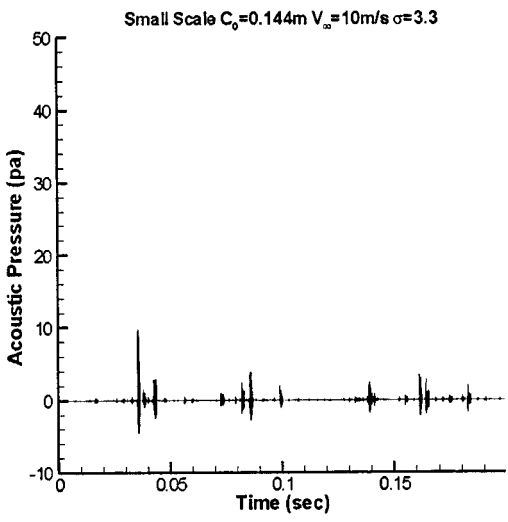


Fig. 10 The acoustic signals for the small scale at three different cavitation numbers

tions were conducted at different cavitation numbers for the three scales to obtain the acoustic signals for conditions above and below cavitation inception. Figures 10–12 illustrate the acoustic signals for three different scales at three different cavitation numbers. High-level peaks of acoustic signals are clearly seen when the

Fig. 11 The acoustic signals for the medium scale at three different cavitation numbers

cavitation number is near the cavitation inception number. It is seen that, as expected, for all scales the number of high-level peaks increases as the cavitation number decreases. However, the larger scale is more sensitive to cavitation number changes since

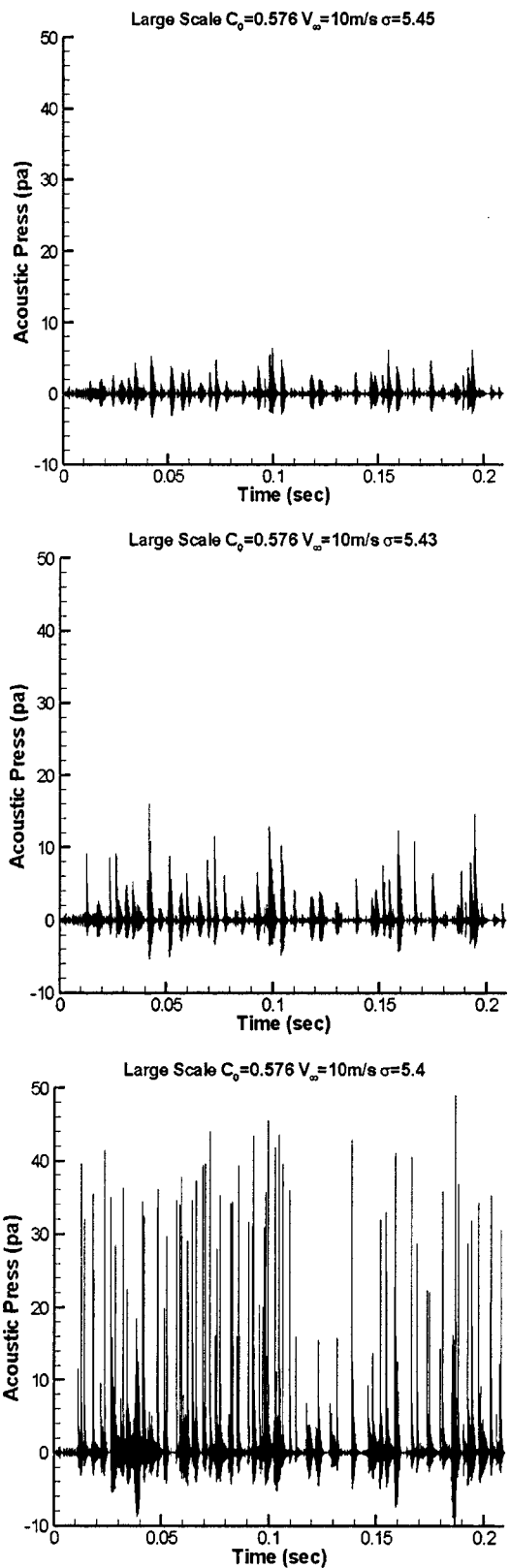


Fig. 12 The acoustic signals for the large scale at three different cavitation numbers

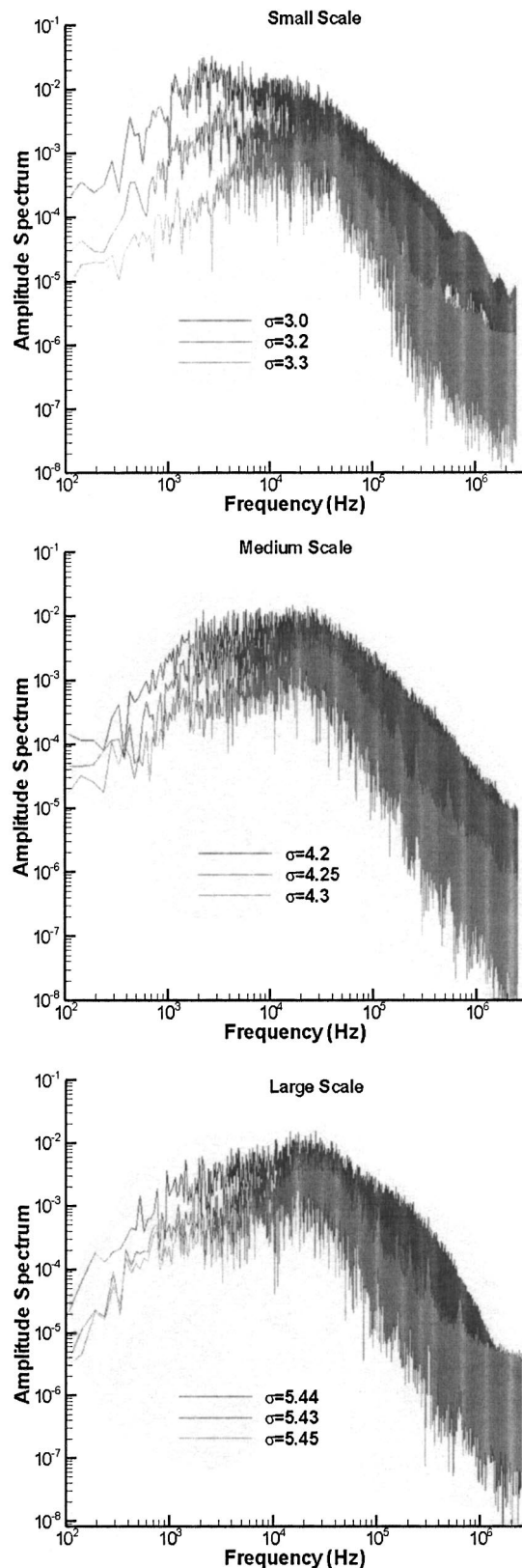


Fig. 13 Amplitude spectra for all three scales at three different cavitation numbers

the number of peaks increases much faster than for the smaller scale as the cavitation number decreases. Figure 13 shows the resulting frequency spectra for the acoustic signals shown in Figs.

10–12. A peak in the frequency range 30–40 kHz is seen at all scales. The amplitude of this peak increases as the cavitation number decreases.

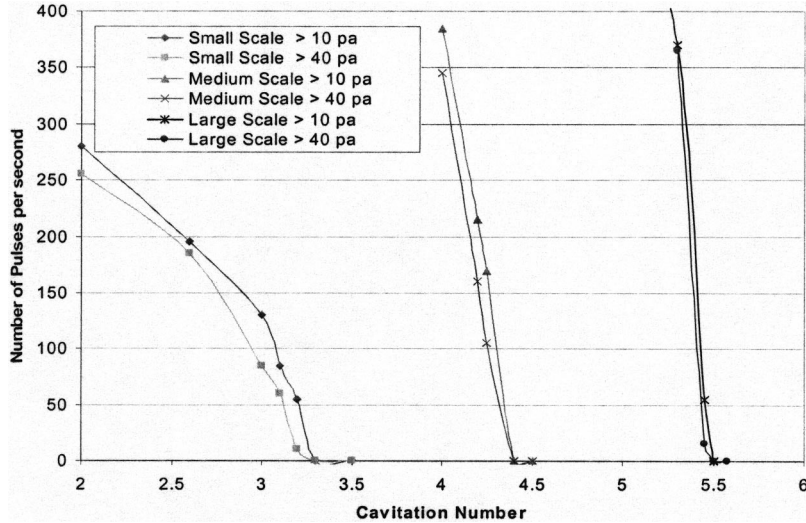


Fig. 14 Number of pressure peaks versus cavitation number deduced at two criteria of acoustic level for the three scales considered

Based on the results shown in Figs. 10–12, we can define a cavitation inception number based on the number of acoustical signal peaks per unit time that exceed a certain level. To deduce the cavitation inception number based on this criterion, a curve for the number of pressure peaks higher than a give acoustic pressure level is created for each cavitation number and for the three scales. Figure 14 shows such curves with two acoustic pressure levels, 10 and 40 Pa, are chosen for each scale. Given a selected criterion based on the number of peaks and acoustic pressure level, one can determine the cavitation inception number from Fig. 14.

The deduced cavitation inception numbers of the three scales for the criteria: 10 peaks/s over 10 Pa and 50 peaks/s over 40 Pa, are shown in Table 2. The deduced cavitation numbers and $-Cp_{\min}$ are fitted with the classical power formula $\sigma_i \propto R_e^\gamma$, and the fitted values of γ are also shown in Table 2. It is seen that different criteria for defining the cavitation inception event can lead to different cavitation inception numbers and different scaling laws. The scaling effect due to the nuclei can be demonstrated by comparing the deduced inception number with $-Cp_{\min}$. The results in Table 2 show that cavitation inception scaling deviates more from $-Cp_{\min}$ when the reference inception criterion becomes less stringent (higher reference pressure amplitude and larger number of peaks). Furthermore, the predicted value of γ is closer to the classical value ($\gamma=0.4$), as the reference inception criterion becomes less stringent. This agrees with many experi-

mental studies usually established in laboratory conditions where background noise and detection techniques lead to high values of the pressure amplitude for inception detection.

3.5 Nuclei Size Distribution Effect. To illustrate how different nuclei size distributions influence the prediction of cavitation inception, a much finer nuclei size distribution ranging from 1 to 10 μm is tested. In the computations the total number of nuclei released in each case was kept the same. This results in a much smaller void fraction ($\alpha \approx 1 \times 10^{-9}$) than in the previous case. Figure 15 shows the acoustical signal obtained at $\sigma=3.0$ and the number of nuclei cavitating for each prescribed nuclei size is shown in Fig. 16. It is seen that, as expected, the number of peaks is dramatically reduced for the smaller nuclei size range when comparing the results to those of the larger nuclei size range. That is because as shown in Fig. 16 near inception the nuclei contributing to the high-level peaks are only the larger bubble sizes.

A series of computations were also conducted at different cavitation numbers for the small and the large scale with the smaller

Table 2 Cavitation inception numbers obtained from the numerical study using various criteria, and power law fit deduced from these results

	Numerical computed values for σ_i			R_e^γ curve fit	
	Small scale	Medium scale	Large scale	γ	Square of correlation coefficient
$-Cp_{\min}$	3.34	4.34	5.48	0.357	0.999
10 peaks/s over 10 Pa	3.28	4.33	5.47	0.369	0.998
50 peaks/s over 40 Pa	3.12	4.28	5.44	0.401	0.994

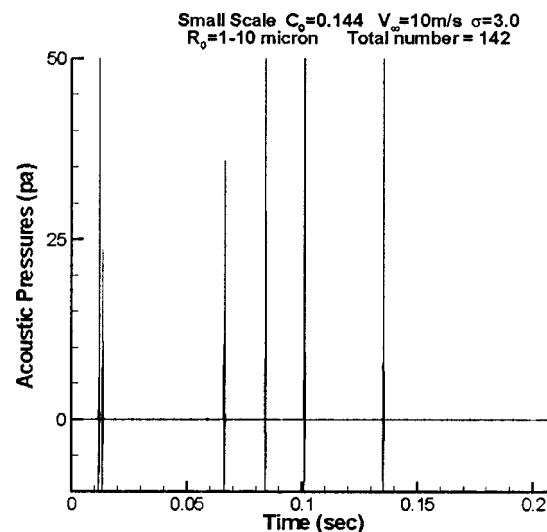


Fig. 15 The acoustic signals for the small scale at $\sigma=3.0$ using the smaller nuclei size range (1–10 μm)

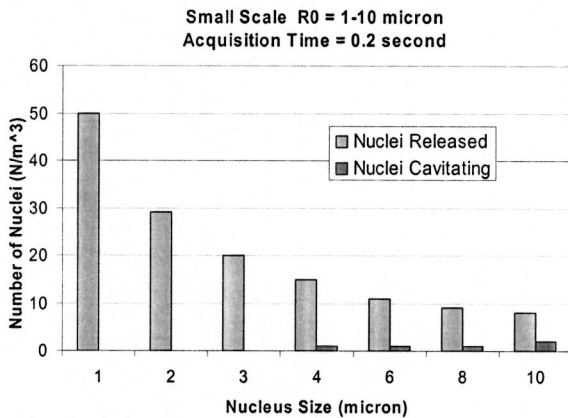


Fig. 16 The number of nuclei released and the number of nuclei cavitating versus nuclei size obtained for the 1–10 μm small nuclei size distribution at $\sigma=3.0$

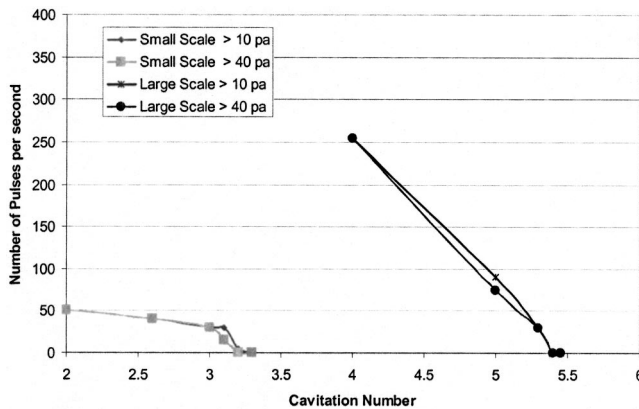


Fig. 17 Number of pressure peaks versus cavitation number deduced at two criteria of acoustic level for the small and large scales considered

Table 3 Cavitation inception numbers obtained from the numerical study using various criteria, and power law fit deduced from these results. For smaller void fraction ($\alpha \approx 1 \times 10^{-9}$).

	Numerical computed values for σ_i		R_e^γ curve fit
	Small Scale	Large Scale	
$-Cp_{\min}$	3.34	5.48	0.357
10 peaks/s over 10 Pa	3.20	5.40	0.377
50 peaks/s over 40 Pa	2.0	5.18	0.687

nuclei size range. Two acoustic pressure levels, 10 and 40 Pa, are also selected to determine the number of pressure peaks for each cavitation number. The resulting curves of number of pressure peaks versus cavitation numbers for the small and large scales are shown in Fig. 17. By comparing with Table 2 we can see very important differences for the small scale when the cavitation inception criteria are less stringent. Also, scaling effects and deviation from classical formula due to nuclei size distribution are seen to significantly increase when nuclei sizes (or void fraction) decreases.

4 Conclusions

The study of the behavior of a realistic distribution of nuclei in the tip vortex flow field of a NACA16020 foil at three scales has enabled observation of several effects:

1. Comparison of the size of the bubble capture area or “window of opportunity” at the various scales shows that the larger scale results in more cavitation events by allowing more nuclei per unit time to be captured by the tip vortex;

2. the numerical results show that different criteria for defining the cavitation inception can lead to a different cavitation inception numbers as well as different scaling laws. By comparing the predicted cavitation inception number with $-Cp_{\min}$, we found that scaling effects (i.e., deviation from $-Cp_{\min}$) due to nuclei increase as the reference inception criteria become less stringent (higher reference pressure amplitude and larger number of peaks);

3. the predicted value of γ in the power formula ($\sigma_i \propto R_e^\gamma$) is closer to the classical value ($\gamma=0.4$), as the reference inception criterion becomes less stringent;

4. the range of nuclei sizes was shown to have an important effect on the prediction of cavitation inception. Differences between predicted cavitation inception number and $-Cp_{\min}$ increase as nuclei sizes (or void fractions) decrease. This implies that scaling effects due to nuclei size distribution are stronger when the water contains only small nuclei (or for low void fraction).

Acknowledgments

This work was conducted at Dynaflo, Inc. (www.dynaflo-inc.com) and has been supported by the Naval Surface Warfare Carderock Division and the Office of Naval Research. This support of Dr. Ki-Han Kim, ONR, and Dr. Young Shen, NSWCCD, is greatly appreciated.

References

- [1] McCormick, B. W., 1962, “On Cavitation Produced by a Vortex Trailing From a Lifting Surface,” ASME J. Basic Eng., **84**, pp. 369–379.
- [2] Fruman, D. H., Dugue, C., Pauchel, A., and Cerruti, P., 1992, “Tip Vortex Roll-Up and Cavitation,” *Eighteenth Symposium on Naval Hydrodynamics*, Seoul, Korea.
- [3] Arndt, R. E., and Dugue, C., 1992, “Recent Advances in Tip Vortex Cavitation Research,” *Proc. International Symposium on Propulsors Cavitation*, Hamburg, Germany, pp. 142–149.
- [4] Farrell, K. J., and Billet, M. L., 1994, “A Correlation of Leakage Vortex Cavitation in Axial-Flow Pumps,” ASME J. Fluids Eng., **116**, pp. 551–557.
- [5] Maines, B., and Arndt, R., 1997, “Tip Vortex Formation and Cavitation,” ASME J. Fluids Eng., **119**, pp. 413–419.
- [6] Arndt, R. E. A., 2002, “Cavitation in Vertical Flows,” Annu. Rev. Fluid Mech., **34**, pp. 143–175.
- [7] Copalan, S., Liu, H. L., and Katz, J., 2000, “On the Flow Structure, Tip Leakage Cavitation Inception and Associated Noise,” *23rd Symposium on Naval Hydrodynamics*.
- [8] Hsiao, C.-T., Chahine, G. L., and Liu, H. L., 2003, “Scaling Effects on Prediction of Cavitation Inception in a Line Vortex Flow,” ASME J. Fluids Eng., **125**, pp. 53–60.
- [9] Ligneul, P., and Latorre, R., 1989, “Study on the Capture and Noise of Spherical Nuclei in the Presence of the Tip Vortex of Hydrofoils and Propellers,” *Acustica*, **68**, pp. 1–14.
- [10] Hsiao, C.-T., and Pauley, L. L., 1999, “Study of Tip Vortex Cavitation Inception Using Navier–Stokes Computation and Bubble Dynamics Model,” ASME J. Fluids Eng., **121**, pp. 198–204.
- [11] Hsiao, C.-T., and Chahine, G. L., 2004, “Prediction of Vortex Cavitation Inception Using Coupled Spherical and Nonspherical Models and UnRANS Computations,” *J. Marine Sci. Technol.*, **8**, No. 3, pp. 99–108.
- [12] Arndt, R. E. A., and Maines, B. H., 2000, “Nucleation and Bubble Dynamics in Vortical Flows,” ASME J. Fluids Eng., **122**, pp. 488–493.
- [13] Hsiao, C.-T., and Pauley, L. L., 1999, “Study of Tip Vortex Cavitation Inception Using Navier–Stokes Computation and Bubble Dynamics Model,” ASME J. Fluids Eng., **121**, pp. 198–204.
- [14] Hsiao, C.-T., and Pauley, L. L., 1998, “Numerical Study of the Steady-State Tip Vortex Flow Over a Finite-Span Hydrofoil,” ASME J. Fluids Eng., **120**, pp. 345–349.
- [15] Hsiao, C.-T., and Pauley, L. L., 1999, “Numerical Calculation of Tip Vortex Flow Generated by a Marine Propeller,” ASME J. Fluids Eng., **121**, pp. 638–645.
- [16] Taylor, L. K., Pankajakshan, R., Jiang, M., Sheng, C., Briley, W. R., Whitfield, D. L., Davoudzadeh, F., Boger, D. A., Gibeling, H. J., Gorski, J., Haussling,

H., Coleman, R., and Buley, G., 1998, "Large-Scale Simulations for Maneuvering Submarines and Propulsors," AIAA Paper 98-2930.

[17] Chorin, A. J., 1967, "A Numerical Method for Solving Incompressible Viscous Flow Problems," *J. Comput. Phys.*, **2**, pp. 12–26.

[18] Roe, P. L., 1981, "Approximate Riemann Solvers, Parameter Vectors, and Difference Schemes," *J. Comput. Phys.*, **43**, pp. 357–372.

[19] van Leer, B., 1979, "Towards the Ultimate Conservative Difference Scheme V. A Second Order Sequel to Godunov's Method," *J. Comput. Phys.*, **32**, pp. 101–136.

[20] Vanden, K., and Whitfield, D. L., 1993, "Direct and Iterative Algorithms for the Three-Dimensional Euler Equations," AIAA-93-3378.

[21] Chahine, G. L., Kalumuck, K. M., Cheng, L.-Y., and Frederick, G., 2001, "Validation of Bubble Distribution Measurements of the ABS Acoustic Bubble Spectrometer With High Speed Video Photography," *4th International Symposium on Cavitation*, California Institute of Technology, Pasadena, CA.

[22] Johnson, V. E., and Hsieh, T., 1966, "The Influence of the Trajectories of Gas Nuclei on Cavitation Inception," *Sixth Symposium on Naval Hydrodynamics*, pp. 163–179.

[23] Haberman, W. L., and Morton, R. K., 1953, "An Experimental Investigation of the Drag and Shape of Air Bubbles Rising in Various Liquids," Report 802, DTMB.

[24] Fitzpatrick, N., and Strasberg, M., 1958, "Hydrodynamic Sources of Sound," *2nd Symposium on Naval Hydrodynamics*, pp. 201–205.

[25] Dacles-Mariani, J., Zilliac, G. G., Chow, J. S., and Bradshaw, P., 1995, "Numerical/Experimental Study of a Wingtip Vortex in the Near Field," *AIAA J.*, **33**, No. 9, pp. 1561–1568.

[26] Billet, M. L., 1984, "Cavitation Nuclei Measurements," *International Symposium on Cavitation Inception*, FED-Vol. 16, pp. 33–42.

[27] Franklin, R. E., 1992, "A Note on the Radius Distribution Function for Microbubbles of Gas in Water," *ASME Cavitation and Multiphase Flow Forum*, FED-Vol. 135, pp. 77–85.

Dynamics and Noise Emission of Vortex Cavitation Bubbles

Jaehyug Choi*, Chao-Tsung Hsiao**, Georges Chahine** and Steven Ceccio*

*The University of Michigan, U.S.A.

** DYNAFLOW Inc., U.S.A.

ABSTRACT

The dynamics and noise emission of cavitation bubbles forming within the core of a single line vortex were examined experimentally and numerically. For the experiment, a steady line vortex was formed downstream of a hydrofoil mounted in the test section of a re-circulating water tunnel, allowing for the detailed examination of the growth, splitting and collapse of individual cavitation bubbles as they experience a reduction and recovery of the local static pressure. The average Reynolds number of the vortices was $Re = 250000$, and the average core radius was 4.5 mm. The growth and collapse of bubbles with maximum aspect ratios of 60 were examined. The acoustic emissions from the bubbles were detected during growth, splitting and collapse. The equilibrium radius of elongated vortex cavitation bubbles are related to the original vortex properties and the local static pressure. The observed bubble radii were between 10% and 15% of the original vortex radius. The behavior of highly elongated (*i.e.* two-dimensional) cylindrical vortex cavitation bubbles for both equilibrium conditions and during bubble growth was calculated. DF_UNCLE® was also used to compute the growth, splitting, and collapse of spherical nuclei in the vortex. The computational results were compared to the experimentally observed bubbles.

INTRODUCTION

The static pressure in the core of a linear vortex is depressed when compared with the pressure far from the vortex, and the magnitude of this depression can be increased if the vortex is stretched along its axis. In some cases, the pressure in the vortex core can fall below the liquid vapor pressure, and it is possible for negative pressure, or tension, to exist in the cores of strong vortices. Vortex cavitation occurs when a small bubble or nucleus explosively grows when exposed to negative pressures in the core. Sometimes vortex cavitation bubbles remain small compared with the vortex core radius, with the nearly spherical bubbles rapidly growing and collapsing within the vortex core. Conversely, the near spherical bubble can expand to fill the core of the vortex and continue to grow along the vortex axis, becoming highly elongated. The growth, splitting, and collapse of vortex cavitation bubbles can produce noise pulses.

Incipient and developed vortex cavitation has been the subject of much study. Concentrated regions of vorticity often occur in the tip regions of lifting surfaces, and rotating machinery can also produce concentrated vortices both at the tips of the propulsor blades as well as downstream of the hub. Under many circumstances, vortex cavitation will be the first detectable cavitation that will occur in the flow, with traveling bubble, partial and cloud cavitation

only occurring during significantly off-design conditions. Moreover, vortex cavitation is often the first form of cavitation in many naval applications. Vortex cavitation is also a common feature of turbulent jets, wakes, and shear layers. A comprehensive review is provided by Arndt (2002).

A recent series of experiments conducted by researchers at the University of Michigan and the U. S. Navy's Naval Surface Warfare Center- Carderock Division illustrated some of the difficulties involved with the prediction and scaling of vortex cavitation inception and noise for flows induced by turbomachinery. The results of these studies are reported in Chesnakas and Jessup (2003), Oweis *et al.* (2005a) and (2005b), and Oweis and Ceccio (2005). In these studies, the location and inception pressure of the cavitation was associated with the presence of multiple, interacting vortices. A variety of vortex-vortex interactions occurring with both co- and counter-rotating vortices of varying strength that can lead to the stretching of smaller vortex filaments, and these smaller vortices can produce cavitation at relatively high pressures due to both stretching of the vortices and the creation of axial flow acceleration in the vortex core. This phenomenon has been observed in the inception of jets and shear layers (O'Hern 1990, Katz and O'Hern 1986, and Iyer and Ceccio, 2002). Such flow complexities make the scaling of vortex inception and noise on practical flows of turbomachinery much more problematic.

Scaling of vortex cavitation has proven challenging. Typically, engineers would like to observe vortex cavitation with model scale experiments then use these results to make a prediction at full-scale conditions. The above description of the vortex cavitation process reveals two significant scale effects. First, the nuclei population on the model and full-scales can differ substantially, leading to "water quality" scale effects. Second, the non-cavitating flow fields of the model and full scale flows can differ, leading to "Reynolds Number" scale effects. A simple example is the case of a single vortex cavitation bubble in an isolated, steady line vortex formed downstream of a stationary hydrofoil. We can match the freestream pressure (cavitation number) and the vortex circulation (which would suggest a matching of the lift coefficients of the two hydrofoils). But, the viscous core size of the two vortices is different since their size scale is different, and this will lead to different minimum core pressures and inception pressures for the same nucleus.

In the present study, we observed the dynamics of single growing and collapsing vortex cavitation bubbles, and compared their dynamics to the underlying flow field. These results are then compared to computations of the vortex bubble behavior using both simple two-dimensional models of elongated cavitation bubbles and more complex bubble dynamics using DF_UNCLE[©]. These results were compared to the experimental observations.

EXPERIMENTAL STUDY

The Experimental Setup: A finite aspect ratio hydrofoil is used to create steady line vortex in the test section of the University of Michigan 9-Inch Water Tunnel. The tunnel has a circular contraction downstream of a series of flow management screens with area contraction ratio 6.4:1. The test section has a 22.9 cm (9 inch) diameter round inlet that is then faired into a rectangular test section with widely rounded corners. The maximum test-section inlet flow velocity is 18 ms⁻¹, and the test section static pressure can be varied from near vacuum to 200 kPa. The tunnel holds 3.8 m³ (1000 gallons) of water that can be deaerated to 10% saturation at atmospheric pressure. Further details regarding the water tunnel are reported in Oweis *et al.* (2004).

A vortical flow is created using a cambered hydrofoil with a non-standard cross section mounted to one window of the test section. The hydrofoil has a rectangular platform of 9.5 cm span and 16.6 cm chord with a rounded tip. Two hydrofoils were fabricated and then modified in the following ways: a wire was attached along the chord near the tip, and the suction side of one hydrofoil was roughened. The incident flow angle was varied from 4.0° to 4.5° to have different circulation and vortex core size. A series of tip and trailing edge vortices are shed near the tip, and these vortices merge to form a single vortex within one-half chord length downstream of the trailing edge. A Venturi section (Figure 1) was mounted at a station 21 cm downstream of the trailing edge to produce a reduction and recovery of the flow static pressure to have a growth and collapse of bubbles. The area of the test section upstream of the Venturi is 0.03778 m² and reaches a minimum of 0.0331 m² at the Venturi throat, yielding an area reduction of 12%. Four acrylic windows permit optical access to the test section flow.

Measurements of vortex cavitation were conducted with free-stream velocities U_∞ in the range of 9.7 to 10.3 ms⁻¹ and a variety of static pressures, P_∞ . The

Reynolds number of the flow based on the free stream velocity (U_∞) and hydrofoil chord length C_O ($Re = U_\infty C_O / \nu$) ranged from 2.01×10^6 to 2.14×10^6 , where ν ($= 1 \times 10^{-6}$ m 2 s $^{-1}$) is the liquid kinematic viscosity. Six pressure taps are installed on the top window to monitor static pressure for three locations before, under and after the Venturi, and a Omega PX203 pressure transducer was used to measure the absolute pressures. The free-stream air content was maintained below 20% saturation at atmospheric pressure (oxygen concentration measured with Orion dissolved oxygen meter Model 810).

Stereo Planar Particle Imaging Velocimetry was used to measure the vortical flow field at a station 1 cm upstream of the Venturi inlet and at 10 cm downstream of the inlet of the Venturi, as shown in Figure 1. A double-pulsed light sheet 5 mm thick was created perpendicular to the mean flow direction with two pulsed Nd:YAG lasers (Spectra Physics model Pro-250 Series), and three cylindrical lenses (60 mm, -150 mm and 200 mm focal length). Acrylic prisms were mounted optically to side windows of the test-section for viewing of the light sheet with reduced optical distortion. Double-pulsed images of the light sheet were acquired with two digital cameras (LaVision FlowMaster 3S) capturing an image with 1280×1024 pixels. 50 mm Nikon lenses were used with Scheimpflug mounts to reduce optical distortion and aid in focusing on the light sheet. Optical distortion of the planar light-sheet images was corrected through a calibration procedure that employed the imaging of a regular grid (crosses separated by 4 mm) that was traversed in the streamwise flow. The grid was immersed in water during calibration. The flow was seeded with $15.3 \mu\text{m}$ average diameter silver coated glass spheres (from Potters Industries). Velocity vectors were produced from the double-pulsed images using the LaVision image analysis software DaVis® 6.0.4. Multi-pass processing with a final window size of 16×16 pixels was used with 50% window overlap in the final pass to produce 159×97 in-plane velocity vectors at 0.56 mm spacing. Since the camera-imaging plane was not parallel to the light sheet, it had an angular shift of 40° with the horizontal direction. The average vortical flow field was determined after processing and averaging 1000 individual vector fields. Oweis and Ceccio (2005) discussed the implication of vortex wandering on the averaged vortical flow field. The wandering of the single vortex in the present experiment was considered negligible. The uncertainty in the in-plane velocity measurements is estimated to be $\pm 3\%$ while the out-of-plane component was estimated to be $\pm 6\%$.

The error of in-plane velocity measurements from the continuity with assumption of uniform axial velocity was estimated to be $\pm 10\%$.

The combination of two tip treatments and two attack angles lead to four flow conditions for the vortex. Table 1 presents the circulation, Γ_O , and the core radius, r_C , derived from a Gaussian fit to the vortical flow field:

$$u_\theta(r, z) = \frac{\Gamma_O(z)}{2\pi r} (1 - e^{-\alpha(r/r_C(z))^2}) \quad (1)$$

These four conditions will be referred to as T1, T2, R1, and R2. The estimated pressure coefficient in the Venturi at the vortex core is shown in Figure 2. The velocity and pressure upstream of the Venturi are U_∞ and P_∞ . The stream-wise position is z , and the radial distance from the vortex axis is r . The SPIV measurements indicated that the vortex had a nominally zero relative axial velocity upstream of the Venturi, and an estimate of the core axial velocity was performed using the methods described by Darmofal *et al.* (2001) to compute the core pressure in the vortex. Details are provided by Choi (2006). We define the free-stream cavitation number as

$$\sigma_\infty = \frac{P_\infty - P_V}{\frac{1}{2}\rho U_\infty^2} \quad (2)$$

The data of Figure 2 was used to compute the cavitation number on the axis of the vortex:

$$\sigma_C(z) = \frac{P_C - P_V}{\frac{1}{2}\rho \left(\beta \frac{\Gamma_O}{2\pi r_C} \right)^2} \quad (3)$$

where $\beta = 0.715$. Images of the vortex cavitation bubbles were acquired with two 8-bit Phantom V9.0 high-speed movie cameras. These cameras were set to an effective resolution of 1632 by 104 pixels at a frame rate of 8000 fps with a 15 μs exposure time. 50 mm Nikon lenses with 12 mm extension rings were used. Each camera has 70mm by 4.5 mm viewing area, with 10 mm of overlap. A set of four 300 W incandescent lights were installed opposite the camera, and a light diffuser was used to prevent glare on the imager. A pulse delay generator (Stanford Research Systems model DG535) was used to trigger the camera with varying delays from the laser pulse that created the nucleus. These movie images were recorded digitally for post-processing.

A high bandwidth hydrophone (Brüel & Kjær Model 8103) was used to detect the cavitation noise created by the bubbles in the vortex. This hydrophone has an upper frequency limit of approximately 80 kHz. The hydrophone was mounted inside the small water reservoir, and placed on the top window of the test

section, and the container was placed in a pool of water on top of the window to enhance the transmission of the acoustic pulses. This hydrophone was placed near the average location of bubble collapse, and the distance between the hydrophone and the bubble collapse is about 30 cm. Signals from the hydrophone were conditioned with a charge amplifier (Brüel & Kjær Model 2635), and digitally acquired using an oscilloscope sampling at 250 kHz with a record length of about 40 ms (Tektronix Model TDS430A).

Experimental Results: The cavitation bubbles that develop in the core region of the vortex develop according to the following steps. First, the nucleus created by the laser pulse convects into a region where the flow is in tension (*i.e.* negative pressure). If the tension is sufficiently strong, the nucleus will grow explosively. After inception the bubble volume begins to grow. However, the bubble will usually retain its near cylindrical shape until it convects into the region of pressure recovery. Figure 3 presents an example of the growth and collapse of cavitation bubbles for each of the four vortex conditions of Table 1. A time series of bubble images are shown, and these images are used to determine the radius, length history of the bubbles. The volume is also computed after measuring the local bubble radii and employing the assumption of bubble axisymmetry. Also presented is the accompanying hydrophone signal created by the bubble during, inception, splitting, and collapse. The cavitation numbers of the flows were selected such that bubble growth and collapse would largely take place in the camera field of view.

The bubbles formed in the vortices share some general features. The growing nucleus begins as a nearly spherical bubble. It then becomes ellipsoidal and ultimately elongated as the extent of the bubble growth in the radial direction is arrested by the increase in pressure away from the vortex axis. The bubble continues to grow along the axis of the vortex while the pressure on the vortex axis remains below vapor pressure, and depending on the duration that the bubble tension, the length of the bubble can grow to many times its diameter. During this period of elongation, disturbances can exist on the bubble interface as it slowly revolves about the bubble axis, and these surface waves can lead to volume oscillations of the bubble and the local fission of the bubble. Then, as the pressure rises, the bubble begins to collapse. The rate at which the bubble surface collapses can vary in the radial and axial directions. Under some conditions, the collapsing bubble may fission to form smaller, nearly spherical sub-bubbles

at its ends, while under other circumstances, the bubbles may split into multiple bubbles near the point of minimum bubble volume. Pulses of noise are often associated with bubble growth, fission, and collapse. The bubble shape and size is a function of both the vortex properties and the free-stream cavitation number. The location where the vortex core pressure falls below vapor pressure will vary with the vortex properties and the cavitation number. But, for the cases examined here, the region of tension begins near the end of the Venturi throat. In some cases, the images of the bubble collapse were captured by the high-speed imaging, while in others, the bubbles collapsed outside the cameras' field of view.

Figure 4 presents the average radius of the observed bubbles for varying cavitation number and vortex properties. 100 individual images for each case were averaged. The magnitude and extent of tension (*e.g.* negative fluid pressure) that the bubbles experience will vary with the cavitation number. For most of the cases, the bubbles begin to grow between $0.4 < z/L < 0.5$. The growth of the bubbles in the radial direction is rapid and occurs at a rate nearly ten times the growth rate in the axial direction, and the response of the bubble mean radius to changes in pressure are also rapid, and the magnitude of the radius begins to decrease as the bubbles convect into the pressure recovery region after the exit of the venturi, where the highest tension region. Figure 5 presents the average bubble aspect ratio as a function of σ_c . These data show that the bubbles quickly become elongated once inception takes place. The aspect ratio is a function of the vortex properties and the cavitation number history. Bubbles with aspect ratios of over 50 were observed.

Figure 6 presents the axial bubble velocities as a function of the local cavitation number. The axial velocities are for both the growth and collapse of the bubbles, and the axial growth rate ($\dot{L} > 0$) also increases with decreasing cavitation number. The trends of decreasing axial collapse rate with increasing cavitation number results from the dynamics of the bubble in the pressure recovery region of the Venturi. Here, the highest cavitation numbers occur when the bubble is near its minimum volume right before the final collapse. Arndt and Maines (2000) analyzed the process of axial bubble growth in order to scale the growth rate with the driving pressure. They derived an equivalent expression of the Rayleigh-Plesset equation for bubble growth in the axial direction assuming a value of the apparent mass of the axially growing bubble that was proportional to the displaced volume of the

bubble. The authors concluded that the rate of axial bubble growth scales with the differential driving pressure,

$$\dot{L}_b \sim \kappa \sqrt{\frac{2(P_C - P_V)}{\rho}} = \kappa \left(\frac{\beta \Gamma_O}{2\pi r_C} \right) \sqrt{\sigma_C} \quad (4)$$

A value of $\kappa \approx 2.1$ was determined from experimentally observed bubble growth for the near-spherical bubbles. Near the point of inception, the growth rate of the radial growth rate of the bubbles is the largest and on the order of 10 ms^{-1} . This is consistent with a value of κ of two or greater. Figure 7 presents the normalized axial growth rate. The bubbles that are highly elongated with a nearly unchanging radius indicate that $\kappa \approx 1$ for the bubble growth rate in the axial direction. These data suggest that the added mass coefficient for the axially expanding bubble is likely not a constant, but varies with the aspect ratio of the bubble.

COMPUTATIONAL STUDY

The dynamics of individual cavitation bubbles were also computed. First, we consider the equilibrium radius of elongated cavitation bubbles and the dynamics of two-dimensional vortex cavitation bubbles. Next, the growth, splitting, and collapse of individual bubbles are computed with DF_UNCLE®, a Navier-Stokes solver modified to permit the computation of fluid-bubble interactions.

Two dimensional bubble simulations: The diameter of a cylindrical bubble in a two-dimensional vortex has been predicted analytically for a Rankine vortex by Arndt and Keller (1992). They employed conservation of angular momentum to show that the radius of the vapor bubble would be $r_b / r_C = 1/\sqrt{2}$ or 71% of the initial core radius. However, it was acknowledged that the observed bubbles were significantly smaller in radius, as in the present study. Following this analysis for a Rankine vortex, we can examine the placement of a vapor cylinder in the core of a Gaussian vortex. The liquid flow field of the cavitating vortex, however, can take on any profile and need not be Gaussian. We can define a Gaussian like profile in this case,

$$u_{\theta,b}(r,z) = \frac{\Gamma_{O,b}(z)}{2\pi(r - \gamma r_b)} (1 - e^{-\alpha[(r - \gamma r_b)/(r_{Cb} - \gamma r_b)]^2}) \quad (4)$$

where $\Gamma_{O,b}$, r_{Cb} , and γ are parameters of the cavitating vortex. The parameter γ can vary between $0 < \gamma < 1$. When $\gamma = 0$, the liquid velocity profile is the same as that of a single-phase vortex, where the

maximum tangential velocity will occur at $r = r_C$, and vapor occupies the region $0 < r < r_b$. The tangential velocity at the bubble interface would be finite with the value

$$u_{\theta,b}(r_b) = \frac{\Gamma_{O,b}}{2\pi r_b (1 - \gamma)} (1 - e^{-\alpha[(r_b(1 - \gamma)/(r_{Cb} - \gamma r_b))]^2}) \quad (5)$$

Conversely, if $\gamma = 1$, the tangential velocity at the bubble interface is zero. Lastly, the bubble contents are at vapor pressure, prescribing a boundary condition on the bubble surface

We need four relationships to close the problem. Conservation of angular momentum and the kinetic energy in the vicinity of the vortex with and without the bubble provide two relations. And, the Euler equation can be integrated to relate the pressure at the bubble interface to the pressure far from the vortex. The fourth parameter, γ , is a free parameter. Figure 8 presents the resulting bubble radius as a function of cavitation number for a range of γ . Also plotted are the experimental data from Figure 4 corresponding to the observations where the bubbles are in a region of tension and the radius has ceased to vary. The data suggest a value of $0.6 < \gamma < 1$. The variation in the equilibrium r_b / r_C for the different vortices suggests that the tangential velocity that develops at the bubble interface may be a function of both the core radius and the vortex circulation, not simply the ratio $\Gamma_O / 2\pi r_C$ that scales the core pressure. Also, data suggest that the value of the tangential velocity at the bubble surface (related to γ in the model) may not be uniquely determined for any single vortex but is the product of the detailed history of the initial bubble growth.

The dynamics of two-dimensional cavitation bubbles were also examined. A small cylindrical “nucleus” was placed at the axis of a Gaussian vortex and allowed to grow after a reduction in pressure. The flow field was assumed to be axisymmetric. The radial and axial equations for mass and momentum conservation were discretized and solved using a Runge-Kutta method for each time-step as the cylindrical bubble volume changed. A pressure boundary condition was set at $r = 10r_C$, the gas in the bubble was assumed to be at constant vapor pressure, and a zero shear-stress condition was imposed on the bubble surface. The bubble growing simulations were performed with pressure gradients for the time ($\Delta P / \Delta t$) with varying ΔP and Δt . The kinematic viscosity $\nu = 1 \times 10^{-6} \text{ m}^2 / \text{s}$ and $\rho = 1000 \text{ kg} / \text{m}^3$ of water were used for the liquid. The applied

tension on the nucleus was achieved over a range of σ_C .

Figure 9 shows the simulation results for varying $\Delta P/\Delta t$ and σ_C . Varying the growth rates ($\Delta P/\Delta t$) did not change the equilibrium bubble radius, which is a function of the final magnitude of the imposed tension. However, an oscillation of the bubble radius is readily seen. For spherical bubbles, volume oscillations can occur when there energy exchange between the stored potential energy of the compressible, non-condensable gas inside the bubble and the kinetic energy of the radially moving liquid around the bubble. However, the pressure within the cylindrical cavitation bubble is fixed at vapor pressure and therefore does not act as a compliance in the system. Instead, the volume change of the bubble redistributes the vorticity of the flow field, which in turn changes the liquid pressure at the bubble interface. If the bubble radius grows too large, the pressure at the bubble surface increases, and the bubble motion is arrested. Similarly, a shrinking bubble can lead to an increase in tension. Since the level of damping in these calculations is quite low, the cylindrical is under-damped, and the application of a sudden tension causes the bubble to grow, overshoot, and then oscillate about the equilibrium radius. The period of the oscillation is on the order of $4 = \text{time}/t^*$, where $t^* = r_C / \sqrt{\Delta P / \rho}$.

Calculations Using DF_UNCLE[©]: A three-dimensional unsteady Navier-Stokes code was developed by DynaFlow Inc. and described by Hsiao and Chahine (2001 and 2004). A summary of the method is provided here. The three-dimensional incompressible Navier-Stokes flow solver, DF_UNCLE[©] is modified from the unsteady Navier-Stokes equation solver (UNCLE) developed at Mississippi State University (Arabshahi *et al.* 1995) to include bubble, cavity, and free-surface effects. The numerical scheme of DF_UNCLE[©] is a finite volume formulation. A moving Chimera grid scheme was adopted with free surface boundary conditions. The Navier-Stokes equations are solved for the global and sub-grids, and interpolation work are performed for overlapping these two grids. In general, solving unsteady Navier-Stokes equations is very time consuming work, so a spherical bubble model is adopted in the early stages of nuclei capture and growth through the use of a modified Rayleigh-Plesset equation for the spherical bubble dynamics. The surface-averaged pressure (SAP) around the bubble is used to solve the Rayleigh-Plesset equation as introduced by Choi *et al.* (2004). Once the bubble radius becomes large, a non-spherical model with a

sub-grid is adopted to solve Navier-Stokes equation with interaction of bubble interface and the flow field. The appropriate normal and tangential stress boundary conditions are enforced on the bubble interface, and the motions of the bubble interface are fully coupled into the liquid flow field.

The growth and collapse of a single cavitation nucleus places on the axis of a liquid vortex was examined. The non-cavitating vortical flow will consist only of a circumferential velocity distribution (*i.e.* no axial or radial flows). Figure 10 shows an image of the grids used in the study before cavitation commences. An O-O type 3-D axisymmetric grid domain ($41 \times 21 \times 25$) was generated on the bubble surface, and H-H type grid ($61 \times 31 \times 31$) was used for the flow field. There are 16 grid points across the core of the vortex before cavitation begins. To have finer grid at the end of bubbles, the staggered grid domain was adopted. The rectangular domain has a size of $3 \times r_C$ by $10 \times r_C$ and the size of spherical grid domain is set to have a size 30 times of the effective bubble radius ($= (3 \cdot V_b / (4\pi))^{1/3}$) during simulations. The spherical grid is re-gridding during simulation for faster and more accurate spatial resolution. Figure 11 shows the overlap of spherical grid and rectangular domain in the three dimensional field. Finally, we constrain the solution to be axisymmetric.

The boundary condition of the grid is set to have prescribed pressure and tangential velocity by the given vortex while the radial velocity is extrapolated, and it is possible to have velocity gradient at the boundary. To simulate both growing and collapsing process, a function of the static pressure for the time is applied as a harmonic form. The tangential velocity of the given vortex profile. The time step was chosen between 0.001 and 0.005 of the characteristic time scale at least, defined as $r_C / u_{\theta,M}$ in the DF_UNCLE[©].

A simple validation case was considered with a step change of static pressure. A reduced pressure was applied to a small bubble in the vortex core and the bubble grows, then the pressure is increased to collapse the bubble. The vortical flow field is weak, and the bubble maintains its near-spherical shape. The volume history of the bubble is then compared with the solution of the spherical Rayleigh-Plesset equation. Figure 12 (a) presents the bubble growing history, and it is shown that the three dimensional code has good agreement with analytical solutions from the Rayleigh-Plesset equations with Rayleigh

initial condition satisfying the Rayleigh-Plesset equation in terms of R_O and P_{go} . Figure 12 (b) shows the validation of collapsing process. The initial bubble has aspect ratio less than 1.5, and equivalent bubble radius based on bubble volume is used for comparison. This case indicates that the code is adequately capturing the near-spherical bubble dynamics.

The growth and collapse of bubbles was computed with varying growth time and pressure histories, as shown in Figure 13. The Reynolds number ($Re_\Gamma = \Gamma_O / v$) was also varied by doubling the vortex core size while maintaining the same initial maximum tangential velocity. Collapsing bubble simulations were performed for bubbles with varying aspect ratio, Reynolds number, collapsing time duration, and collapse pressure. The test matrix of the simulations is shown in Table 2.

The results of the simulations have been non-dimensionalized with the vortex core radius as the length scale, and the time-scale $t^* = r_C / \sqrt{\Delta P / \rho}$ (ΔP is pressure depression due to vortical flow). In physical coordinates, the core radius is 4 mm and 8 mm, depending on the scale of the given vortex ($Re_\Gamma = 200000$ and 400000), and the maximum tangential velocity is 5.7 ms^{-1} . The non-dimensional timescale, $t^* = 0.54$ and 1.08 msec in this study. The SAP model transitions to the non-spherical model when $r_{b,eq} \sim 200 \mu\text{m}$.

Vortex Bubble Growth From A Nucleus: With DF_UNCLE® it is possible to compute the growth of a small cavitation bubble at the axis of the vortex. The influence of Re on the growth of vortex cavitation bubbles was first examined. Figure 14 presents the time history of the vortex cavitation bubble growth for two Re and varying pressure gradient with two growth duration ($\Delta t_G = 2\text{msec}$ and 5msec). The equilibrium bubble radius is plotted as a function of time, which is defined with assumption of cylindrical bubbles to have same bubble length and volume with cylinder shape. The dynamics of the bubble growth are strongly influenced by the axial and radial pressure gradients in addition to time gradient. Pressure gradients along the vortex axis are produced by the dynamics of the bubble, while radial pressure gradients are due to both the bubble dynamics and the vortex induced pressure field. As the bubble interface grows in the axial direction, it may continue to experience tension. However, the growth of the bubble in the radial direction will

ultimately be arrested by the increasing fluid pressure away from the vortex axis.

The radius of the growing bubbles in Figure 14 (a) oscillate as the inertia of the flow surrounding the bubble leads the bubble to grow into a flow region where the liquid pressure is greater than vapor pressure. The bubble radius is then rebounds. This cycle continues until a near equilibrium bubble radius is achieved. Figure 14 (b) also shows the rebound of the bubbles in the radial direction, but oscillation is less than smaller vortex due to different dynamics along the radial direction of the vortex flow field. The axial growth can also experience rebounding, but this is mainly due to an interaction with the local flow field modification caused by the bubble growth. This behavior is similar to that computed for the two-dimensional cylindrical bubble growth. Figure 15 and 16 shows cross sections of the bubble shape and the in-plane velocities of the liquid and bubble interface for the case Figure 14 (a) and (b).

For the case of a rapid pressure drop, *i.e.* higher $\Delta P / \Delta t$, the influence of Re variation is pronounced. The Reynolds number scales with Γ_O which is proportion to the product of $r_C \cdot u_{\theta,M}$. The radial pressure gradient is a function of Γ_O / r_C which is proportional to $u_{\theta,M}$, although the functional relationship is complex. Consequently, differences are observed between the two Re cases because of the differences in the radial pressure gradients of the two vortices.

The growth of the elongated bubble is illustrated for $\sigma_C = -0.4$ and $\Delta t_G = 2\text{msec}$ in Figure 16 with generating neck of the elongated bubble. The bubble grows to become an oblate spheroid and then continues to grow in the axial direction. However, radial shape oscillations of the bubble can lead to flow interactions between the radial and axially induced flows. Radial pinching of the bubble near its center can lead to significant flows near the bubble ends. Figure 17 shows close-up of Figure 16 with velocity vectors and pressure contour around bubble, illustrating possible pinching during growth. The axial growth rates of the bubbles were computed and normalized with the σ_C as was done in section 2 for the experimentally observed bubbles. Figure 18 shows the average bubble growth rates in the axial direction for two different Re . The band illustrates the range of the experimental data in section 2. The computed results fall near the band of observed data. Recall that the value of σ_C used to scale the data in

section 2 was an average value along the bubble axis, while the computed results were for a uniform external pressure. Also, the experimental results are for non-axisymmetric bubbles, while the numerical results are axisymmetric. Nevertheless, the data are quite similar.

The elongated bubbles were allowed to grow to an aspect ratio of up to 10. Then, the average radius of the bubble was computed. These data were compared to the predicted envelope of possible equilibrium radii for very elongated bubbles shown in Figure 8. The DF_UNCLE[©] radii are within the predicted envelope of the equilibrium radii, except for the lowest Re and highest tension case. However, as was also shown for the two-dimensional calculation, the scaled bubble radii are 2 to 3 times larger than the experimentally observed bubbles. This is possibly due to difference in the pressure fields of the computed and measured bubbles. There exists a pressure gradient along the vortex axis in the experimental setup, while this gradient was not imposed on the calculated flow field. And, the dynamics of the bubble is sensitive to both the axial and radial pressure gradient. Moreover, the actual cavitation bubbles are three dimensional with a wavy interface, and this may lead to a reduced mean circumferential velocity at the bubble interface and a correspondingly smaller equilibrium radius.

Vortex Bubble Collapse: A series of bubbles were allowed to grow to a particular ratio of length to diameter. Then, the imposed pressure was increased to initiate bubble collapse. The data in Figure 19 show the bubble radius history for the bubbles with aspect ratios range from 2 to 5 before collapse. Figure 20 shows the bubble cross section for case (d) with splitting at the both end of the bubble. The splitting is due to a higher collapse rate in the radial direction compared to the collapse rate along the (lower pressure) vortex axis. Figure 21 shows a close-up of the velocity field for $t/t^* = 0.6$ along with the local static pressure, leading to splitting at both end of the bubble. There are high pressure regions at the bubble neck which can lead to splitting. And, high pressure at the axial extents of the bubble can produce a reentrant jet.

DISCUSSION AND CONCLUSIONS

The growth, splitting, and collapse of single vortex cavitation bubbles were examined experimentally and numerically. The properties of the line vortex strongly determine the shape and dynamics of the

bubble, although scaling with the vortex strength and core radius was not sufficient to collapse the data relating to the bubble dimensions and dynamics. The observed axial diameter of the elongated cavitation bubbles was a fraction (< 12%) of the non-cavitating core radius, and this was a function of the vortex properties, the free-stream pressure, and possibly the detailed process of bubble growth that determine the local tangential fluid velocity at the bubble interface. The bubbles could grow to large aspect ratios, with values larger than 50. The axial growth rates of the bubbles scaled with the vortex core pressure, and were larger in magnitude near the points of inception and final collapse. Bubble splitting was on average associated with the start of bubble collapse. The traditional scaling variables of vortex cavitation (*i.e.* $\Gamma_O, r_C, \sigma_C, r_{b,M}$) are important parameters that will scale the basic features of the bubble inception, growth, and collapse. However, the diameter of elongated bubbles is not uniquely determined by the non-cavitating vortex properties and appears to be influenced by the detailed process of inception. And, the bubble diameter scales the diameter of the sub-bubbles that form at its ends.

The growth and collapse of individual vortex cavitation bubbles were also examined with both two-dimensional and axisymmetric simulation of the fully coupled bubble flow interactions. Computation of cylindrical bubble growth illustrated how growing vortex cavitation bubbles can lead to complex bubble-flow interactions and bubble wall oscillations in the radial direction. This behavior was also observed in the axisymmetric DF_UNCLE[©] calculations. Changes in the Reynolds number resulted in noticeable differences in bubble growth for low values of core tension, but increasing the tension increased the growth rates and made these differences less pronounced. The growing and collapsing bubbles could exhibit complex volume-time histories, and radial flows induced by the expanding of collapsing bubbles could lead to changes in pressures and flow at the axial extent of the bubbles. Bubbles would undergo fission upon collapse through the production of sub-bubbles at the extreme ends of the original elongated bubble. And, since the radius of the elongated bubble is much smaller than its length, the bubble could collapse in the radial direction much sooner, leading to splitting. The axial growth rates of the bubbles were similar to those observed in the experiments. The equilibrium radius of the highly elongated cavitation bubbles fell within an envelope, but the measured and computed radii differed. This was likely due to subtle but significant differences in the experimental and

computed axial pressure fields of the vortical flow. These results illustrate how sensitive the dynamics of vortex cavitation bubbles are to the underlying flow, and this has implications for the scaling of vortex cavitation.

ACKNOWLEDGEMENTS

This work was supported by the Office of Naval Research under grant number N00014-03-1-0430, Dr. K-Han Kim, Program Manager.

REFERENCES

Arabshahi, A., Taylor, L. K. & Whitfield, D. L. 1995 UNCLE: Toward a comprehensive time accurate incompressible Navier-Stokes flow solver. *AIAA-95-0050* Reno, NV

Arndt, R. 2002 Cavitation in vortical flow. *Annu. Rev. Fluid Mech.* **34**, 143–175

Arndt, R. & Maines, B. 2000 Nucleation and bubble dynamics in vortical flows. *J. Fluids Eng.* **122**, 488-493

Arndt, R. & Keller, A. 1992 Water quality effects on cavitation inception in a trailing vortex. *J. Fluids Eng.* **114**, 430-438

Chesnakas, C., & Jessup, S. 2003 Tip vortex induced cavitation on a ducted propulsor. *Proc. 4th ASME-JSME Joint Fluids Eng. Conf.*, FEDSM2003-45320, Honolulu, Hawaii.

Choi, Jaehyug 2006 *Dynamics and noise emission of vortex cavitation bubbles*. Ph.D thesis, The University of Michigan, Ann Arbor

Choi, J. K., Hsiao, C.-T. & Ghahine, G. L. 2004 Tip vortex cavitation inception study using the Surface Averaged Pressure (SAP) model combined with a bubble splitting model. *25th Symposium on Naval Hydrodynamics* CANADA

Darmofal, D. L., Khan, R., Greitzer, E. M. & Tan, C. S. 2001 Vortex core behavior in confined and unconfined geometries: a quasi-one-dimensional model. *J. Fluid Mech.* **449**, 61-84

Hsiao, C-T & Chahine, G. L. 2001 Numerical simulation of bubble dynamics in a vortex flow using Navier-Stokes computations and moving Chimera grid scheme. *Proc. CAV2001* Pasadena, CA

Hsiao, C-T & Chahine, G. L. 2004 Prediction of tip vortex cavitation inception using coupled spherical and nonspherical bubble models and Navier-Stokes computations. *J. of Marine Sci. and Tech.* **8**, 99-108

Iyer, C. O. & Ceccio, S. L. 2002 The influence of developed cavitation on the flow of a turbulent shear layer. *Phys. Fluids*, **14**, 10, 3414-3431

Katz, J & O'Hern, T. J. 1986 Cavitation in large scale shear flow. *J. Fluids Eng.*, **108**, 373-376

Kuhn, de Chizelle Y., Ceccio, S. L. & Brennen, C. E. 1995 Observations and scaling of traveling bubble cavitation. *J. Fluid Mech.* **293**, 99-126

O'Hern, T. J. 1990 An experimental investigation of turbulent shear flow cavitation. *J. Fluid Mech.* **215**, 365-391

Oweis, G. & S. L. Ceccio 2005 Instantaneous and time averaged flow fields of multiple vortices in the tip region of a ducted propulsor. *Exp. in Fluids*, **38**, 615-636

Oweis, G. F., Choi, J. & Ceccio, S. L. 2004 Dynamics and noise emission of laser induced cavitation bubbles in a vortical flow field. *J. Acoust. Soc. Am.* **115**(3), 1049-1058

Oweis, G., D. Fry, C. J. Chesnakas, S. D. Jessup, & S. L. Ceccio, 2005a Development of a Tip-Leakage Flow: Part 1- The Flow Over a Range of Reynolds Numbers. *J. Fluids Eng.* (in press)

Oweis, G., D. Fry, C. J. Chesnakas, S. D. Jessup, & S. L. Ceccio, 2005b Development of a Tip-Leakage Flow: Part 2- Comparison between the Ducted and Un-ducted Rotor. *J. Fluids Eng.* (in press)

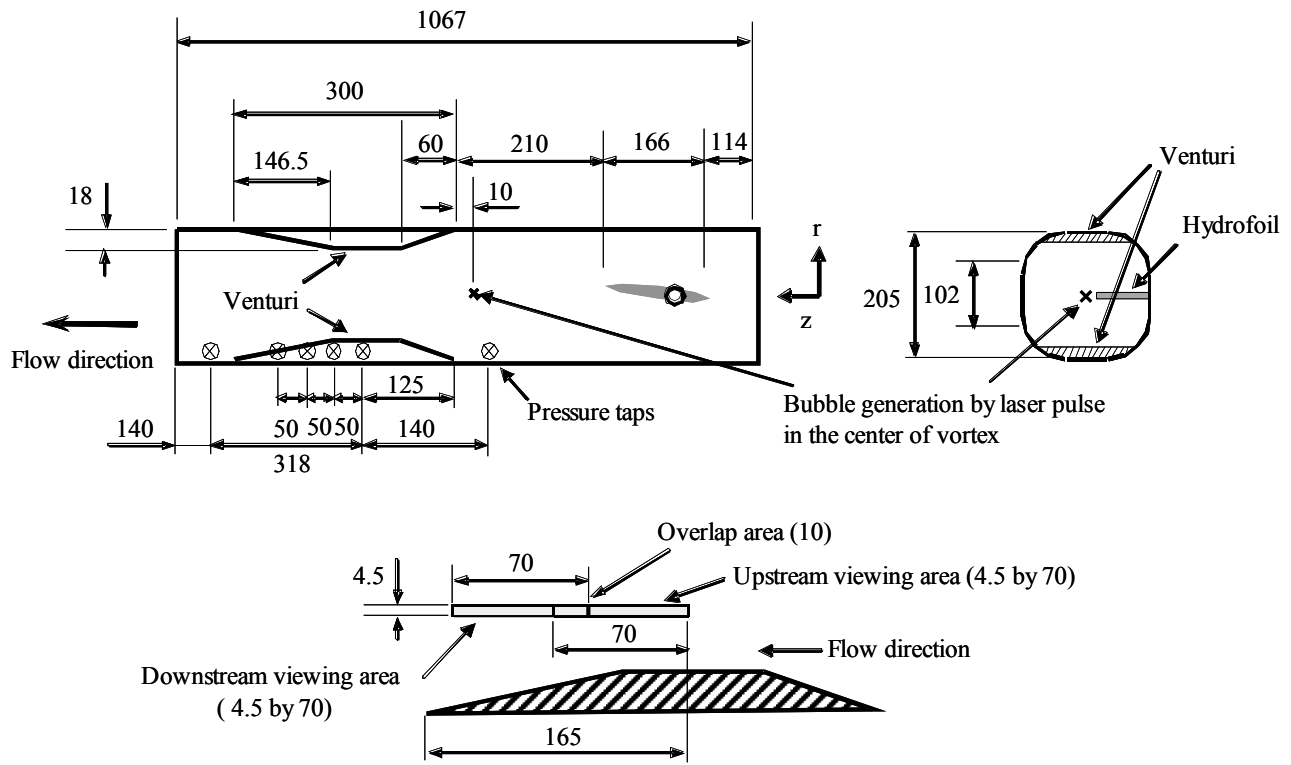
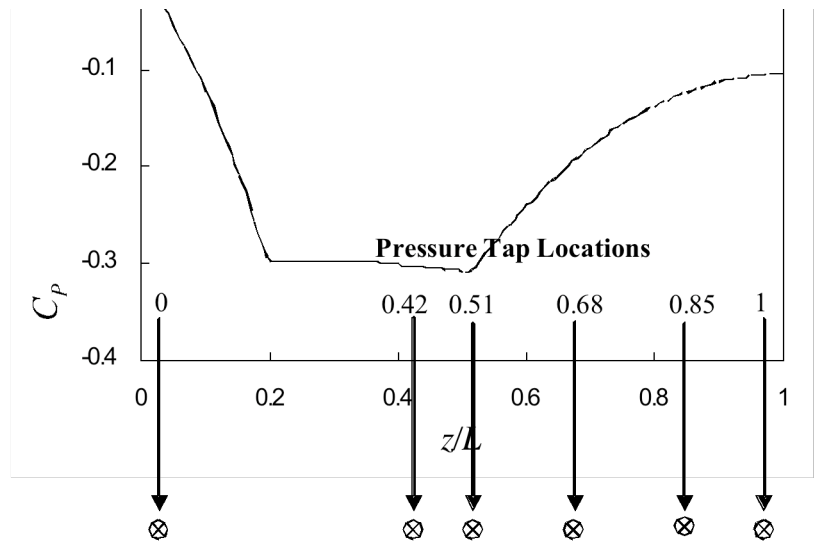
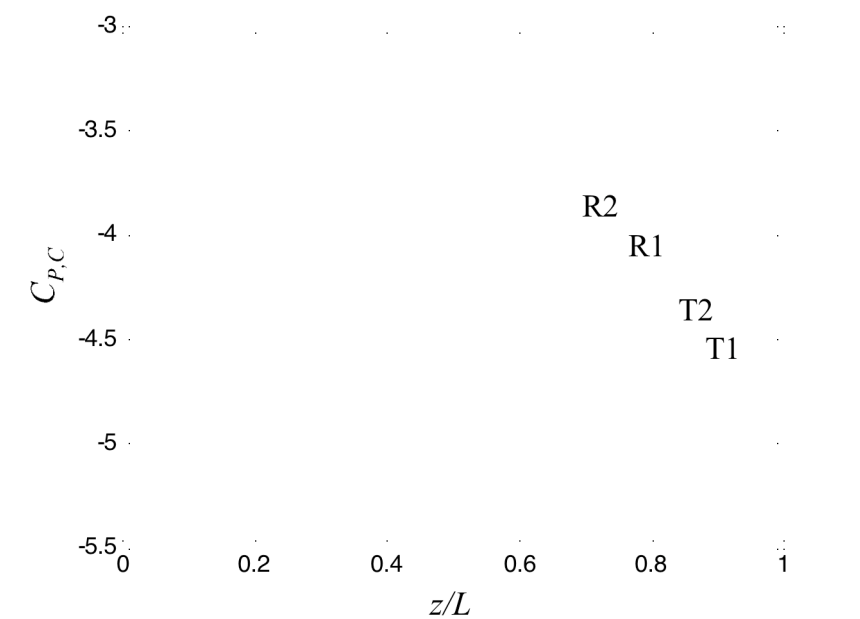


Figure 1. Schematic diagram of the Venturi in the water tunnel test section; the location of the hydrofoil and the laser-induced bubble are also illustrated. The field-of-view of the two high-speed cameras are shown. Dimensions are in millimeters



(a)

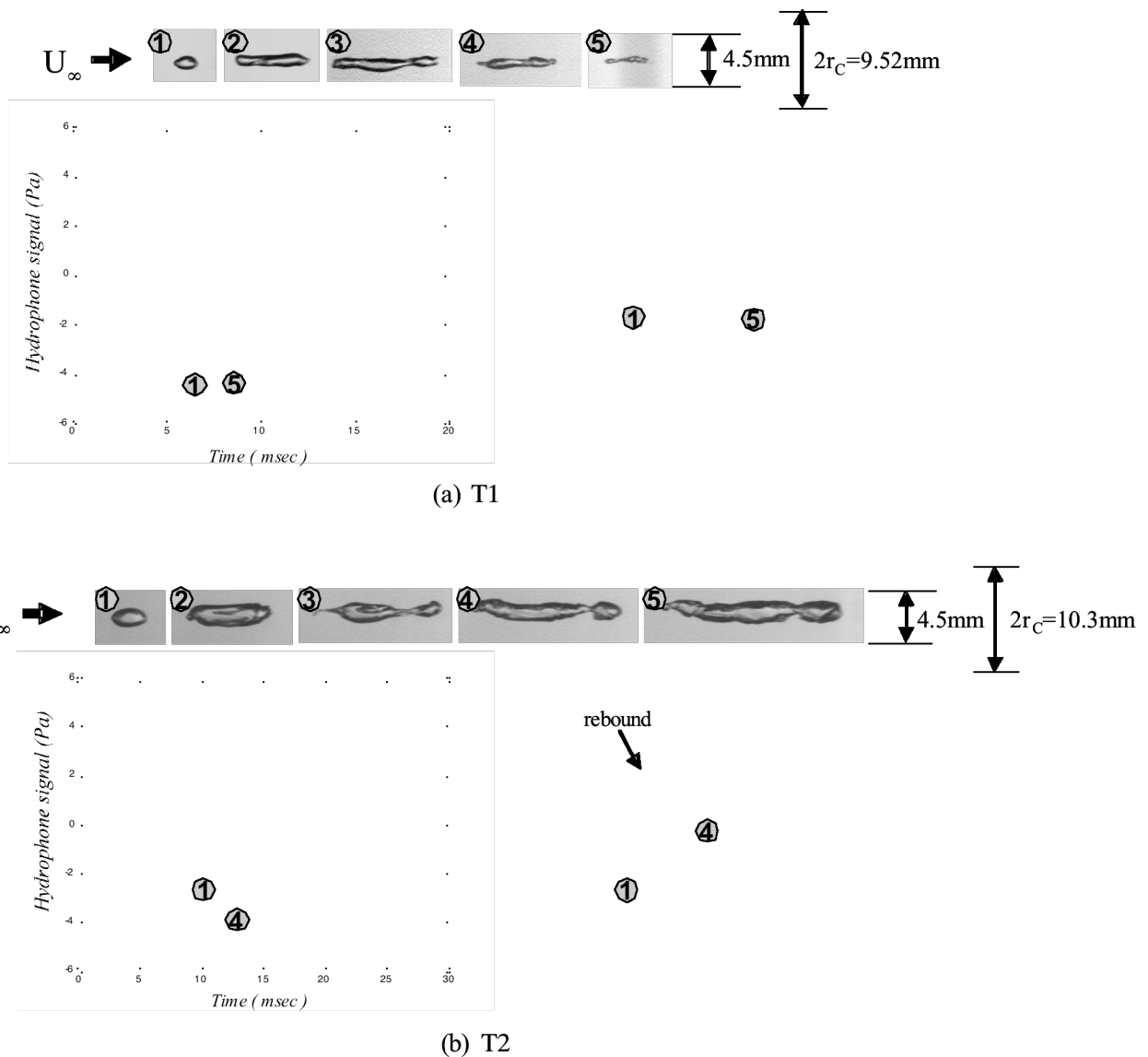


(b)

Figure 2. The estimated pressure coefficient, (a) in the Venturi, $C_p = (P(z) - P_\infty)/\rho U_\infty^2/2$ where $P(z)$ is the local pressure in the Venturi, away from the edge of the vortex core, (b) at the vortex core, $C_{p,C} = (P_C(z) - P_\infty)/(\rho \beta \Gamma_o / (2\pi r_C)^2/2)$ as a function of position along the center of the Venturi, z/L ; Conditions are shown in Table 1.

	$\alpha=4^{\circ}$ (1)		$\alpha=4.5^{\circ}$ (2)	
	Γ_o , m ² /s	r_C , mm	Γ_o , m ² /s	r_C , mm
Foil with trip (T)	0.252 +/-0.015	4.76 +/-0.31	0.288 +/-0.018	5.15 +/-0.35
Foil with roughness (R)	0.257 +/-0.013	3.75 +/-0.20	0.302 +/-0.015	4.20 +/-0.23

Table 1. Experimental conditions for the vortex properties in the Venturi with two different hydrofoil configurations. The vortex properties were identified from 1000 individual vector fields; $U_{\infty} = 10 \text{ ms}^{-1}$. The four conditions are referred to as T1, T2, R1, and R2.



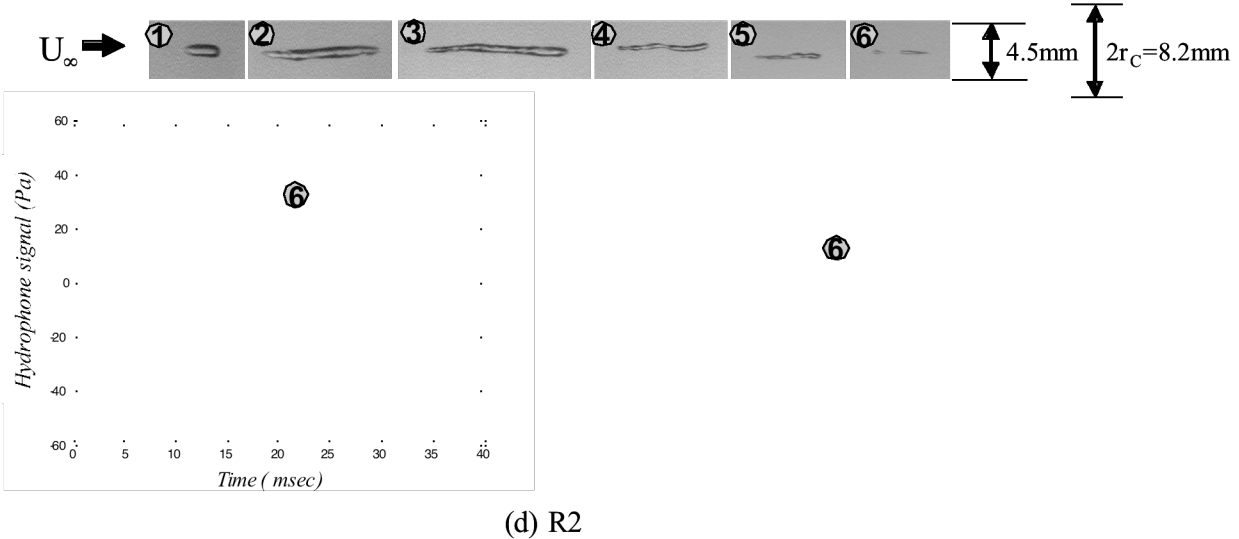
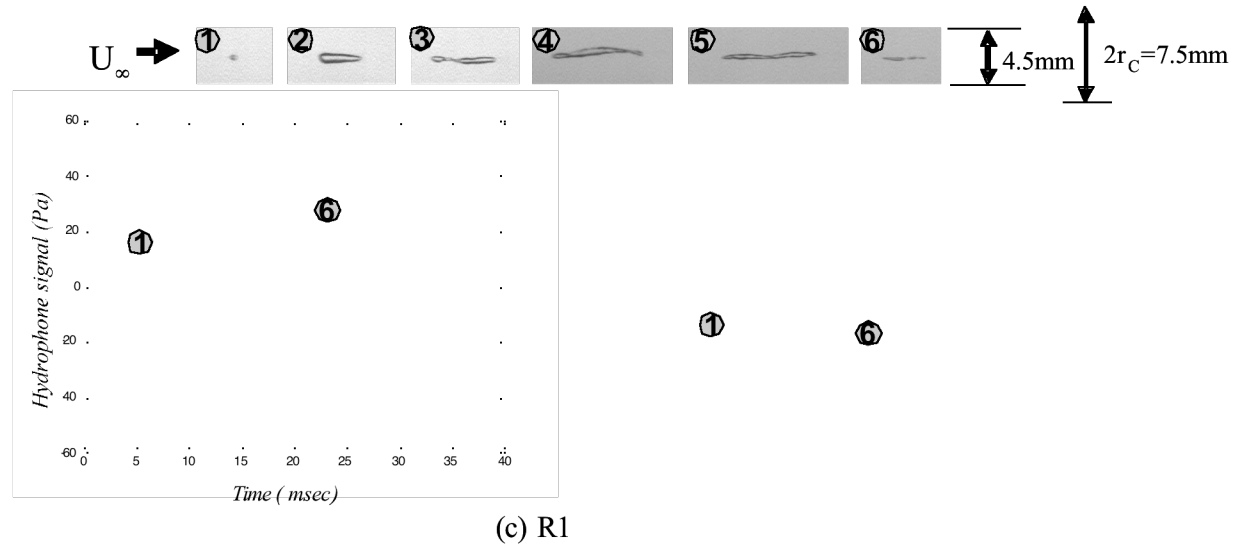


Figure 3. Images of individual cavitation bubbles taken from a video record to illustrate the bubble shape history and have varying time intervals. The video record was used to compute the length and average radius of the bubble as a function of position within the Venturi. Also shown are the corresponding acoustic signal detected from the hydrophone; (a) T1, $\sigma_\infty=1.74$, (b) T2, $\sigma_\infty=1.74$, (c) R1, $\sigma_\infty=2.75$, (d) R2, $\sigma_\infty=2.95$.

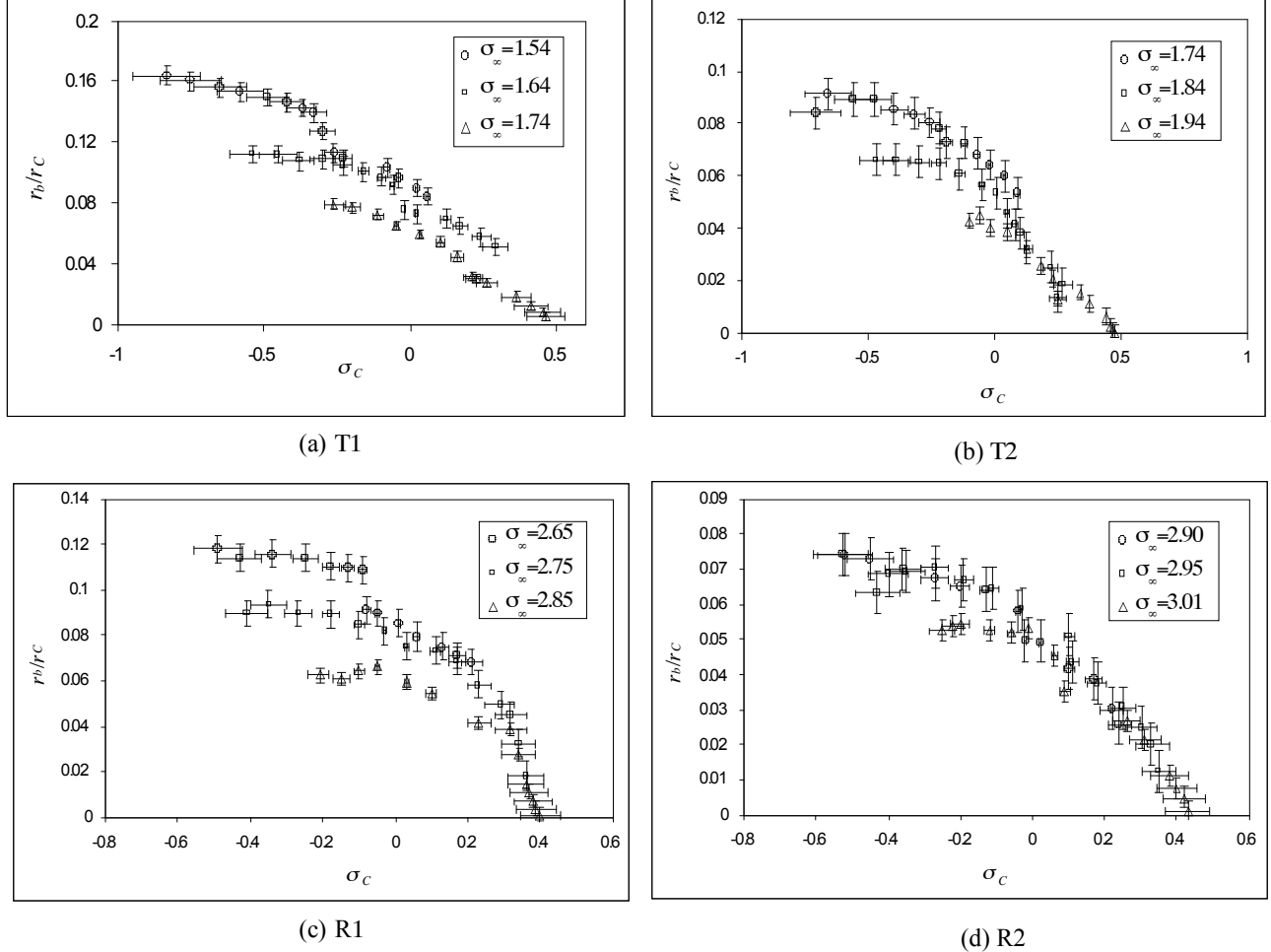


Figure 4: Average bubble radius as a function of the cavitation number at the vortex axis for varying freestream cavitation numbers; conditions are given in Table 1.

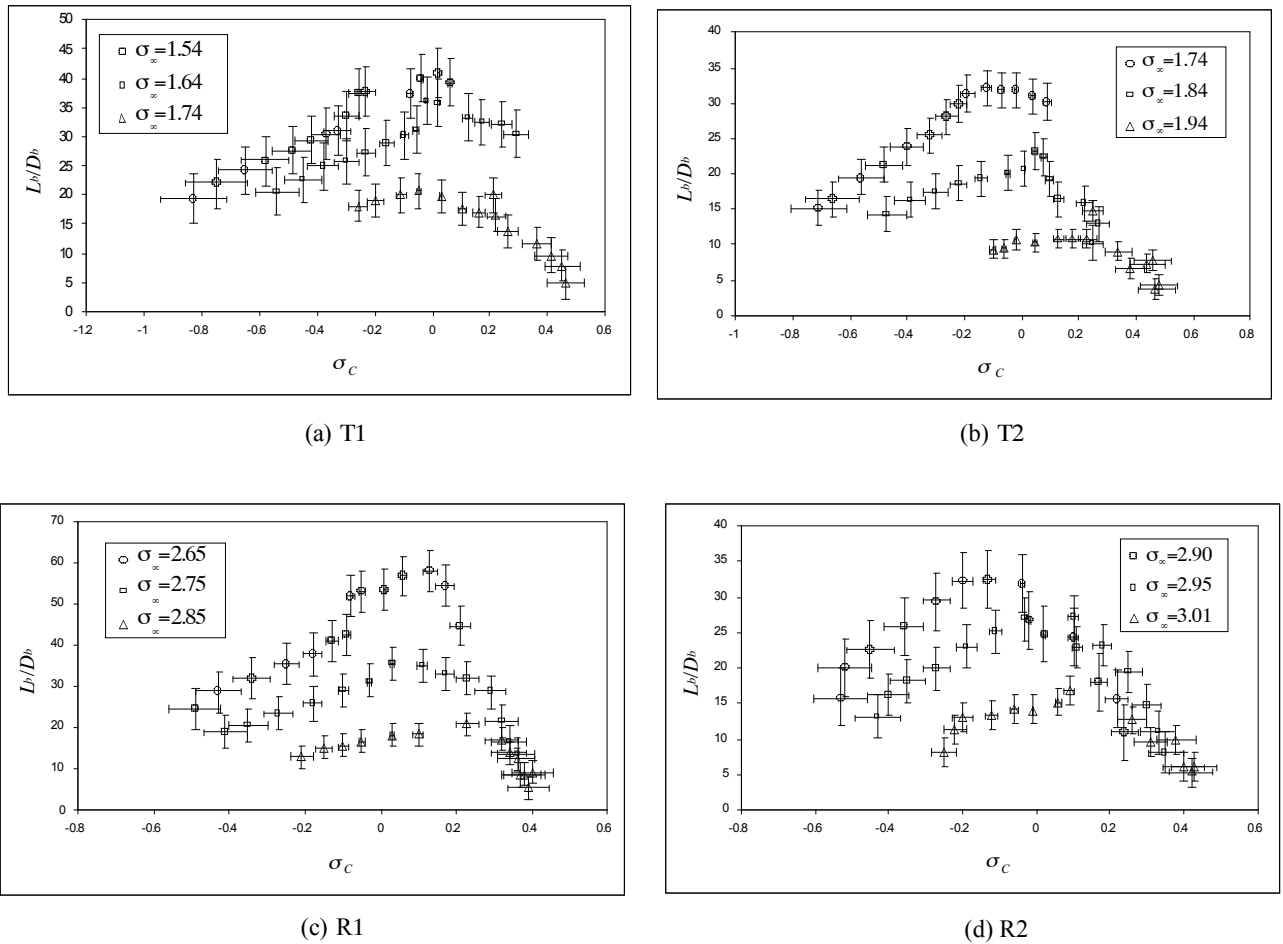


Figure 5: Average bubble aspect ratio as a function of the cavitation number at the vortex axis for varying freestream cavitation numbers; conditions are given in Table 1.

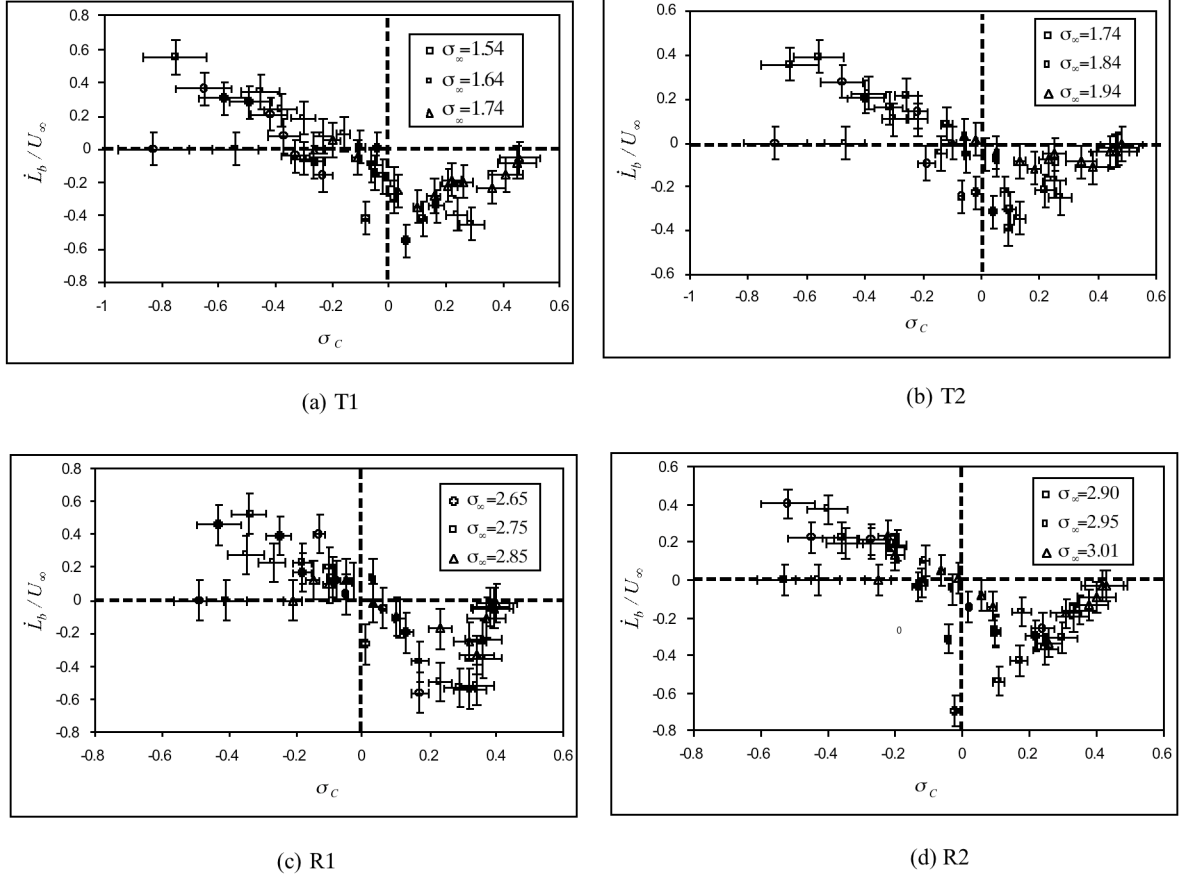


Figure 6. The rate of axial growth and collapse as a function of the cavitation number at the vortex axis for varying free-stream cavitation numbers; conditions are given in Table 1.

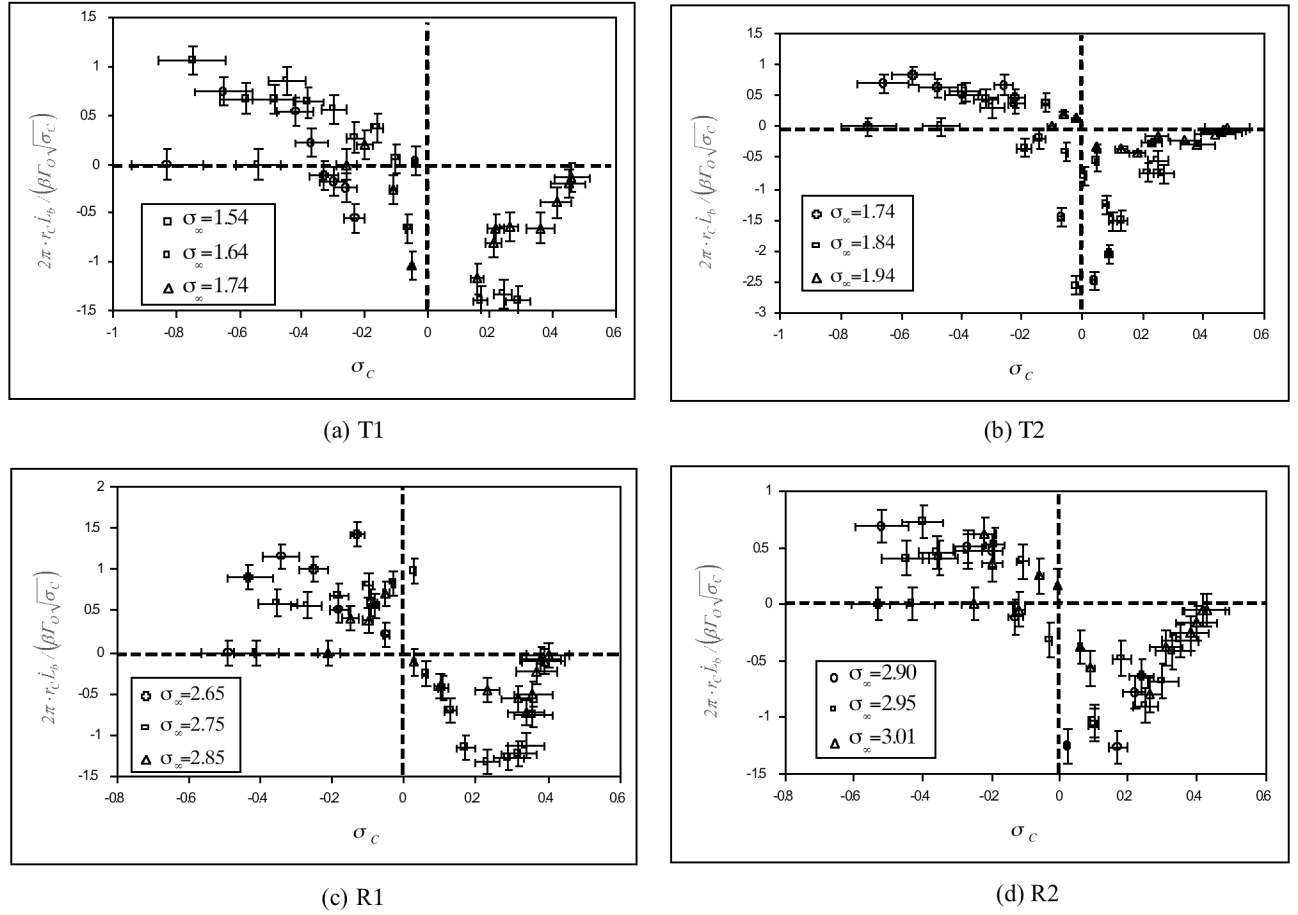


Figure 7. The scaled rate of axial growth and collapse as a function of the cavitation number at the vortex axis for varying freestream cavitation numbers. Conditions are given in Table 1.

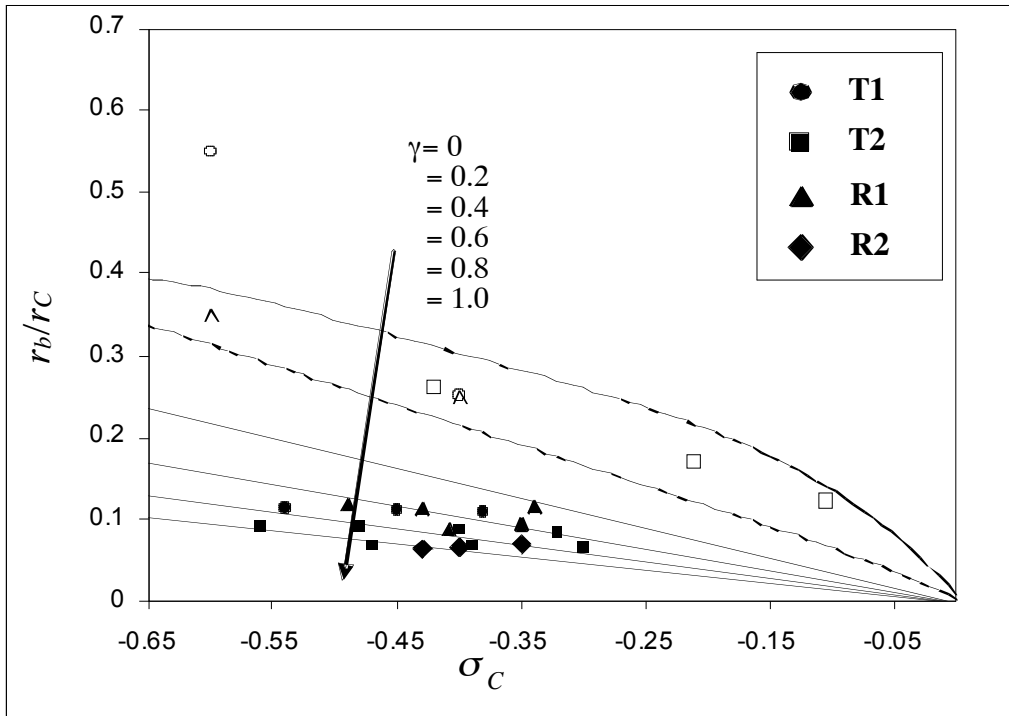
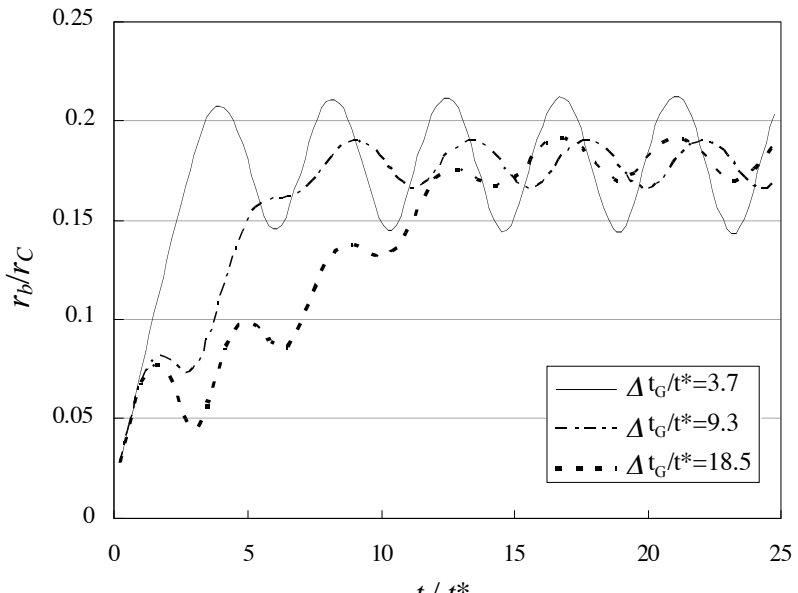
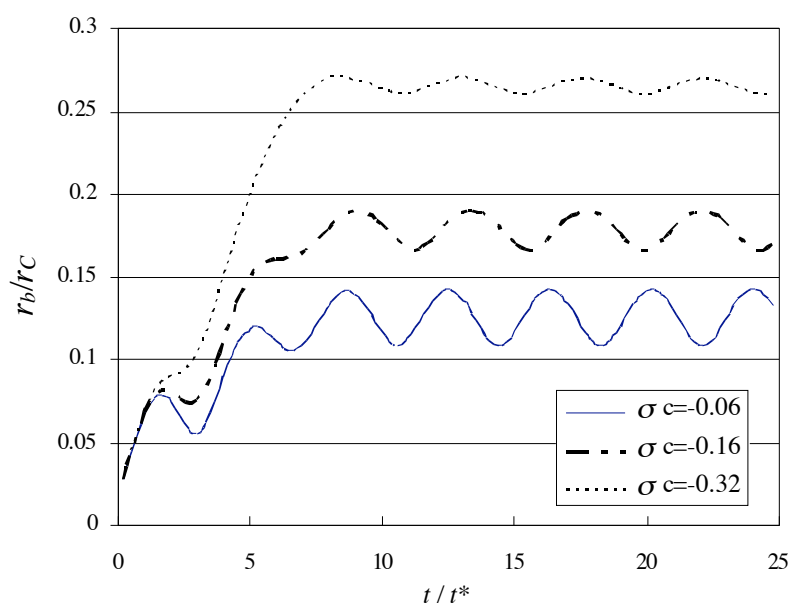


Figure 8. r_b/r_C plot for single vortex, counter-rotating vortex, 2-D simulation in the domain of equilibrium bubble radius. Solid line shows two dimensional bubble simulation results at equilibrium status with various flow modification factor (γ) in the Gaussian vortex; DF_UNCLE© simulation: $Re_f = 2 \times 10^5$ (O), 4×10^5 (\triangle) and two dimensional bubble simulation (\square)

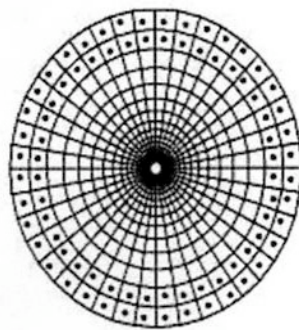


(a) $\sigma_C = -0.16$

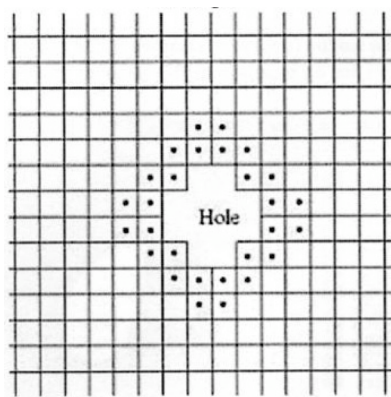


(b) $\Delta t_G/t^* = 9.3$

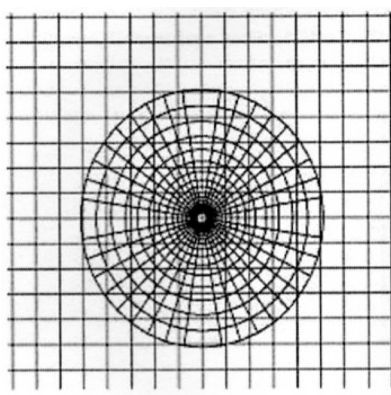
Figure 9. Two-dimensional transient bubble simulation with assumption of cylindrical bubble shape; $t^* = r_C / \sqrt{\Delta P / \rho}$ where ΔP is pressure drop due to vortex, $Re_T = 2 \times 10^5$, $r_C = 4\text{mm}$ where $Re_T = \Gamma_O / \nu$; (a) $\sigma_C = -0.16$ (b) $\Delta t_G/t^* = 9.3$.



Sub grid

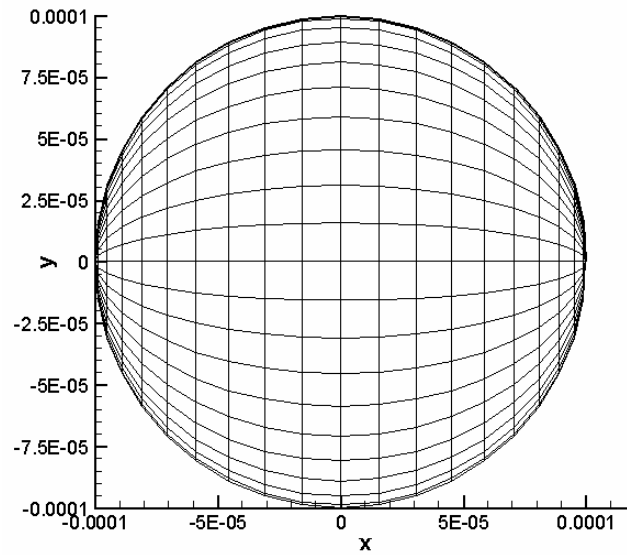


Global grid

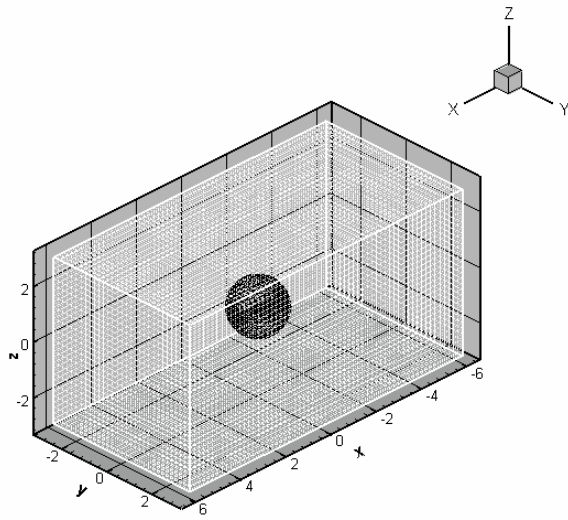


Overall grid

Figure 10. Two-dimensional illustration of a chimera grid system and localization of the hole and of overlap points marked with solid dot. (Hsiao *et al.* 2004)

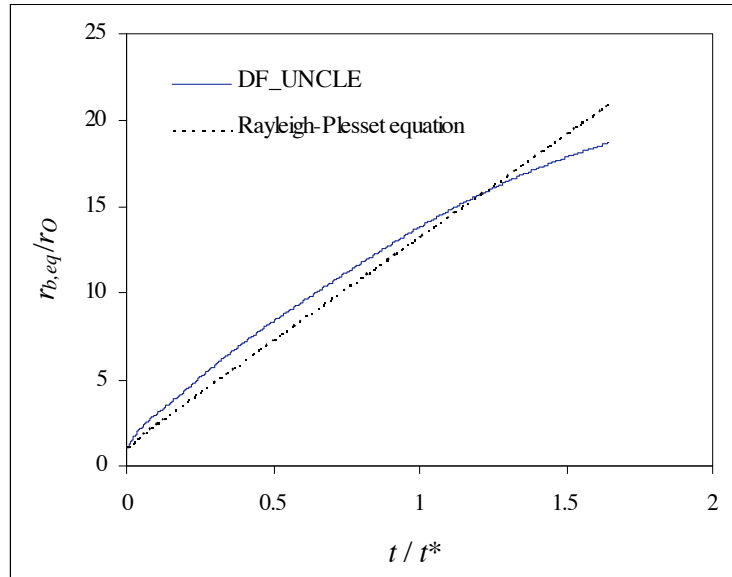


(a) Spherical grid

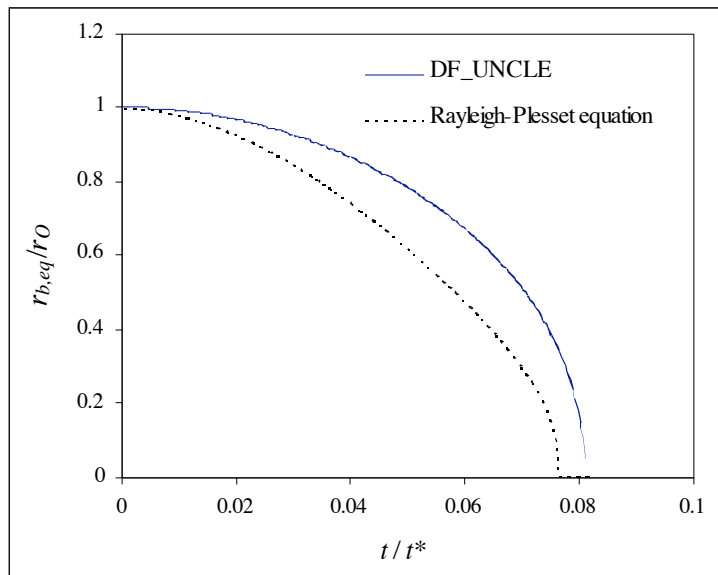


(b) Global grid

Figure 11. Grid domain used in the simulations; A total of 41x21x21 grid points are specified to generate the spherical type grid in which 41 by 21 grid points are used on the bubble surface. For the rectangular pipe grid, a total of 61x31x 31 grid points are used.

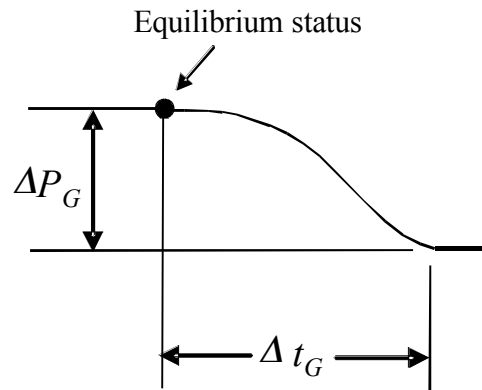


(a) Growing process

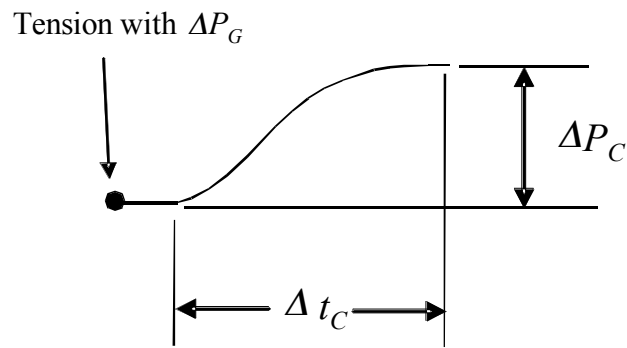


(b) Collapsing process

Figure 12. Comparison of bubble radius between the current code and the analytical solution of Rayleigh-Plesset equation for near spherical bubbles ($L_b/D_b < 1.5$) ; $t^* = r_C / \sqrt{\Delta P / \rho}$ where ΔP is pressure drop due to vortex, $Re_r = 4 \times 10^5$, $r_C = 6\text{mm}$ (a) $R_o = 100\mu\text{m}$, $P_C = -2.5\text{kPa}$ (b) $P_C = 35\text{kPa}$, $r_{b,eq,0}/r_C = 0.3$



(a) Growing simulation



(b) Collapsing simulation

Figure 13. Pressure time history in the simulation starting with equilibrium status for growing simulation. ΔP_G is pressure depression for growth and ΔP_C is pressure rise for collapse with growth time (Δt_G) and collapse time (Δt_C).

Δt_G	Re_Γ	
	$2 \cdot 10^5$	$4 \cdot 10^5$
2msec	$2 \cdot \sigma_C$	$2 \cdot \sigma_C$
5msec	$2 \cdot \sigma_C$	$2 \cdot \sigma_C$

(a) Growing process

Δt_C	Re_Γ	
	$2 \cdot 10^5$	$4 \cdot 10^5$
2msec	$2 \cdot \sigma_C$	$3 \cdot L_b/D_b$
5msec	$2 \cdot \sigma_C$	$3 \cdot L_b/D_b$

(b) Collapsing process

Table 2: Test matrix of three-dimensional bubble simulation by using DF_UNCLE[©] (a) Growing process (b) Collapsing process; $\sigma_C = (P_C - P_v)/(\rho u_{\theta, \max}^2/2)$, $Re_\Gamma = \Gamma_0/\nu$. P_C is pressure at the vortex core at infinite time and P_v is vapor pressure.

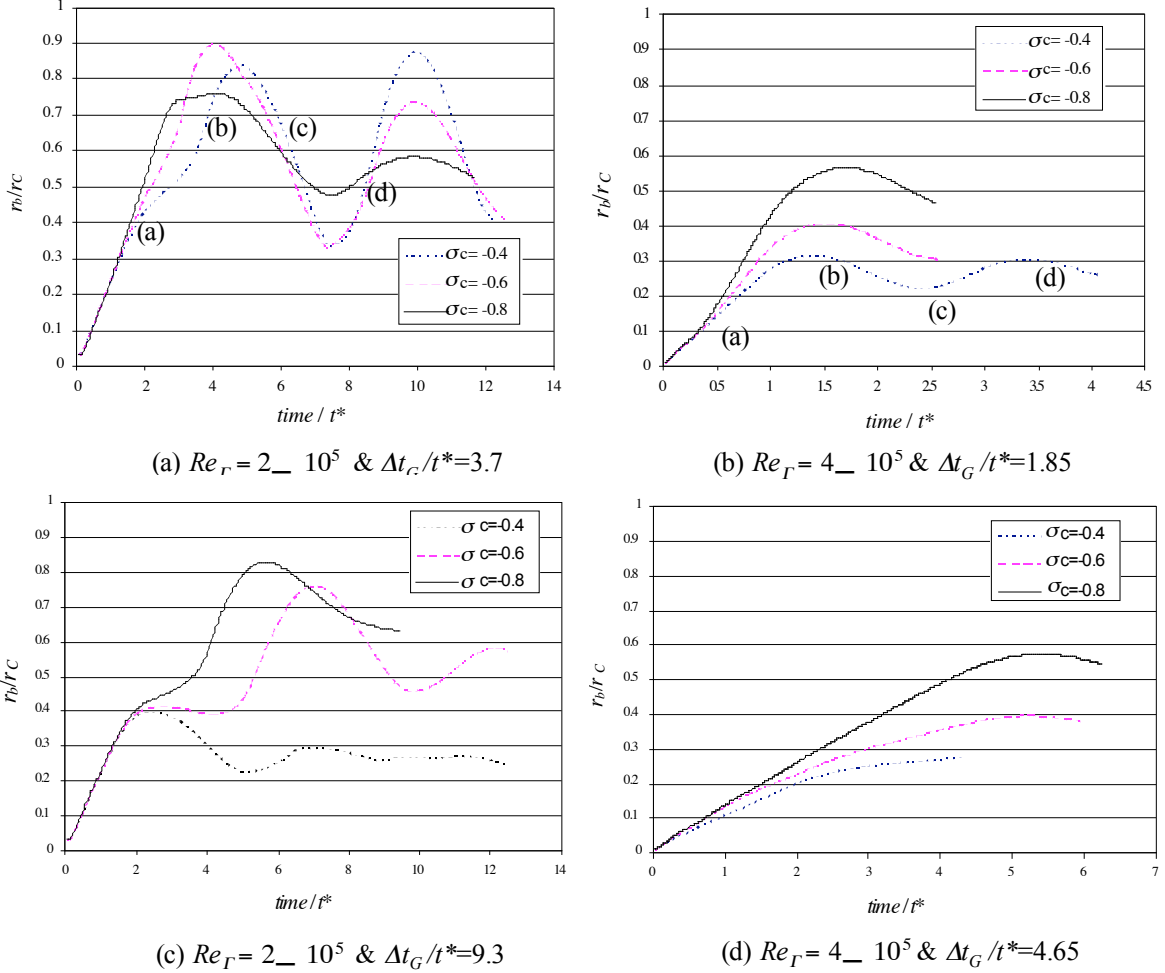
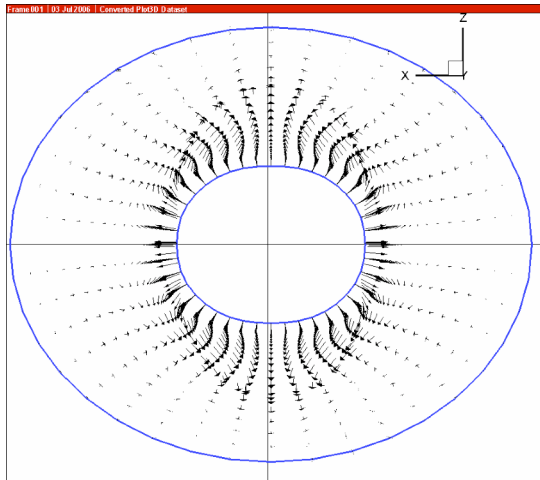
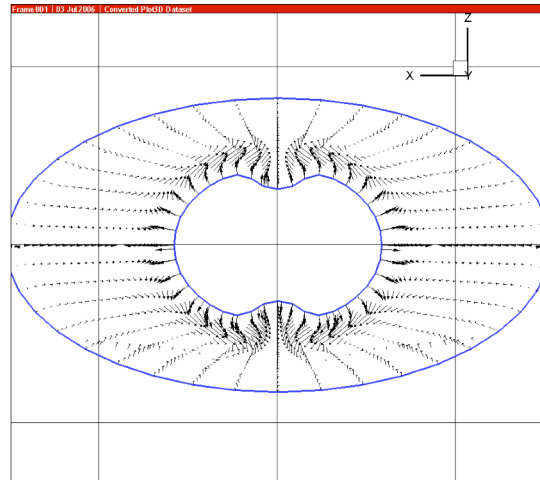


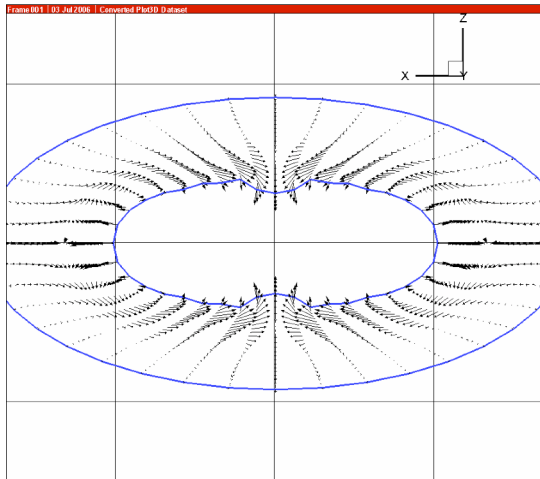
Figure 14. Bubble radius normalized by vortex core radius during growing process with various Reynolds number and growth time for prescribed tension, time is normalized with $t^* = r_C / (\Delta P / \rho)^{1/2}$, ΔP is pressure depression due to given vortex. r_b is defined from cylindrical assumption to have same bubble volume and length.



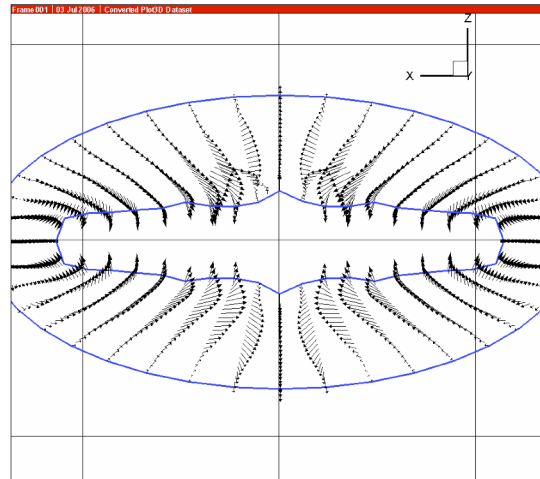
(a) $t/t^* = 2$



(b) $t/t^* = 4$



(c) $t/t^* = 6$



(d) $t/t^* = 8$

Figure 15. History of simulated bubble geometry during growing with velocity field; $Re_F = 2 \times 10^5$, $\sigma_C = -0.4$ and $\Delta t_G/t^* = 3.7$. The four images correspond to the four times labeled in Figure 14 (a).

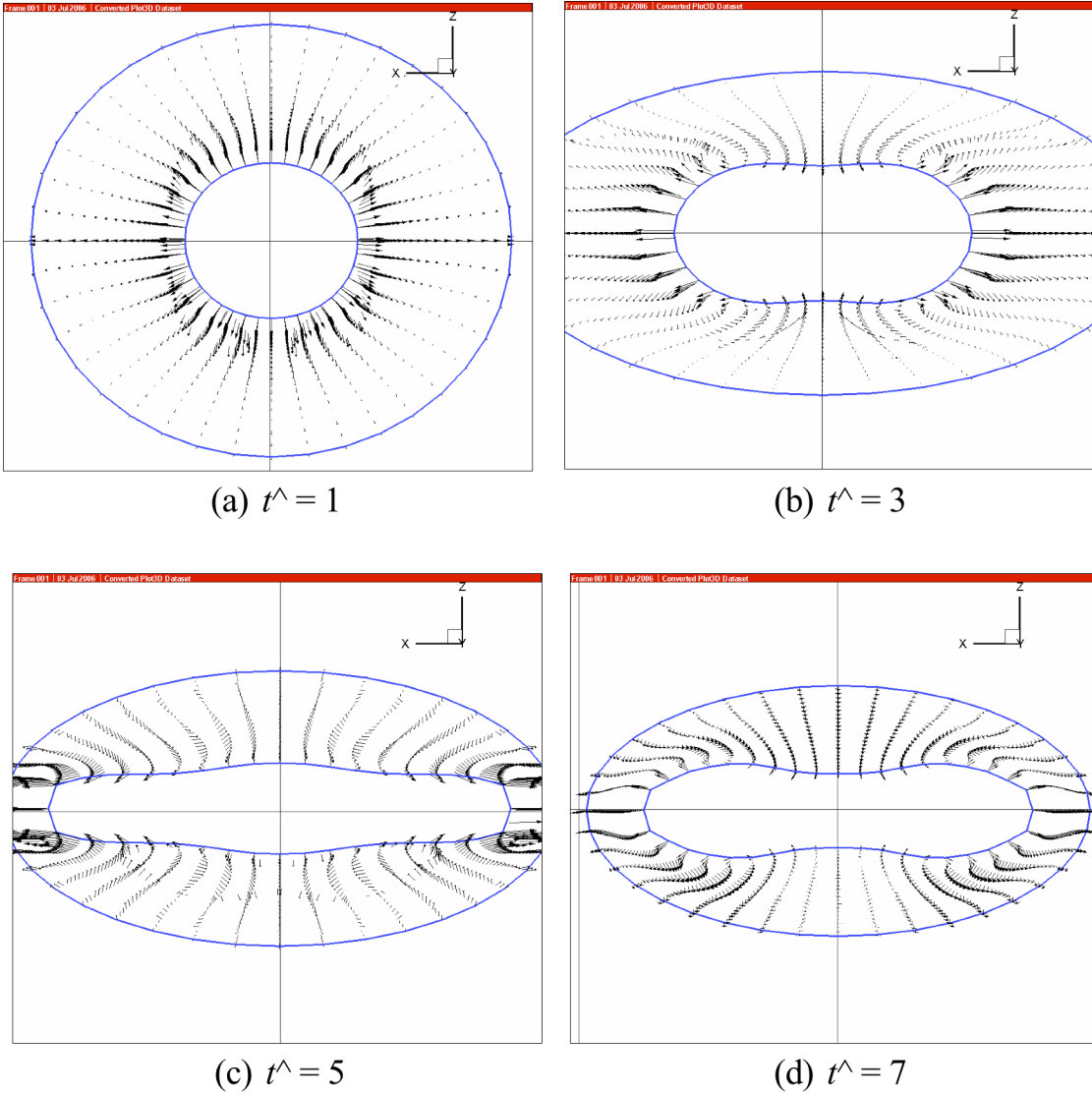


Figure 16. History of simulated bubble geometry during growing with velocity field; $Re_F=4\times 10^5$, $\sigma_C=-0.4$ and $\Delta t_G/t^*=1.85$. The four images correspond to the four times labeled in Figure 14 (b).

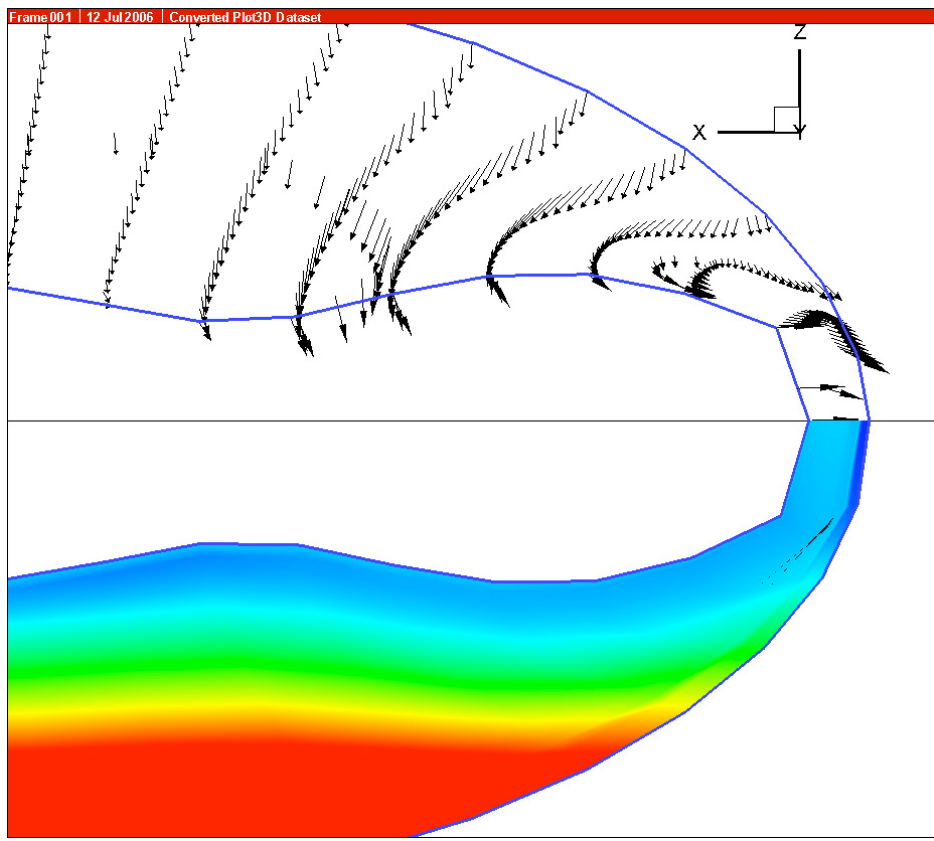
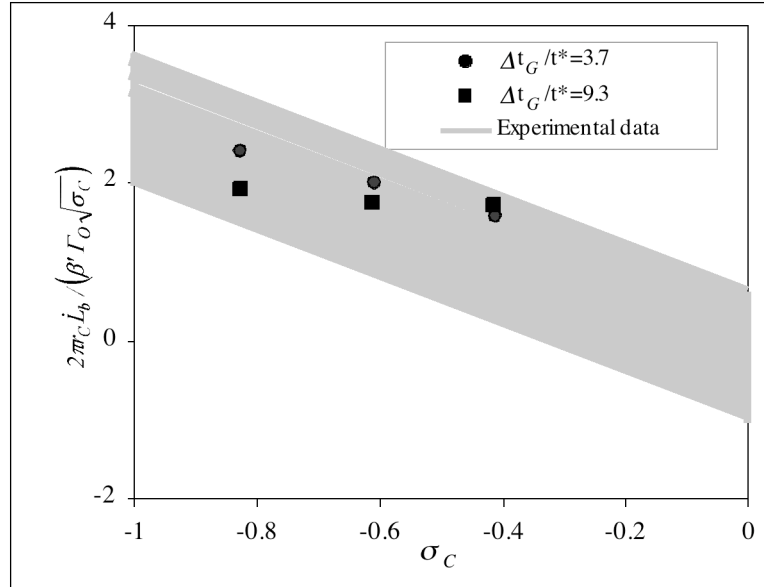
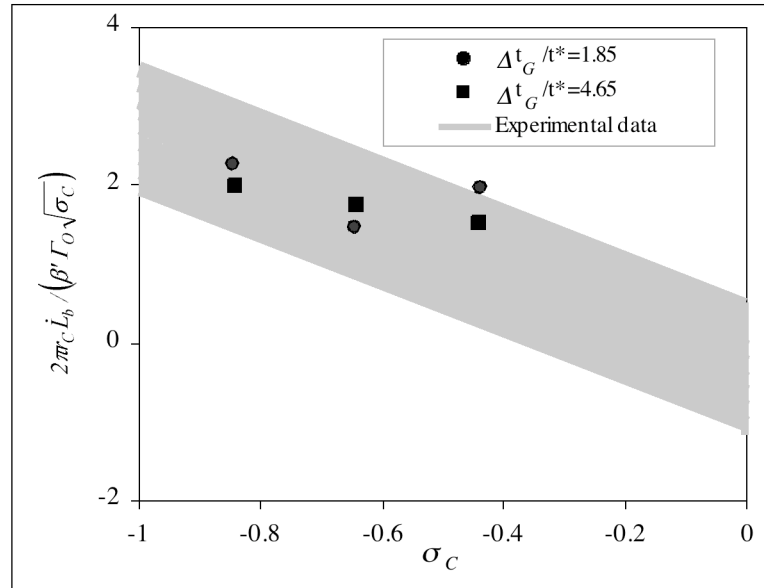


Figure 17. Close up of the velocity and pressure field of the bubbles; $t/t^* = 8$, $Re_F = 4 \times 10^5$, $\sigma_C = -0.4$



(a) $Re_F = 2 \times 10^5$



(b) $Re_F = 4 \times 10^5$

Figure 18. The scaled ratio of bubble growth ratio in the axial direction as a function of the cavitation number at the vortex axis with various growth time with prescribed tension. Compared with experimental data in the flow with axial pressure gradient.

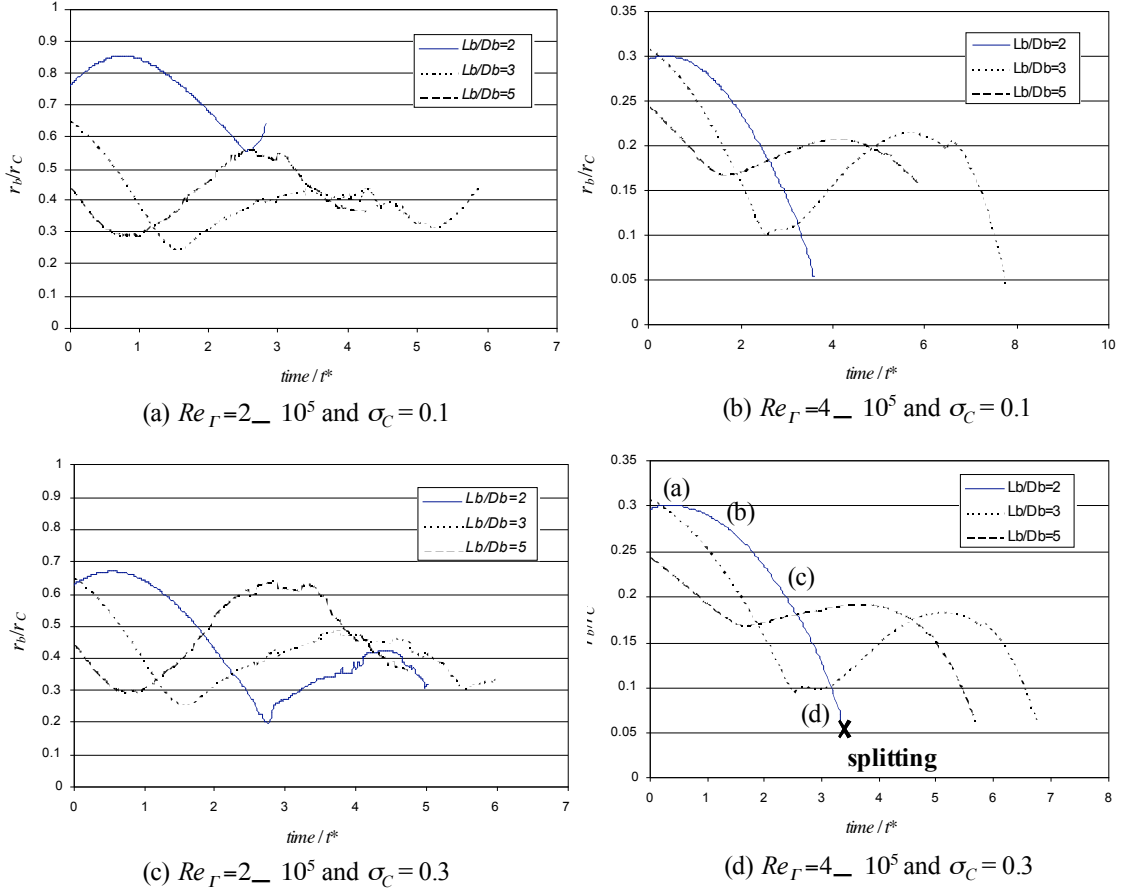
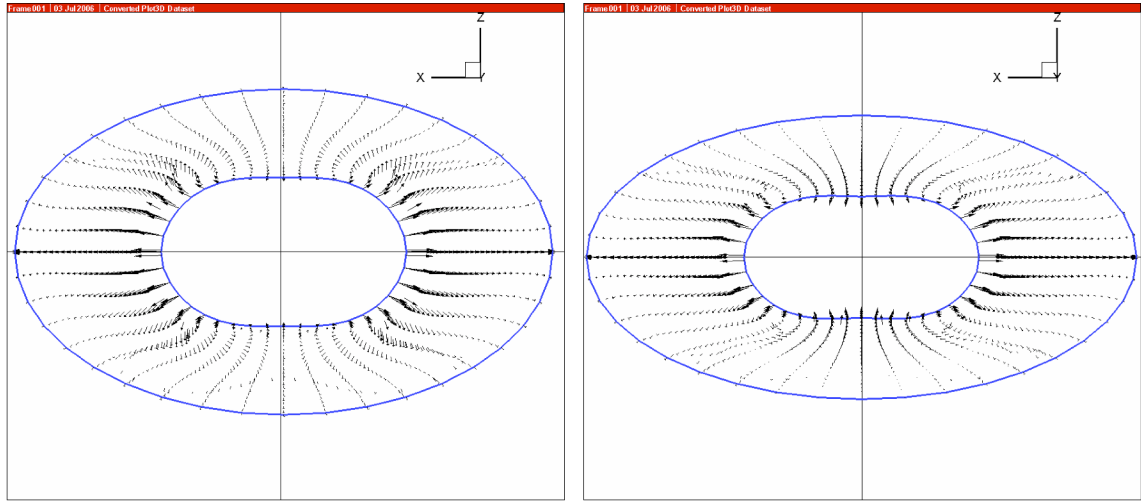
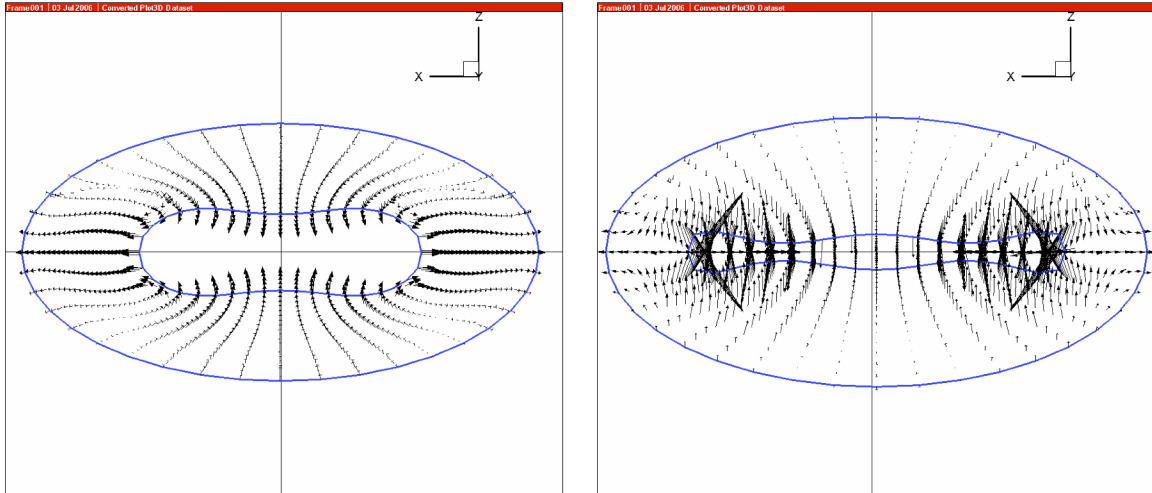


Figure 19. Bubble radius normalized by vortex core radius during collapsing process with various aspect ratio and Reynolds number; $\sigma_C = 0.1$ and 0.3 & $\Delta t_G/t^*=3.7(Re_F=2\times 10^5)$ and $1.85(Re_F=4\times 10^5)$, time is normalized with $t^*=r_C/(\Delta P/\rho)^{1/2}$, ΔP is pressure depression due to given vortex. r_b is defined from cylindrical assumption to have same bubble volume and length.



(a) $t/t^* = 1$

(b) $t/t^* = 2$



(c) $t/t^* = 4$

(d) $t/t^* = 6$

Figure 20. History of simulated bubble geometry with velocity field; $Re_F=4\times 10^5$, $\sigma_C=0.3$, $L_b/D_b = 2$. The four images correspond to the four times labeled in Figure 19 (d).

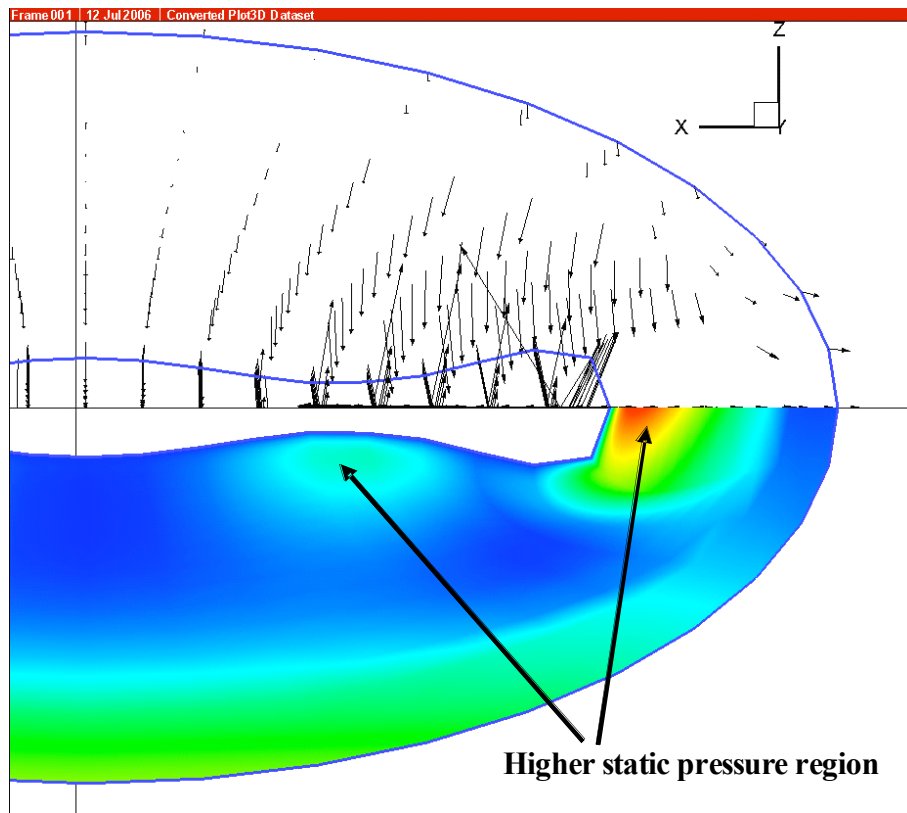


Figure 21. Close up of the velocity and pressure field of the bubbles during splitting; $t/t^* = 6$, $Re_T = 4 \times 10^5$, $\sigma_C = 0.3$, $L_b/D_b = 2$

Effect of Unsteady Turbulent Fluctuations on Vortex/Vortex/Nuclei Interaction

C.-T. Hsiao and G. L. Chahine
(DYNAFLOW, INC., USA)

ABSTRACT

Vortex/vortex interaction between the tip-leakage vortex and the trailing-edge vortex in a ducted propulsor was studied using direct numerical simulation of the Navier-Stokes equations. A reduced computational domain was used with boundary and initial conditions provided by a RANS solution. In addition, turbulence-like random velocity fluctuations were imposed at the inlet boundary of the computational domain to take into account upstream turbulent fluctuations. Computations with different fluctuation levels were conducted and their effects on the vortex/vortex interaction and on the resulting time-varying minimum pressure and its location were compared. The effect of the resulting unsteady flow field on bubble dynamics and on the initiation of cavitation events was also investigated using a computational model which integrated a discrete multiple bubble dynamics and the unsteady Navier-Stokes flow solver. The resulting predicted cavitation inception indices and cavitation inception locations in the ducted propulsor flow field were found in very good agreement with the experimental observations.

1. Introduction

Ducted propulsors, waterjets and pumps produce a tip-leakage vortex in addition to the trailing-edge vortex found on conventional open propellers. Recent experimental observations of cavitation inception on such a ducted propulsor (Chesnakas and Jessup 2003) have indicated that the interaction between the two vortices may cause cavitation inception to occur in the region where the two vortices merge much farther downstream than usually observed on open propellers. However, predictions of cavitation inception using the pressure field either obtained by Reynolds-Averaged Navier-Stokes (RANS) computations (Kim 2002, Brewer et al. 2003, Yang 2003) or inferred from experimental velocity field measurements (Oweis *et al.* 2003) are in poor agreement with the experimental observations in terms

of both the cavitation inception number and the inception location. One main reason for the discrepancy stems from the interaction of the highly unsteady vortical structures emanating from the blades, and which are not adequately captured by an averaging (time and space) numerical method such as RANS.

In a previous study (Hsiao and Chahine, 2004), we demonstrated that predictions can be significantly improved when the interaction between the vortical structures is better captured using a direct numerical simulation of the Navier-Stokes equations in the region of interest. The description of the instantaneous and local variations of the physical quantities in the flow field of the two interacting vortices (leakage vortex and tip vortex) was achieved in a reduced domain and the bubble dynamics effects were taken into account. The boundary conditions were used to match the reduced domain solution to the RANS solution. The predicted cavitation inception number and the location of the inception were found to agree much better than previous numerical studies with the experimental measurements. Although the improvements were significant, the predicted location of cavitation inception was still farther upstream than that observed in the experiments and did not vary much over time contrary to the observations which showed a large regions where incepting cavitation events occurred intermittently.

The present communication improves on the previous work by including important features stemming from the inclusion of incoming unsteady flow field fluctuations from the upstream flow field. While any unsteadiness of the flow field due to the vortex/vortex interaction can be resolved by the direct numerical simulation, the turbulence fluctuations entering the computational domain are inherently filtered out when the RANS solution is applied at the inlet boundary. To investigate the importance of unsteady velocity and pressure fluctuations as well as vortex wandering on the results, the magnitude of the

velocity components and the location of the two vortices were made to vary in time at the entrance of the computational domain in manners similar to experimental observations. To do so, random fluctuations with realistic characteristic amplitudes and frequencies were imposed. Based on existing PIV and laser anemometry experimental observations, the locations of the tip-leakage and trailing-edge vortices at the restricted domain entrance were oscillated around their averaged positions with various amplitudes and frequencies within the range of the measured values. Similar fluctuations were imposed on the transverse and longitudinal velocities.

Realistic bubble nuclei distribution were also propagated through the computed unsteady flow field and occurrence of cavitation events was monitored using DF_MULTI_SAP[®], a nuclei tracking and multiple bubble dynamics code that we developed to study cavitation inception and noise generation (Hsiao and Chahine, 2005, Chahine, 2004).

2. Numerical Approach

2.1 Reduced Computational Domain

As a continuation of the numerical study of Hsiao and Chahine (2004) of the flow field around a rotating ducted propulsor, the present study also considers the NSWCCD Propeller 5206. This ducted propulsor has three blades with a constant chord of 0.3812m from hub to tip and a tip diameter of 0.8503m, and operates in a duct having a diameter of 0.8636m. The detailed propulsor geometry and experimental observations can be found in Chesnaks and Jessup (2003) and Oweis *et al.* (2003). Several numerical studies (Kim 2002, Brewer *et al.* 2003 and Yang 2003) used RANS codes to obtain the flow field for this propulsor under the same operating conditions of an advance coefficient, $J=0.98$, and an inflow velocity, $U_\infty = 6.96 \text{ m/s}$. This results in a Reynolds number based on the blade tip radius and the inflow velocity equal to $\text{Re} = 3 \times 10^6$.

To improve the numerical solution from the RANS computations, we constructed a reduced computational domain behind the trailing edge of the propulsor blade that included the region of interaction of the two vortices. The basic computational domain had a square cross area of $0.094\text{m} \times 0.094\text{m}$ and extended to a downstream location 0.34 m from the tip trailing edge. Figure 1 illustrates the location of this reduced computational domain relative to the ducted propulsor.

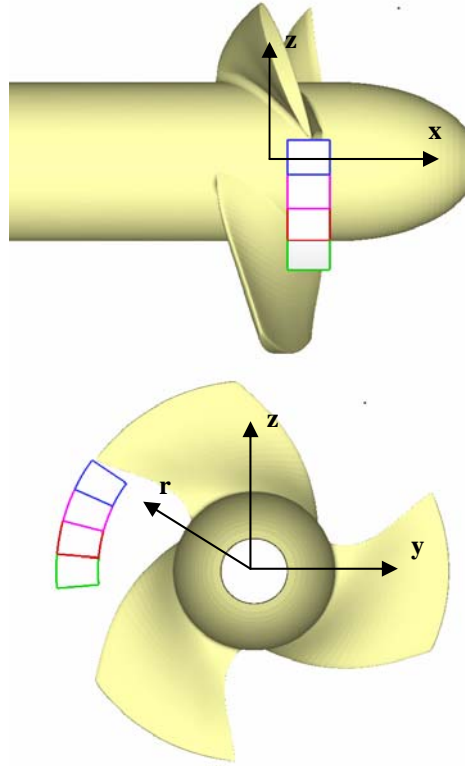


Figure 1. A view of the reduced computational domain used in the current computations.

2.2 Navier-Stokes Computations

For the study of vortex/vortex interaction in the reduced domain, the flow is obtained via direct numerical simulation of the Navier-Stokes equations without any turbulence modeling. Since the computations are conducted in a rotating frame attached to the propeller blade, steady-rotating reference frame source terms, *i.e.* the centrifugal force and the Coriolis force terms, are explicitly added to the momentum equation. The resulting unsteady incompressible continuity and Navier-Stokes equations written in non-dimensional vector form and Cartesian notations are given by:

$$\nabla \cdot \mathbf{u} = 0, \quad (1)$$

$$\frac{D\mathbf{u}}{\partial t} = -\nabla p + \frac{1}{R_e} \nabla^2 \mathbf{u} + \Omega^2 \mathbf{r} - 2\Omega \times \mathbf{u}, \quad (2)$$

where $\mathbf{u} = (u, v, w)$ is the velocity, p is the pressure, \mathbf{r} is the radial position vector, and Ω is the angular velocity. $R_e = \rho u^* L^* / \mu$ is the Reynolds number, with u^* and L^* being the characteristic velocity and length. ρ is the liquid density and μ is its dynamic viscosity. In the current numerical simulation, the characteristic velocity and length are chosen to be the inflow velocity, $U_\infty = 6.96 \text{ m/s}$, and

the propeller tip radius, $R_{\text{tip}} = 0.425\text{m}$, respectively. This results in a characteristic time equal to 0.06 sec.

To solve Equations (1) and (2) numerically, a three-dimensional incompressible Navier-Stokes solver, DF_UNCLE, developed by the Mississippi State University (Vanden and Whitfield, 1993) and modified by DYNAFLOW for cavitation studies is exercised. DF_UNCLE is based on the artificial-compressibility method (Chorin 1967) in which a time derivative of the pressure is added to the continuity equation as:

$$\frac{1}{\beta} \frac{\partial p}{\partial t} + \nabla \cdot \mathbf{u} = 0, \quad (3)$$

where β is an artificial compressibility factor. As a consequence, a hyperbolic system of equations is formed that is solved using a time marching scheme. This method can be marched in pseudo-time to reach a steady-state solution. To obtain a time-dependent solution, a Newton iterative procedure is performed at each physical time step in order to satisfy the continuity equation. In the present study the time-accurate solution was obtained when the maximum normalized velocity divergence was less than 1.0×10^{-3} . Detailed descriptions of the numerical scheme can be found in Vanden and Whitfield (1993).

2.3 Initial and Boundary Condition

Initial conditions for the direct numerical simulations of the Navier-Stokes equations in the reduced computational domain were deduced from the steady-state RANS solution of the full ducted propulsor flow obtained by Yang (2003). Figure 2 shows the pressure contours of the RANS solution at different streamwise locations. The unsteady computations reached a virtually steady-state solution when the inlet boundary condition was imposed to be the RANS mean flow solution. Figure 3 shows the converged solution. This solution was utilized as the initial condition for the numerical simulations shown below in which upstream unsteady turbulent fluctuations were imposed at the domain inlet.

Figure 4 illustrates the reduced computational domain and its boundaries: inlet and outlet boundaries, three side boundaries, and one shroud boundary bounded by the shroud wall. At the inlet boundary, the method of characteristics (MOC) was applied with the three components of the velocities specified. At the outlet boundary, all variables were extrapolated from the inner domain except for the grid points on the shroud wall where the initial values of the pressures were fixed. For the three side boundaries and the shroud boundary, both velocities and pressures were

imposed with the averaged flow solution obtained by the RANS computations.

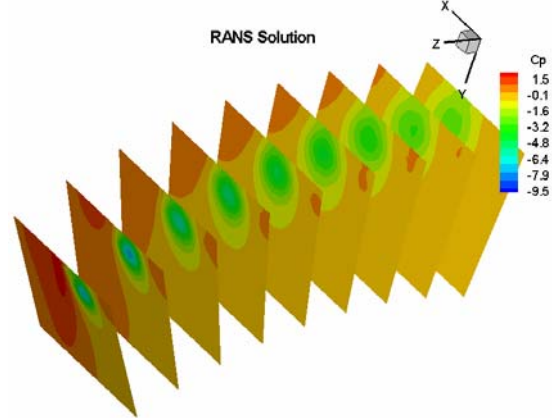


Figure 2. Pressure field in the reduced computational domain interpolated from the RANS solution.

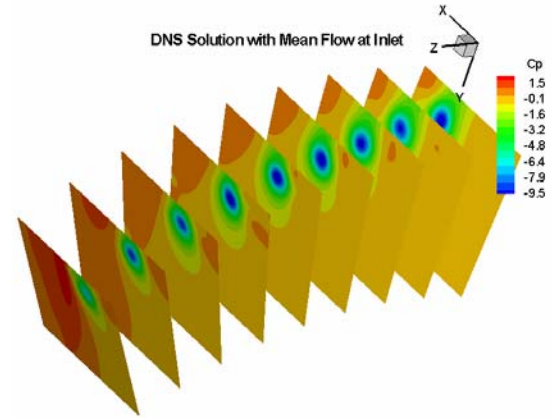


Figure 3. Converged unsteady pressure field solution using the direct solution of the Navier-Stokes in the reduced computational domain.

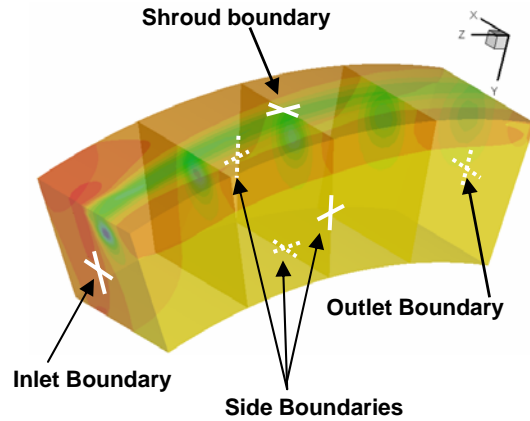


Figure 4. The reduced computational domain used for the direct solution of the Navier-Stokes equations.

To simulate the upstream turbulent fluctuations, the components of the velocity at the inlet boundary were made to vary in time and space about the RANS mean flow solution. This is achieved by superposing an unsteady fluctuating velocity field, \mathbf{u}' , onto the mean flow solution as:

$$\mathbf{u} = \bar{\mathbf{u}} + \mathbf{u}'(\mathbf{x}, t), \quad (4)$$

where $\bar{\mathbf{u}}$ is the velocity field obtained from the RANS computations and \mathbf{x} is the coordinate vector in the propulsor x - r plane. To better delineate the fluctuating velocity components at the inlet boundary, a “streamwise” velocity component, $u'_s(\mathbf{x}, t)$, was defined in the normal direction to the x - r plane. In addition a cross-stream component, $u'_x(\mathbf{x}, t)$ and a radial component, $u'_r(\mathbf{x}, t)$ were defined.

PIV measurements near the location of the inlet boundary conducted by Oweis *et al.* (2003) have revealed the presence of multiple vortices including the stronger primary tip-leakage vortex, and a secondary vortex, the trailing-edge vortex. The relative locations of these two main vortices in the x - r plane are shown in Figure 5 with the streamwise vorticity contours. It was observed that the primary vortex wanders in a circular fashion, while the secondary vortex wanders in an elliptical fashion. The unsteadiness of the velocity field was seen to be a combination of the vortex wandering and of randomly distributed velocity fluctuations, which have the highest magnitudes at the centers of the vortex regions.

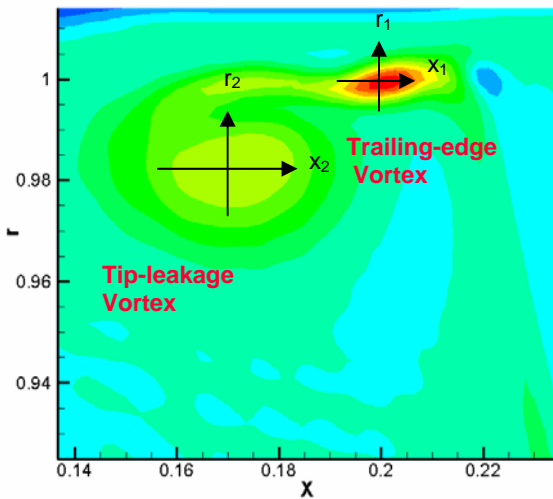


Figure 5. Relative locations of the tip-leakage vortex and the trailing-edge vortex illustrated with the streamwise vorticity contours in the x - r plane.

To numerically reproduce this unsteadiness, the field of unsteady velocity fluctuations was

constructed by superposing two fluctuation sources undergoing random wandering: one associated with the tip-leakage vortex and the other associated with the trailing-edge vortex. We utilized the following expressions for the unsteady velocity fluctuations. For simplicity, we show here the “streamwise” component only:

$$u'_s(\mathbf{x}, t) = A_{u1}g_1(\mathbf{x}, t)f_1(t) + A_{u2}g_2(\mathbf{x}, t)f_2(t), \quad (5)$$

where A_{u1} and A_{u2} are the amplitudes of the oscillations for the trailing-edge and the tip-leakage vortex respectively. $g_1(\mathbf{x}, t)$ and $g_2(\mathbf{x}, t)$ represent the spatial variations and have a Gaussian distribution form as follows:

$$g_j(\mathbf{x}, t) = e^{-\left(\frac{\|\mathbf{x}-\mathbf{x}_{oj}(t)\|}{a_j}\right)^2}, \quad j=1, 2. \quad (6)$$

a_j is vortex core radius (a_1 for trailing-edge vortex and a_2 for tip-leakage vortex). $\mathbf{x}_{oj}(t)$ is the instantaneous location of each vortex center in the x - r plane. To simulate the wandering of the vortex center, $x_{oj}(t)$ and $r_{oj}(t)$ are defined by:

$$x_{oj}(t) = x_{oj}(0) + A_{xj} \sum_{i=1}^n \sin(2\pi\omega_i t + 2\pi\phi(\omega_i)), \quad (7)$$

$$r_{oj}(t) = r_{oj}(0) + A_{rj} \sum_{i=1}^n \sin(2\pi\omega_i t + 2\pi\phi(\omega_i)),$$

where $x_{oj}(0)$ and $r_{oj}(0)$ are the initial coordinates of the vortex center. A_{xj} and A_{rj} are the amplitudes of the wandering, ω_i is the motion frequency, and $\phi(\omega)$ is a phase shift randomly selected between 0 and 1.

In the PIV measurements, the tip-leakage vortex was seen to wander in a circular pattern about the mean location. The standard deviation of the distance of the vortex center from the mean location was measured to be about one vortex core size near the trailing edge. Although multiple secondary vortices were identified in the PIV measurements, the strongest one identified as the trailing-edge vortex was observed to wonder in an elliptical pattern. Figure 6 shows the loci of the vortex centers obtained by specifying $A_{x1}=4a_1$ and $A_{r1}=a_1$ for the trailing-edge vortex and $A_{x2}=a_2$ and $A_{r2}=a_2$ for the tip-leakage vortex with 50 frequencies ranging from 1 to 10 Hz.

In addition to the spatial variations, Equation (5) also includes a temporal variation, $f(t)$, which is composed of N_t different frequencies, ω_i , with phase lag $\phi(\omega_i)$ randomly distributed between 0 and 1. $f(t)$ has the following form:

$$f_j(t) = \frac{1}{A_t} \sum_{i=1}^{N_t} \sin(2\pi\omega_i t + 2\pi\phi_j(\omega_i)), \quad (8)$$

where A_t is a factor to ensure that the fluctuation function takes a unit value at the highest amplitude of oscillations. For the current simulations, 100 different

frequencies ranging from 1 to 100 Hz were applied. To ensure that the shortest temporal fluctuations can be well resolved, a time step size of 0.5 ms was used in the real time marching. This allows the numerical simulations to have 20 time steps for the shortest oscillation period.

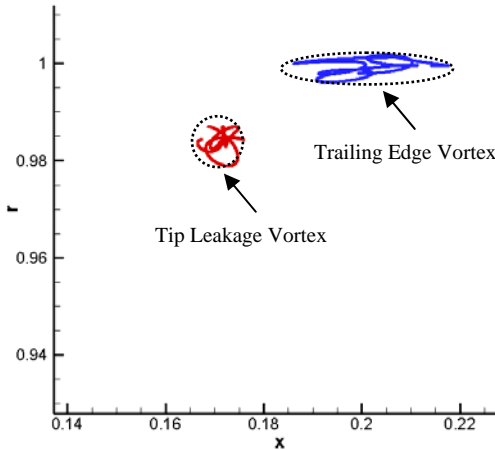


Figure 6. The loci of the trailing-edge and tip-leakage vortices centers during wandering simulated using Equation (7).

2.4 Bubble Dynamics Models

To investigate the effect of the unsteady vortex/vortex interaction flow field on bubble dynamics and cavitation occurrence a multiple bubble dynamics and trajectory model, DF_MULTI_SAP[®], was integrated with DF_UNCLE and unsteady computations were conducted. In DF_MULTI_SAP[®] the bubble transport is modeled via the motion equation described by Johnson and Hsieh (1966) while the bubble dynamics is simulated by solving a surface Averaged Pressure (SAP) Rayleigh-Plesset equation (Hsiao and Chahine, 2003ab). In this numerical approach, each bubble is tracked in the flow field by a Lagrangian scheme, which combines the RANS solution and the DNS solution by oversetting the grids of the reduced domain on the overall propulsor grids. As a bubble is released upstream of the reduced domain the flow field from the RANS solution is used. Once the bubble enters the reduced domain, the flow field obtained from the direct Navier-Stokes simulation method is applied.

3. Results and Discussion

3.1 Grid and Domain Size Independence Study

The simulation of vortex/vortex interaction in the reduced computational domain was conducted with the turbulence model turned off. Hsiao and Chahine (2004) showed a significant improvement in the prediction of the pressure field using the direct

numerical simulation with the RANS mean flow inlet boundary condition when a fine grid was used. The grid-independence study for this reduced domain indicated that the grid size needed to be at least 3 mm in the streamwise direction and 0.5 mm in both cross directions to get a good grid resolved solution. Figure 7 shows the fully developed cavitating vortex core experimentally observed by Chesnaks and Jessup (2003) at a cavitation number, $\sigma = 5.6$, and the numerical predictions of vortex core obtained by RANS and DNS and illustrated with iso-pressure surfaces at $C_p = -5.6$.

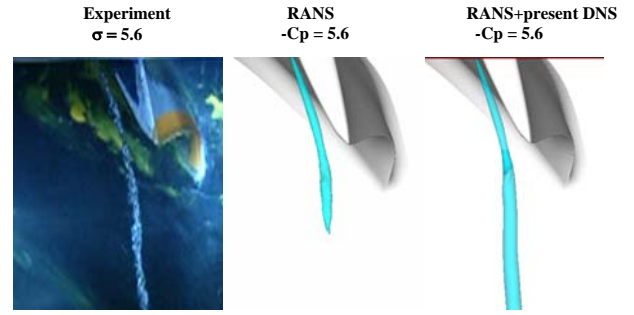


Figure 7. Comparison of the fully developed cavitation in the vortex core at $\sigma = 5.6$ (Chesnaks and Jessup 2003) and the numerical predictions of vortex core obtained by RANS and DNS and illustrated with iso-pressure surfaces at $C_p = -5.6$.

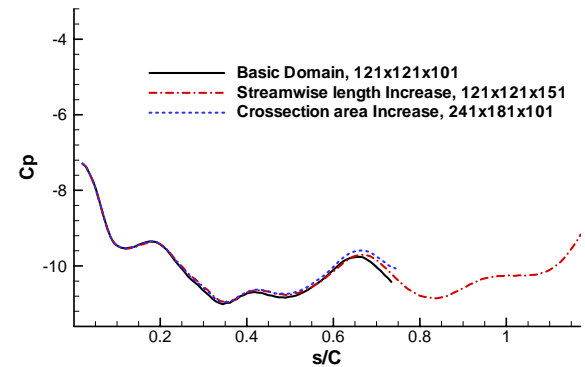


Figure 8. Comparison of the pressure coefficient variations along the vortex line center between two streamwise grid resolutions for the basic computational domain.

We further investigated the effect of the computational domain size on the solution. Two much larger computational domains with the same grid resolution were constructed. One was obtained by doubling the domain length in the x direction and extending it 50% of the length in the radial r direction. The second computational domain was

constructed by extending by 50% the length in the streamwise direction. The resulting pressure coefficients of the two larger computational domains were compared to those of the basic domain. Figure 8 shows the pressure coefficients along the primary vortex center versus the streamwise location, s/C , where s is the arc distance from the tip trailing edge and C is the blade chord length. It is seen that the solution changed only slightly (less than 1%) between the three cases.

3.2 Effect on Vortex/Vortex Interaction

To study the effects of the upstream unsteady fluctuations on the vortex/vortex interaction, added fluctuations to the mean velocity at the inlet boundary were imposed. In Figure 9, the amplitude of the fluctuations was specified to be 10% of U_∞ for all components of the fluctuating velocity. To illustrate the structure of the vortices and their unsteady interaction, iso-surfaces of the streamwise vorticity at $\omega_s=240$ are plotted for five time steps and are shown in Figure 9. It is seen that the trailing-edge vortex wraps around the tip-leakage vortex without merging with it immediately behind the blade trailing edge. Time sequence animations reveal highly unsteady interactions between the two vortices. It is seen that the trailing-edge vortex breaks from time to time into disconnected filaments or separated regions of high vorticity.

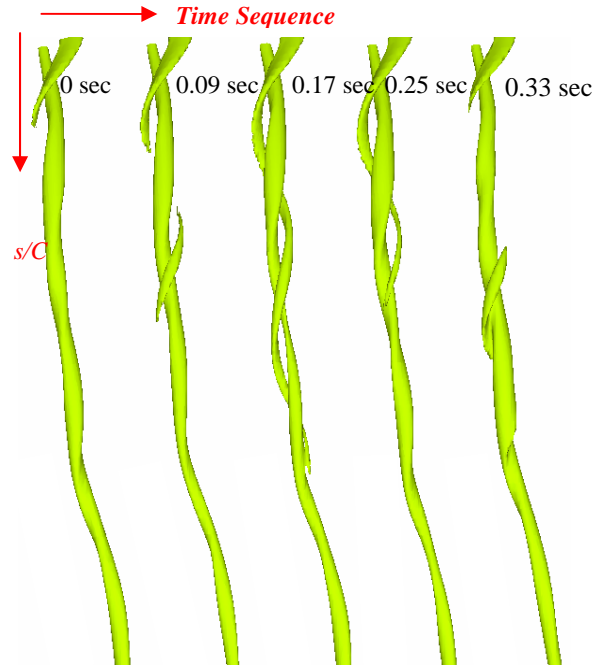


Figure 9. Tip-leakage vortex and trailing-edge vortex illustrated with iso-surfaces of the streamwise vorticity at $\omega_s=240$ for five different time steps.

Another way to illustrate the effects of the unsteady fluctuations on the vortex/vortex interaction is to track the pressure coefficient, C_p , along a vortex centerline in the streamwise direction. Figure 10 shows such C_p curves at five time steps. These correspond to the iso-surfaces of streamwise vorticity shown in Figure 9. We can clearly see that the minimum pressure location shifts over time erratically between $s/C = 0.35$ and 0.8 . The numerical simulation was continued until 0.5 s which is one half the period of the slowest fluctuation. The C_p curves oscillate about the curve at $t=0$ s, which is the DNS solution with the inlet boundary condition being the RANS mean flow. The envelope of the C_p curves oscillations during the 0.5 s period is shown in Figure 11. It is seen from the lower bound curve that the minimum pressure coefficient, $C_{p\min}$, reaches about -12 at three locations, *i.e.* $s/C = 0.35, 0.5$ and 0.8 .

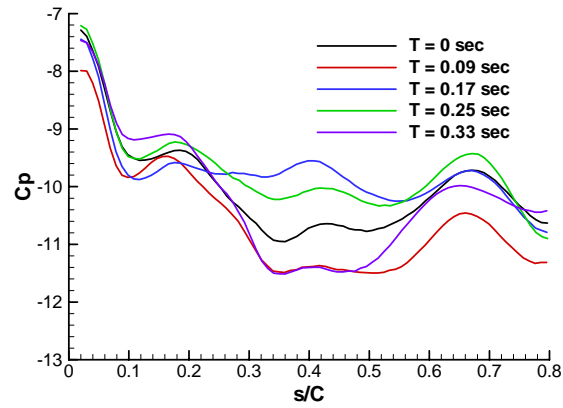


Figure 10. Computed local minimum pressure coefficients along the main vortex streamwise direction at five time steps.

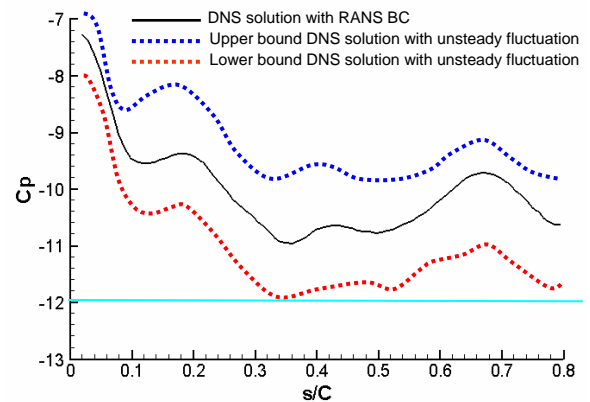


Figure 11. Envelope of the oscillating C_p curves between $t=0$ and $t=0.5$ s.

Computations using higher velocity fluctuation levels imposed on the cross flow velocities were conducted to investigate their effects on the vortex/vortex interaction. The resulting time variations of the minimum pressure coefficient, Cp_{min} , are shown in Figure 12 for three different velocity fluctuation levels: 10%, 20% and 40%. Note that the x-axis shown in Figure 12 is the non-dimensional time starting from $t = 15$, time at which unsteady velocity fluctuations were imposed at the inlet boundary. It is seen that for the 10% case the minimum pressure coefficient fluctuated moderately remaining in the -11 to -12 range. These variations increased significantly as the imposed fluctuation levels of the cross flow were increased further. The location where the minimum pressure occurred for each of these three cases was recorded every 12 ms and is shown in Figure 13. It is seen that the locations of these minima Cp_{min} varied between 0.3 and 0.8 chord length downstream from the tip trailing edge with a strong tendency for clustering near 0.35, 0.55 and 0.75. Unlike the fluctuations of Cp_{min} , the locations of Cp_{min} appears here much less sensitive to the imposed velocity fluctuation levels.

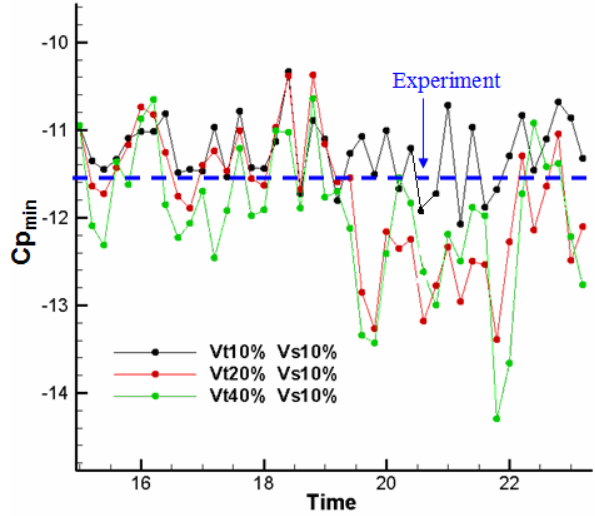


Figure 12. Time variations of the Cp_{min} for three different fluctuation levels imposed on the cross flow velocity components.

Another unsteady computation was conducted with the amplitude of the fluctuations of the streamwise velocity increased to 20% of U_∞ and the cross flow velocity fluctuation kept at 10% of U_∞ . As in the cross flow case, increasing the fluctuation level of the streamwise component did not change the clustering locations of Cp_{min} . However, it is seen from Figure 14 that increasing the fluctuations level in the streamwise velocity component led to even larger

fluctuations in the amplitude of Cp_{min} than when the cross flow velocity components were increased.

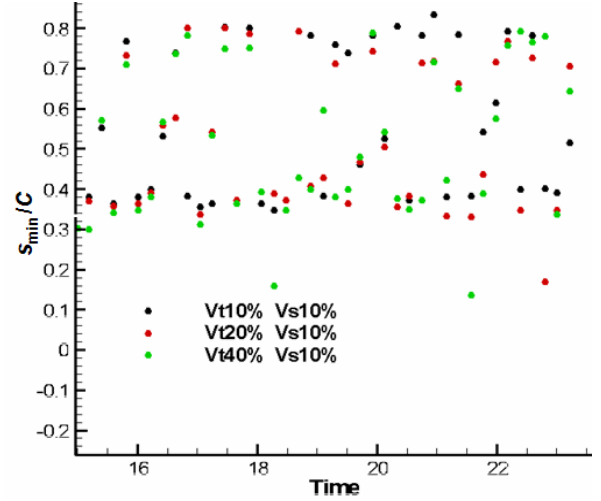


Figure 13. Comparison of the location of Cp_{min} versus time for three different fluctuation levels imposed on the cross flow velocity components.

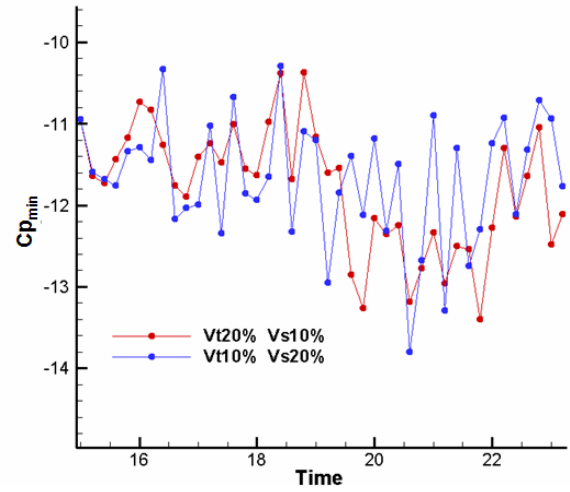


Figure 14. Time variations of the Cp_{min} for increasing levels of the cross flow velocity and streamwise velocity fluctuations.

3.3 Effect on Bubble Dynamics and Cavitation Noise

The effect of the upstream unsteady velocity fluctuations on the bubble dynamics and on cavitation noise was also investigated. A fluctuation level of 10% of U_∞ for all the velocity components was used during the simulation of bubble dynamics behavior through the unsteady vortex/vortex interaction flow field. The selected cavitation number was equal to 10.75. A nuclei distribution was selected and is shown in Figure

15. These bubbles were randomly released into the computational domain and presence and absence of unsteady velocity fluctuations imposed at the inlet boundary were compared. Details of the nuclei release method can be found in Hsiao and Chahine (2004). As the nuclei traveled through the computational domain, the acoustic signals from all bubbles were recorded at the shroud wall at a location 0.5 chord length downstream of the tip trailing edge.

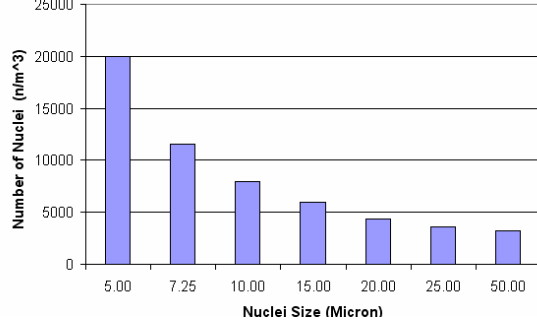


Figure 15. Nuclei size distribution used in the bubble tracking computations.

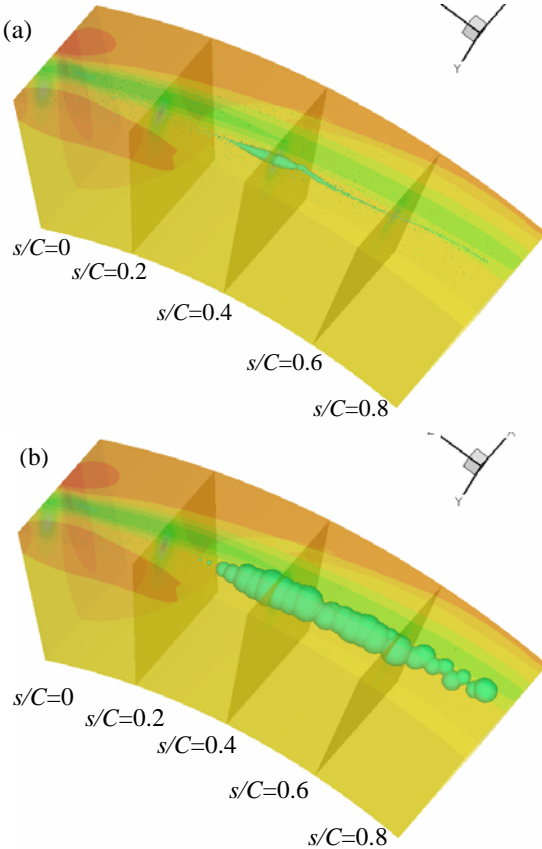


Figure 16. Comparison of the appearance of cavitating bubbles (size and locations) between (a) using mean flow inlet boundary conditions and (b) imposing 10% unsteady velocity fluctuations to the mean flow at $\sigma=10.75$.

To illustrate the effect of the upstream unsteady velocity fluctuations on the bubble dynamics, all bubbles were represented to scale at their respective locations and were superposed and shown in Figure 16. This figure clearly illustrates that the presence of fluctuations increases significantly the region of cavitation observation. While the visible cavitating bubbles with the RANS solution used upstream were all concentrated near $s/C = 0.4$, visible bubbles are observed in a much wide region, *i.e.* from $s/C = 0.3$ to 0.8, when upstream velocity fluctuations are taken into account. Furthermore, much larger cavitation bubbles are observed for the later case. The acoustic signals emitted in both cases are shown in Figure 17. It is seen that in the presence of fluctuations the number of cavitation events and the magnitudes of the acoustic signals are also significantly increased. This implies that the detected cavitation inception number is higher when unsteady fluctuations of the flow field are taken into account.

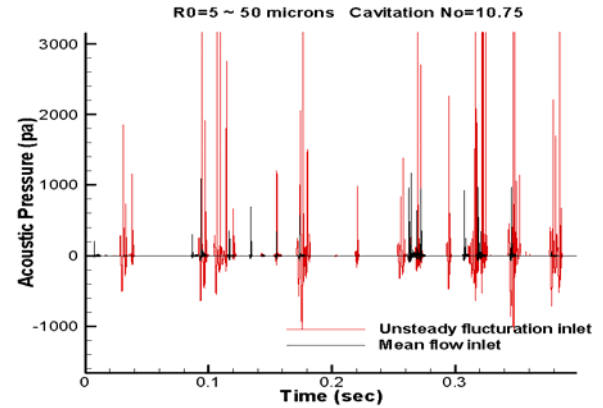


Figure 17. Acoustic signals emitted by the cavitating bubbles propagated in the computational domain. Stronger and more numerous signals are seen when unsteady fluctuations are added to the mean flow - $\sigma=10.75$.

4. Conclusions

The interactions between the tip-leakage vortex and the trailing-edge vortex of a ducted propulsor were studied in a reduced computational domain in the region of interaction of the two vortices using direct numerical simulations of the Navier-Stokes equations. To take into account the presence of upstream turbulent fluctuations which are averaged out by the RANS procedure, turbulence-like velocity fluctuations derived from PIV measurements were added to the RANS solution at the inlet boundary of the computational domain.

The simulations clearly indicated strong unsteadiness in the interaction between the two vortices. The tailing-edge vortex wrapped around the tip-leakage vortex without merging with it immediately behind the blade trailing edge and at times broke out into separated filaments (separated regions of high vorticity). These unsteady interactions resulted in time-varying pressures such that the value of the minimum pressure and the location of this minimum varied with time. The minimum pressure was found to occur at different locations between 0.3 and 0.8 chord length downstream the tip-trailing edge. Three locations showed very high probability of minimum pressure occurrence: 0.35, 0.55 and 0.75. The amplitude of the imposed fluctuations affected significantly the values of the minimum pressure. However, the minimum pressure locations remained the same and were much less sensitive to the fluctuation levels. It was also found that increasing the fluctuations level of the streamwise velocity component led to larger variations of the minimum pressure than did the fluctuations of the cross flow velocity component.

Comparison of cavitating bubble sizes and locations at the same cavitation number in presence or absence of upstream velocity fluctuations showed that the turbulent fluctuations resulted in a much wider region of cavitation occurrence. Similarly, the acoustic signals showed more numerous and higher peaks implying earlier cavitation inception detection when upstream unsteady fluctuations were present.

ACKNOWLEDGMNETS

This work was conducted at DYNAFLOW, INC. (www.dynaflow-inc.com) and was supported by the Office of Naval Research under contract No. N00014-04-C-0110 monitored by Dr. Ki-Han Kim. We gratefully acknowledge his support. The RANS solution of the full propulsor flow was provided by C. I. Yang from NSWCD and the experimental data was provided by Christopher J. Chesnakas and Stuart Jessup from NSWCD. Their help and cooperation are greatly appreciated.

REFERENCES

- [1] Brewer, W.H., Marcum, D.L., Jessup, S.D., Chesnakas, C., Hyams, D.G., Sreenivas, K., "An Unstructured RANS Study of Tip-Leakage Vortex Cavitation Inception," Proceedings of the ASME Symposium on Cavitation Inception, FEDSM2003-45311, Honolulu, Hawaii, July 6-10, 2003.
- [2] Chesnakas, C.J., Jessup, S.D., "Tip-Vortex Induced Cavitation on a Ducted Propulsor," Proceedings of the ASME Symposium on Cavitation Inception, FEDSM2003-45320, Honolulu, Hawaii, July 6-10, 2003.
- [3] Chorin, A. J., "A Numerical Method for Solving Incompressible Viscous Flow Problems," Journal of Computational Physics, Vol. 2, 1967, pp. 12-26.
- [4] Hsiao, C.-T., Chahine, G.L., Liu, H.L., "Scaling Effects on Prediction of Cavitation Inception in a Line Vortex Flow," ASME Journal of Fluids Engineering, Vol. 125, 2003a, pp. 53-60.
- [5] Hsiao, C.-T., Chahine, G.L., "Scaling of Tip Vortex Cavitation Inception Noise with a Statistic Bubble Dynamics Model Accounting for Nuclei Size Distribution," ASME Journal of Fluids Engineering, Vol. 127, No. 1, 2005, pp. 55-65.
- [6] Hsiao, C.-T., Chahine, G.L., "Numerical Study of Cavitation Inception due to Vortex/Vortex Interaction in a Ducted Propulsor," 25th Symposium on Naval Hydrodynamics, St. John, Canada, 2004.
- [7] Chahine, G.L., "Nuclei Effects on Cavitation Inception and Noise," 25th Symposium on Naval Hydrodynamics, St. John, Canada, 2004.
- [8] Johnson, V.E., Hsieh, T., "The Influence of the Trajectories of Gas Nuclei on Cavitation Inception," Sixth Symposium on Naval Hydrodynamics, 1966, pp. 163-179.
- [9] Kim, J., "Sub-Visual Cavitation and Acoustic Modeling for Ducted Marine Propulsor," Ph.D. Thesis, 2002, Department of Mechanical Engineering, The University of Iowa, Adviser F. Stern.
- [10] Oweis, G., Ceccio, S., Chesnakas, C., Fry, D., Jessup, S., "Tip Leakage Vortex (TLV) Variability from a Ducted Propeller under Steady Operation and its Implications on Cavitation Inception," 5th International Symposium on Cavitation, Osaka, Japan, November 1-4, 2003.
- [11] Vanden, K., Whitfield, D. L., "Direct and Iterative Algorithms for the Three-Dimensional Euler Equations," AIAA-93-3378, 1993.
- [12] Yang, C.I., Jiang, M., Chesnakas, C.J., and Jessup, S.D., 2003, "Numerical Simulation of Tip Vortices of Ducted-Rotor", NSWCCD-50-TR-2003/46

Modeling of Bubble Generated Noise in Tip Vortex Cavitation Inception

Jin-Keun Choi, Georges L. Chahine

Dynaflow, Inc., 10621-J Iron Bridge Road, Jessup, Maryland 20794-9381, USA

jkchoi@dynaflow-inc.com, glchahine@dynaflow-inc.com, www.dynaflow-inc.com

Summary

Observations of bubble nuclei in tip vortex flows indicate bubble elongation followed by a splitting. Non-spherical simulations capture this dynamics and show reentrant jet formation and emission of very high noise. However, applying the non-spherical method to a field of nuclei is prohibitively expensive. In this paper, we attempt to overcome this difficulty by performing simulations with an improved spherical model accounting for the pressure gradient through a Surface Averaged Pressure (SAP) method and also accounting for bubble splitting. Non-spherical numerical simulations are used to develop splitting criteria and to characterize the offspring split sub-bubbles and the resulting noise. These criteria are implemented in the SAP spherical model. Numerical results with single bubble and with a realistic field are presented. From this study, it is concluded that the visual detection of the cavitation is not affected by the inclusion of successive nuclei splitting because the sub-bubbles never grow larger than the first maximum size. However, bubble splitting has a strong effect on cavitation acoustic signature due to noise from the reentrant jets. This jet noise contributes to a distinct peak in the noise spectrum. The noise from sub-bubbles contributes to the shifting of the spectrum towards high frequencies.

PACS no. 43.30.Nb, 43.50.Ed, 43.25.Yw

1. Introduction

Due to the complexity of the cavitation inception and noise generation processes, modeling of cavitation noise in a tip vortex flow field is a very challenging task. Several experimental studies [1, 2, 3, 4, 5] have shown the importance of bubble nuclei on cavitation inception and scaling. Many numerical studies have been conducted under various simplifying assumptions and thus have been focused on the influence of only a limited set of parameters. A broad background and a recent review of researches on this subject can be found in [6]. Most models accept that tip vortex cavitation inception is due to traveling bubble nuclei, and use a spherical bubble dynamics model coupled with a motion equation to predict cavitation inception. Latorre [7] and Ligneul and Latorre [8] applied this approach to deduce noise emission from cavitation in a Rankine line vortex. Hsiao and Pauley [9] further applied this approach to study tip vortex cavitation inception with the tip vortex flow field computed by Reynolds Averaged Navier-Stokes (RANS) equations.

Conducting numerical cavitation experiments using a distribution of nuclei as in a real liquid has been very successful in providing a numerical tool to study tip vortex cavitation inception and its scaling. We have developed

a Surface Averaged Pressure (SAP) spherical bubble dynamics model [10, 11, 12, 13] that has provided bubble dynamics results very similar to those obtained using a 3-D two-way interaction model (Figure 1). The SAP model is especially appropriate for simulations with a large number (e.g. $\sim 10^5$ in the example shown in Figure 2) of bubble nuclei because of its reasonable memory and computational time requirements. The success of this model in the study of cavitation inception is partly due to the fact that the spherical approximation is valid at cavitation numbers near and above the cavitation inception number. This is illustrated in Figure 3 which shows emitted acoustic signal versus cavitation number, σ , and bubble shapes in the various σ regions.

On the other hand, our recent studies with a more precise non-spherical axisymmetric method [15, 16, 14, 17, 18] revealed that the bubble nucleus behavior at cavitation numbers just below the cavitation inception number is associated with extreme bubble elongation and splitting. Experimental validations of splitting bubble behavior were reported in Choi and Chahine [15, 14] for bubbles in restricted flow domain and in Rebow *et al.* [19] for tip vortex flow fields. Furthermore, these studies showed that the bubble splitting is followed by strong reentrant jets in the resulting offspring bubbles (Figure 4) and by the emission of very high pressure signals. A pressure signal is generated at the bubble splitting; however, much stronger pressures may be subsequently generated during the impact of the reentrant jets and the collapse of the offspring bubbles.

Received 14 July 2006,
accepted 16 January 2007.

Modeling of Bubble Generated Noise in Tip Vortex Cavitation Inception

Jin-Keun Choi, Georges L. Chahine

Dynaflow, Inc., 10621-J Iron Bridge Road, Jessup, Maryland 20794-9381, USA

jkchoi@dynaflow-inc.com, glchahine@dynaflow-inc.com, www.dynaflow-inc.com

Summary

Observations of bubble nuclei in tip vortex flows indicate bubble elongation followed by a splitting. Non-spherical simulations capture this dynamics and show reentrant jet formation and emission of very high noise. However, applying the non-spherical method to a field of nuclei is prohibitively expensive. In this paper, we attempt to overcome this difficulty by performing simulations with an improved spherical model accounting for the pressure gradient through a Surface Averaged Pressure (SAP) method and also accounting for bubble splitting. Non-spherical numerical simulations are used to develop splitting criteria and to characterize the offspring split sub-bubbles and the resulting noise. These criteria are implemented in the SAP spherical model. Numerical results with single bubble and with a realistic field are presented. From this study, it is concluded that the visual detection of the cavitation is not affected by the inclusion of successive nuclei splitting because the sub-bubbles never grow larger than the first maximum size. However, bubble splitting has a strong effect on cavitation acoustic signature due to noise from the reentrant jets. This jet noise contributes to a distinct peak in the noise spectrum. The noise from sub-bubbles contributes to the shifting of the spectrum towards high frequencies.

PACS no. 43.30.Nb, 43.50.Ed, 43.25.Yw

1. Introduction

Due to the complexity of the cavitation inception and noise generation processes, modeling of cavitation noise in a tip vortex flow field is a very challenging task. Several experimental studies [1, 2, 3, 4, 5] have shown the importance of bubble nuclei on cavitation inception and scaling. Many numerical studies have been conducted under various simplifying assumptions and thus have been focused on the influence of only a limited set of parameters. A broad background and a recent review of researches on this subject can be found in [6]. Most models accept that tip vortex cavitation inception is due to traveling bubble nuclei, and use a spherical bubble dynamics model coupled with a motion equation to predict cavitation inception. Latorre [7] and Ligneul and Latorre [8] applied this approach to deduce noise emission from cavitation in a Rankine line vortex. Hsiao and Pauley [9] further applied this approach to study tip vortex cavitation inception with the tip vortex flow field computed by Reynolds Averaged Navier-Stokes (RANS) equations.

Conducting numerical cavitation experiments using a distribution of nuclei as in a real liquid has been very successful in providing a numerical tool to study tip vortex cavitation inception and its scaling. We have developed

a Surface Averaged Pressure (SAP) spherical bubble dynamics model [10, 11, 12, 13] that has provided bubble dynamics results very similar to those obtained using a 3-D two-way interaction model (Figure 1). The SAP model is especially appropriate for simulations with a large number (e.g. $\sim 10^5$ in the example shown in Figure 2) of bubble nuclei because of its reasonable memory and computational time requirements. The success of this model in the study of cavitation inception is partly due to the fact that the spherical approximation is valid at cavitation numbers near and above the cavitation inception number. This is illustrated in Figure 3 which shows emitted acoustic signal versus cavitation number, σ , and bubble shapes in the various σ regions.

On the other hand, our recent studies with a more precise non-spherical axisymmetric method [15, 16, 14, 17, 18] revealed that the bubble nucleus behavior at cavitation numbers just below the cavitation inception number is associated with extreme bubble elongation and splitting. Experimental validations of splitting bubble behavior were reported in Choi and Chahine [15, 14] for bubbles in restricted flow domain and in Rebow *et al.* [19] for tip vortex flow fields. Furthermore, these studies showed that the bubble splitting is followed by strong reentrant jets in the resulting offspring bubbles (Figure 4) and by the emission of very high pressure signals. A pressure signal is generated at the bubble splitting; however, much stronger pressures may be subsequently generated during the impact of the reentrant jets and the collapse of the offspring bubbles.

Received 14 July 2006,
accepted 16 January 2007.

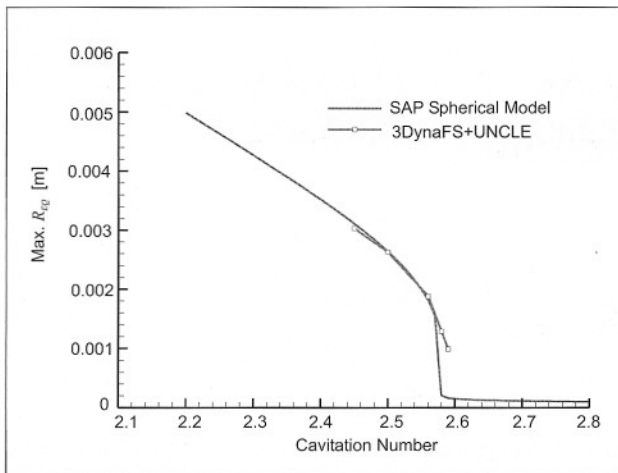


Figure 1. Comparison of maximum bubble sizes from SAP spherical model and those from a non-spherical bubble model. Note the excellent agreement between the SAP spherical model and the 3-D two-way interaction model (3DynaFS[©]+DF_UNCLE) from Hsiao and Chahine [12].

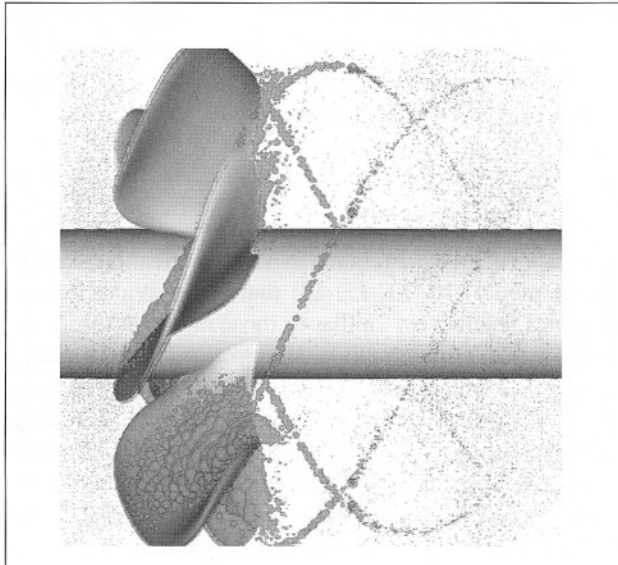


Figure 2. Example of SAP spherical model applied to a propeller flow field.

The fact that the pressure signal from the subsequent behavior of the offspring bubbles is much higher than that from the collapse (splitting) of the original bubble suggests the need to include the bubble splitting in the SAP model in on-going and future studies. In addition, bubble splitting results in the modification of the original nuclei size distribution, which is included in the present model.

In order to avoid the higher computational cost of non-spherical methods and, at the same time, to include bubble splitting effects in the simulation of a real nuclei bubble field, we need to identify the conditions for occurrence and to model the bubble splitting. Through an extensive series of non-spherical simulations under various conditions, we have developed rules for the conditions under which a bubble splits, the timing of the splitting, and the characteris-

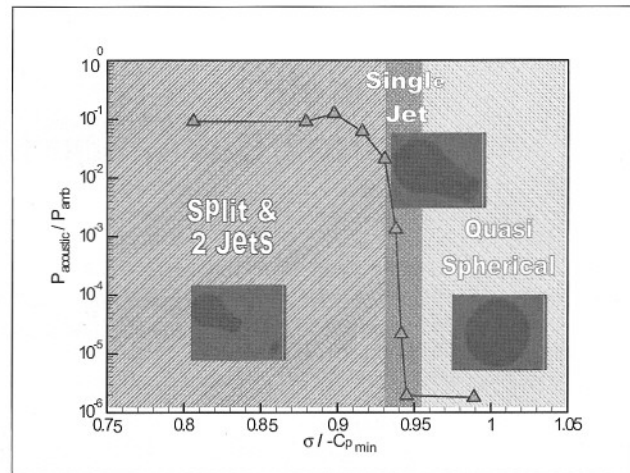


Figure 3. Peak acoustic pressure generated by bubble growth and collapse in a vortex flow field as a function of cavitation number. Note that the bubble behavior near and above the cavitation inception (approx. 2.58 in this case) is quasi-spherical. (from Choi and Chahine [14]).

tics of the resulting offspring bubbles. These rules are then implemented in the upgraded SAP spherical model resulting in dynamic modification of the bubble nuclei sizes and distribution during a SAP simulation.

In this paper, we illustrate the method for the study of cavitation inception in the flow field of a tip vortex. First, the non-spherical numerical studies on bubble splitting leading to the development of splitting criteria and characterization of the resulting offspring bubbles are introduced and the implementation of the model within the context of the SAP spherical model is described. Numerical results with single and multiple bubble nuclei are then presented, and the effect of inclusion of bubble splitting on the cavitation inception prediction is discussed.

2. Numerical models for bubble simulations

2.1. Surface averaged pressure model

A spherical bubble model is valid as long as the pressure difference across the bubble due to the pressure gradient of the fluid around the bubble is negligible compared to the surface tension of the bubble. The spherical model used in this study is based on Rayleigh-Plesset equation [20] with some modifications as described in Hsiao *et al.* [10, 12] including Gilmore's [21] modification to account for the liquid compressibility which becomes important when bubble surface velocity becomes comparable with the speed of sound in the liquid c .

$$\begin{aligned} \left(1 - \frac{\dot{R}}{c}\right) R \ddot{R} + \frac{3}{2} \left(1 - \frac{\dot{R}}{3c}\right) \dot{R} = \\ \frac{1}{\rho} \left(1 + \frac{\dot{R}}{c} + \frac{R}{3c} \frac{d}{dt}\right) \left[p_v + p_{g0} \left(\frac{R_0}{R}\right)^{3k} \right. \\ \left. - p(t) - \frac{2\gamma}{R} - \frac{4\mu\dot{R}}{R} \right] - \frac{|u - u_b|^2}{4}, \end{aligned} \quad (1)$$

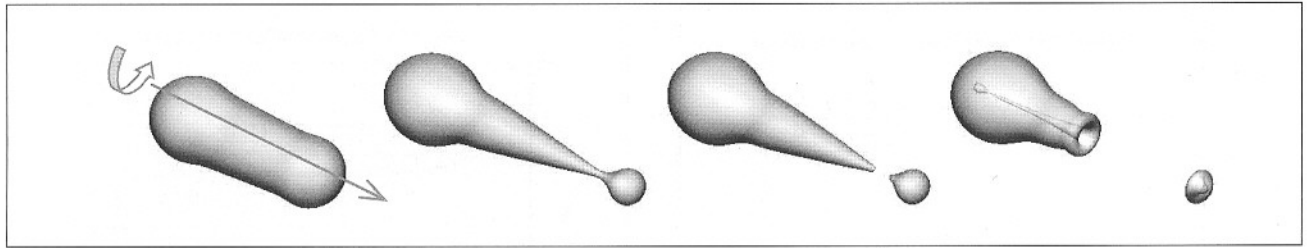


Figure 4. Bubble splitting and jet development of a nucleus captured by a tip vortex (in time sequence from left to right). (from Choi and Chahine [14]).

where R is the bubble radius, R_0 is the initial bubble radius, μ is the liquid viscosity, γ is the surface tension parameter, p_{g0} is the initial gas pressure inside the bubble with the polytropic gas constant k , and $p(t)$ is the time varying pressure that the bubble encounters. The dots over R represent the time derivatives, and the last term accounts for the pressure due to the slip velocity which is the difference between the liquid velocity, \mathbf{u} , and the bubble velocity, \mathbf{u}_b . In the Surface Averaged Pressure (SAP) spherical model, $p(t)$ is taken as the area weighted average of the outside liquid pressure over the bubble surface. This allows for a much more realistic description of the bubble behavior as it is captured by the vortex. That is, once the bubble reaches the vortex axis, the encounter pressure will increase as the bubble grows enabling a more realistic balancing of the bubble dynamics.

The bubble trajectory during capture is predicted by an equation of motion given by Johnson and Hsieh [22],

$$\frac{d\mathbf{u}_b}{dt} = -\frac{3}{\rho} \nabla p + \frac{3C_D}{4R} |\mathbf{u} - \mathbf{u}_b| (\mathbf{u} - \mathbf{u}_b) + \frac{3\dot{R}R}{R} (\mathbf{u} - \mathbf{u}_b), \quad (2)$$

where the drag coefficient C_D is determined from the empirical formula by Haberman and Morton [23]. With a prescribed pressure and velocity field, a Runge-Kutta fourth-order scheme is applied to integrate equations (1) and (2) through time to provide the bubble trajectory and its volume variation during bubble capture by the tip vortex. Under the assumption of small bubble, the so called one-way coupling, which considers only the effect of the flow field on the bubble behavior, is applied.

2.2. Non-spherical model

For a more general description of the bubble deformation in a vortex field, non-spherical bubble geometry should be modeled. In the present study, an axisymmetric formulation is used to take advantage of the axisymmetric vortex field. We use the spherical model during the capture of the bubble where the bubble remains practically spherical, and switch to non-spherical model when it reaches the vortex axis. An alternative approach is a fully three-dimensional method that is used in other studies [12].

The velocity field is expressed with the Helmholtz decomposition as the sum of the gradient of a scalar potential ϕ and a rotational flow field. The flow due to the bubble

presence is assumed to be expressed by $\nabla\phi$ and the rotational flow field of the tip vortex is assumed to remain not affected by the bubble presence and dynamics [24]. Since the potential flow field due to the bubble presence satisfies the Laplace equation $\nabla^2\phi = 0$, Green's identity is applied to construct the integral equation for the potential ϕ and the normal derivative of the potential $\partial\phi/\partial n$.

The boundary conditions on the bubble surface are the continuity of the normal stresses (the dynamic condition) and the condition that the fluid normal velocities should be equal to the interface normal velocities (the kinematic condition). On the bubble surface, $\partial\phi/\partial n$ is obtained as the solution of the integral equation, while ϕ is given from the dynamic boundary condition. The pressure inside each bubble is assumed homogeneous, and the gas inside each bubble is assumed to be composed of both vapor of the liquid and non-condensable gas. The pressure at any instant is given by the sum of the partial pressures of the liquid vapor and of the non-condensable gas. Vaporization of the liquid is assumed to occur at a fast enough rate so that the vapor pressure inside the bubble remains equal to the equilibrium liquid vapor pressure at the ambient temperature. The non-condensable gas is assumed to satisfy a polytropic law with an exponent k , and thus pV^k remains constant regardless of the bubble volume $V(t)$ that varies with time.

$$p = p_v + p_{g0} \left(\frac{V_0}{V(t)} \right)^k - \gamma C, \quad (3)$$

where V_0 is the initial volume of the bubble and C is the local surface curvature. Once the solution is obtained at any time step, the pressure signal at given field points can be calculated by using the unsteady Bernoulli equation.

A bubble placed on the vortex axis usually elongates along this axis. Oftentimes the elongation is so extreme that the bubble eventually splits into smaller sub-bubbles. When this happens, a special treatment is necessary to continue the simulation. When a node approaches the axis within a specified small distance, neighboring nodes are tested to find the two nodes that are closest to the axis. The segment connecting these two nodes is removed by placing the two end nodes of the segment exactly on the axis. Many variables including potential and velocities need to be extrapolated to the new position and the node and segment indices as well as the bubble index are updated. The gas pressure must remain constant through the split unless

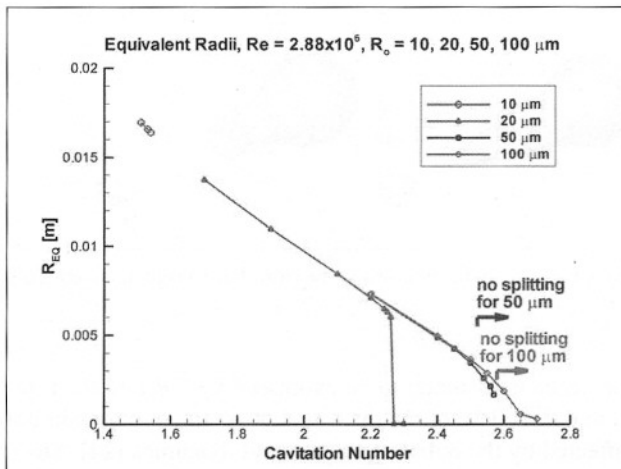


Figure 5. The maximum equivalent bubble radius of a bubble captured in a tip vortex as predicted by the axisymmetric boundary element method (2DynaFS[©]). Four initial nuclei sizes, 10, 20, 50, and 100 μm , are considered.

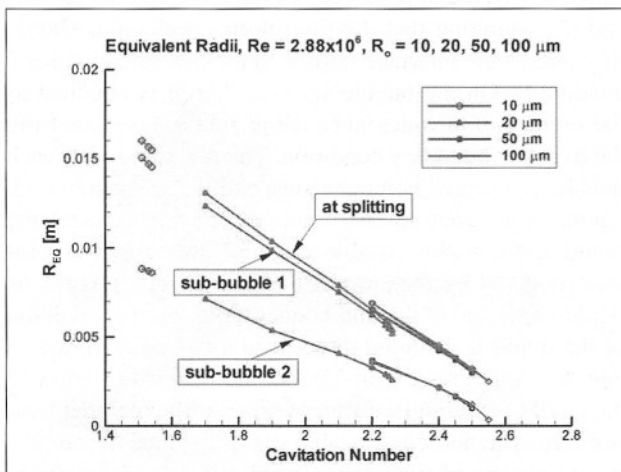


Figure 6. Variation with the cavitation number of the equivalent radii of a bubble captured in a vortex just before the splitting and of the two sub-bubbles generated from the splitting. These are predicted by the axisymmetric boundary element method (2DynaFS[©]). Four initial nuclei sizes, 10, 20, 50, and 100 μm , are considered.

the process involves energy loss which is not considered in the present study.

3. Bubble splitting model

In our previous work [15, 16, 14, 17], using a boundary element method we have developed a bubble splitting model based on axisymmetric simulations of a bubble nucleus under various conditions in a typical tip vortex flow field of a hydrofoil. In this section, we characterize the observations of the bubble splitting.

The tip vortex flow fields used in the development of the splitting model are those of an elliptic hydrofoil. For numerical values we used 1 m chord and 1.5 m half span subject to 2.88 m/s inflow and of the same hydrofoil of

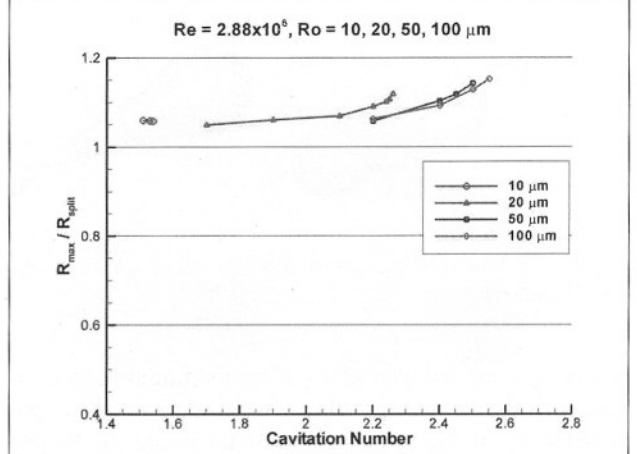


Figure 7. Characterization of bubble splitting: The ratios of the maximum equivalent radius, R_{\max} , relative to the equivalent radius just before the splitting, R_{split} , for the four initial nuclei sizes, 10, 20, 50, and 100 μm .

0.5 m chord at the same inflow velocity. The corresponding dimensionless numbers are $Re = 2.88 \cdot 10^6$ and $Re = 1.44 \cdot 10^6$, and the circulation over the chord length times the inflow velocity is 0.43. These flow fields are computed by using the modified Mississippi State University UnRANS code, DF_UNCLE [12]. A bubble nucleus which is released upstream of the flow field is tracked first by the SAP spherical model until the tip vortex captures it, and then our axisymmetric BEM code, 2DynaFS[©], takes over the computation to continue description of the non-spherical behavior. Splitting criteria are derived from observations of the equivalent radius (defined as the radius of a sphere of the same volume) at which a bubble splits and the equivalent radii of the two generated sub-bubbles. As shown in Figure 5 and Figure 6, these radii form a common set of curves regardless of the initial nucleus size within the range of 10 to 100 μm . When these radii are normalized by the equivalent bubble radius just before the splitting, they have nearly constant values over a wide range of cavitation numbers as shown in Figure 7 to Figure 9. The ratio of the maximum equivalent radius, R_{\max} , to the equivalent radius just before the splitting is very close to 1.06, and the radii of the two sub-bubbles just after the split are 0.95 R_{\max} and 0.55 R_{\max} regardless of the initial bubble size. These observations are the basis for the bubble splitting criterion and the initial size of the resulting sub-bubbles that are used below.

The axial location of the sub-bubble centers obtained from the computations with various initial bubble nuclei size is shown in Figure 10. The sub-bubble centers normalized by the equivalent radius at splitting, R_{split} , fall on the same curves throughout the range of cavitation numbers we have studied. The center position of the downstream sub-bubble is observed to be near $4.4R_{\text{split}}$, and the axial location of the upstream sub-bubble varies from approximately $-1.0R_{\text{split}}$ for the low cavitation numbers to 0.0 at the cavitation number where splitting starts to occur.

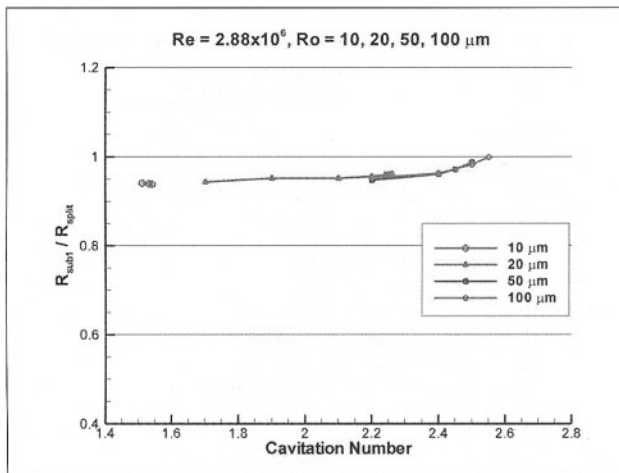


Figure 8. Characterization of bubble splitting: The ratios of the equivalent radii of the larger sub-bubble, $R_{\text{sub}1}$, relative to the equivalent radius just before the splitting, R_{split} , for the four initial nuclei sizes, 10, 20, 50, and 100 μm .

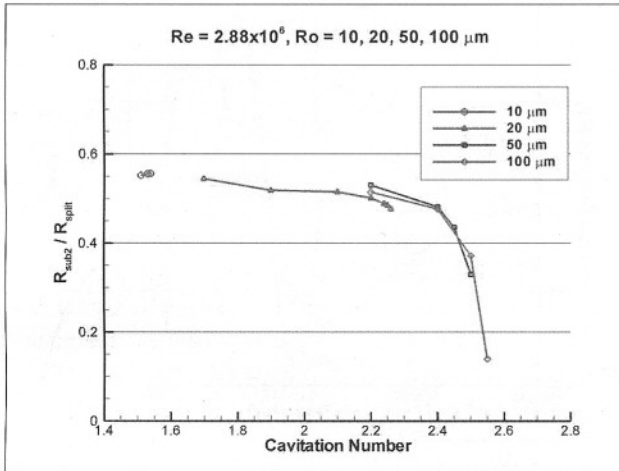


Figure 9. Characterization of bubble splitting: The ratios of the equivalent radii of the smaller sub-bubble, $R_{\text{sub}2}$, relative to the equivalent radius just before the splitting, R_{split} , for the four initial nuclei sizes, 10, 20, 50, and 100 μm .

The radial velocity of the sub-bubbles just after the split was found to be close to zero for both sub-bubbles. It was also found that the initial locations of the sub-bubbles depend weakly on the Reynolds numbers but more strongly on the cavitation numbers. For cavitation numbers in the mid-low range relative to the inception ($0.6 \leq \sigma/\sigma_i \leq 0.9$), the locations of the sub-bubbles relative to the bubble center just before the splitting are fairly constant and are $-1.0R_{\text{split}}$ and $4.4R_{\text{split}}$, respectively for the upstream and the downstream sub-bubbles.

Based on the observations of the bubble splitting described above, the following bubble splitting model for low cavitation numbers (or smaller nuclei) was developed. The model consists of a splitting criterion and initial conditions for the sub-bubbles.

Bubble splitting criterion: After a bubble has grown explosively ($\sigma < \sigma_{\text{inception}}$), it will split at the beginning of

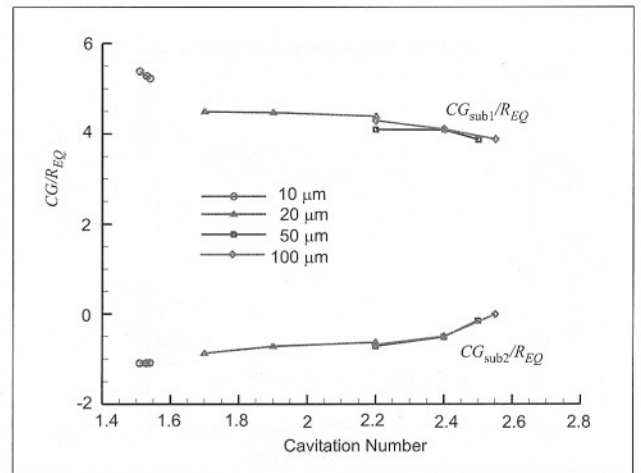


Figure 10. Characterization of bubble splitting: The axial locations of the sub-bubbles just after the splitting normalized by the equivalent radius just before the splitting, R_{split} . Four initial nuclei sizes, 10, 20, 50, and 100 μm are considered.

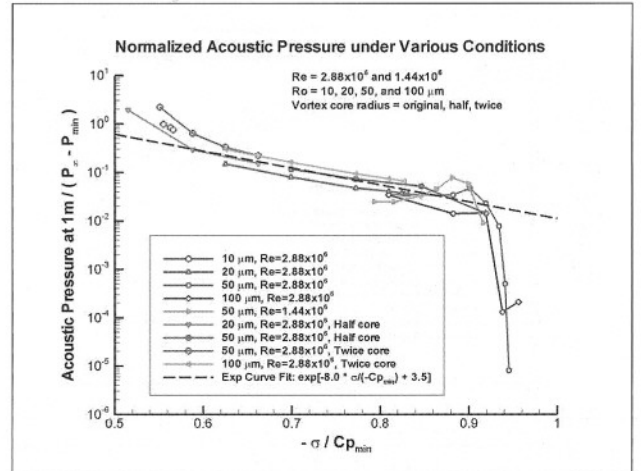


Figure 11. Acoustic pressure signals predicted by the axisymmetric boundary element method (2DynaFS[©]) which allows bubble elongation and splitting. Data for two Reynolds numbers, four initial nuclei sizes, and three vortex core sizes fall on very closely near the curve fit.

the collapse once its radius reaches 95% of the maximum radius.

Initial condition of sub-bubbles: The radii of the larger and smaller sub-bubbles are respectively, 0.95 and 0.55 of the radius at splitting, R_{split} . The initial gas pressure in each sub-bubble is that of the original bubble pressure at splitting, and the initial radial velocities are zero. The initial location of the larger sub-bubbles is $1.0R_{\text{split}}$ upstream of the original bubble center, and that of the smaller one is $4.4R_{\text{split}}$ radii downstream of the original bubble center.

4. Reentrant jet noise model

The peak-to-peak values of the acoustic pressure signal obtained from various simulations are shown in Figure 11. The pressure is normalized by the distance between the

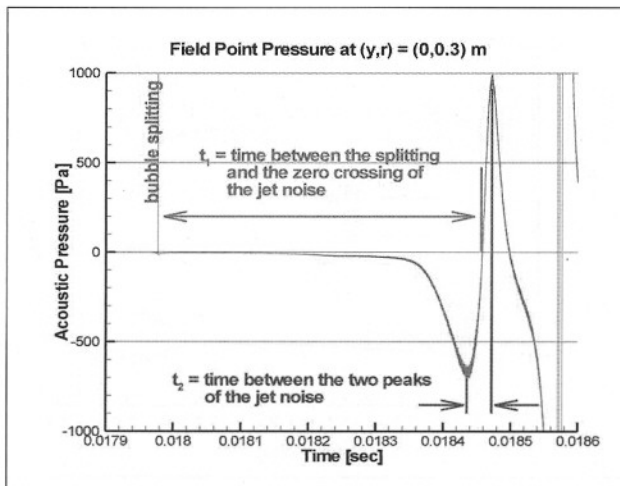


Figure 12. Typical pressure signal from the reentrant jet after a bubble splitting.

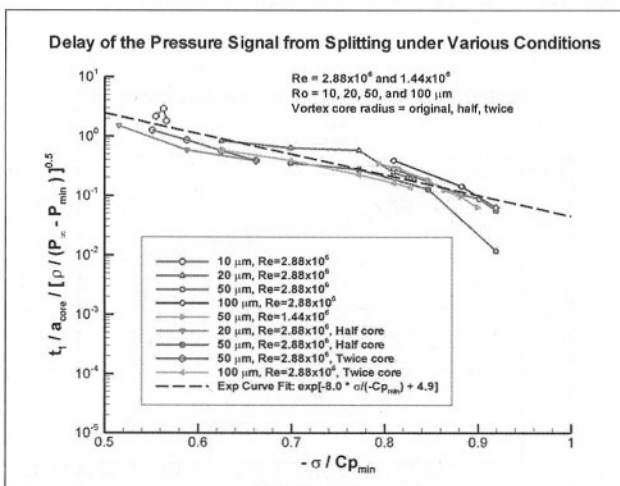


Figure 13. Exponential curve fit of the time delay, t_1 , from the splitting moment to the acoustic pressure from the jet.

noise source and the observation point and the difference of the ambient pressure and the minimum pressure in the vortex core, $(p_\infty - p_{\min})$. The cavitation number is normalized by the negative of the minimum pressure coefficient, $-Cp_{\min}$. The normalized acoustic pressure data predicted under various conditions, which include two Reynolds numbers, four bubble nucleus sizes, and three scales of vortex core size, fall on a common curve regardless of these conditions. We can use this observation to develop a model for the reentrant jet noise.

The modeling of the jet noise is based on the observations of a typical acoustic pressure from the reentrant jet as shown in Figure 12. To model the timing of the jet noise, the time delay between the splitting and the zero crossing of the jet noise is defined as t_1 , and the time interval between the minimum and the maximum of the jet noise is defined as t_2 . These two time intervals are normalized by a time scale similar to the Rayleigh time, $a_{\text{core}} \sqrt{\rho / (p_\infty - p_{\min})}$, where a_{core} is the vortex core radius at the minimum pressure location, ρ is the density of water.

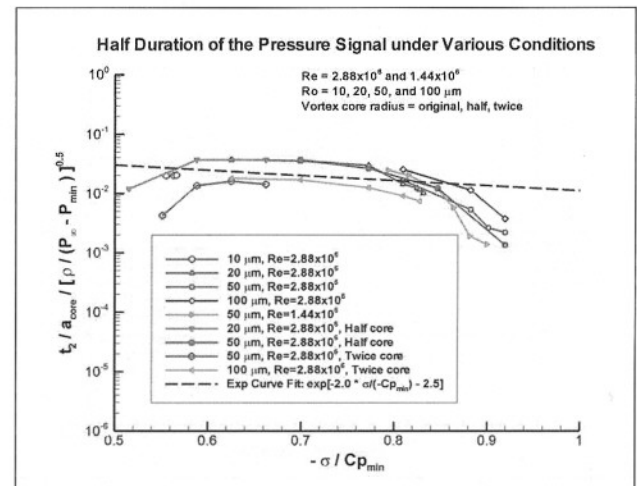


Figure 14. Exponential curve fit of the half duration, t_2 , of the acoustic pressure from the jet.

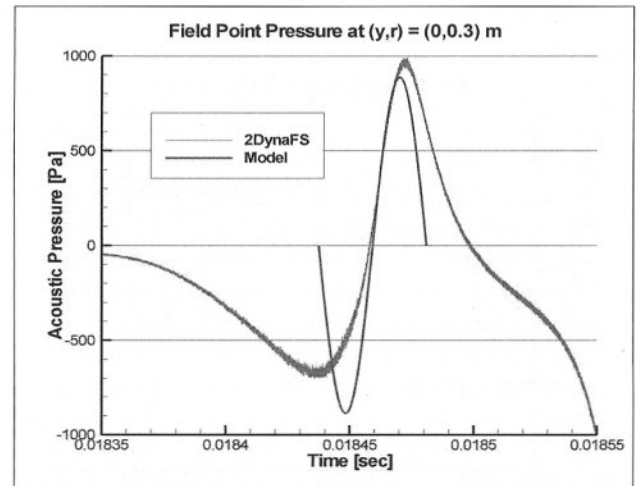


Figure 15. Comparison of the pressure signal from the reentrant jet between the 2DynaFS[®] prediction and the model equation at $\sigma = 2.10$.

The normalized time delays between the bubble splitting and the acoustic signal due to the jet, t_1 , for various conditions collapse on top of the others as shown in Figure 13, and the half durations of the signal, t_2 , also form a common curve for a range of cavitation numbers in Figure 14. These normalized data are fit into exponential curves resulting in the following expressions:

$$\begin{aligned} \bar{p}(\bar{\sigma}) &= \exp(-8.0\bar{\sigma} + 3.5), \\ \bar{t}_1(\bar{\sigma}) &= \exp(-8.0\bar{\sigma} + 4.9), \\ \bar{t}_2(\bar{\sigma}) &= \exp(-2.0\bar{\sigma} - 2.5), \end{aligned} \quad (4)$$

where the bar over the variables means a normalized value. Then, the acoustic pressure signal due to the jet is modeled with the following sine signal,

$$\bar{p}_{\text{jet}}(\bar{t}) = \frac{\bar{p}(\bar{\sigma})}{2} \sin\left(\frac{\bar{t} - \bar{t}_1(\bar{\sigma})}{\bar{t}_2(\bar{\sigma})}\pi\right), \quad \bar{t}_1 - \bar{t}_2 \leq \bar{t} \leq \bar{t}_1 + \bar{t}_2. \quad (5)$$

The jet noise from this model is compared with the original pressure signal for $\sigma = 2.10$ in Figure 15. The duration

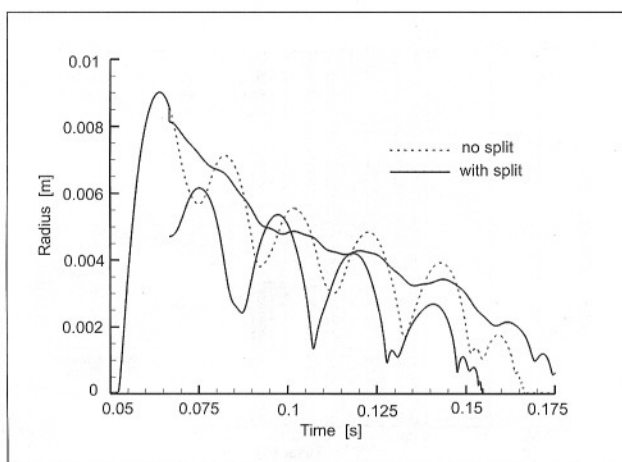


Figure 16. Bubble radius history predicted with $20 \mu\text{m}$ nucleus at $\sigma = 1.70$.

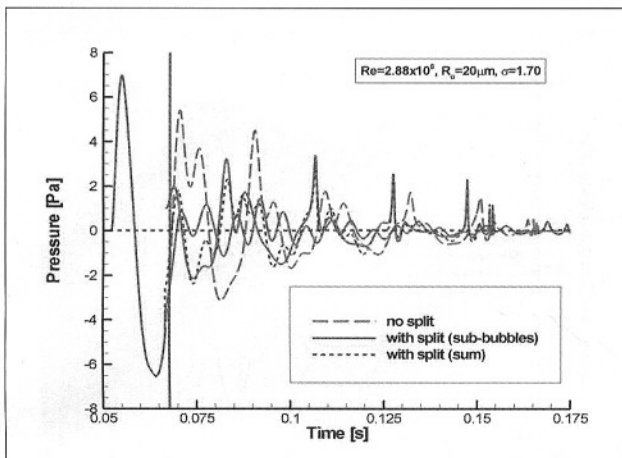


Figure 17. Acoustic pressure signals predicted with $20 \mu\text{m}$ nucleus at $\sigma = 1.70$.

of the signal from the model is shorter than the original signal due to an underestimation of t_2 from the curve fit for this case. We will improve this approximation in our future studies.

5. Single splitting of a nucleus

The SAP spherical model described above is first applied to a $20 \mu\text{m}$ nucleus at $\sigma = 1.70$. The tip vortex flow field used here is the same flow field in which the splitting model was developed [15, 17, 18]. The resulting time history of the bubble radius is shown in Figure 16 and the associated acoustic pressure signal is shown in Figure 17. When the nucleus grows to its maximum size and reaches 95% of the maximum radius, it splits into two sub-bubbles as expected from the model explained earlier. The larger sub-bubble shrinks monotonically after the split, while the smaller sub-bubble begins with a small growth followed by violent collapses and rebounds. The acoustic pressure has an initial peak corresponding to the initial growth of the nucleus, followed by a sharp jet noise after the split. Then, there are two contributions to the acoustic pressure, one for each sub-bubble. The resulting signal from the sub-

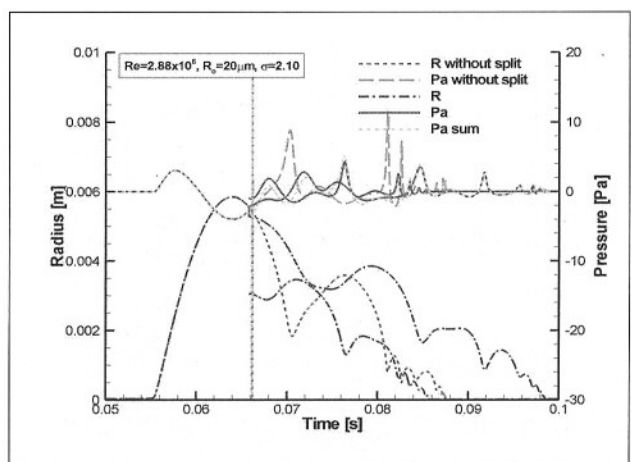


Figure 18. Bubble radius and the acoustic pressure signal as functions of time predicted with $20 \mu\text{m}$ nucleus at $\sigma = 2.10$.

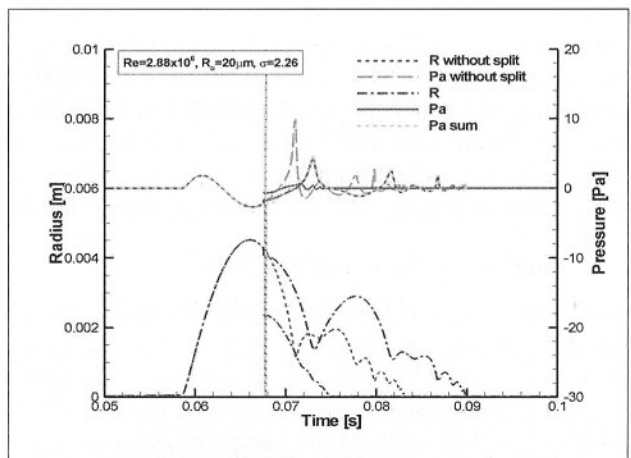


Figure 19. Bubble radius and the acoustic pressure signal as functions of time predicted with $20 \mu\text{m}$ nucleus at $\sigma = 2.26$ (cavitation inception).

bubbles has a smaller maximum peak than that without splitting.

Another simulation of a $20 \mu\text{m}$ nucleus at a higher cavitation number, $\sigma = 2.10$, is shown in Figure 18. In this case, both sub-bubbles experience collapse and rebound cycles. However, the combined pressure signal still has smaller peaks than that from the simulation without the splitting if the strong jet noise of about 800 Pa appearing at 0.066 s is excluded. In Figure 19, the bubble behavior at the cavitation inception number is shown. In this case, the larger sub-bubble is more active, yet producing weaker signal than the simulation without splitting.

Based on the results of the three cavitation numbers, we can arrive at the following conclusions for a single split of a nucleus. Visual detection of cavitation, which is based on detecting the maximum bubble size, is not affected by the splitting because the sub-bubble sizes are always smaller than the maximum size observed before the inclusion of splitting in the model and never grow larger than this. The acoustic pressure signal with splitting has a strong jet noise, but the resulting signals of the collapsing

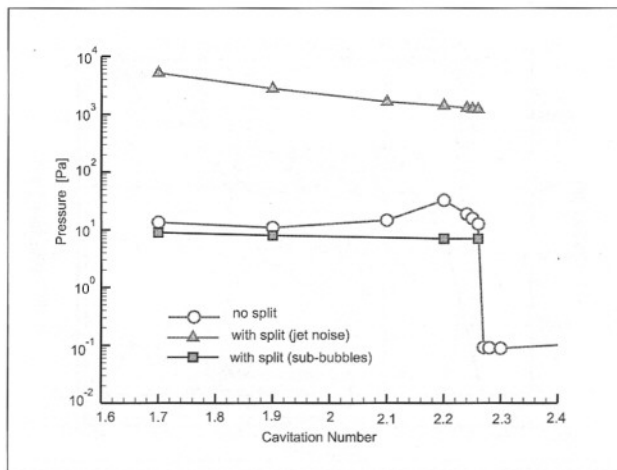


Figure 20. Maximum of the acoustic pressure signal vs. cavitation numbers predicted with $20\text{ }\mu\text{m}$ nucleus.

sub-bubbles are smaller than such a signal of one big bubble without splitting. This is more obviously seen in Figure 20, where the maximum of the resultant acoustic pressure signal from sub-bubble collapses for each cavitation number is always slightly smaller than the maximum peak observed from original SAP simulations without splitting.

5.1. Simulation of a nuclei flow field

Simulations with a realistic field of multiple nuclei as measured in a liquid can provide an insight for the cavitation noise in a real flow field. The above SAP spherical model is applied to the same tip vortex flow field at $\sigma = 2.10$ with a set of 100 nuclei of the same size $20\text{ }\mu\text{m}$. The nuclei are distributed randomly in space within a rectangular box of $0.1\text{ m} \times 0.01\text{ m} \times 0.006\text{ m}$ just in front of the blade tip and the computation stops when all these bubbles have gone through the $0.01\text{ m} \times 0.006\text{ m}$ window. Note that the same nuclei population is assumed everywhere in the flow domain, but only the nuclei coming through this window have the opportunity to grow explosively. This distribution corresponds to a void fraction of $5.59 \cdot 10^{-7}$. The acoustic pressure signal from this simulation is shown in Figure 21. Compared to the acoustic signal without splitting, the signal with splitting is much noisier due to the jet noise, but the contribution from the sub-bubble collapses is weaker than the signal without splitting.

The amplitude spectrum can be obtained from the pressure signal, $p(t)$, through the finite Fourier transformation,

$$P(f, T) = \int_0^T p(t) e^{-i2\pi f t} dt, \quad (6)$$

where T is the time duration for the finite Fourier transformation and f is the frequency. The amplitude spectrum of the acoustic signal is shown in Figure 22. When the spectrum with splitting but without the jet noise is compared with the spectrum with splitting, the noise contents of frequency lower than $50\text{--}100\text{ kHz}$ have decreased and those at higher frequency have increased. This redistribution of the frequency contents is due to the smaller sub-bubbles

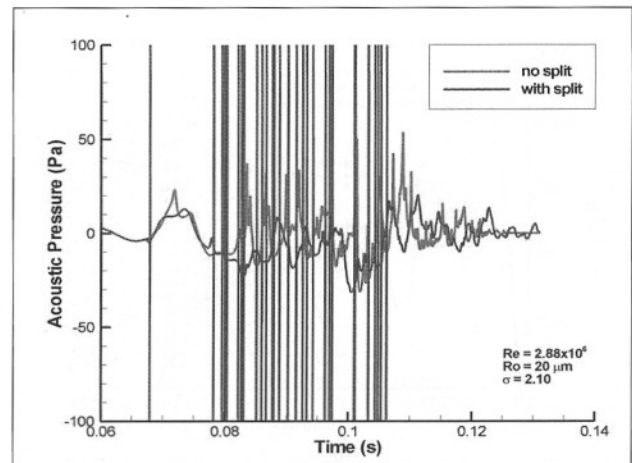


Figure 21. Acoustic pressure signal from 100 nuclei of size $20\text{ }\mu\text{m}$ with splitting compared to that without splitting.

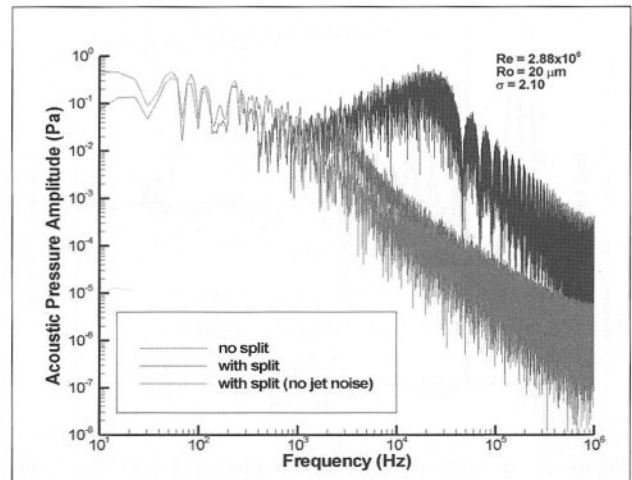


Figure 22. Amplitude spectrum of the acoustic pressure signal from 100 nuclei of size $20\text{ }\mu\text{m}$ with splitting compared to that without splitting. Also shown is the influence of the inclusion of the reentrant jet noise on the results.

created by the bubble splitting. If the jet noise is considered, the spectrum has a peak at 25 kHz . This frequency corresponds to the duration of the jet noise, $40\text{ }\mu\text{s}$, at this cavitation number.

6. Multiple splitting

The bubble splitting model used above is based on the non-spherical axisymmetric bubble simulations starting from the first cycle of the bubble growth. In such simulations, the numerical computations usually cannot be continued through the collapse and rebound of the sub-bubbles because of the touchdown of the developed reentrant jets and the instabilities of the collapsing bubbles. Therefore, the non-spherical simulations cannot tell if the newly born sub-bubbles would split again or not. The first cycle usually has the strongest growth because it occurs just after the nucleus passes the minimum pressure region of the

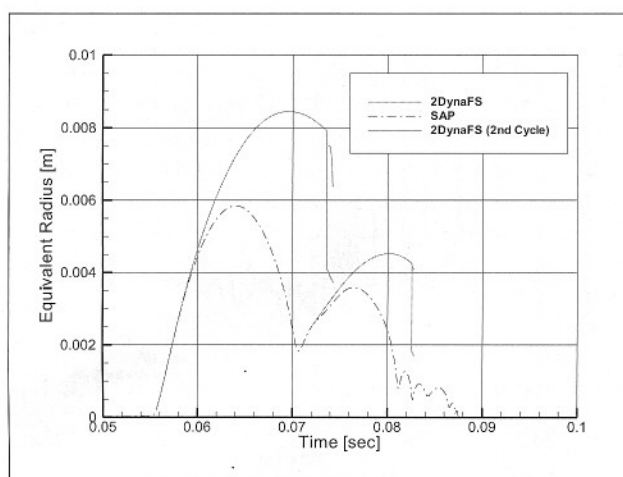


Figure 23. Two 2DynaFS[©] simulations, one starting from the beginning of the first cycle and the other from the second cycle of the bubble growth predicted by SAP with $20\text{ }\mu\text{m}$ nucleus at $\sigma = 2.10$.

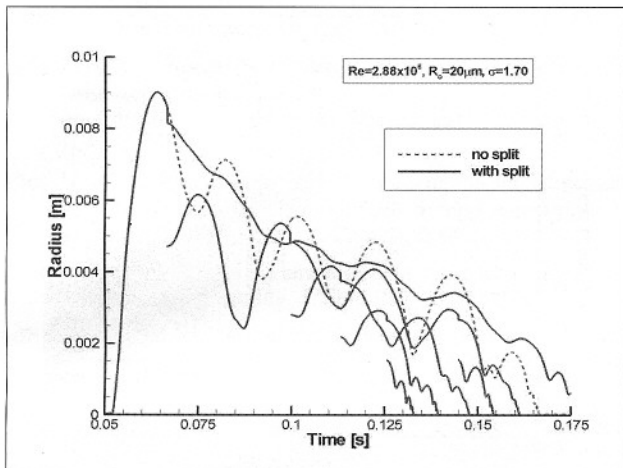


Figure 24. Bubble radii of the sub-bubbles from a $20\text{ }\mu\text{m}$ nucleus with multiple splitting at $\sigma = 1.70$.

tip vortex. The bubble growth in the second and later cycles is weaker than the first because the pressure becomes higher and higher as the bubble moves downstream. Would the sub-bubble placed a little downstream of the minimum pressure region of the tip vortex split again? This question can be answered by performing a non-spherical simulation from the second cycle of the SAP spherical simulation because the local pressure encountered by the bubble nucleus a bubble cycle downstream would be very similar to that of the sub-bubble after the splitting.

In Figure 23, two 2DynaFS[©] simulations are shown, one starting from the beginning of the first cycle and the other from the beginning of the second cycle of the SAP prediction. Even though the local pressure encountered by the bubble in the second cycle is higher than that of the first, the bubble elongates and splits in the same way. The only major difference between the two cases is the amount of the growth, i.e. about 400 times in the first cycle vs. about twice in the second cycle. The characteristics of the

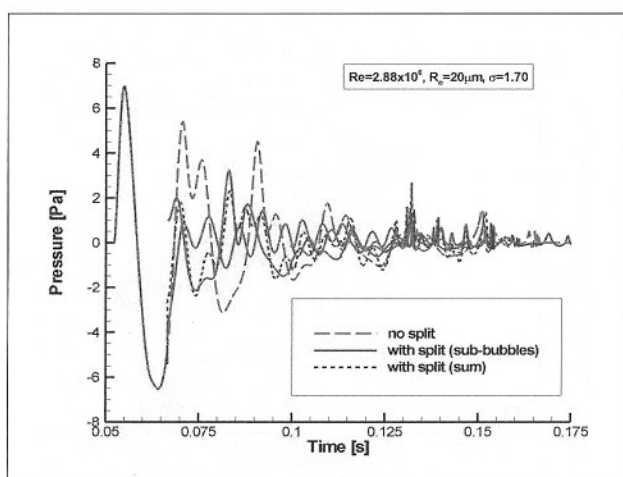


Figure 25. Acoustic pressure signals of the sub-bubbles and their sum from a $20\text{ }\mu\text{m}$ nucleus with multiple splitting at $\sigma = 1.70$.

Table I. Characteristics of the bubble splitting in the first and the second cycles.

	1st cycle	2nd cycle
$R_{eq,split}/R_{eq,max}$	0.95	0.94
$R_{eq,1}/R_{eq,split}$	0.95	0.97
$R_{eq,2}/R_{eq,split}$	0.55	0.43

splitting in the second cycle are very similar to those in the first cycle as summarized in Table I.

Because the sub-bubbles also split under very similar criteria as the first splitting, we can apply the same bubble splitting model to successive splitting of the sub-bubbles. Results from such a simulation are shown in Figure 24 for a $20\text{ }\mu\text{m}$ nucleus. The bubble radii obtained for a cavitation number of 1.70 show several radii curves due to successive splits. None of the sub-bubbles grow larger than the first maximum radius reached by the initial nucleus. The corresponding acoustic pressure signal shown in Figure 25 becomes very complex with many new small signals appearing as the sub-bubbles become smaller and smaller. The amplitude spectrum of the combined signal is shown in Figure 26. Compared to the spectrum without splitting, the spectrum with multiple splitting has richer contents over all frequencies above a couple of hundreds kHz.

The successive splits of sub-bubbles can also be applied to simulations in the field of nuclei. Following the nuclei distribution used by Hsiao and Chahine [11], 142 nuclei of size distributions between 5 and $50\text{ }\mu\text{m}$, as shown in Figure 27, are randomly distributed in the box-like volume of $0.1\text{ m} \times 0.01\text{ m} \times 0.006\text{ m}$ just in front of the blade tip. The void fraction based on the bubble distribution and the box-like volume is $1.46 \cdot 10^{-6}$.

The acoustic pressure signal obtained from the simulation is shown in Figure 28, and its amplitude spectrum is shown in Figure 29. The pressure signal obtained from the distribution of nuclei sizes with multiple splits has smaller peaks, and has increased higher frequency con-

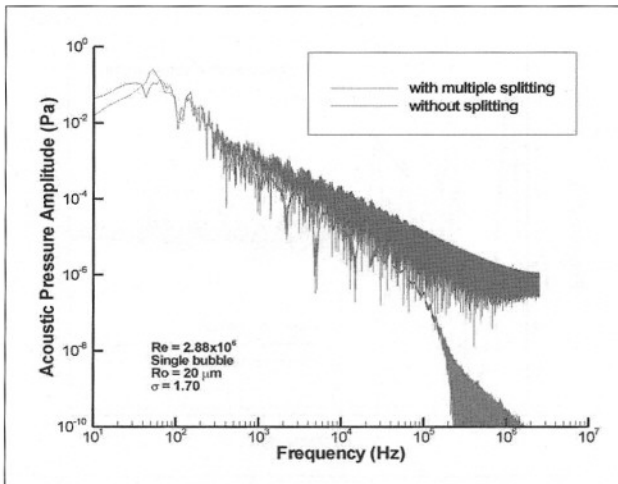


Figure 26. Amplitude spectrum of the acoustic pressure signal from $20 \mu\text{m}$ nucleus with multiple splitting at $\sigma = 1.70$.

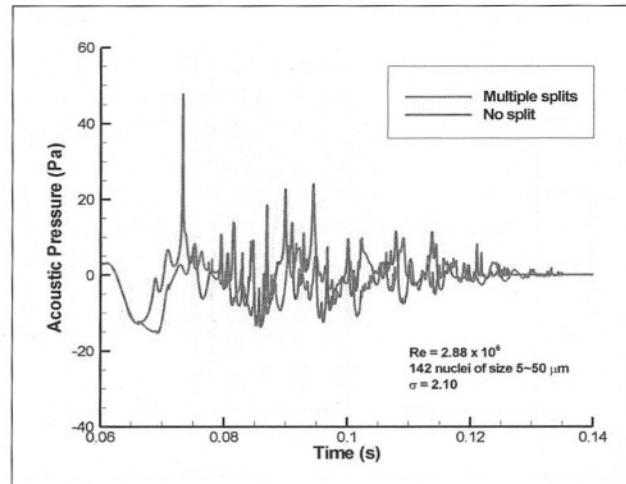


Figure 28. Acoustic pressure signal from 142 nuclei of size distribution from 5 to $50 \mu\text{m}$ with multiple splitting at $\sigma = 2.10$ compared to that without splitting.

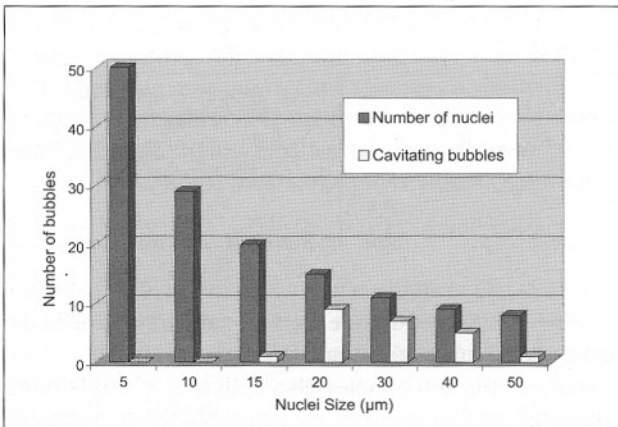


Figure 27. Distribution of 142 nuclei of sizes from 5 to $50 \mu\text{m}$ and the resulting number of nuclei that cavitate in the simulation.

tents (approximately higher than 10 kHz) and less low frequency contents (approximately lower than 10 kHz) than that without splits.

7. Conclusions

In order to further develop a tool to study scaling of cavitation inception and noise, we have developed a Surface Averaged Pressure (SAP) spherical model combined with a bubble splitting model derived from non-spherical bubble simulations. The method accounts for a cascade of splits of the sub-bubbles and includes noise from reentrant jets. During the development of the model, we have found that the bubble can lead to splitting even further downstream of the minimum pressure region, allowing successive multiple splitting of the sub-bubbles. Our numerical simulations show that at least the second splitting of sub-bubbles has characteristics very similar to those of the first splitting. This enhanced SAP model is applied to single and multiple nuclei simulations in a typical tip vortex flow field.

Application of the model to various conditions and bubble sizes show that visual detection of the cavitation is not

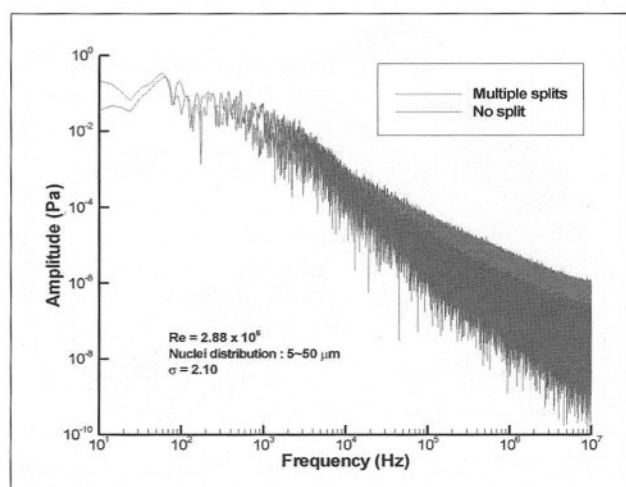


Figure 29. Amplitude spectrum of the acoustic pressure signal from 142 nuclei of size distribution from 5 to $50 \mu\text{m}$ with multiple splitting at $\sigma = 2.10$ compared to that without splitting.

affected by the inclusion of the successive nuclei splitting because the sub-bubbles never grew larger than the first maximum size. However, bubble splitting has the following effects on the acoustic detection of cavitation: (a) The noise from reentrant jets after the split dominates the pressure signal from the rebounds of the original nucleus and sub-bubbles created from it through splitting. The jet noise contributes to a distinct peak in the spectrum. (b) The resulting acoustic pressure from the rebounds of the sub-bubbles is smaller than the pressure from the rebounds of the original nucleus without splitting. However, compared to the spectrum without splitting, the sub-bubble noise has an amplitude spectrum with more high frequency content and less low frequency content. This trend of shifting of frequency contents in the spectrum is a direct result of the bubble population redistribution from the large size original nucleus to many small size sub-bubbles.

Acknowledgement

This work was conducted at Dynaflow, Inc. The research has been supported by the Office of Naval Research under the contract number N00014-04-C-0110 monitored by Dr. Ki-Han Kim. The authors greatly appreciate this support. Authors would like to thank Dr. Chao-Tsung Hsiao for his assistance especially with regards to the Surface Averaged Pressure (SAP) Model.

References

- [1] B. W. McCormick: On cavitation produced by a vortex trailing from a lifting surface. *J. Basic Eng.* **84** (1962) 369–370.
- [2] R. E. A. Arndt: Cavitation in fluid machinery and hydraulic structures. *Ann. Rev. Fluid Mech.* **13** (1981) 273–328.
- [3] D. H. Fruman, C. Dugue, P. Cerruti: Tip vortex roll-up and cavitation. ASME Cavitation and Multiphase Flow Forum, FED **109** (1991) 43–48.
- [4] D. H. Fruman, F. Castro, A. Pauchet, T. Pichon: On tip vortex turbulence, wandering and cavitation occurrence. 2nd Int. Symposium on Cavitation, Tokyo, Japan, 1994.
- [5] C. J. Chesnakas, S. D. Jessup: Tip-vortex induced cavitation on a ducted propulsor. Proc. ASME Symposium on Cavitation Inception, FEDSM2003-45320, Honolulu, Hawaii, 2003.
- [6] G. L. Chahine: Nuclei effects on cavitation inception and noise. Keynote presentation, 25th Symposium on Naval Hydrodynamics, St. John's, Canada, 2004.
- [7] R. Latorre: TVC noise envelope – an approach to tip vortex cavitation noise scaling. *J. Ship Res.* **26** (1982) 65–75.
- [8] P. Ligneul, R. Latorre: Study on the capture and noise of spherical nuclei in the presence of the tip vortex of hydrofoils and propellers. *Acustica* **68** (1989) 1–14.
- [9] C.-T. Hsiao, L. L. Pauley: Study of tip vortex cavitation inception using Navier-Stokes computation and bubble dynamics model. *J. Fluids Eng.* **121** (1999) 198–204.
- [10] C.-T. Hsiao, G. L. Chahine, H. Liu: Scaling effects on prediction of cavitation inception in a line vortex flow. *J. Fluid Eng.* **125** (2003) 53–60.
- [11] C.-T. Hsiao, G. L. Chahine: Effect of vortex/vortex interaction on bubble dynamics and cavitation noise. Proc. 5th Int. Symposium on Cavitation, CAV2003, Osaka, Japan, 2003.
- [12] C.-T. Hsiao, G. L. Chahine: Prediction of vortex cavitation inception using coupled spherical and non-spherical models and Navier-Stokes computations. *J. Marine Science and Technology* **8** (2004) 99–108.
- [13] C.-T. Hsiao, G. L. Chahine: Scaling of tip vortex cavitation inception noise with a bubble dynamics model accounting for nuclei size distribution. *J. Fluids Eng.* **127** (2005) 55–65.
- [14] J.-K. Choi, G. L. Chahine: Noise due to extreme bubble deformation near inception of tip vortex cavitation. *Physics of Fluids* **16** (2004) 2411–2418.
- [15] J.-K. Choi, G. L. Chahine: A numerical study on the bubble noise and the tip vortex cavitation inception. *J. Ship and Ocean Technology* **7** (2003) 13–33.
- [16] J.-K. Choi, G. L. Chahine: Non-spherical bubble behavior in vortex flow fields. *Computational Mechanics* **32** (2003) 281–290.
- [17] J.-K. Choi, G. L. Chahine, C.-T. Hsiao: Characteristics of bubble splitting in a tip vortex cavitation. Proc. 5th Int. Symposium on Cavitation, CAV2003, Osaka, Japan, 2003.
- [18] J.-K. Choi, G. L. Chahine: Tip vortex cavitation inception study using the Surface Averaged Pressure (SAP) model combined with a bubble splitting model. 25th Symposium on Naval Hydrodynamics, St. John's, Canada, 2004.
- [19] M. Rebow, J.-K. Choi, J. Choi, G. L. Chahine, S. L. Ceccio: Experimental validation of BEM code analysis of bubble splitting in a tip vortex flow. 11th Int. Symposium on Flow Visualization, University of Notre Dame, Notre Dame, IN, 2004.
- [20] M. S. Plesset: Dynamics of cavitation bubbles. *J. Applied Mechanics* **16** (1948) 228–231.
- [21] F. R. Gilmore: The growth or collapse of a spherical bubble in a viscous compressible liquid. Engineering Division Report 26-4, California Institute of Technology, 1952.
- [22] V. E. Johnson, T. Hsieh: The influence of the trajectories of gas nuclei on cavitation inception. 6th Symposium on Naval Hydrodynamics, 1966, 163–179.
- [23] W. L. Haberman, R. K. Morton: An experimental investigation of the drag and shape of air bubble rising in various liquids. DTMB Report 802, David Taylor Model Basin, 1953.
- [24] G. L. Chahine, K. Sarkar, R. Duraiswami: Strong bubble/flow interaction and cavitation inception. Technical Report 94003-IONR, Dynaflow, Inc., 1997.

Numerical Study of Cavitation Inception due to Vortex/Vortex Interaction in a Ducted Propulsor

C.-T. Hsiao and G. L. Chahine

DYNAFLOW, INC.

10621-J Iron Bridge Road, Jessup, MD 20794

Email: ctsung@dynafollow-inc.com, glchahine@dynafollow-inc.com

<http://www.dynaflow-inc.com>

ABSTRACT

Cavitation inception in a ducted propulsor was studied numerically using Navier-Stokes computations and bubble dynamics models. Experimental observations of the propulsor model and previous numerical computations using Reynolds-Averaged Navier-Stokes (RANS) codes indicated that cavitation inception occurred in the region of interaction of the leakage and trailing tip vortices. The RANS simulations failed however to predict correctly both the cavitation inception index value and the inception location. To improve the numerical predictions, we complemented here the RANS computations with a direct Navier-Stokes simulation in a reduced computational domain including the region of interaction of the two vortices. Initial and boundary conditions in the reduced domain were provided by the RANS solution of the full ducted propulsor flow. Bubble nuclei were released in this flow field, and spherical and non-spherical bubble dynamics models were exercised to investigate cavitation inception. This resulted in a solution in much better agreement with the experimental measurements than the original RANS solution. Both the value of the cavitation inception index and the location of the cavitation inception were very well captured. The characteristics of the emitted acoustic signals and of the bubble shapes during a cavitation event were also computed.

1. Introduction

Prediction of vortex cavitation inception on marine propulsors is of great interest to naval applications and has been the subject of many studies seeking scaling laws for the prediction of cavitation inception. Existing scaling laws are typically formulated using data from open propellers and are not applicable to ducted propellers. Unlike most open propellers, which generally form a single trailing vortex, a ducted propeller typically exhibits two well-defined vortices: a trailing vortex formed near each blade tip trailing edge, and a stronger leakage vortex generated in the gap region between the blade and the duct wall. These two unequal co-rotating vortices introduce small-scale unsteady motions during vortex merging that add to the fluctuations resulting from upstream turbulence and vortex wandering^{1,2}

Recent experimental observations of cavitation inception on a ducted propulsor³ have indicated that the interaction between the tip-leakage vortex and the trailing-edge vortex cause cavitation inception to occur in the region where the two vortices merge. However, predictions of cavitation inception using the pressure field obtained by Reynolds-Averaged Navier-Stokes (RANS) computations^{5,6,7} or inferred from experimental velocity measurements⁴ were in poor agreement with the experimental observations in terms of both cavitation inception number and inception location.

A preliminary controversial conclusion made by Chesnaks and Jessup³ was that cavitation inception does not necessarily occur in the minimum pressure region. This conclusion, however, was drawn based on the inferred pressure field obtained from the measured average tangential velocities, using an assumed Rankine vortex profile. This not only neglects the effect of the axial velocities on the pressure field, but also relies on

time-averaged tangential velocities which could be significantly smaller than the instantaneous values, especially at downstream locations where vortex wandering may be significant. RANS computations with inadequate turbulence models and grid resolution can also result in over-diffusion and dissipation of the vortex flow^{8,9}. This usually leads to a significant under-prediction of the velocities in the vortex core at the downstream locations. In a combined numerical and experimental study of a tip vortex flow, Dacles-Mariani *et al.*⁸ used the measured flow field to specify the inflow and outflow boundary conditions of the vortex flow and investigated vortex preservation in the wake region. With the turbulence model turned off and significant grid refinement they were able to match the numerical solution results to the experimental measurements.

In the previous RANS simulations of the present propulsor flow, not only the flow field was not well resolved, also the effects of bubble dynamics on cavitation inception were not included. In our previous studies^{10,11,12} we have shown that inclusion of bubble dynamics can significantly affect the predictions of cavitation inception for both steady-state tip vortex flows and unsteady vortex/vortex interaction flow fields.

In the present study we aim at improving the numerical predictions of cavitation inception for a ducted propulsor in two ways: refinement of the flow field solution and inclusion of bubble dynamics. We consider a reduced computational domain which includes the region of interaction of the two vortices but excludes for simplicity the propulsor solid surfaces, and a direct Navier-Stokes simulation is conducted using initial and boundary conditions provided by RANS computations of the full ducted propulsor flow field. Then, a corrected spherical bubble dynamics model developed by Hsiao and Chahine^{10,11} and a two-way flow-coupled non-spherical bubble dynamics model

developed by Hsiao and Chahine^{12,13} are applied to study bubble dynamics and to predict cavitation inception.

2. Numerical Approach

2.1 Flow Configuration

We consider the three-bladed NSWCCD Propeller 5206, a rotating ducted propulsor with tip diameter of 0.8503m and a constant chord of 0.3812m from hub to tip. This propeller operates in a duct having a diameter of 0.8636m. Detailed propulsor geometry and experimental observations are described by Chesnakas and Jessup³. Numerical studies^{5,6,7} using several RANS codes, described the flow field of this propulsor when operating under an advance coefficient, $J=0.98$, with an inflow velocity, $U_\infty = 6.96 \text{ m/s}$. The corresponding Reynolds number based on the blade tip radius and the inflow velocity was $R_e = 3 \times 10^6$. Although the numerical studies all gave results in reasonable agreement with the experimental measurements for the averaged local flow field quantities, the predicted cavitation inception number, σ_i , varied between 6.5 and 8.0, and the inception location, x_i , was about 0.1 chord length downstream from the tip trailing edge. However, the experimental observations gave much larger values for both inception number and location: $\sigma_i \sim 11.5$, and $x_i \geq 0.5$.

To improve on the RANS numerical solution, we constructed a reduced computational domain behind the trailing edge of the propulsor blade that included the region of interaction of the two vortices and excluded propulsor solid surfaces. The basic computational domain had a square cross area of $0.094\text{m} \times 0.094\text{m}$ and extended from

the tip trailing edge to 0.34 m downstream from the tip trailing edge. Figure 1 illustrates the location of this reduced computational domain relative to the ducted propulsor.

2.2 Navier-Stokes Computations

In the reduced domain, the flow is obtained via direct numerical solution of the Navier-Stokes equations without turbulence modeling. Since the present computation is conducted in a rotating frame attached to the propeller blade, source terms, *i.e.* the centrifugal force and the Coriolis force terms, are added to the momentum equation. The resulting unsteady incompressible continuity and Navier-Stokes equations written in non-dimensional vector form and Cartesian notations are given as

$$\nabla \cdot \mathbf{u} = 0, \quad (1)$$

$$\frac{D\mathbf{u}}{Dt} = -\nabla p + \frac{1}{R_e} \nabla^2 \mathbf{u} + \Omega^2 \mathbf{r} - 2\Omega \times \mathbf{u}, \quad (2)$$

where $\mathbf{u} = (u, v, w)$ is the velocity, p is the pressure, \mathbf{r} is the radial position vector, Ω is the angular velocity, $R_e = \rho u^* L^* / \mu$ is the Reynolds number, u^* and L^* are the characteristic velocity and length, ρ is the liquid density, and μ is the liquid dynamic viscosity.

To solve Equations (1) and (2) numerically, a three-dimensional incompressible Navier-Stokes solver, DF_UNCLE, initially developed by the Mississippi State University and modified by DYNAFLOW is applied. DF_UNCLE is based on the artificial-compressibility method¹⁴ in which a time derivative of the pressure is added to the continuity equation as

$$\frac{1}{\beta} \frac{\partial p}{\partial t} + \nabla \cdot \mathbf{u} = 0, \quad (3)$$

where β is an artificial compressibility factor. As a consequence, a hyperbolic system of equations is formed that can be solved using a time marching scheme. The method can be marched in pseudo-time to reach a steady-state solution. To obtain a time-dependent solution, a Newton iterative procedure is performed at each physical time step in order to satisfy the continuity equation. In the present study the time-accurate solution is obtained when the maximum normalized velocity divergence is less than 1.0×10^{-3} . Detailed descriptions of the numerical scheme can be found in Ref. 15.

2.3 Initial and Boundary Conditions

Since the unsteady Navier-Stokes computations were conducted in the reduced domain, appropriate initial conditions are required. These conditions were obtained from the steady state solution of the full ducted propulsor flow obtained by Yang⁷ using a RANS computation. The original coarser RANS solution was interpolated for the present finer reduced domain unsteady computations. Figure 2 shows the interpolated RANS pressure contours at different streamwise locations to indicate the position of the main vortex in the reduced domain. Figure 3 shows the pressure contours and the velocity vectors at the inlet $x-r$ plane boundary. The two co-rotating vortices (the tip-leakage vortex and the trailing edge vortex) can be readily seen. The tip-leakage vortex is much stronger than the trailing-edge vortex.

Figure 4 shows the reduced computational domain and its boundaries. In addition to the inlet and outlet boundaries, there are three side boundaries in the liquid domain and one boundary bounded by the duct wall. At the inlet boundary, the method of characteristics was imposed with the three components of velocities specified based on

the RANS solution. At the outlet boundary, all variables were extrapolated from the inner domain except for the grid points on the duct wall where the initial RANS value of the pressure was fixed. For the three side boundaries, both velocities and pressures were imposed as given by the RANS solution.

2.4 Bubble Dynamics Models

Two bubble dynamics models, a “corrected” spherical model and a non-spherical model, were used in this study. The spherical bubbles were tracked using a Lagrangian scheme in a flow field combining the reduced domain and the RANS domain outside of it. The grids of the reduced domain were overset to the overall propulsor grids. As a bubble was released upstream of the propeller, it was subjected to the flow field given by the RANS solution. Once the bubble entered the reduced domain, the flow field obtained by the direct simulation of the Navier Stokes equations was applied. Bubble transport was modeled via the motion equation described by Johnson and Hsieh¹⁶ while the bubble dynamics was simulated by solving the Surface Averaged Pressure (SAP) spherical bubble model equations developed by Hsiao and Chahine^{10,11}.

The non-spherical bubble dynamics model was embedded in the unsteady Navier-Stokes solver, DF-UNCLE, with appropriate free surface boundary conditions and a moving Chimera grid scheme^{12,13}. Since unsteady Navier-Stokes computations are time-consuming, this non-spherical model was combined with the spherical model mentioned above. The spherical model was used to track the bubble during its capture by the vortex and the non-spherical model was turned on only after the bubble size exceeds a preset limit value. When the non-spherical model was turned on, the flow field due to the

spherical bubble motion and volume change is superimposed on the liquid phase flow field solution to provide an initial condition for the unsteady viscous computations. This model allowed the bubble to deform non-spherically and a full two-way interaction between the bubble and the flow field could be obtained. Detailed description of this model and numerical implementations can be found in Refs 12, 13 and 17.

3. Results and Discussion

3.1 Grid and Domain Size Independence Study

The simulation of the vortex/vortex interaction in the reduced computational domain was conducted with no turbulence modeling. The mean RANS flow solution was specified at the inlet boundary and different grid resolutions and computational domain sizes were considered. Unsteady turbulent fluctuations from upstream are being simulated in on-going efforts and are the subject of a second publication¹⁸.

For the basic computational domain size described in Section 2.1, we generated a 4-block grid with a total of 101 grid points in the streamwise direction and three different density cross flow grids: 61×61 , 121×121 and 181×181 , in order to study the influence of grid resolution. All grid points were evenly distributed without stretching. This resulted in a uniform grid size of 3 mm in the streamwise direction and 0.5 mm in both cross directions for the finest grid. At least 34 grid points were within the vortex core in each direction for the finest grid since the vortex core size had a diameter at the trailing edge of about 17mm.

Figure 5 shows a comparison of the resulting pressure coefficients, C_p , along the vortex center line for the three grid densities. We can also observe convergence of the

simulations as the grid is refined. The maximum differences in Cp_{min} between the 121×121 and the 181×181 grids are within 3%. We can however observe a major difference between the RANS solution and the present computations as one moves downstream. While the RANS solution gives for the minimum pressure coefficient, Cp_{min} , a value of about -8.5 at a distance of about 0.1 chord length, the present computations yield a value of -11.2 at a location 0.35 chord length downstream from the tip trailing edge. These values are much closer to the experimental results.

To further examine the grid dependence, we doubled the number of grid points in the streamwise direction with the cross plane having 121×121 grid points. As shown in Figure 6 , doubling the grid resolution in the streamwise direction only slightly changed the solution.

In addition to the grid resolution, we also studied the effect of the computational domain size on the solution by constructing two larger computational domains while maintaining the same grid resolution as the 121×121×101 case. One of the computational domains was constructed by doubling the domain length in the azimuthal direction and extending it 50% of length in radial direction. Note that the top boundary in the radial direction was always bounded by the duct wall. The second computational domain was constructed by extending 50% of the length in the streamwise direction. The resulting pressure coefficients along the vortex center line obtained with these two larger computational domains are compared to the basic domain and shown in Figure 7. It is seen that all three cases produced practically the same solution (less than 1% difference).

Since increasing the grid and domain size from the basic computational domain (121×121×101 grid points) only yielded small differences in the pressure coefficients,

this basic domain size and grid resolution were used for subsequent bubble dynamics computations in order to minimize CPU time.

3.2 Prediction of Cavitation Inception for Single Phase Flow

In Figure 5 the pressure coefficient along the vortex centerline obtained by the RANS computation is compared to the present direct Navier Stokes unsteady computations in the reduced domain. Major differences are seen between these two results. The RANS computation predicts $Cp_{min}=-8.2$ at $s/C=0.1$ where s is the helical arc distance from the tip trailing edge and C is the chord length, while the present simulations show $Cp_{min}=-11.2$ at $s/C=0.35$ for the $181\times 181\times 101$ grid, which is much closer to the experimental observations. This indicates cavitation inception at $\sigma \sim 11.5$ at about 0.5 chord length downstream of the trailing edge. The failure of the RANS computations is probably due to excessive vortex diffusion and dissipation.

Another qualitative comparison can be made between the two solutions by displaying the same iso-pressure surfaces obtained in each case as shown in Figure 8. This is similar to visualizing the cavitating vortices at different cavitation numbers. The present results agree with the experimental observations which show a long-extended fully cavitated vortex core at $\sigma = 5.6$ (see Figure 9).

It is important to examine the flow field near the location where the pressure reaches its minimum value. Hsiao and Chahine¹⁹ have shown that the two co-rotating vortices periodically approach each other and get closer during the vortex merger. The present computations show that as they move closer, the flow in the axial direction is accelerated and results in further decrease of the pressure at the vortex center. The

computed Cp and axial velocity along the vortex center line are shown together in Figure 10. We can observe that the pressure correlates very well with the axial velocity and is in phase opposition. As the velocity reaches a maximum value, the pressure in the vortex center drops to a minimum. The axial velocity variations are, however, mostly ignored by other investigations.

We would like to point out that, although the computations in the present study was unsteady, the simulation actually converged to a quasi steady-state solution since the input solution to the inlet boundary was steady. The instability due to strong vortex/vortex interaction as shown in Ref. 19 was not observed in the present problem. This is probably due to the relatively weak trailing-edge vortex in the problem. Indeed, Hsiao and Chahine¹⁹ have shown that as the relative strength of the main vortex is increased, the merger of the two co-rotating vortices occurs faster and the unsteady interaction becomes weaker.

3.3 Area of Bubble Capture: “Window of Opportunity”

The “window of opportunity” through which a nucleus needs to enter to be captured by the vortex and generate strong acoustic signals has been studied for a finite-span tip vortex flow by Hsiao and Chahine¹¹. It is also important to determine this “window of opportunity” for the current flow field because with the knowledge of the location and size of this small window, we are able to distribute and follow nuclei more efficiently. In addition, this concept provides physical understanding of the flow field and of the nuclei that are captured by the vortex. Near inception, the size of the “window of opportunity” is directly related to the probability of cavitation event occurrence.

To establish the “window of opportunity” a rectangular release area was specified upstream of the tip leading edge of the propulsor in the $x-r$ plane where bubble nuclei were released from a 15×11 grid points array. Figure 11 illustrates the location of the release area relative to the propulsor blade. A high arbitrary value for the cavitation number was selected ($\sigma=12.0$) such that each nucleus was tracked and the minimum pressure it encountered during its travel was recorded and assigned to the release point. The corresponding bubble size increased during its path in the propeller flow field by less than 10 %. This enabled us to plot a contour of the minimum encountered pressure coefficient for the release grid array and to obtain a contour plot of the cavitation probability in the “window of opportunity” for each case. This selection was to obtain a bound of the area where bubbles passing through this area would be affected by the vortex field. The details on the encountered pressures vary with the selection of σ but the area geometric bounds do not. The capture area concept enabled minimization of the number of bubbles that needed to be tracked in the propeller flow domain.

Figure 12 shows contours of the minimum encountered pressure coefficients for three different nuclei sizes, $R_0 = 5, 10, 20 \mu\text{m}$. The contours are blanked out for the release points where the nuclei collided with the propeller surface. It is seen that the size of the “window of opportunity” becomes smaller and its location shifts closer to the propeller pressure side surface as the nucleus size decreases. This brings out an important selection concept on the probability of cavitation for waters containing very small nuclei. Not only much lower pressures are needed to get such waters to cavitate (smaller bubbles require much lower pressures to grow explosively¹¹) but also fewer of

them can participate into the cavitation event because of the reduced window of opportunity.

3.4 Single Bubble Dynamics for Prediction of Cavitation Inception

Experimental observations conducted by Chesnakas and Jessup³ using a high speed video camera and a hydrophone were able to capture the bubble and its emitted acoustic signal during a cavitation event. According to the duration of the acoustic signal, the cavitation events were categorized into “popping” and “chirping” events. They stated that the “popping” event had a very short duration of noticeable acoustic signal less than 0.3 ms and that the bubble virtually remained spherical when its size was less than 0.1 mm in diameter. The “chirping” event had a much longer duration ranging from 0.3 to 10 ms, and the bubble had an elongated shape. They found that all the cavitation inception events occurred near or behind a location 0.5 chord length downstream of the tip trailing edge.

To simulate different cavitation events, we investigated the bubble behavior and the emitted acoustic signal during bubble dynamics for different initial nuclei sizes at different cavitation numbers. We found that “popping” cavitation events can be observed for small bubbles. Figure 13 shows the bubble size variation and the emitted acoustic signal for an initial nucleus size, $R_0=6 \mu\text{m}$ at $\sigma=10.47$. It is seen that the maximum bubble size achieved is about 0.1mm in diameter and that the noticeable acoustic signal only lasts about 0.3ms. Figure 14 shows an example for a “chirping” event in which the bubble grows to a much larger size (~1.7 mm) and the duration of the acoustic signal is much longer (~2.5 ms) for an initial nucleus size, $R_0=20\mu\text{m}$ at $\sigma=10.75$.

Figure 13 and 14 also show the pressure encountered by the bubble during its journey. There is a small time delay for the bubble to grow to its maximum size after encountering the minimum pressure. This delay significantly increases when a cavitation event is produced by a small size nucleus. An example of such a cavitation event is shown in Figure 15 for $R_0=5\text{ }\mu\text{m}$ at $\sigma=10.3$.

To illustrate where the cavitation events occur in the flow field, the bubble trajectory and size variations are plotted with the propulsor blade and some iso-pressure surfaces as shown in Figure 16. It is seen that for larger initial nuclei radius, R_0 , the cavitation events occur at a location slightly earlier than the experimental observations while for smaller R_0 the bubbles grow to a maximum size near the location 0.5 chord length downstream of the tip trailing edge.

Bubble dynamics was also studied using our non-spherical models¹². Figure 17 compares the bubble shapes obtained with the spherical and the non-spherical model for $R_0=20\mu\text{m}$ at $\sigma=10.75$. It is seen that both models predicted almost the same maximum growth size. In non-spherical model the bubble elongated in the axial direction and took a quasi-cylindrical shape as it grew. However, for $R_0=20\text{ }\mu\text{m}$ at $\sigma=10.85$ the bubble remained almost spherical at its maximum size as shown in Figure 18. For both cases the bubble started to collapse after reaching its maximum size. The non-spherical computations, however, failed here to continue once strong deformations developed over the bubble surface during the collapse.

3.5 Multiple Bubble Dynamics for Prediction of Cavitation Inception

In order to simulate a realistic nuclei flow field as exists in nature or in the waters of a cavitation tunnel, Hsiao and Chahine¹¹ used a statistical nuclei distribution model and showed that the nuclei size distribution has a strong influence on the prediction of cavitation inception. Nuclei size distribution studies in water tunnels, lakes and oceans²⁰ show a power-law distribution for the number density distribution function, $n(R) \approx 1/R^\alpha$, where R is the nucleus radius and the exponent α lies between 3.5 and 4.0. Since the nuclei size distribution is not available for the experiments conducted on the ducted propulsor investigated here, we have selected two very different nuclei size distributions, with $\alpha=3.0$ and 4.5, which encompass the nuclei size distributions reported for natural waters. We then compared their effect on the prediction of cavitation inception. The first nuclei size distribution contained relatively larger nuclei sizes ranging from 2.5 to 25 μm while the other one contained smaller nuclei sizes ranging from 2.5 to 10 μm . In both cases we randomly released the nuclei from a $0.02\text{m} \times 0.03\text{m}$ window in the computational domain. A total of 600 nuclei were released within a 0.4 second period. The nuclei size number density distribution and the total number of nuclei released for both cases are shown in Figure 19.

As the nuclei traveled through the computational domain, the emitted acoustic signals were monitored. The acoustic pressure was monitored on the duct wall at a location 0.5 chord length downstream of the tip trailing edge. A series of computations were conducted at different cavitation numbers for both nuclei distributions to obtain acoustic signals for conditions above and below cavitation inception. Figure 20 illustrates the acoustic signals for the larger size nuclei distribution at three different cavitation numbers.

From the results shown in Figure 20, we can define a cavitation inception number based on the number of cavitation events per unit time exceeding a certain value. Here a cavitation event is defined arbitrarily as occurring when an oscillating bubble emits an acoustic signal higher than 100 Pa. The curve of the number of cavitation events per second versus cavitation number is shown in Figure 21. It can be seen that there is a critical cavitation number above which no cavitation events occur. For nuclei size distribution No. 1 (larger bubbles) an abrupt rise in the number of cavitation events is seen when the cavitation number is below the critical cavitation number. Based on these curves one can determine the cavitation inception number for both cases by defining a criterion. For example, if one defines that 10 events per second are needed for cavitation inception, then we obtain a cavitation inception number $\sigma_i=10.9$ for the larger nuclei size distribution and $\sigma_i=10.6$ for the smaller nuclei size distribution can be deduced from Figure 21. Actually, the selection of the amplitude of the threshold peak and number of peaks per unit time should be a function of the application and of the detection capability of the observer. Therefore, we do not intend to propose a criterion here but to illustrate that the use of a bubble dynamics model can provide the researchers with a tool to predict the cavitation inception number similar to what is actually done in experimental observations. Chesnakas and Jessup (2003) in their experimental study defined the cavitation inception criterion as one event per second and obtained a cavitation inception number about 11.5. This inception number is very close to the critical cavitation number (~ 10.9) for the larger nuclei size distribution, but these results depend on the two criteria selected: amplitude of the peak and number of peaks per unit time.

4. Conclusions

In order to address grid resolution issues in RANS computations numerical simulations of the two interacting vortices in a ducted propulsor flow field were conducted in a reduced computational domain. It was found that numerical vortex diffusion and dissipation were significantly reduced with grid refinement. The resulting solutions illustrated with iso-pressure surfaces agree much better than the RANS computations with experimental observations for fully developed cavitation in the vortex core. The value of the cavitation inception number and the location of cavitation inception also agree significantly better with the experimental observations. No instability was seen in the vortex/vortex interactions due to the large strength of the tip-leakage vortex relative to the trailing-edge vortex. This leads to rapid merging of the two vortices. Further grid refinement and perturbed input conditions may be required to resolve any such instability.

The location and size of the “window of opportunity” through which a nucleus needs to enter to be captured by the vortex was identified for different nuclei sizes.

Bubble dynamics studies showed that the characteristics of the acoustic signals and bubble shapes as well as the location of cavitation inception resemble those observed experimentally. A bubble dynamics model tracking multiple bubbles was also applied to study the effect of nuclei size distribution and to predict cavitation inception in real flow field conditions. Different nuclei size distributions and various definitions of the cavitation inception criterion were found to influence the cavitation inception number. However, the range of cavitation inception numbers ($\sigma_i \sim 10.8-11.0$) was found to agree

much better than previous studies ($\sigma_i \sim 6.5-8.2$) with the experimental measurements ($\sigma_i \sim 11.5$).

ACKNOWLEDGMNETS

This work was conducted at DYNAFLOW, INC. (www.dynaflow-inc.com) and was supported by the Office of Naval Research under contract No. N00014-04-C-0110 monitored by Dr. Ki-Han Kim. Dr. Kim's support is gratefully appreciated. The RANS solution of the full propulsor flow was provided by Dr. C. I. Yang from NSWCD and the experimental data was provided by Dr. Christopher J. Chesnakas and Dr. Stuart D. Jessup from NSWCD. Their cooperation and help are greatly appreciated.

REFERENCES

- ¹ A. L. Chen, J. D. Jacob, and O. Savas, "Dynamics of co-rotating vortex pairs in the wakes of flapped airfoils," *J. Fluid Mech.* **382**, 155 (1999).
- ² W. J. Devenport, C. M. Vogel, and Zsoldos, "Flow structure produced by the interaction and merger of a pair of co-rotating wing-tip vortices," *J. Fluid Mech.* **394**, 357 (1999).
- ³ C. J. Chesnakas and S. D. Jessup, "Tip-vortex induced cavitation on a ducted propulsor," Proceedings of the ASME Symposium on Cavitation Inception, FEDSM2003-45320, Honolulu, Hawaii, July 6-10, 2003.

⁴ G. Oweis, S. Ceccio, C. J. Cheskanas, D. Fry, and S. D. Jessup, "Tip leakage vortex (TLV) variability from a ducted propeller under steady operation and its implications on cavitation inception," 5th International Symposium on Cavitation, Osaka, Japan, November 1-4, 2003.

⁵ W. H. Brewer, D. L. Marcum, S. D. Jessup, C. J. Chesnakas, D.G. Hyams, and K. Sreenivas, "An unstructured RANS study of tip-leakage vortex cavitation Inception," Proceedings of the ASME Symposium on Cavitation Inception, FEDSM2003-45311, Honolulu, Hawaii, July 6-10, 2003.

⁶ J. Kim, "Sub-visual cavitation and acoustic modeling for ducted marine propulsor," Ph.D. Thesis, The University of Iowa, 2002.

⁷ C. I. Yang, M. Jiang, C.J. Chesnakas, and S.D. Jessup, "Numerical simulation of tip vortices of ducted-rotor", NSWCCD-50-TR-2003/46, 2003.

⁸ J. Dacles-Mariani, G. G. Zilliac, J. S. Chow, and P. Bradshaw, "Numerical/experimental study of a wingtip vortex in the near field," AIAA J., **33**, 1561 (1995).

⁹ C.-T. Hsiao and L. L. Pauley, "Numerical study of the steady-state tip vortex flow over a finite-span hydrofoil," ASME J. Fluids Eng. **120**, 345 (1998).

¹⁰ C.-T. Hsiao, G. L. Chahine, H. L. Liu, "Scaling effects on prediction of cavitation inception in a line vortex flow," ASME J. Fluids Eng. **125**, 53 (2003).

¹¹ C.-T. Hsiao, G.L. Chahine, "Scaling of tip vortex cavitation inception noise with a statistic bubble dynamics model accounting for nuclei size distribution," ASME J. Fluids Eng. **127**, 55 (2005).

¹² C.-T. Hsiao, and G.L. Chahine, “Prediction of vortex cavitation inception using coupled spherical and non-spherical models and Navier-Stokes computations,” *J. Marine Science and Technology*, **8**, 99 (2004).

¹³ C.-T. Hsiao, and G.L. Chahine, “Numerical simulation of bubble dynamics in a vortex flow using moving Chimera grid and Navier-Stokes computations,” Fourth International Symposium on Cavitation CAV2001, Pasadena, CA, June 20-23, 2001.

¹⁴ A. J. Chorin, “A numerical method for solving incompressible viscous flow problems,” *J. Computational Physics*, **2**, 12 , 1967.

¹⁵ K. Vanden, D. L. Whitfield, “Direct and iterative algorithms for the three-dimensional Euler equations,” AIAA-93-3378, 1993.

¹⁶ V.E. Johnson, T. Hsieh, “The influence of the trajectories of gas nuclei on cavitation inception,” Sixth Symposium on Naval Hydrodynamics, pp. 163, 1966.

¹⁷ G.L. Chahine, “Nuclei Effects on Cavitation Inception and Noise,” 25th Symposium on Naval Hydrodynamics, St. John, Canada, 2004.

¹⁸ C.-T. Hsiao, and Chahine, G.L., “Effect of Unsteady Turbulent Fluctuations on Vortex/Vortex/Nuclei Interaction,” 26th Symposium on Naval Hydrodynamics, Rome, Italy, 2006.

¹⁹ C.-T. Hsiao, and G.L. Chahine, “Effect of vortex/vortex interaction on bubble dynamics and cavitation noise”, Fifth International Symposium on Cavitation CAV2003, Osaka, Japan, November 1-4, 2003.

²⁰ R.E. Franklin, “A note on the radius distribution function for microbubbles of gas in water,” ASME Cavitation and Mutliphase Flow Forum, FED-Vol. 135, pp.77, 1992.

To be published in Journal of Ship Research 2008

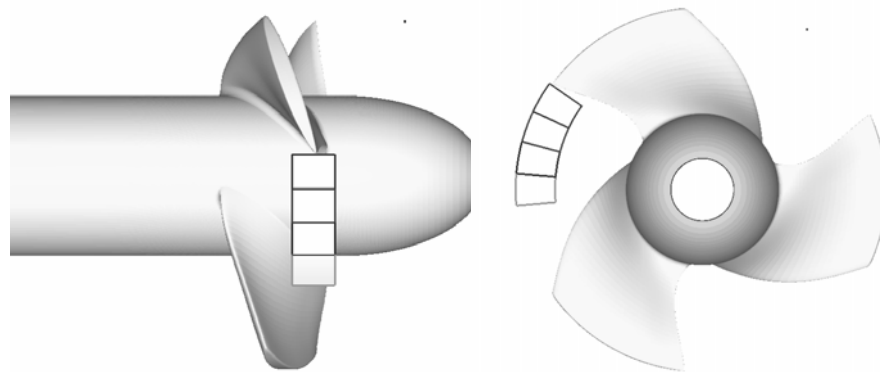


Figure 1. A view of the reduced computational domain in the three-bladed NSWCCD Propeller 5206 used for the current computations.

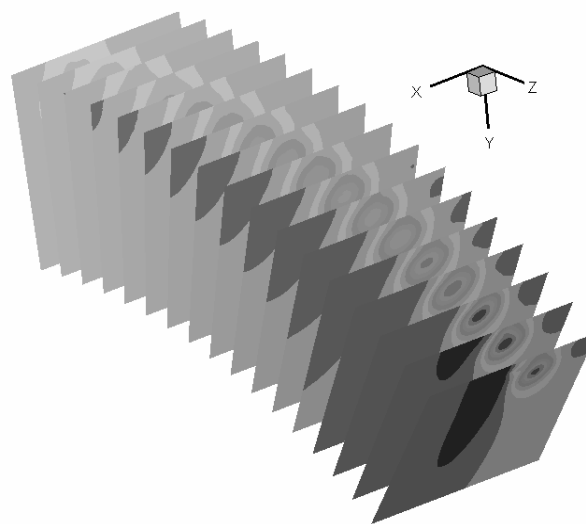


Figure 2. Pressure field in the reduced computational domain interpolated from the RANS solution.

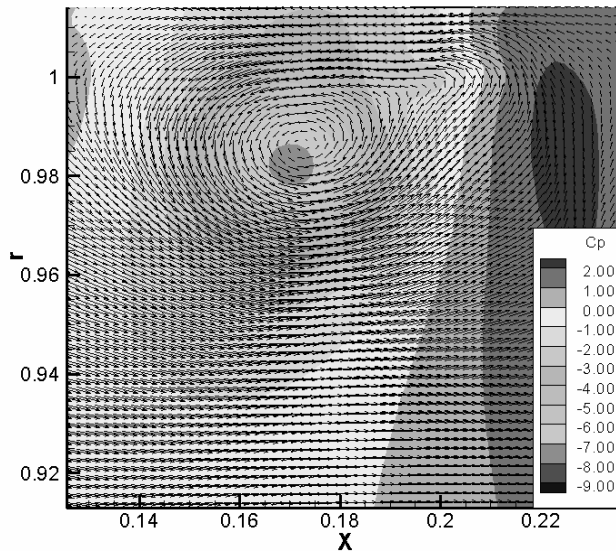


Figure 3. Pressure contours and velocity vectors imposed at the inlet boundary of the reduced domain in the $x-r$ plane.

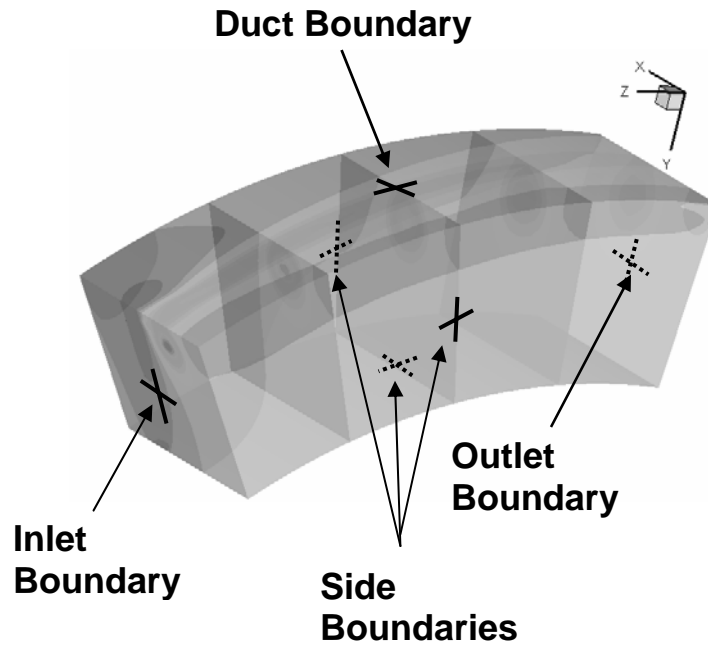


Figure 4. Geometry of the reduced computational domain bounded by six boundaries with different imposed boundary conditions.

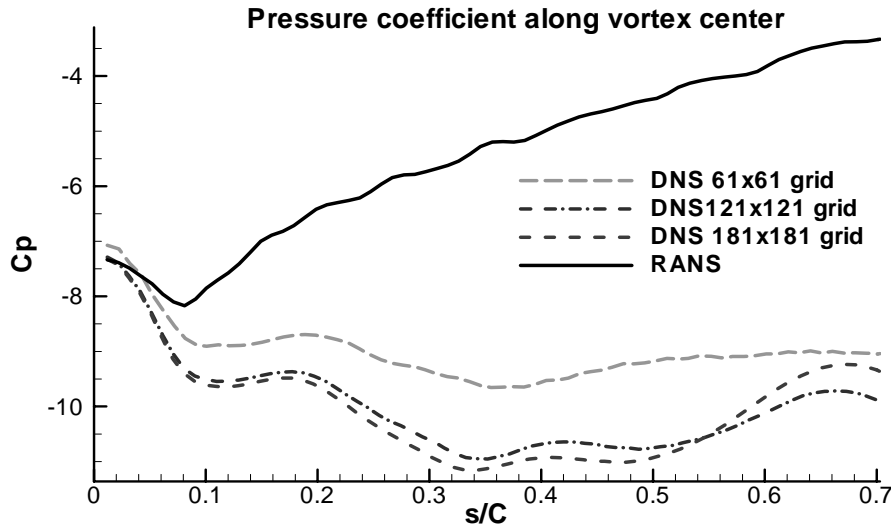


Figure 5. Comparison of the variation of the pressure coefficient along the vortex centerline between the RANS solution and the present Navier-Stokes numerical simulations with three different grid resolutions.

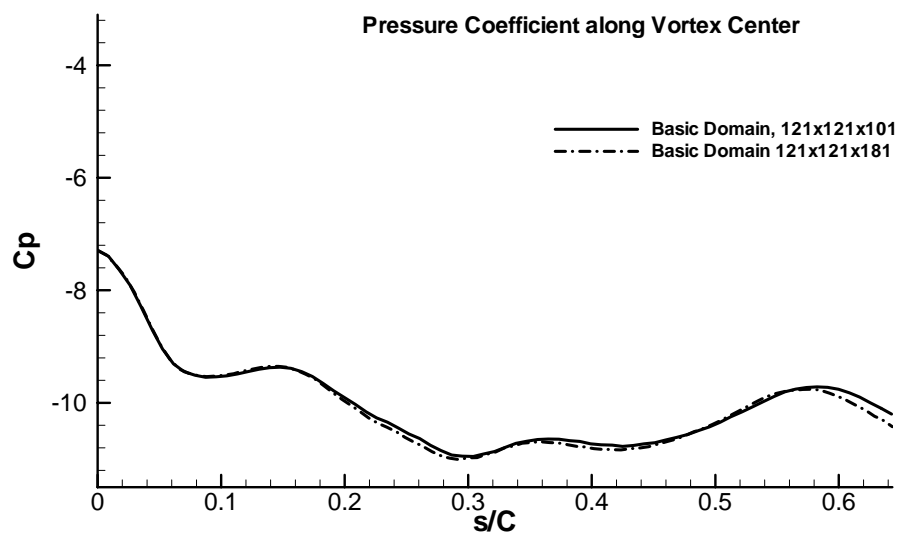


Figure 6. Comparison of the pressure coefficient variation along the vortex centerline for two streamwise grid resolutions.

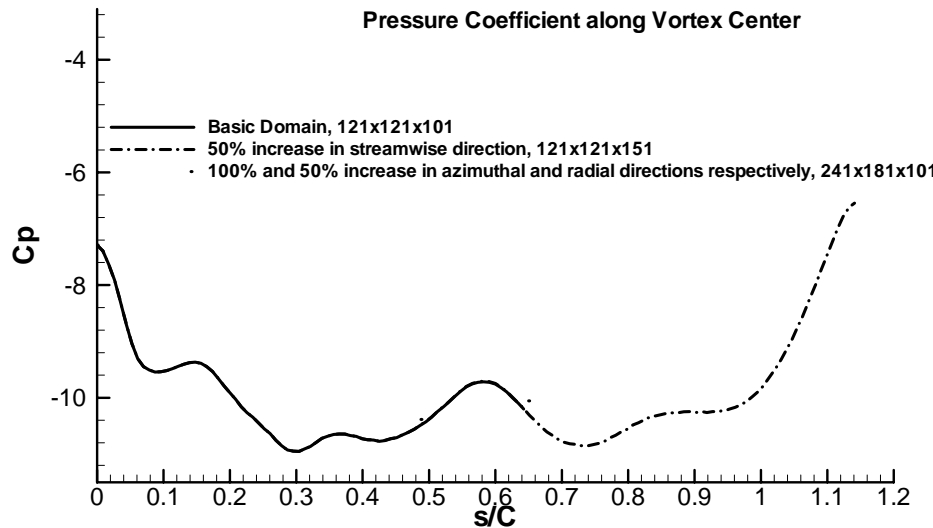


Figure 7. Comparison of the pressure coefficient variation along the vortex centerline for three computational domain sizes.

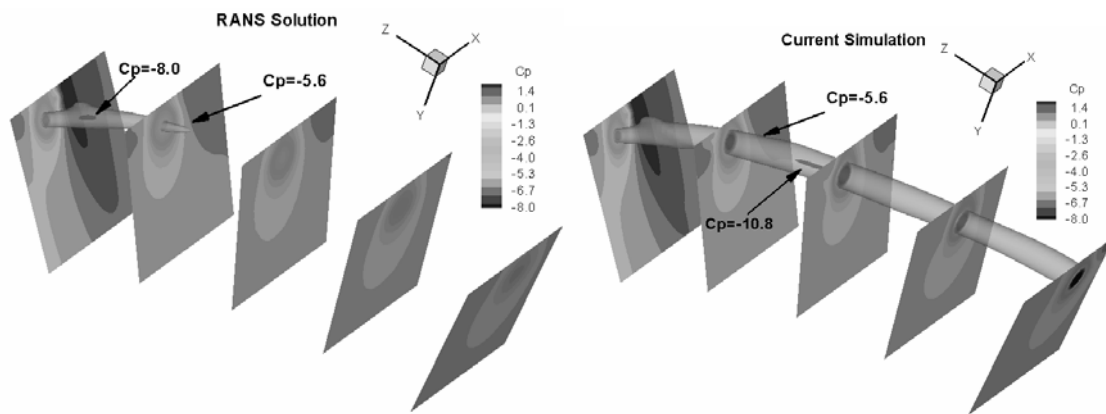


Figure 8. Iso-pressure surfaces at various cavitation numbers as obtained by the RANS solution and the present Navier-Stokes numerical solution with the 121x121x101 grid. This is equivalent to showing cavitation extent at these cavitation numbers.

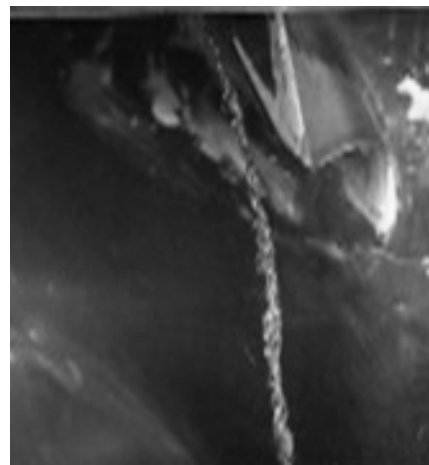


Figure 9. Fully developed cavitation in the vortex core at $\sigma = 5.6$ (Chesnakas and Jessup 2003).

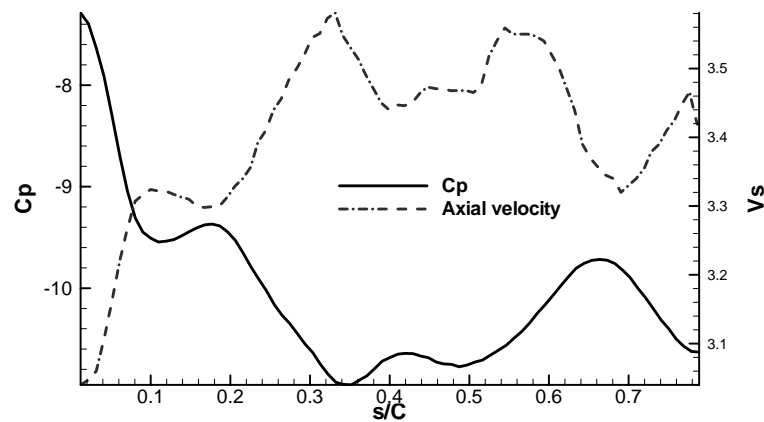


Figure 10. Pressure coefficient and axial velocity as a function of the distance from the tip trailing edge.

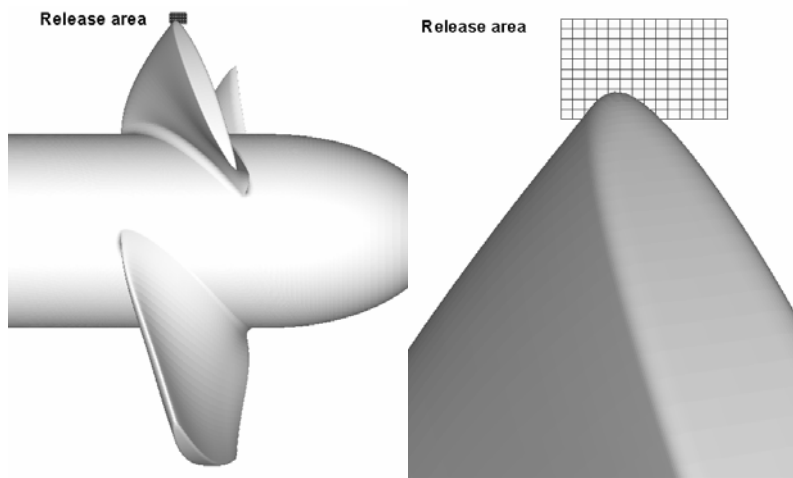


Figure 11. The location of the release area for establishing the “window of opportunity”.

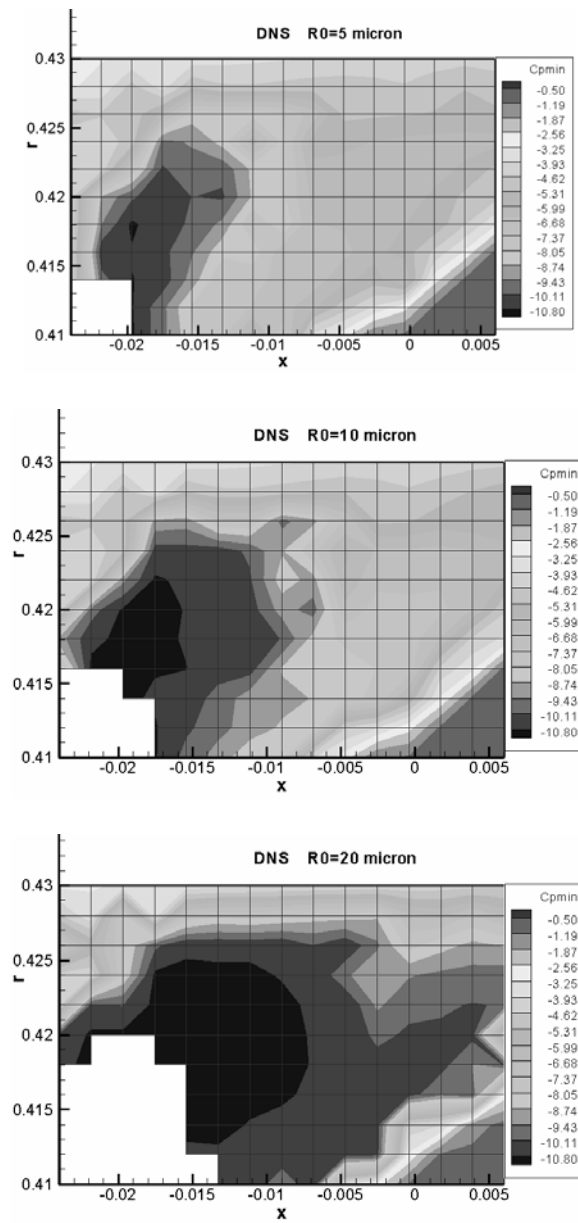


Figure 12. Contours of the bubble encountered $C_{p\min}$ for released nuclei with $R_0=5$, 10, and 20 microns.

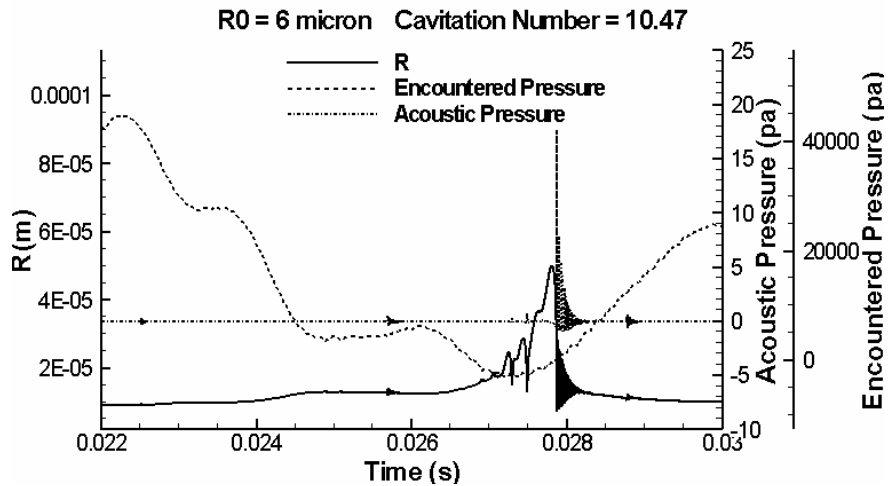


Figure 13. Bubble radius, emitted acoustic pressure signal, and encountered pressure during a cavitation event for $R_0 = 6\mu\text{m}$ at $\sigma=10.47$.

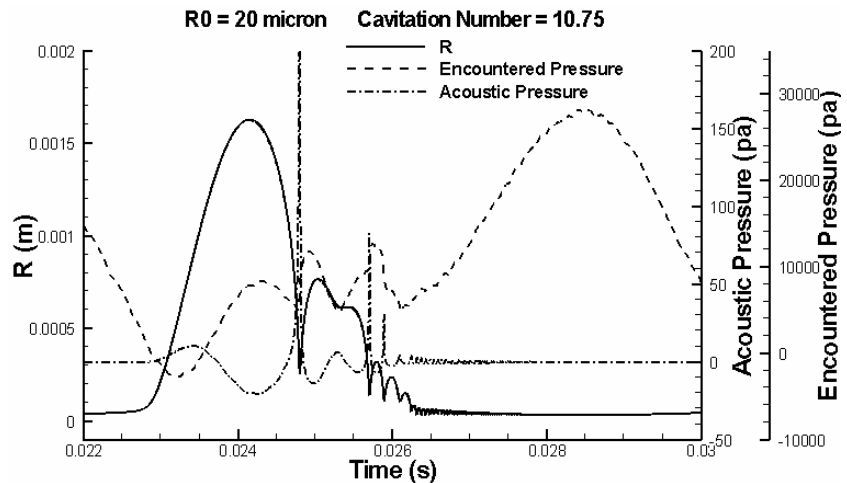


Figure 14. Bubble radius, emitted acoustic pressure and encountered pressure during a cavitation event for $R_0 = 20 \mu\text{m}$ at $\sigma=10.75$

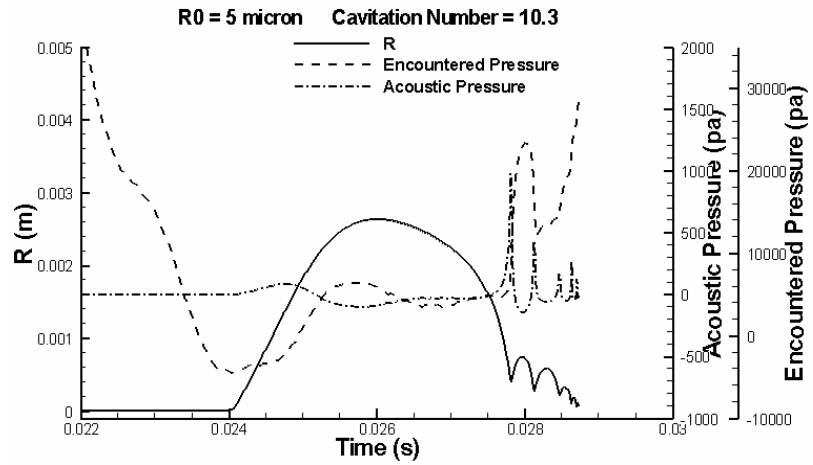


Figure 15. Bubble radius, emitted acoustic pressure and encountered pressure during a cavitation event for $R_0 = 5 \mu\text{m}$ at $\sigma=10.3$.

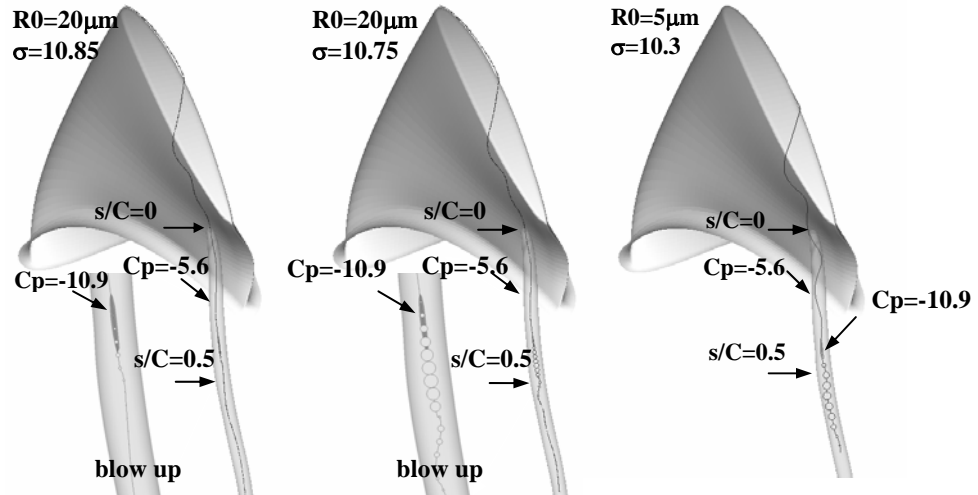


Figure 16. Bubble trajectories and size variations during a cavitation event for three different initial radii and cavitation numbers. Also shown are some iso-pressure contours.

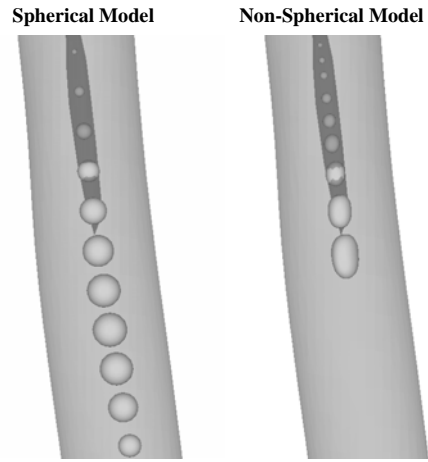


Figure 17. Computed bubble sizes and shapes using both spherical and non-spherical models shown with two levels of iso-pressure for $R_0 = 20 \mu\text{m}$ at $\sigma = 10.75$.



Figure 18. Computed bubble sizes and shapes of non-spherical modes for $R_0 = 20 \mu\text{m}$ at $\sigma = 10.85$.

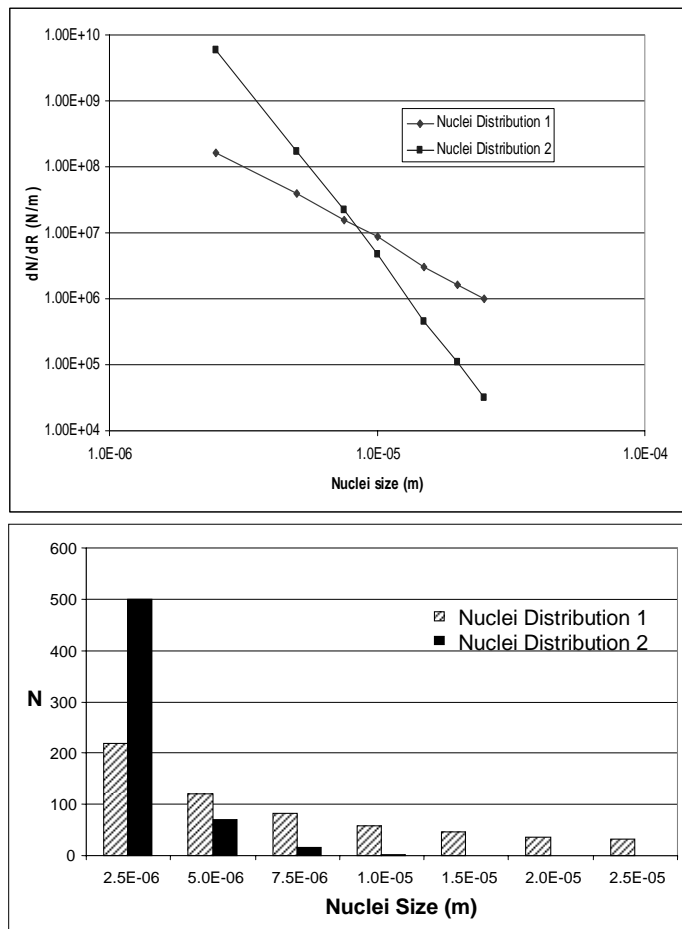


Figure 19. Nuclei size distribution and number of nuclei released versus nuclei size for two different nuclei size distributions considered in this study.

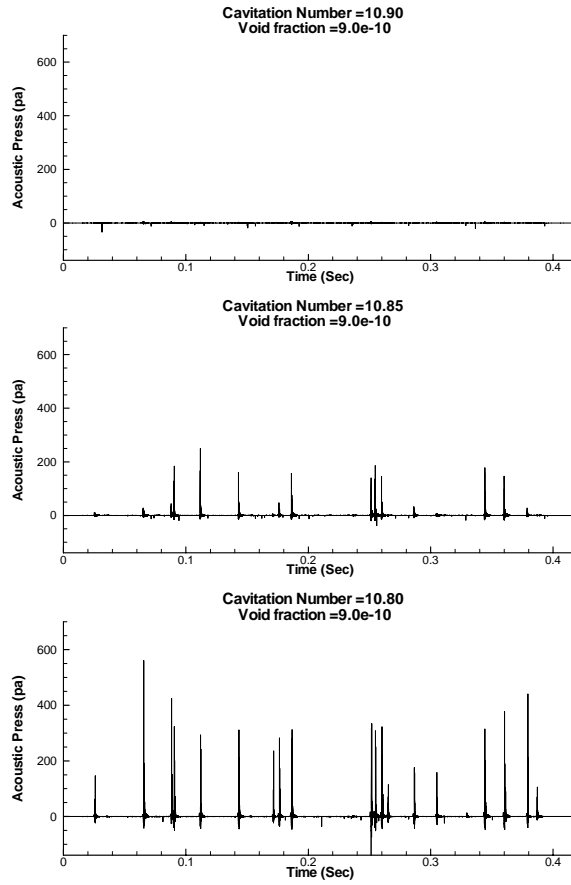


Figure 20. Acoustic signals for the large size nuclei distribution case at three different cavitation numbers.

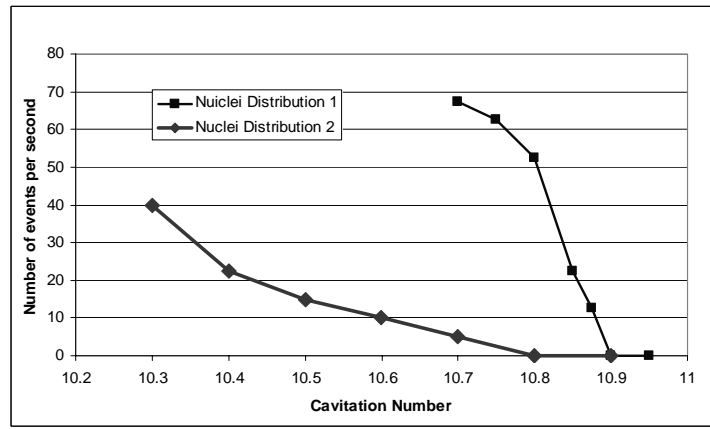


Figure 21. Number of events per second versus cavitation number for the nuclei size distributions shown in Figure 19.